Operando Characterisations of All-Solid-State Batteries

Ziyang Ning

St Cross College

Department of Materials

University of Oxford

A thesis submitted for the degree of

Doctor of Philosophy

Trinity 2021

Declaration of Originality

I, Ziyang Ning, hereby declare that this doctoral thesis, which is approximately 49,252 words in length, has been written by me that it is the record of work carried out by me. This thesis has not been submitted in any previous application for a higher degree.

Ziyang Ning

Trinity 2021

Acknowledgements

First, I would like to thank my supervisors, Prof. James Marrow and Prof. Peter G. Bruce, for their supervision and great support throughout my DPhil study to make this thesis possible. I will be forever grateful for their guidance and the great examples of scientists they set with their own dedication and devotion to science. I would like to express my greatest appreciation to the Chinese Scholarship Council for funding my DPhil study. In the same spirit, I would like to thank the Faraday Institution and the Henry Royce Institute for funding the research activities and providing the research equipment.

I must extend my appreciation towards my assessors, Prof. Richard Todd and Prof. Mauro Pasta, who had generously shared their wealth of knowledge and expertise during the completion of my studies. I would like to offer my special thanks to Dr. Paul Adamson for his help with my research and thesis revision. I owe my deepest gratitude to all my group members, both past and present, for their support and all the good times. In particular, I would like to thank Dominic Spencer Jolly for all the invaluable discussions we have had and his great support especially during the hardest times of my DPhil study. I will miss the days when we stood in the car park of PSI, ate pizzas, and discussed research and future plans after only three hours of sleep. I would like to thank Dr. Gareth O. Hartley, Dominic Melvin, Dr. Yang Chen, and Dr. Guanchen Li for their help and the fruitful discussions we have had, which helped advance my understanding of Li dendrite formation in all-solid-state batteries. My greatest appreciation also goes to Shengda Pu, Chen Gong, Dr. Boyang Liu, Dr. Xiangwen Gao, Dr. Junfu Bu, Dr. Jitti Kasemchainan, Dr. Stefanie Zekoll, Varnika Agarwal, Robin De Meyere, Thomas Zillhardt, Dr. Johannes Ihli, Dr. Anne Bonnin, Dr. Oxana Magdysyuk, Dr. Andrew Bodey, Dr. Silvia Cipiccia, and Dr. Genoveva Burca for their assistance with experiments. Special thanks to Shengda Pu for driving me between Oxford, Diamond Light Source, and ISIS Neutron and Muon Source in the late nights and wee hours for the preparation of samples and the remediation of my experiments. Speeding on the empty highway, singing along *The Scientist*

by Coldplay, with all the tiredness and exhaustion blown away by the wind, was the most poetic moment in my DPhil study.

Finally, I owe my deepest gratitude to my parents, Guanghui Ning and Li Yang. Thank you for your selfless love, your understanding, and all the sacrifices you made for me along the way. Without your support, I know I would not have got to where I am. My sincere thanks and love go to my girlfriend and bride-to-be, Yanru Zhou. Thank you for your love and support. The days with your company have been shining with a dazzling light in my life, illuminating the darkest valley that I walked through for the exploration of the unknown. Thanks for accepting who I am, for sharing my dreams, and for sharing the burdens and happiness in our past life and the life to come.

Abstract

The work in this thesis is focused on the mechanistic investigations of all-solid-state battery degradation associated with a lithium metal anode, via the development of operando characterisation techniques, and ultimately enabling the reliable application of lithium metal anode in all-solid-state batteries.

In **Chapter 3**, the interfacial degradation with the Li metal anode on Li stripping is explored. The void formation is recognised as a form of interfacial degradation that leads to voltage polarisation, local current flux enhancement, and ultimately failure of the cell. The evolution of voids in response to the passage of current is characterised, quantitatively analysed, and with the effects from stack pressure and cycling temperature determined.

Chapter 4 explores the solid electrolyte cracking and dendrite formation as a response to Li plating towards the Li metal anode. The spallation is observed as a way of cracking in solid electrolyte associated with the transverse crack that propagates across the whole cell. The crack propagation and the distribution of lithium inside the crack is tracked as function of the charge passed. The propagation process of Li dendrite and its implication are discussed.

In **Chapter 5**, models are proposed to explain the dendrite initiation and propagation in all-solid-state batteries based on experimental observations. The assumptions and predictions of the models are explored and discussed. Guided by the models, effective approaches are explored to improve the performance the all-solid-state batteries.

Publication List

1. Ning, Z., Jolly, D. S., Li, G., De Meyere, R., Pu, S. D., Chen, Y., ... & Bruce, P. G. (2021). Visualizing plating-induced cracking in lithium-anode solid-electrolyte cells. *Nature Materials* (2021).

2. Kasemchainan, J., Zekoll, S., Jolly, D. S., Ning, Z., Hartley, G. O., Marrow, J., & Bruce, P. G. Critical stripping current leads to dendrite formation on plating in lithium anode solid electrolyte cells. *Nature Materials*, 18(10), 1105-1111 (2019).

3. Spencer Jolly, D., Ning, Z., Darnbrough, J. E., Kasemchainan, J., Hartley, G. O., Adamson, P., ... & Bruce, P. G. Sodium/Na β ″alumina interface: Effect of pressure on voids. *ACS Applied Materials & Interfaces*, 12(1), 678-685 (2019).

4. Spencer Jolly, D., Ning, Z., Hartley, G. O., Liu, B., Melvin, D. L., Adamson, P., ... & Bruce, P. G. Temperature Dependence of Lithium Anode Voiding in Argyrodite Solid-State Batteries. *ACS Applied Materials & Interfaces* (2021).

5. Rees, G. J., Spencer Jolly, D., Ning, Z., Marrow, T. J., Pavlovskaya, G. E., & Bruce, P. G. Imaging Sodium Dendrite Growth in All-Solid-State Sodium Batteries Using ^{23}Na T_2-Weighted Magnetic Resonance Imaging. *Angewandte Chemie International Edition*, 60(4), 2110-2115 (2021).

List of Abbreviations

ASSB	All-solid-state batteries
SE	Solid electrolyte
SEI	Solid electrolyte interphase
CCD	Critical current density
CCS	Critical stripping current density
CCP	Critical plating current density
WE	Working electrode
CE	Counter electrode
RE	Reference electrode
SPS	Spark plasma sintering
XRD	X-ray diffraction
PXRD	Powder X-ray diffraction
SEM	Scanning electron microscopy
BSE	Backscattering electrons
AE	Auger electrons
SE	Secondary electrons
EDX	Energy dispersive X-ray spectroscopy
FIB	Focused ion beam
DEMS	Differential electrochemical mass spectroscopy
SIMS	Secondary ion mass spectrometry
XCT	X-ray computed tomography
ROI	Region of interest
FOV	Field of view
DVC	Digital volume correlation
EIS	Electrochemical impedance spectroscopy
OCV	Open circuit voltage

AC	Alternating current
DC	Direct current
SIF	Stress intensity factor
THF	Tetrahydrofuran

Table of Contents

Chapter 1. Introduction

1.1 Introduction

The advancement of mankind is based on the advancement of energy utilisation, i.e. humanity's ability to use and store energy of different forms. The technical revolution in last few centuries was powered by variations of the combustion reaction, the fire that marked the dawn of humanity. But industrialisation and associated improvement in quality of life comes at a price: pollution of the environment and the emission of greenhouse gases that drives global climate change. If humankind is to minimise its greenhouse gas emissions and environmental pollution, the combustion of fossil fuels must be replaced by the usage of renewable energy resources. However, due to the intermittent nature of renewable energy resources, energy storage systems are needed. For high energy density and easy assembly, rechargeable Li-ion batteries have been chosen as one of the most promising solution to energy storage of renewable energy systems.

Apart from energy storage, since the initial commercialisation by Sony in 1991, rechargeable Li-ion batteries have been developed to power an increasingly diverse range of applications[1,2]. As each application has intrinsically different requirements, the batteries must be improved from every dimension (energy density, rate performance, lifetime, safety, etc.) to achieve the performance that each application demands, especially the burgeoning market of portable devices and electric vehicles.

Tremendous efforts have been made to optimise the performance of Li-ion batteries by developing better cathode and anode materials. The huge difference in capacity between Li metal and the other negative electrodes makes Li metal the optimal anode for Li-ion batteries. However, due to the unstable and flammable nature of the liquid electrolyte, viable application of Li metal anode in rechargeable Li-ion batteries have not yet been achieved, despite all these research efforts.

The all-solid-state battery, where the liquid electrolyte is replaced with a solid electrolyte, is a promising future direction for battery research. Thanks to the rigid nature of solid electrolyte, it is believed to be able to suppress the Li dendrite growth, thus to enable the use of Li metal anode. With much lower flammability and toxicity, all-solid-state batteries can also enhance the safety and durability of batteries, while simultaneously improve the versatility in cell-assembly and design, due to the removal of separator and anodic current collector.

Despite appearing simple at first glance, the usage of Li metal anode in all-solid-state batteries is still facing grand challenges for both charge and discharge. Extensive efforts are required to fully understand the fundamental mechanisms behind the interfacial degradation and contact loss during discharge; and more critically, the inevitable dendrite ingress on charge.

This chapter aims to serve as an introduction to the work performed in this thesis and summarises the recent advances in understanding the degradation and failure of all-solid-state batteries with alkali metal anodes, and the remaining challenges. Firstly, a general introduction to Li-ion batteries and its challenges when using a Li metal anode is given. The concept of all-solid-state batteries is then proposed, with its advantages over liquid-state batteries demonstrated. The main section of this chapter focuses on the modes of degradation and failure in all-solids-state batteries on charge and discharge. Recent investigations of cell failure using X-ray computed tomography have also been summarised. Finally, an insight into the specific aims of this work is given.

1.2 All-solid-state batteries and challenges

1.2.1 Fundamentals of Li-ion batteries

A battery consists of several electrochemical cells that are connected in series or in parallel to provide the voltage and capacity the device demands. Each cell is composed of a positive electrode (cathode) and a negative electrode (anode), separated by an electrolyte, which enables

ion transfer between two electrodes. Batteries can be divided into two types: primary batteries (non-rechargeable) and secondary batteries (rechargeable). Lithium batteries, widely confused with Li-ion batteries, particularly refers to primary batteries with a Li metal anode, where the electrochemical reactions are irreversible. Due to their high cost per unit and outstanding charge density, primary lithium batteries have been widely used in long-life, critical devices, such as pacemakers or watches. Li-ion batteries, on the contrary, are rechargeable batteries, where the electrochemical reactions are reversible for discharge/charge. With superior volumetric and gravimetric energy densities among rechargeable batteries, and a much lower cost compared with primary batteries, Li-ion batteries have been widely employed to power portable devices and electric vehicles.

Chemistry, performance, cost and safety characteristics vary across different types of Li-ion batteries. But the current Li-ion batteries that are conquering the market are based on the use of a graphite anode instead of Li metal, and use of a lithiated transition metal oxide cathode. The layer-structured anode and cathode allow the reversible Li-ion intercalation/deintercalation cycles during charge and discharge. The reactions inside Li-ion batteries are illustrated in an example of graphite-$LiCoO_2$ cell shown in **Fig. 1.1** below[3].

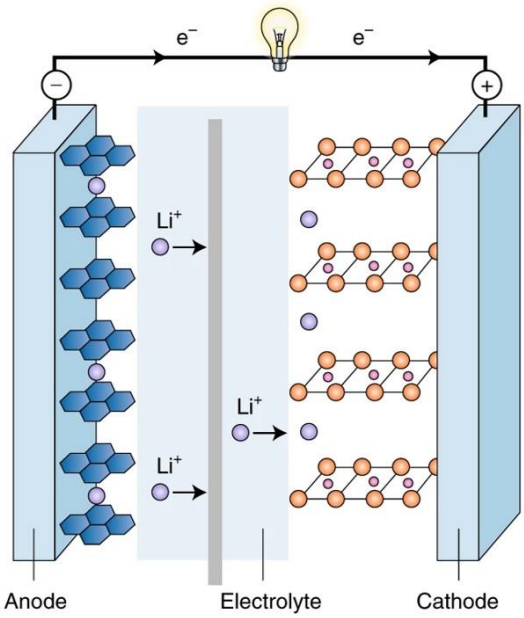

Fig. 1.1. Schematic illustrating the reactions that take place in a Li-ion battery during battery discharge. (adapted from Goodenough[3])

The corresponding electrochemical reactions at positive and negative electrodes, and the total reaction are also discussed below to reveal the mechanisms of reactions.

$$\text{Positive electrode: } LiCoO_2 \rightleftharpoons Li_{1-x}CoO_2 + xLi^+ + xe^- \quad (1.1)$$

$$\text{Negative electrode: } 6C + xLi^+ + xe^- \rightleftharpoons Li_xC_6 \quad (1.2)$$

$$\text{Total reaction: } 6C + LiCoO_2 \rightleftharpoons Li_xC_6 + Li_{1-x}CoO_2 \quad (1.3)$$

On charge, Li^+ ions migrate from the cathode through the electrolyte medium to the anode, where the Li^+ ions are intercalated into the layers of graphite, which at the same time regains electrons from the external current. The intercalation of Li into graphite occurs via first-order phase transition reactions through stages such as LiC_{24}, LiC_{27}, and LiC_{12} to a stable condition of LiC_6[4]. The opposite deinsertion reaction occurs upon discharging. Li^+ ions migrate from the anode to the cathode, and are accommodated within the structure of the cathode materials. To

maintain charge neutrality, one electron per Li^+ ion is simultaneously released to the external circuit, powering the connected device.

While the application of graphite with an inherent layered-structure as the anode seems straightforward compared with cathode materials, the discovery and development of cathode candidates were actually far ahead of the anode. The lack of a viable anode remains a long-term bottleneck that impedes the commercialisation of rechargeable Li-ion batteries.

The concept of electrochemical intercalation and its potential application was clearly defined by 1972[5]. The discovery of materials that can react with alkali metal in a reversible way laid the foundation for the development of high-energy rechargeable Li systems. In 1972, Ti_2S was introduced by Whittingham as the positive electrode in a battery against a Li metal anode[6]. Ti_2S with a favourable layered-structure and outstanding electrical conductivity was the best intercalation compound identified at the time. In spite of its high capacity and reversible cycling, due to the relatively low voltage of the cell, and crucially the dendrite formation resulting from the repeated deposition of the Li metal anode, the project was abandoned only a few years later.

In the meantime, significant advances in intercalation materials also occurred in oxides, which have the benefits of high capacities and voltages. P.A. Christian showed that V_6O_{13} with three-dimensionally bounded host lattices can function well as a cathode material, which broke the belief that reversible intercalation and sufficient diffusivity can only be achieved in van der Waals compounds[7]. Later, Goodenough investigated Li_xMO_2 (where *M* is Co, Ni, or Mn) as cathode materials, a family of compounds that are still used extensively in today's batteries for their outstanding specific capacities[8,9]. Significantly, the well-functioning transition metal oxide cathodes also suggest that fabricating a battery in a discharged state is feasible, as well as a charged state, which means Li metal anode as a Li^+ source for the cathode is not essential in battery design[3,10]. The toxicity, cost, and structural instability of $LiCoO_2$ also led to extensive research efforts towards safer, cheaper, and more stable cathode materials. Olivine-type or spinel-type materials such as $LiFePO_4$ and $LiMnPO_4$ have shown to be promising alternatives, especially in applications where the specific capacity is not so critical[11].

Despite the extensive discovery of cathodes, the concept of Li-ion was only implemented almost ten years later, owing to the lack of a suitable material for the negative electrode. Lithium dendrite formation is unavoidable in a Li metal/liquid electrolyte combination, as the uneven Li growth on the Li metal anode will eventually turn into a dendritic structure, penetrate the separator, and lead to a short-circuit. The initial approach to avoid the dendrite issue is to replace the Li metal anode with an alloy of Al. However, due to the extreme volume expansion and contraction during charge and discharge respectively, the alloy anode only survives for a limited number of cycles. Inspired by Goodenough's discovery of cathode materials in a discharged state, Akira Yashino explored graphitic carbon as an intercalation type anode material, which showed decent reversibility (>80% capacity retention after 500 cycles) with carefully selected electrolytes[12]. With a combination of graphitic carbon as anode, and $LiCoO_2$ as cathode, the C/$LiCoO_2$ rocking-chair cell was created, and later commercialised by Sony in 1991. With a potential exceeding 3.6 V and gravimetric energy density as high as 120 – 150 Wh kg^{-1}, batteries of this type remains dominant in various applications till today[13,14].

Though the C/$LiCoO_2$ battery has shown to be successful, further exploration of new anode materials hasn't stopped. Silicon (Si) and Tin (Sn) were investigated as promising anode candidates, due to their outstanding specific capacity[15–17]. However, such alloy-type anode materials share the short-coming of rapid degradation in a few cycles, as the volume-change degradation of Al-based alloy anode also applies to the other alloy anodes. Lithium titanium oxide ($Li_4Ti_5O_{12}$) has also been studied as a promising anode candidate due to its structural stability even at high rate with negligible volume change[18]. However, due to its high potential compared with graphite, which effectively reduces the output voltage of the cell, and low specific capacity, the application of $Li_4Ti_5O_{12}$ has been limited.

There are still huge ongoing efforts focused on searching for graphite alternatives with both larger capacities and slightly more positive intercalation voltages compared to Li/Li^+. Li transition metal nitrides ($Li_{3-x}Co_xN$), intermetallic alloy (Cu_6Sn_5, InSb, etc.), and MO-type rocksalt (where M is Co, Ni, Fe, Cu or Mn) have all been investigated as anode materials, while

none of them have outperformed graphite, and become commercialised[19]. The persistent pursuing for a better anode is driven by the fact that graphite, with a specific capacity of 360 mAh g^{-1}, is far from an ideal anode compared with Li metal anode, where the latter is the most electropositive (-3.04V versus standard hydrogen electrode), and the lightest (0.53 g cm^{-3}) metal, with a specific capacity 10 times higher than that of graphite (3860 mAh g^{-1}). So, what is preventing us from using Li metal anode in a rechargeable Li-ion battery?

1.2.2 Challenges of Li anode with liquid electrolyte

For the Li metal anode, the deposition of Li on charge and the desorption of Li on discharge are normally termed as plating and stripping, respectively. The major problems of Li metal anode to overcome are: (i) dendrite formation, (ii) electrolyte consumption as a result of uncontrolled reaction with metallic lithium, (iii) mechanical instabilities including fracture of the solid electrolyte interphase (SEI) layer and resultant low Coulombic efficiency (CE)[20].

The term *dendrite* comes from the description of a typical crystallisation process. The dendritic growth of a metal during deposition is intrinsically preferred, and this remains a key obstacle for the commercialisation of Li metal anodes[21]. A variety of causes hold for the tendency of deposited Li to grow to form a whisker (dendrite): (i) capillary effects which restrict the transport field to the tip of any protrusion at the interface thus favour lengthening and branching of Li metal; (ii) deposition of Li at an interfacial protrusion may lower the Ohmic resistances for ion transport, and thus is electrochemically preferred; (iii) due to lower surface energy, deposition on an existing interfacial protrusion is preferred against creating new nucleation sites; (iv) concentration polarisation ($t_{Li^+} < 1$) will lead to preferred growth of lithium dendrites; (v) the asymmetry in cycling, which leads to morphological inhomogeneities on the Li anode, will accelerate the formation of dendrites with local current hot spots.

Whilst the intrinsic preference to form Li whiskers remains a grand challenge for the application of Li metal anodes, the interactions between Li and liquid electrolyte adds to the difficulty and

complexity of commercialisation[22]. Due to its high reactivity, Li metal inevitably reacts with liquid electrolytes once in contact and subsequently forms a SEI (solid electrolyte interface) film on the electrode/electrolyte interface[23]. While the formation of SEI consumes the Li metal anode, the SEI film could sometimes serve as a protective layer between the Li metal anode and liquid electrolyte[24]. Whether the SEI is protective or not largely depends on the ion/electron transport properties of the SEI film. An ideal SEI film should be a perfect ionic conductor but electronic insulator, which only allows Li deposition to occur between the Li metal anode and the SEI. However, SEI films are commonly ion-electron-mixed-conductors, which allows Li to be freshly plated at in the interface between the SEI and the liquid electrolyte[25]. Such deposition will lead to a continuous reaction between Li metal and liquid electrolyte, thus continuous growth of SEI, which in return makes Li deposition at the SEI/liquid electrolyte interface more preferred. The consumption of Li metal by continuous reaction directly leads to low coulombic efficiency of the cell and severe cell degradation during cycling.

Apart from continuous reactivity, mechanical stability of the SEI film also plays a critical role in determining the viability of Li metal anode, given the considerable volume change during charge and discharge. While the SEI film forms at the pristine state when the Li metal anode and the liquid electrolyte are in contact, Li plating on charge will lead to volume expansion of the Li metal anode and subsequently breakage of the SEI film. A local current density hot-spot that leads to the dendritic growth of Li metal will form where the SEI breakage occurs and Li metal is exposed to the liquid electrolyte, due to the relatively lower ohmic resistance. As well as volume expansion on Li plating, volume contraction on stripping could also be detrimental. While Li plating leads to interfacial protrusion of deposited lithium, the uneven stripping behaviour disintegrates the previously plated Li into Li debris. As the stripping further proceeds, and with the bad mechanical stability of the SEI film, the Li debris detaches from the bulk Li anode and loses electrochemical activity[26]. This part of Li is termed as “inactive lithium” or “dead lithium”, which contributes significantly to the low coulombic efficiency of Li metal

anode[27]. The morphological evolution of Li metal anode on plating and stripping is well presented in **Fig. 1.2** below.

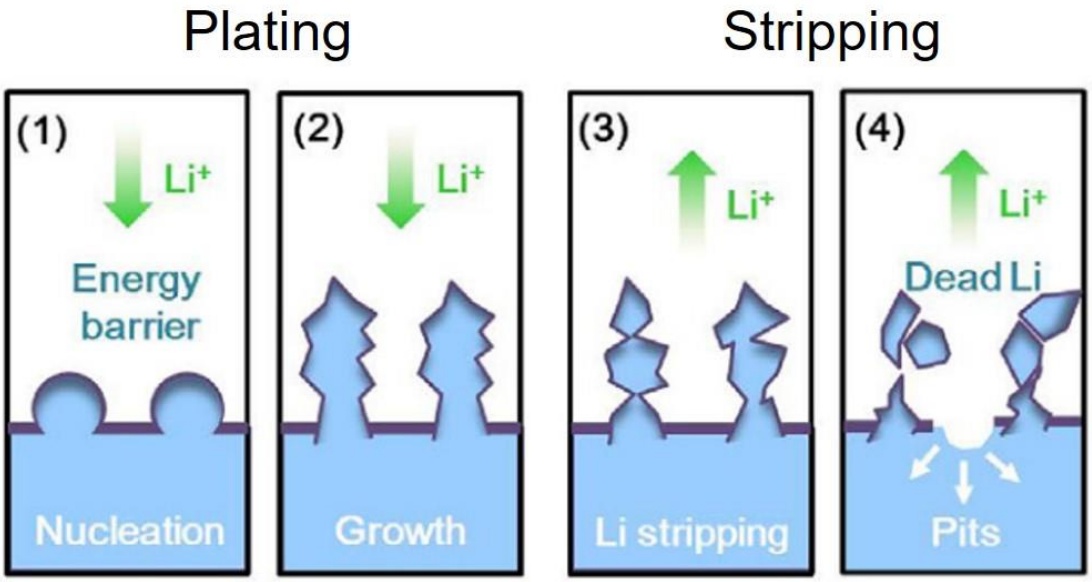

Fig. 1.2. Schematic outlining the schematic evolution of Li metal anodes during plating and stripping. (Reproduced from Dasgupta et al.[26])

Facing the great potential of Li metal anode and the remaining challenges, remarkable efforts have been made to explore preventative strategies from various perspectives including manipulation of electrolyte chemistry, deposition of an artificial SEI layer to block interfacial reaction, and a composite anode to host Li while serving as a conduction framework[28–30]. While none of the strategies have been proven to solve the issues with the Li metal anode completely, due to the inevitable reaction, it is worth investigating whether or not liquid electrolytes can be replaced by solid electrolytes, which have the potential to suppress the reactivity and dendritic growth of Li metal anode.

1.2.3 Why all-solid-state batteries?

Solid electrolytes can be divided into two major types: inorganic solid electrolytes, which are ceramics in nature; and organic solid electrolytes, which are polymers. Polymer electrolytes

appear to be a more promising candidate in the first place, as they are compliant, easy to manufacture, and able to compensate for the volume changes of the anode and cathode via elastic or plastic deformation[31]. However, solid polymer electrolytes suffer from a much lower conductivity compared with liquid electrolyte, which requires the cell with solid polymer electrolyte to be operated at 80 °C to achieve a reasonable speed of charge/discharge[32,33]. Moreover, while the compliant nature of solid polymer electrolyte allows it to maintain an intimate contact with electrode materials, it also allows easy lithium dendrite penetration through the solid polymer electrolyte that leads to cell failure[34].

The inorganic solid electrolytes, with their non-flammability, lower toxicity, much faster conduction kinetics compared with solid polymer electrolytes, and their rigid nature, which in principle suppresses dendrite formation, have been explored as a promising alternative to traditional liquid electrolyte[35]. The solid electrolyte can act as both an ionic conductor and a physical separator between two electrodes, as it is intrinsically a physical barrier for dendrite penetration. Therefore, all-solid-state batteries can simplify the cell design by reducing the use of inactive components and safety packaging in the cell, thus increasing the battery's energy density[36].

In addition, while the degradation and dendrite formation in liquid state batteries are largely related to the formation of an unstable SEI, inorganic solid electrolytes present much better stability against Li metal, which could resolve the issue of interfacial instability. Although some solid electrolytes could form an ion-electronic-mix-conductor with Li metal, thus continuously consumes the Li metal anode, most promising solid electrolyte candidates form no interphase or a self-limiting interphase of a few nm when in contact with Li metal, which guarantees a higher coulombic efficiency and longer battery lifetime[37–40].

The replacement of liquid electrolyte with inorganic solid electrolyte could also deliver a wider range of cell operation temperature, as electrolyte freezing, boiling, and decomposition at extreme temperatures wouldn't hold for inorganic solid electrolytes. Moreover, the low activation energies for fast-ion conduction in solid electrolyte help reduce the variation of ionic

conductivity with temperature change, ensuring reliable operation in a wide temperature range[41,42]. Due to the lattice-hopping-based conduction in inorganic solid electrolyte and a unity transference number, no bulk polarisation would be expected in all-solid-state batteries, potentially leading to higher power capabilities[43,44].

Despite all these advantages, the wide application of all-solid-state batteries is still a work in progress. While the drawbacks of liquid electrolytes have been largely overcome, different but significant challenges have been identified for all-solid-state batteries with Li metal anode, and remain to be resolved.

1.2.4 Challenges facing all-solid-state batteries

Despite all the aforementioned disadvantages of liquid electrolyte, good wetting and mobility of liquid electrolyte allows it to easily infiltrate into porous electrodes and separator, providing fast ion transfer between electrodes. Therefore, only a small amount of liquid electrolyte needs to be used in cell manufacturing along with a very thin separator (~10 μm). However, for all-solid-state batteries, not only the separator needs to be replaced with solid electrolyte, but also the gap between electrode particles needs to be filled with solid electrolyte, which significantly increases the mass of inactive components in the cell. As shown in the calculation done by Janek and Zeier, only with a Li metal anode, that has a theoretical energy density of 3860 mAh g^{-1} can a significant improvement in energy density (volumetric and gravimetric) be achieved, given the large loading of solid electrolyte, **Fig. 1.3**[32]. So, the usage of Li metal anode in all-solid-state batteries is not just preferred, but a must, which is still facing various challenges.

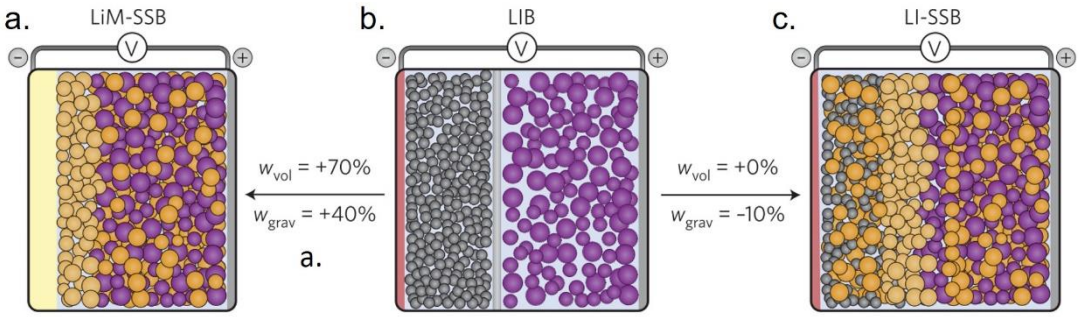

Fig. 1.3. Schematic of battery architectures for conventional Li-ion batteries (b) and all-solid-state batteries (**a** & **c**). The volumetric and gravimetric energy densities are represented by w_{vol} and w_{grav}. Compared with a conventional Li-ion battery, replacement of the separator to a solid electrolyte of the same thickness, leads to no improvement in volumetric energy density, and decrease in gravimetric energy density (**b** to **c**). Only with the application of Li metal anode, can the volumetric and gravimetric energy densities of the cell be significantly improved (**b** to **a**). (Adapted from Janek and Zeier[32])

The first and most pressing challenge to deal with is the lithium dendrite penetration into solid electrolytes during cell cycling. While it is believed that solid electrolytes with their rigidity and considerable shear moduli should be capable of suppressing and even blocking completely the formation of the dendrites[45,46], recent reports have demonstrated that a soft metal such as lithium, is still able to penetrate into the solid electrolyte and fracture the electrolyte into pieces[47–50]. Extensive efforts have been made to fully understand the fundamental mechanisms of lithium dendrite initiation and propagation in all-solid-state batteries, however, no consensus on the failure mechanism and no effective strategies to prevent dendrites have been achieved. With a unity transference number, the ion-depletion based dendrite theory that governs liquid electrolyte and solid polymer electrolytes apparently does not hold for all-solid-state batteries. The observation of dendrite penetration in all-solid-state batteries, and the models proposed so far will be discussed in more details in **Chapter 1.4**.

The second challenge is stabilisation of interfaces. While solid electrolytes present better stability against Li metal compared with liquid electrolyte, the formation of ionically resistive

or electron-conducting decomposition products can inhibit the performance of all-solid-state batteries[51]. In addition, with the narrow electrochemical stability window of solid electrolytes, stable interfaces with both Li metal anode and cathode materials can hardly be achieved at the same time. Almost all the promising candidates of solid electrolytes, which present desirable ionic conductivities ($> 1\times10^{-3}$ S/cm) and good stability against Li metal anode, are not stable with commercially used cathode ($LiCoO_2$, NMC, etc.). The interfacial reactions between the solid electrolyte and the cathode particles could be more detrimental than the anodic interface, as cathode particles require both electronic and ionic conduction, and the decomposition product at the cathode interface can easily block one of these conduction processes[52–54]. Numerous experimental and computational efforts have been made to address the issues related to interfacial stability, elucidating a rational approach towards a combination of two solid electrolyte materials to guarantee the anodic as well as cathodic stability.

The third challenge is maintenance of physical contact in all-solid-state batteries. As solid electrolytes cannot infiltrate the gaps between electrode particles as the liquid electrolyte does, the ionic diffusion in all-solid-state batteries relies on the contact of solid particles. In addition, due to the rigidity of the solid electrolyte[55], volume change cannot be easily compensated by elastic or plastic deformation as with a solid polymer electrolyte. Therefore, the point contacts between electrolyte and electrodes are particularly sensitive to stress developed on electrochemical cycling of electrode materials, leading to crack formation and interfacial delamination, and subsequently cell degradation[56–58]. Apart from the contact issues on the cathode side, the contact between Li metal anode and solid electrolyte also remains a challenge, as the interfacial contact can be lost due to localised inhomogeneous stripping at a rate faster than that of lithium being replenished to the interface[59,60]. Such contact loss can lead to locally enhanced current density, and eventually dendrite formation when the local current density exceeds a critical level[61]. It is imperative to alleviate the issue of physical contact in all-solid-state batteries. Effective strategies must be based on a mechanistic understanding of interfacial contact loss and potential mechanism to maintain the contact.

The solutions to these challenges hinge on our mechanistic understanding of the corresponding degradation process. Therefore, a standard solid electrolyte system with great commercialisation potential must be selected to provide further insight into cell failure via experimental investigation.

1.2.5 Sulphide-based solid electrolytes

Due to the step improvement in energy density, safety, and cell performance that all-solid-state batteries could potentially bring about, extensive efforts have been made to explore promising solid electrolyte candidates. Among them, the most promising electrolytes can be divided into two types: oxide-based solid electrolytes and sulphide-based solid electrolytes. Common oxide-based electrolytes include NASICON-type electrolyte (e.g. $Li_{1+x}Al_xGe_{2-x}(PO_4)_3$), Perovskite-type electrolyte (e.g. $Li_{3x}La_{2/3-x}TiO_3$), Garnet-type electrolyte (e.g. $Li_7La_3Zr_2O_{12}$), LISICON-type electrolyte (e.g. γ-Li_3PO_4), and LiPON solid electrolyte ($Li_xPO_yN_z$, $x=2y+3z-5$)[62]. Solid oxide electrolytes present good environmental stability against the ambient air, therefore manufacturing is much easier compared with air or moisture sensitive materials. They have a relatively wider electrochemical stability window among solid electrolyte candidates, mostly presenting good stability against lithium metal. However, the ionic conductivities of solid oxide electrolytes are barely satisfactory (1×10^{-5} ~ 1×10^{-3} S/cm), which remains the main obstacle towards commercialisation. In addition, the rigidity of oxide electrolyte particles results in their poor ability to compensate volume changes during cycling, poor wetting of the electrode particles, and overwhelming grain boundary resistance. Costly sintering at high temperature (~1200 ℃) is required to densify the solid oxide electrolyte pellets, in order to reduce the grain boundary resistance, which adds to the difficulty in large-scale application[63,64]. Lastly, oxide-based solid electrolytes present high interfacial resistance. This can be eliminated by complex surface treatment as recently reported[65], but surface treatments involving polishing and high temperature heating in vacuum or Ar-filled atmosphere, inevitably adds to the complexity of electrolyte processing.

Meanwhile, sulphide-based solid electrolytes have been considered as more promising candidates, as they are soft and more conductive than the oxides. The more compliant nature of sulphide-based solid electrolytes allows them to maintain better interfacial contact with electrode particles, and to achieve a satisfactory relative density merely by cold mould pressing[55]. Although almost all the sulphide-based solid electrolytes are not thermodynamically stable against lithium metal, some of them form a self-limiting interphase with lithium metal, which does not significantly increase the interfacial resistance[66,67]. Moreover, wettability between lithium and sulphide-based solid electrolytes is better than that of the oxides, which inhibits the inhomogeneous plating/stripping of lithium during cycling to some extent[68,69]. The main drawback of sulphide-based solid electrolytes is that they are highly reactive to moisture to from toxic H_2S, which causes the strict requirements for the preparation of sulphide electrolytes. However, large-scale production of sulphide-based electrolytes is still feasible within an acceptable cost in a dry room. The main types of promising sulphide-based solid electrolytes are Li_2S-P_2S_5 based electrolytes, Thio-LISICON, and argyrodite electrolytes. A brief history of each type of sulphide electrolyte along with their properties will be discussed to justify the choice of argyrodite as an ideal system for mechanistic studies.

The sulphide-type solid electrolytes are closely related to a LISICON-type solid electrolyte, γ-Li_3PO_4, with O^{2-} replaced by S^{2-}. Weaker interaction between S^{2-} and Li^+ than that between O^{2-} and Li^+ contributes towards higher Li-ion mobility, thus higher ionic conductivities than the oxide counterparts. In 2000, Kanno et al. replaced O^{2-} with S^{2-} in LISICON-type solid electrolyte for the first time, and prepared six different species of thio-LISICON electrolytes: Li_2GeS_3, Li_4GeS_4, Li_2ZnGeS_4, $Li_{4-2x}Zn_xGeS_4$, Li_5GaS_4, and $Li_{4+x+\delta}(Ge_{1-\delta'-x}Ga_x)S_4$[70]. The last two types were synthesised based on Li_4GeS_4 by substituting the Li^+ with Zn^{2+}, and Ge^{4+} with Ge^{3+}. While the transition from oxide solid electrolyte to sulphide electrolyte apparently increases the complexity in electrolyte preparation, the benefit in ionic conductivity is disappointingly not rewarding. The $Li_{4+x+\delta}(Ge_{1-\delta'-x}Ga_x)S_4$ shows the highest ionic conductivity among the six species, and it was still only 6.5×10^{-5} S cm^{-1}. One year later, Kanno et al. prepared another

new thio-LISICON solid electrolyte $Li_{4-x}Ge_{1-x}P_xS_4$ based on Li_4GeS_4 via partially doping P^{5+} at Ge^{4+} sites[71]. The ionic conductivity of such thio-LISICON increases with P content and reaches a maximum of 2.17×10^{-3} S cm^{-1} for $x = 0.75$. Based on different superlattice structures, the $Li_{4-x}Ge_{1-x}P_xS_4$ system can be categorised into three composition regions: region I ($0 < x < 0.6$), region II ($0.6 < x < 0.8$), and region III ($0.8 < x < 1$). In 2011, Kamaya et al. synthesised a new thio-LISICON electrolyte $Li_{10}GeP_2S_{12}$, which fit into region II of thio-LISICON with $x = 2/3$, but exhibits a completely different structure. This electrolyte presents an outstanding ionic conductivity of 1.2×10^{-2} S cm^{-1} at 27 °C, comparable to that of liquid electrolytes[72]. The structure of $Li_{10}GeP_2S_{12}$ is shown in **Fig. 1.4**.

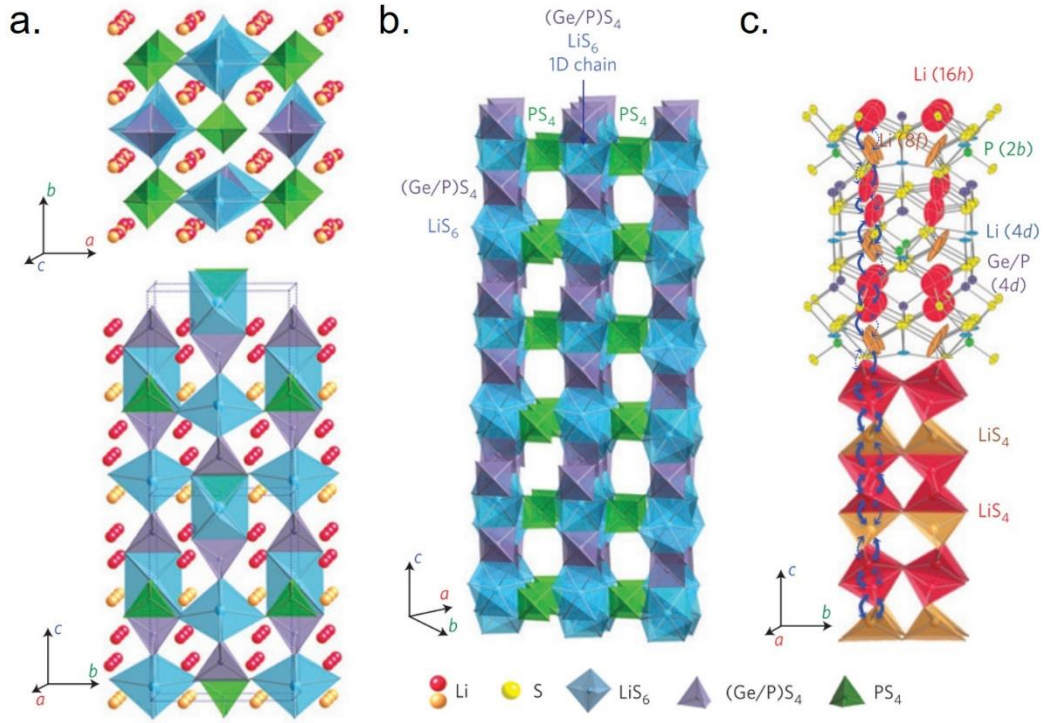

Fig. 1.4. Crystal structure of $Li_{10}GeP_2S_{12}$, **a.** framework and mobile Li-ions, **b.** framework structure showing 1D chains, **c.** conduction pathways of Li-ions. (Adapted from Mitsui et al.[72])

The 3D framework of $Li_{10}GeP_2S_{12}$ is composed of $(Ge_{0.5}P_{0.5})S_4$ tetrahedra, LiS_4 tetrahedra, LiS_6 octahedra, and PS_4 tetrahedra. The superior ionic conductivity originates from the 1-dimensional conduction pathways formed by the Li-ions inside the LiS_4 tetrahedra (16 h and 8 f sites). Assisted by first principles calculation, cation-substituted species of thio-LISICION,

$Li_{10\pm1}MP_2X_{12}$ (*M*=Ge, Si, Sn, Al, P; *X*=O, S, Se), were investigated by Ong et al[73]. It was predicted that $Li_{10}SiP_2S_{12}$, $Li_{10}SnP_2S_{12}$, $Li_{11}AlP_2S_{12}$, and $Li_9P_3S_{12}$ show similar properties with $Li_{10}GeP_2S_{12}$. In 2016, Kato et al. reported the Cl-doped Si-analogue of $Li_{10}GeP_2S_{12}$, $Li_{9.54}Si_{1.74}P_{1.44}S_{11.7}Cl_{0.3}$, which presents an unprecedented ionic conductivity of 2.5×10^{-2} S cm^{-1}, the highest among the reported Li-ion electrolytes[74].

Despite the outstanding conductivity of thio-LISICON, severe decomposition between $Li_{10}GeP_2S_{12}$ with Li metal anode was observed by Janek et al. using *in-situ* XPS[75]. Such instability apparently reduced the excitement about highly-conductive thio-LISICON in the field, as this makes the application of Li metal anode impossible, which is a significant advantage of all-solid-state batteries.

Prior to development of thio-LISICON solid electrolytes, extensive efforts have been made to study the glass and glass-ceramic Li_2S-P_2S_5. In 2005, Mizuno et al prepared 70 Li_2S-30P_2S_5 solid electrolytes of ceramic, glass, and glass-ceramic forms[76]. While glass and glass-ceramic samples showed satisfactory ionic conductivities of 5.4×10^{-5} S cm^{-1} and 3.2×10^{-3} S cm^{-1} respectively, ionic conductivity of the ceramic sample was much lower at 2.6×10^{-8} S cm^{-1}. Later, Hayashi et al. employed mechanical milling to prepare $x$$Li_2S$-(100-$x$)$P_2S_5$, which was much easier than the melt-quench method[77]. The ionic conductivity of various $x$$Li_2S$-(100-$x$)$P_2S_5$ solid electrolytes was found to increase with lithium amount, reaching a maximum of 2×10^{-4} S cm^{-1} with x = 75. However, by combining mechanical milling and heating, Hayashi et al. obtained glass-ceramic 80Li_2S-20P_2S_5 with an improved ionic conductivity of 9×10^{-4} S cm^{-1} [78]. The role of heating in increasing the ionic conductivity needs to be further investigated. Tatsumisago et al. made extensive efforts to study the 80Li_2S-20P_2S_5 glass-ceramic solid electrolytes, which was shown to contain the precipitation of Li_3PS_4, Li_7PS_6, and an unknown crystal[79]. While 80Li_2S-20P_2S_5 shows good ionic conductivity, Li_3PS_4, Li_7PS_6 synthesised by solid-state reaction exhibits low ionic conductivities. Therefore, the high ionic conductivity of 80Li_2S-20P_2S_5 may be attributed to the stabilised high-temperature phases of Li_3PS_4 and Li_7PS_6[80,81]. With the phase transformation of Li_3PS_4 and Li_7PS_6 being reported at 150 – 200 °C,

the existence of high-temperature phases was evidenced. To ensure ideal conductivity, the temperature of the heat treatment should be precisely controlled to just above the first crystallisation temperatures to obtain and maintain the metastable phases, otherwise thermodynamically stable phases will be formed at higher temperatures, which are less conductive.

In 2007, the unknown crystal was confirmed to be $Li_7P_3S_{11}$ by Tatsumisago via synchrotron X-ray powder diffraction, which contains $P_2S_7^{4-}$ and PS_4^{3-}. As Li-ions are located around $P_2S_7^{4-}$ ditetrahedra and PS_4^{3-} tetrahedra, fast Li-ion conduction can be expected due to the interstitial sites and open space between $P_2S_7^{4-}$ ditetrahedra and PS_4^{3-} tetrahedra[82]. By optimising heat treatment conditions, Seino et al. obtained Li_2S-P_2S_5 glass-ceramic with $Li_7P_3S_{11}$ metastable phase and minimised the grain boundaries in microstructure, which improved the contact between grains and achieved an ionic conductivity of 1.7×10^{-2} S cm^{-1} [83]. Although $Li_7P_3S_{11}$ presents satisfactory ionic conductivity, as a glass-ceramic electrolyte, it also presents drawbacks as they are rigid, inflexible, and extremely brittle, which does not allow application of $Li_7P_3S_{11}$ as a thin membrane in practice.

The last type of sulphide is the argyrodite-type sulphide solid electrolyte Li_6PS_5X (X = Cl, Br, I), which was firstly synthesised by Deiseroth et al[84]. This type of solid electrolyte was named as argyrodite based on their similar structures to Cu^{2+} and Ag^+ argyrodites. The six sulphur and halogen atoms form 136 tetrahedral holes, four of which are formed by sulphur atoms (S1) only, and are occupied by P atoms. The remaining 132 holes, partially occupied by Li atoms, are formed by sulphur atoms (S2), and halogen atoms (X). The 3D structure of Li_6PS_5X is shown in **Fig. 1.5** below[85].

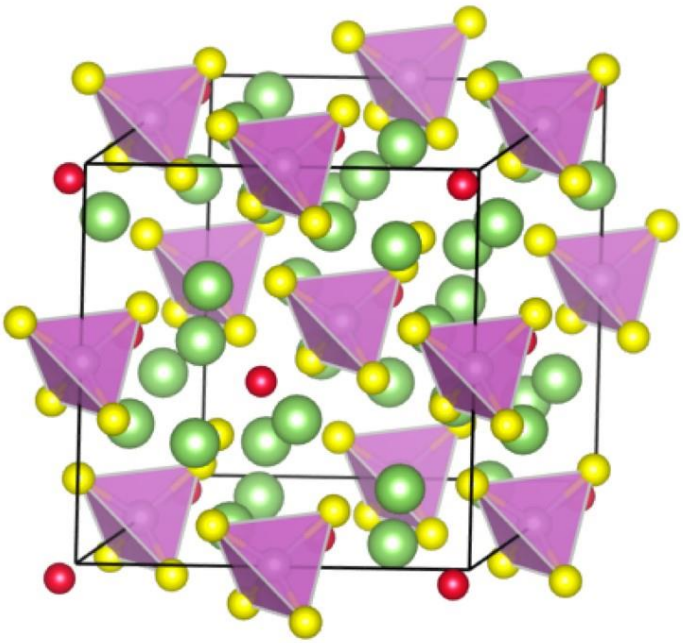

Fig. 1.5. Lattice structure of Li_6PS_5X with the lowest energy from DFT calculations. Li^+ in green, S^{2-} in yellow, PS_4^{3-} polyhedral in purple, and X in red. (Reproduced from Ong et al.[85])

Different types of argyrodite solid electrolytes present different extents of disordering. While it is fully disordered for Li_6PS_5Cl, mixed ordered and disordered structure for Li_6PS_5Br, Li_6PS_5I is fully ordered. Li_6PS_5Br shows the highest ionic conductivity among all, indicated by NMR measurement. With intensive research by Adams et al. on the synthesis of argyrodite solid electrolytes, the best preparation method was confirmed to be mechanical ball-milling followed by annealing at 550 °C[86–89]. The annealed products showed ionic conductivities of 1.9×10^{-3} S cm^{-1} for Li_6PS_5Cl, 6.8×10^{-3} S cm^{-1} for Li_6PS_5Br, and 4.6×10^{-7} S cm^{-1} for Li_6PS_5I, respectively. Bond valence analysis showed Li-ion diffusion pathways with low activations energies for long range transport in Li_6PS_5Cl and Li_6PS_5Br, which accounted for their high ionic conductivities[87].

While highly conductive argyrodite solid electrolytes can be synthesised with success via ball-milling, ball-milling is very energy consuming and can hardly be implemented in scale-up electrolyte preparation. Solution-based preparative methods were therefore pursued with a dissolution-reprecipitation process from an ethanol solution. However, such attempts were not

successful, as the prepared Li_6PS_5Cl showed a significantly decreased ionic conductivity of 1.4 × 10^{-5} S cm^{-1} [90]. Recently, Nazar et al. developed a promising solution-engineered approach for Li_6PS_5X synthesis with a mixture of tetrahydrofuran (THF) and ethanol as the solvent[91]. Not only Li_6PS_5X solid electrolytes with comparable ionic conductivities to the ball-milling method were obtained, but also $Li_{6-y}PS_{5-y}Cl_{1+y}$ solid electrolytes with further improved ionic conductivities based on a precise control of precursors. In 2019, Nazar et al. for the first time synthesised the antimony argyrodite solid electrolytes $Li_{6+x}M_xSb_{1-x}S_5I$ (M = Si, Ge, Sn). Combined synchrotron X-ray and neutron diffraction with impedance spectroscopy, they obtained $Li_{6.6}Si_{0.6}Sb_{0.4}S_5I$ with the optimal S^{2-}/I^- anion site disorder and Li^+ cation site disorder, which presented an outstanding ionic conductivity of 1.48 × 10^{-2} S cm^{-1} at room temperature after cold-press, and up to 2.4 × 10^{-2} S cm^{-1} after sintering[92]. Whilst comparable ionic conductivity to that of thio-LISICON solid electrolyte has been achieved, antimony argyrodite solid electrolyte also maintain a good stability against Li metal of normal argyrodite, showing great potential for practical applications.

While all-sulphide based solid electrolytes present satisfactory ionic conductivities, the superior stability against Li metal anode seems to be unique in argyrodites solid electrolytes. The best stability of argyrodite among different species originate from the interphase it formed with Li metal anode, which is composed of Li_2S, Li_3P and LiX (X = Cl, Br) and can serve as an *in-situ* protective passivating layer[67]. Extremely slow kinetics were also found in the formation of the interphase as it proved to self-limit after only a few nm[93]. With ideal ionic conductivity, less brittleness, good stability, commercial availability, and potential in large scale application, Li_6PS_5Cl was chosen in this work as a model solid electrolyte to pursue for a mechanistic understanding of anodic degradation in all-solid-state batteries.

1.3 Interfacial degradation in all-solid-state batteries

The anodic degradation of all-solid-state batteries can be simply divided into two different types: response of the interface to lithium plating and response of the interface to lithium stripping. While lithium plating subsequently leads to electrolyte disintegration and cell failure, thus requiring insightful mechanistic understanding, the anodic response to lithium stripping is also of paramount importance, as interfacial degradation can trigger dendrite formation on plating. For successful all-solid-state batteries, the Li/SE interface must be well-designed to achieve satisfactory stability and sufficiently fast kinetics. Therefore, the phenomena and mechanisms of interfacial degradation must be well investigated and understood. In this chapter, three major forms of interfacial degradation will be discussed respectively, as well as their impact on all-solid-state battery cycling.

1.3.1 Chemical and electrochemical stability

The stability between the Li metal anode and the solid electrolyte is of paramount importance for all-solid-state batteries, as reaction and formation of SEI could significantly undermine the charge transfer across the interface. The interface stability between solid electrolyte and a specific electrode material is given by the corresponding electrochemical stability window, which takes both purely chemical potential driven reactions and electric potential driven reactions into account.

The stability between two materials has been widely estimated with the band gap theory. Upon reduction at the anode side, the position of the conduction band minimum, which is taken as the lowest unoccupied molecular orbital, gives an estimate of the electrochemical stability window of solid electrolyte[94]. Electrons will transfer from the Li metal to the solid electrolyte if the conduction band minimum of the solid electrolyte lies below the Fermi level of lithium metal, ε_F, thus the interface is unstable, **Fig. 1.6a**. However, such an estimation does not take the simultaneous transfer of lithium ions into account, which is in the same direction as the electrons to maintain charge neutrality[95]. This makes the band gap approach a rough

approximation, which could only provide an upper limit of the electrochemical stability window.

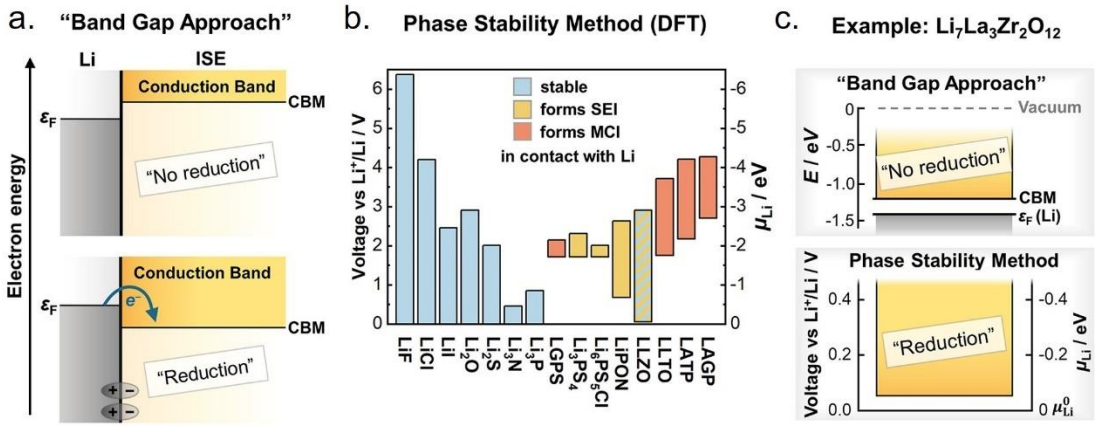

Fig. 1.6. a. Electrochemical stability window of a solid electrolyte in contact with Li metal anode based on the Fermi level consideration, with and without the reduction taking place at the interface. **b.** Thermodynamic potential windows of various potential solid electrolytes and their decomposition productions, evaluated by the phase stability method. **c.** Difference in the prediction of electrochemical stability in contact with Li metal anode based on two different methods, for the example of $Li_7La_3Zr_2O_{12}$ solid electrolyte. (Adapted from Janek et al.[96])

The electrochemical stability window of the interface can be more precisely estimated by the phase stability method, which is based on density-functional theory and can strictly yield the thermodynamic stability window[97–99]. The electrochemical stability windows of various promising solid electrolytes are shown in **Fig. 1.6b**, suggesting that all superionic solid electrolytes are electrochemically unstable with Li metal anode and form an SEI at the chemical potential μ_{Li}^0. While all the solid electrolytes are thermodynamically unstable against the Li metal anode, such values might only be regarded as the lower limit of the electrochemical stability window, as the interfacial reactions may be hindered or limited from a kinetic perspective. Wagemaker et al. recently proposed a stoichiometry stability method, which treated the solid electrolyte as a phase with a broad stoichiometry (lithiated/delithiated), and the electrochemical stability window is computed by the potential limits of (de)lithiation[100]. This theory is based on the assumption that the solid electrolyte may get homogeneously

(de)lithiated and may remain kinetically stable, before a heterogenous reaction that turns the interface into lithium-poor or -rich phases takes place. Despite the strict assumption, the theory provides better agreement with experimental findings, suggesting that kinetic stabilisation also plays a key role in determining the stability of the interface.

While all promising solid electrolytes are thermodynamically unstable against the Li metal anode, such instability is not necessarily detrimental in practical operation, as it is the evolution of the interphase rather than the formation that determines the feasibility of a solid electrolyte. Based on different behaviours of interphase evolution, Wenzel et al. distinguished Li/SE interfaces/interphases into three types[51]: (a) a nonreactive, fully stable Li/SE interface, where no interphase forms; (b) a reactive and progressively growing Li/SE, where a mixed conducting interphase forms[101,102]; (c) a thermodynamically unstable but kinetically self-limiting Li/SE interface based on the formation of an almost exclusively ion conducting SEI, **Fig. 1.7**.

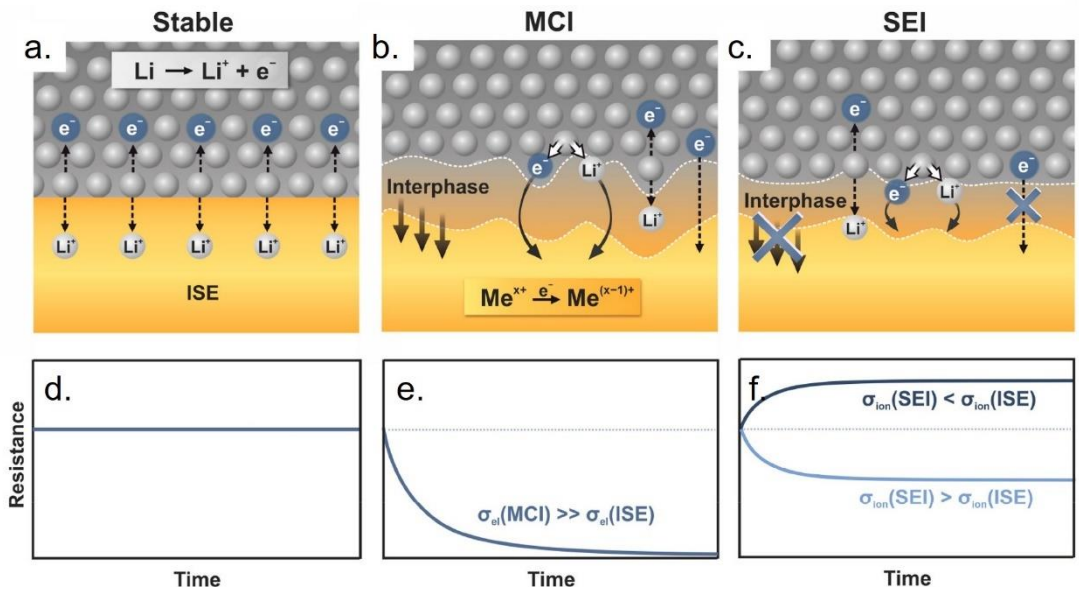

Fig. 1.7. Schematic showing the three types of interphase/interface between Li metal anode and solid electrolytes. **a.** Thermodynamically stable interface. **b.** Reactive mix-ionic/electronic conducting interphase. **c.** Kinetically stable interphase with low electronic conductivity. **d.** to **e.** The expected change of interphase/interface resistance change along time of respective type of interphase/interface. (Adapted from Janek et al.[96])

To quantify the progressive growth of SEI, and how the electronic conductivity of the interphase plays an important role in evolution, an equation for a diffusion controlled solid-state reaction has been applied by Wenzel et al. as shown in **Eq. 1.4**[103], with σ_{el} = electronic conductivity of the solid electrolyte, σ_{Li^+} = ionic conductivity of the solid electrolyte, l_{SEI} = thickness of the SEI, $\nabla\mu_{Li}$ = the local chemical potential gradient of lithium metal across the interphase layer.

$$j_{Li} = \frac{\sigma_{el}\sigma_{Li^+}}{F^2(\sigma_{el} + \sigma_{Li^+})}\nabla\mu_{Li} \approx \frac{\overline{\sigma_{el}\sigma_{Li^+}}}{F^2(\overline{\sigma_{el}} + \overline{\sigma_{Li^+}})}\frac{\mu_{Li}^0}{l_{SEI}} \quad (1.4)$$

Eq. 1.4 predicts the growth rate of the interphase of solid electrolytes in contact with lithium metal anode, showing the increase of the interphase resistance with time depends on the ionic and electronic conductivities of the interphase compounds to a great extent. It also suggests that with a nonzero chemical potential gradient in a nonsymmetric cell, the SEI will continuously grow if the electronic conductivity is not infinitely low, but with a decreasing rate. Case c in **Fig. 1.7c**, which is the practical condition for all promising solid electrolytes, requires strictly an infinitely low electronic conductivity of the SEI. As shown in **Fig. 1.6b**, Li_2S, Li_3P, Li_2O, and LiCl, which are typical interphase composition resulting from the decomposition of argyrodite, thiophosphates and LiPON, present dominant ionic conductivity, ensuring the self-limiting nature of their SEIs and good performance with Li metal anode. Among all the practically relevant solid electrolytes, LLZO-type garnets are the only ones that keep their chemical and structural integrity in contact with a lithium metal anode. Recent investigations by TEM show a slight reduction of Al doped LLZO and formation of a lithium-rich interphase in contact with a Li metal anode[104]. In addition, recent XPS studies also confirm the reduction of Zr^{4+} and the formation of an oxygen-deficient interphase[105]. However, it is believed that such a small driving force for decomposition of LLZO is probably insufficient to nucleate the thermodynamically stable bulk products, thus LLZO retains its unique interfacial stability.

1.3.2 Vacancy injection

Apart from reactivity between the solid electrolyte and Li metal anode, the maintenance of a good interface during stripping also remains a challenge in practical applications, due to the significant volume change of the Li metal anode, low plasticity of solid electrolyte, as well as the limited vacancy diffusion in lithium. The morphological degradation of the interface is not limited to the Li/SE interface, but is a common phenomenon that stems from the general nature of metal electrodes at a solid/solid interface, which has been investigated in previous work on silver electrodes. The mechanisms of vacancy injection and the resultant void accumulation during stripping will herein be briefly discussed, as well as their implications for the design of a practical Li/SE interface.

On stripping of Li metal anode, which is Li metal dissolution driven by the current, the process of charge transfer can be denoted as below using Kroeger-Vink notation.

$$Li_{Li}(Li) = \left[Li_{Li}^{\times}(SE) - V'_{Li^+}(SE)\right] + e'(Li) + V_{Li}^{\times}(Li) \quad (1.5)$$

During the stripping process, a lithium ion passes through the Li/SE interface, leaving an electron $e'(Li)$ and a vacancy inside the lithium metal (near interface region). The Li^+ ion then occupies a vacant site in the solid electrolyte, $V'_{Li^+}(SE)$, close to the interface. Due the difference in lattice constants and structure between Li metal and solid electrolyte, the Li/SE interface will at best be a semi-coherent interface, or most likely an incoherent interface. Therefore, an ideal layer-by-layer dissolution, which is reasonable for coherent interfaces, does not hold for the dissolution of lithium at most Li/SE interfaces[106]. Instead, the injected metal vacancy $V_{Li}^{\times}(Li)$ needs to diffuse away from the interface to maintain the interfacial contact. The vacancies may then diffuse into the Li anode bulk or be annihilated at a site of repeatable growth (dislocations or grain boundaries) as shown in **Fig. 1.8**.

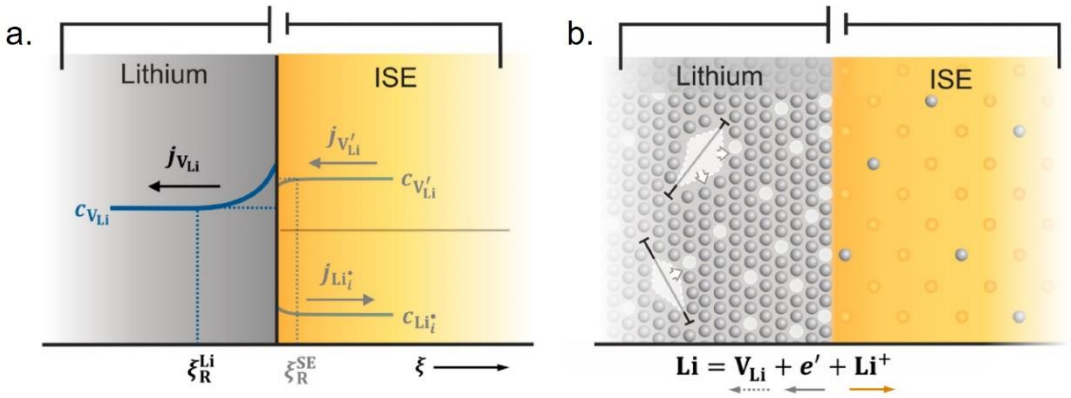

Fig. 1.8. a. Schematic outlining the vacancy relaxation process where the pores are not yet formed at the interface. ξ_R^{Li} marks the defect relaxation region in the Li metal anode near the interface. **b.** Schematic outlining the microscopic interface process during Li stripping, assuming vacancy driven ionic transport. In the Li metal anode, dislocations can act as sinks for vacancies, increasing the vacancy concentration gradient. (Adapted from Janek et al.[96])

Thus, the morphological stability of the interface relies on the equilibrium between the injection rate of vacancies and vacancy diffusion into the metal anode. Once the vacancy diffusion into the metal anode is overwhelmed by the vacancy injection at the interface, interfacial voids will form due to the build-up of vacancies, deteriorating the interfacial contact. Whilst understanding the kinetics of vacancy injection is important in preventing interfacial degradation, little work has been done to quantitatively analyse the current density limit for vacancy build-up. A kinetic model has been developed by Schmalzried and Janek to estimate the critical anodic current density below which a stationary vacancy concentration at the interface can be maintained, **Eq. 1.6** and **Eq. 1.7**[107].

$$j_v = \left(1 - \frac{c_V(\xi = 0)}{c_V^0}\right) C_v^0 \sqrt{\frac{D_V}{\tau_V}} \qquad 1.6$$

$$i_{crit} = z \cdot F \cdot j_V \qquad 1.7$$

With τ_v = relaxation time for the establishment of the vacancy equilibrium concentration, z = number of charge of the ion (z = 1 for Li^+), c_V^0 = equilibrium bulk concentration of vacancies,

$c_V(\xi = 0)$ = vacancy concentration in the lithium at the interface, D_V = diffusion coefficient of vacancies in Li metal. As the relaxation time of lithium vacancies, τ_V, remains unknown, a critical anodic current density was estimated in the range of 10 ~ 100 μA/cm^2 [108].

While the model suggests a rough range of critical anodic current density, which could guide the practical operating conditions of Li metal anode without any pressure, the model neglects the interfacial effects on the lithium vacancy transport. In addition, while the conditions to maintain an equilibrium state of vacancy transport was predicted, the process of vacancy accumulation was not involved in the model. To fully understand the interfacial degradation of Li metal anode, the consequence of exceeding such a critical anodic current density also needs to be investigated, as well as other potential strategies to overcome the low current density limit from vacancy transport.

1.3.3 Void accumulation

Above a critical current anodic density, vacancies build up at the interface, and as a consequence leads to morphological changes at the interface. However, the nature of the morphological change at the interface was barely explored, due to the buried nature of the interface in all-solid-state batteries. Extensive efforts were made to indirectly investigate the effect of morphological change on cell cycling via electrochemical tests.

Pioneering work on this topic can be traced back to the early 1980s, where the change of electrode overpotential in Li/Li_3N/Li cells was attributed to the change in interfacial contact area induced by Li stripping[109,110]. In recent studies, galvanostatic plating-stripping with impedance spectroscopy with a two-electrode set-up was employed to investigate the interfacial degradation mechanisms of Li metal anodes, in regards to the increase in cell impedance during cycling[111]. Such deterioration in anodic interface was ascribed to the Li/SE contact loss due to morphological changes. By using *in-operando* impedance spectroscopy measurement, Janek et al. corroborated the correlation between formation and growth of voids at the interface with the increase in interface impedance, and confirmed the existence of voids with ex-situ SEM[108]. By

forming an intimate contact for the counter electrode with a stack pressure of 400 MPa, the overpotential from the counter electrode was excluded, allowing them to investigate the impedance response to Li stripping. A better way to investigate the electrochemical response to interfacial morphological changes is to employ a three-electrode set-up, where the reference electrode remains unchanged and provides a constant overpotential for comparison of the working electrode conditions. Koshikawa et al. used a three-electrode set-up in Li/LLZO/Li cell, to demonstrate that the increase in cell overpotential was only caused by Li stripping, and concluded that contact loss due to void formation is the root cause of the increased overpotential[112]. However, as the characterisations of interfacial voids in all the aforementioned studies were done with ex-situ SEM or even cross-sectional SEM, due to the compliant nature of Li metal anode, the morphology of interfacial voids is not necessarily representative of that in a practical case. A gap remains in bridging the change in electrochemical response with the evolution in interfacial morphology. A non-destructive, and ideally *in-situ* capable technique is required, to better understand the origin of the anodic interfacial degradation.

Apart from these experimental efforts, modelling works also engage in understanding the void accumulation during Li stripping. Jow and Liang used the Sand's equation, which was widely applied in understanding liquid-state batteries, to quantitatively analyse the temporal depletion of Li at the anodic interface[110]. Although a reasonable estimation of the vacancy diffusion coefficient was achieved, the modelling was oversimplified, as the adatom diffusion process and the significant variation in local current density which play critical roles once there is contact loss were ignored in this model. A complicated three-dimensional microkinetic model is indeed desired for the quantitative analysis, which is unlikely to follow one-dimensional diffusion kinetics. Moreover, other factors such as surface adhesion, double-layer attractive forces, vacancy mobility variation along the incoherent interface from the bulk, and importantly the stack pressure on Li metal anode, which helps the Li transport in the anode, might all need to be taken into account in a comprehensive model that reflects practical conditions. More

efforts and scientific advances need to be made to achieve a complete mechanistic understanding of anodic interfacial degradation.

1.4 Mechanisms of dendrite formation

As well as anodic interfacial degradation, dendrite formation and propagation remain a greater challenge for all-solid-state batteries. Inorganic solid electrolytes were investigated and employed to work with Li metal anode based on the mechanistic understanding of dendrites in liquid electrolyte, and solid polymer electrolyte, as well as the belief that inorganic solid electrolytes with their rigid nature could suppress dendrite formation. However, recent studies have overturned this belief, showing dendrite penetration and severe solid electrolyte disintegration in solid electrolytes that were judged to have satisfactory shear moduli and fracture toughness. This makes the application of the Li metal anode, the biggest advantage of all-solid-state batteries, unreliable in practical operations. Great efforts have been made to explore and understand the mechanism(s) of dendrite formation in all-solid-state batteries. Nevertheless, little advance has been achieved due to the buried nature of dendrites in all-solid-state batteries and in consequence the technical difficulty of following the formation of dendrites.

Whilst it is critical to characterise dendrite formation in all-solid-state batteries directly to contribute to a mechanistic understanding by developing advanced techniques, it is equally important to follow the previous studies on dendrite mechanisms in liquid and solid polymer electrolytes, to understand whether and why the proposed mechanisms do or do not hold for dendrite formation in all-solid-state batteries. In this section, the dendrite phenomena and mechanisms in different battery systems will be reviewed, with a brief discussion on the current status in understanding of dendrites in all-solid-state batteries and their limitations.

1.4.1 Dendrites in liquid electrolytes

Due to the inevitable dendrite formation with a Li metal anode, graphite has replaced the Li metal anode in large-scale applications of Li-ion batteries since 1990s. However, great efforts to understand and prevent dendrite formation with Li metal anode in liquid electrolytes have never come to an end, due to the great potential of Li metal anodes in improving the energy density of Li-ion batteries. While it has been demonstrated that electrolyte additives, the introduction of artificial SEI layers, and an electrolyte with hugely increased salt concentration, can improve the morphological stability of Li deposition at low currents, a grand challenge remains in suppressing dendrites at practical current densities (1 mA/cm^2) and areal capacities (1 mAh/cm^2)[113–117].

After decades of investigation, a consensus in dendrite mechanisms has only been reached recently. The prevailing explanation of Li dendrite formation is based on the simpler case of aqueous copper electrodeposition, where fractal dendritic growth results from long-range diffusion-limited growth[118]. However, unlike the copper dendrite in electrodeposition, it is well-established that dendrite formation can be divided into two stages in Li-ion batteries: the formation of mossy-dendrites which are observed to grow from the roots, and the fractal dendrites which grow at the tips and propagate to the other electrode in a fast manner, similar to the copper dendrite. In 2016, Bazant et al. revealed the whole process of dendrite transition from a mossy structure to a fractal structure for the first time, together with the corresponding cell overpotential response[119]. Their proposed theory that is based on a transition from a reaction-limited process to a diffusion-limited process has been widely recognised as a feasible model to explain dendrite formation in liquid electrolytes.

The stark difference between copper electrodeposition and lithium deposition comes from the inevitable reaction between Li metal anode and the liquid electrolyte. During the electrodeposition of copper, where there is no SEI, copper forms a whisker-free yet compact deposit before the formation of fractal dendrites. The mossy Li dendrites were observed to grow

from their roots in the early stages, as the mossy dendrites were pushed towards the electrolyte with the shape of the tips barely changed. Later when the mossy dendrites grow into the open electrolyte, the mossy dendrites also thicken and grow in volume as a “rising dough”. At the microscopic scale, the mossy dendrites consist of many individual Li whiskers, separated by the insulating SEI on the surface. Based on the morphology of the mossy dendrite, its growth kinetics, and the fact that mossy dendrite formation was observed at current densities far below a critical level, the formation of mossy dendrite is attributed to a reaction-limited deposition.

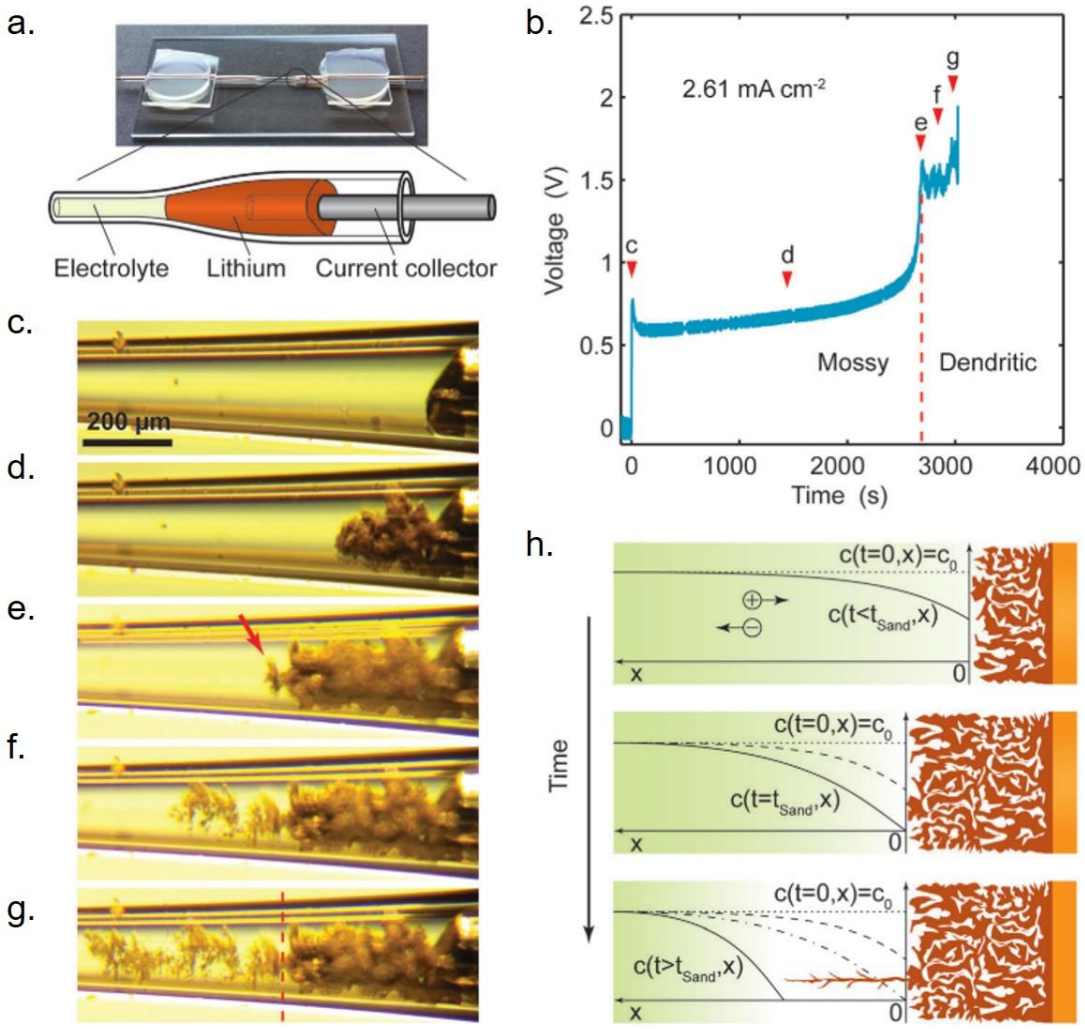

Fig. 1.9. *In-situ* observation of lithium deposition in a capillary tube filled with electrolyte solution under optical microscope. **a.** a photo of the experimental set-up. **b.** voltage responses of the cell to a constant current of 2.61 mA cm^{-2} at different stages of lithium deposition. **c.** to **e.** images from the *in-situ* observation of lithium deposition vial optical microscope. The red

arrow in **e.** marks the emergence of dendritic lithium. **h.** schematic illustrates the growth mechanisms of lithium deposition at different stages of concentration polarisation. (Adapted from Bazant et al.[119])

The formation of fractal dendrites, which directly leads to short-circuit of the cell, is of more mechanistic research interest. Based on its similarity with the dendrite in copper electrodeposition, the formation of a fractal dendrite was attributed to diffusion limitation, which was supported by the step increase in cell voltage coinciding with the formation of fractal dendrites, **Fig. 1.9 b** & **e**. Sand's formula was therefore employed to describe the formation of fractal Li dendrites, **Eq. 1.8**[119],

$$t_{sand} = \pi D_{app} \frac{(z_C C_0 F)^2}{4(J t_a)^2} \quad 1.8$$

With z_c = the charge number of the cation, c_o = the bulk salt concentration in liquid electrolyte, F = the Faraday's constant, J = the current density, and $t_{Li} = 0.38$, $t_a = 1 - t_{Li}$ are the transference numbers of lithium cations and associated anions in the electrolyte. As the Sand's time has been well determined in the *in-situ* observations (the time before the step increase in voltage), the apparent diffusion coefficient was precisely estimated, and was a good match with experimentally measured values, which was a strong evidence for the feasibility of the model. So, the limiting current density for fractal deposition has also been estimated by **Eq. 1.9**,

$$J_{lim} = 2 z_C C_0 F D_{app} (t_a L)^{-1} \quad 1.9$$

Where L = the distance between electrodes. To make an estimation of a more battery relevant onset, the Sand's time was converted to the Sand's capacity by multiplying with the corresponding current density, **Eq. 1.10**.

$$C_{sand} = J t_{sand} = \pi D_{app} \frac{(z_C C_0 F)^2}{4 J {t_a}^2} \quad 1.10$$

The Sand's capacity sets a simple design constraint to avoid Li dendrite formation, limiting the capacity that is allowed to pass at a certain current density. This dependence has been verified

by a set of experiments to detect fractal dendrite formation at various current densities, **Fig. 1.10**.

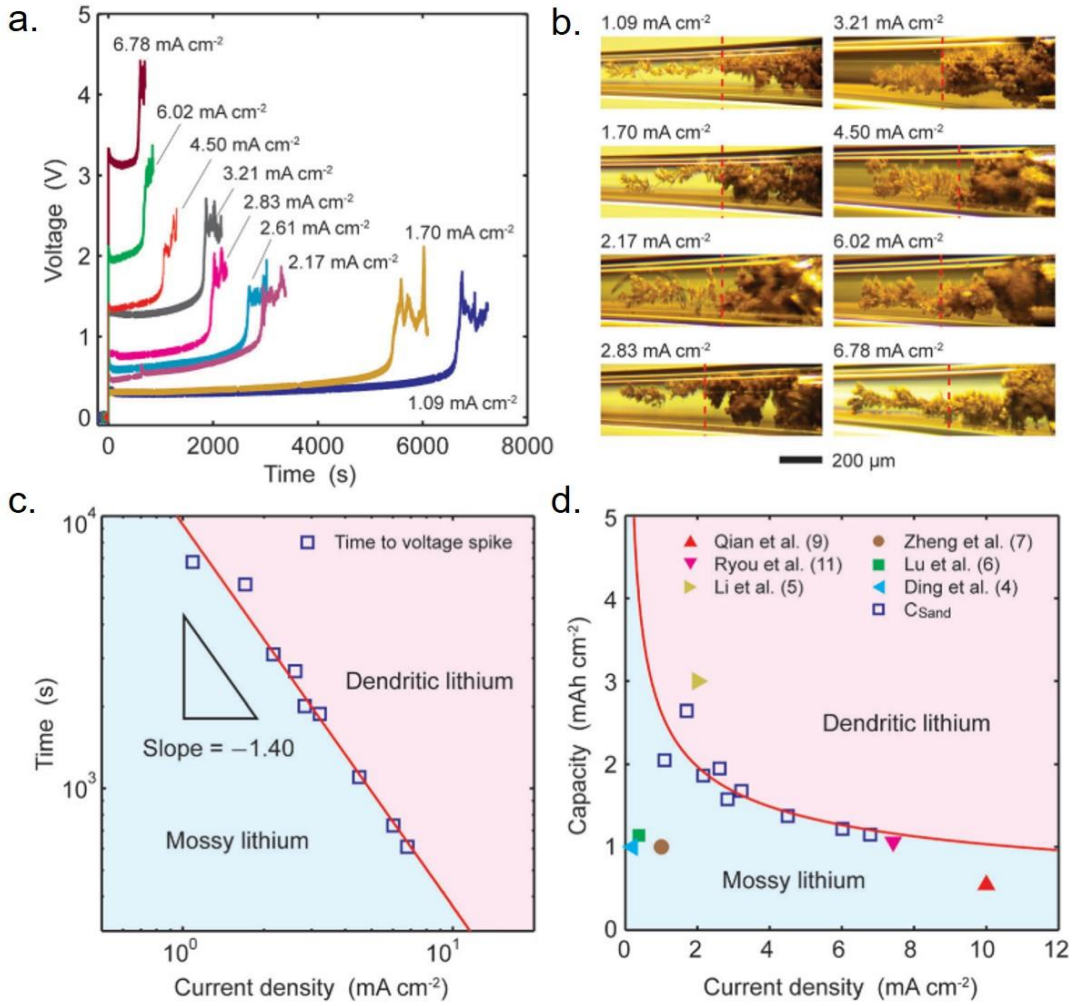

Fig. 1.10. a. Voltage responses of the cell at various applied current densities. **b.** Optical images demonstrating the clear transition of morphology in deposited lithium at various current densities. **c.** Log-log plot of the experimental Sand's time with different current densities. **d.** Sand's capacity at different current densities. (Adapted from Bazant et al.[119])

However, it is worth noting that the Sand's capacity can only provide a rough estimation for practical cases, as the salt concentration may vary due to continuous SEI formation during the lifetime of a Li-ion battery. In short, detrimental dendrite formation in liquid electrolyte, originates from the salt depletion around the plating electrode due to electrolyte polarisation. The salt concentration, diffusion coefficient, and crucially the transference number of anions

set the upper limit of applicable current density, below which the salt depletion might not be critical. Whilst the salt concentration and diffusion coefficient can be easily improved based on better selection of materials, the transference number of anions can hardly be modified[120], which leaves dendrite suppression in liquid electrolytes an arduous goal to achieve.

1.4.2 Dendrite formation in polymer electrolytes

Dendrite formation in a solid polymer electrolyte is mechanistically similar to a liquid electrolyte, as a non-unity transference number and the depletion of Li salt are also valid in polymer electrolyte. However, unlike a liquid electrolyte, where the Li dendrites grow freely towards the open electrolyte, the solid polymer electrolyte could act as physical barrier to suppress the inhomogeneous deposition of Li to some extent. In addition, the reactivity between Li and solid polymer electrolyte is not as severe as that in liquid electrolyte. A mossy dendrite structure was not observed in solid polymer electrolyte, as the deposited lithium whiskers were not isolated from each other by the insulating SEI[121]. Instead of a mossy dendrite structure, the dendrites in solid polymer electrolyte start with a lithium protrusion at the interface into the solid polymer electrolyte. Thus, whether such dendrite formation is detrimental largely depends on the propagation kinetics once the interfacial protrusion forms on plating.

In 2003, Monroe and Newman put forth a dendrite propagation model to describe the dendrite growth kinetics with a solid polymer electrolyte. The Barton Bockris theory of dendrite growth was corrected to incorporate well-defined thermodynamic reference points[122]. The Monroe and Newman model suggests that dendrite growth always accelerates across the cells due to a gradually enhanced current flux concentration. The growth of dendrites could be slowed by lowering the current density applied, but short-circuit seems to be inevitable, and is only a matter of charge and time. It was also found that cell failure can be slowed by increasing the interelectrode distance, but such an improvement has a limit as the distance lengthens as this increasing the resistance of the cell in the meantime[46].

However, the difference between solid electrolyte and liquid electrolyte was not fully acknowledged in this model, leaving the effect of surface forces on the rate of dendritic propagation to be further explored. In 2005, Monroe and Newman employed linear elasticity theory to analyse the effect of bulk mechanical forces on electrode stability, predicting different behaviour of dendrite growth upon solid polymer electrolytes with different shear moduli and Poisson's ratios[123].

In that work, the dendrite growth kinetics were described by a modified Butler-Volmer equation in the form of

$$i_n = i_{0,ref}\, exp\left[\frac{(1-\alpha_a)\Delta u_{e^-}}{RT}\right]\left[\exp\left(\frac{\alpha_a F \eta_s}{RT}\right) - \exp\left(\frac{\alpha_c F \eta_s}{RT}\right)\right] \qquad 1.11$$

Where R = gas constant, F = the Faraday's constant, T = temperature, η_s = surface overpotential, i_n = current density normal to the deformed interface, $i_{0,ref}$ = the current density at the undeformed interface, α_a and α_c = anodic and cathodic transfer coefficients, respectively, and Δu_{e^-} = the electrochemical potential change in electrons within the electrode induced by local strain or interfacial shape change.

The deposition behaviour at the interface relies on the value of Δu_{e^-}, as current at the deformed interface will be larger than the undeformed interface, which contributes to dendrite propagation when Δu_{e^-} is positive, and otherwise dendrite suppression when Δu_{e^-} is negative. Based on this, a stability parameter, Δu, was defined by **Eq. 1.12**, where A and ω are amplitude and frequency of interfacial displacement induced Li deposition (for peak, $A\cos(\omega x) > 0$, and for valley $A\cos(\omega x) < 0$).

$$\frac{\Delta u_{e^-}}{A\cos(\omega x)} \equiv \Delta u \qquad 1.12$$

The interface is unstable and the dendrite grows when the stability parameter is positive, as deposition is preferred on the peaks of the deformed electrode surface rather than the undeformed surface. The interface is stable when the stability parameter is negative, as

deposition on the peaks of the deformed electrode surface is slower compared with the undeformed surface.

Given a certain amplitude and frequency of displacements, the electrochemical potential change Δu_e- relies on the interfacial forces, including surface tension, deformation forces, and compressive forces, whose effects are determined by the shear moduli and Poisson's ratios of solid polymer electrolyte and Li metal anode. Their effects on the stability parameter are quantified and plotted in **Fig. 1.11**.

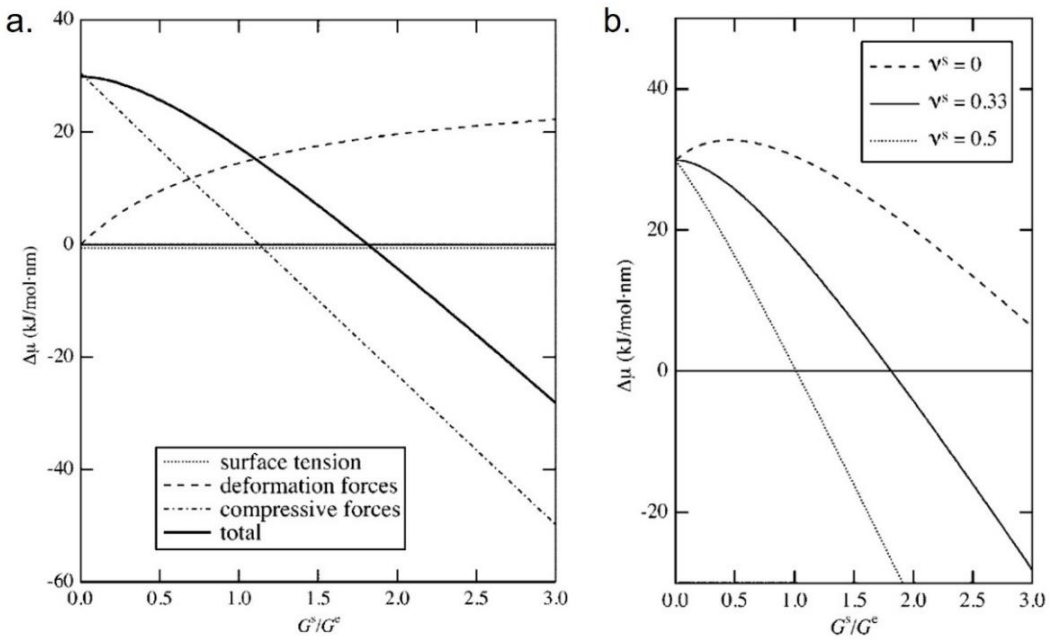

Fig. 1.11. a. Contributions from compressive forces, deformational forces, and surface forces to the interfacial stability parameter of Li deposition, as a function of separator shear modulus. Poisson's ratio is set to 0.33. **b.** Interfacial stability parameter as a function of shear modulus and Poisson's ratio. Stable Li deposition is predicted when the shear modulus of the separator is about twice the shear modulus of lithium metal.

As shown in the plot, the stability turns negative when the shear modulus of solid polymer electrolyte is higher than about twice the shear modulus of lithium metal, with a practical Poisson's ratio of 0.33. It predicts lithium dendrite suppression can be achieved at the interface when the shear modulus of solid polymer electrolyte is high enough. Such a prediction is in a

sense supported by the experimental result that lithium dendrites can be inhibited when the lithium electrodes are coated with conductive inorganic glasses. However, at the whole electrolyte scale, such a conclusion remains a theoretical prediction, as the shear modulus of a polymer can hardly achieve the required level to suppress dendrites. Despite the lack of experimental validation, the prediction is impactful in solid polymer electrolyte research, as it explains the instability of Li deposition in the system, and crucially, guides the design of the next generation of solid electrolytes with the capability of suppressing dendrite growth completely. Thereafter, extensive efforts are made to explore inorganic solid electrolytes, based on this prediction.

1.4.3 Dendrites in all-solid-state batteries

With the belief that a solid electrolyte with a sufficiently high shear modulus can suppress dendrite formation completely, inorganic solid electrolytes have been employed as the electrolyte and separator for the application of Li metal anodes. In addition, inorganic solid electrolytes have a transference number of t_{Li^+} close to one, which prevents extensive local ion depletion during current load. Therefore, Li deposition should be stable in all-solid-state batteries, even at considerable current densities. However, recent studies[124–126] show that inorganic solid electrolytes with orders of magnitude higher shear moduli than lithium still cannot suppress dendrite growth, suggesting a different mechanism of dendrite formation in all-solid-state batteries, which is not yet well understood.

The current density, above which the cell short-circuit occurs, is defined as the critical current density (CCD), and is a well-established term in all-solid-state battery research. To achieve fast charge and reliable cycling, a CCD larger than 5 mA/cm^2 is desired. CCDs for inorganic solid electrolytes are commonly below 1 mA/cm^2 at room temperature, and far below practically relevant cycling conditions. Despite much stronger mechanical properties, and an almost unity transference number, the CCD of an all-solid-state battery is not improved sufficiently compared with liquid electrolyte and solid polymer electrolyte. Certainly, mechanistic

investigations are needed to explain why lithium, as a soft metal, is able to penetrate through the solid electrolyte and lead to cell failure.

A few decades ago, extensive work was done on understanding cell failure of beta-alumina solid electrolytes with a sodium metal anode[127–130]. Although many concepts and mechanisms proposed during this period were developed for liquid sodium metal anodes, some concepts and understanding can be transferred to the solid Li metal anode. Cell failures in Na/beta-alumina cells were categorised into two modes at the time[128,130]: mode I degradation, which describes rapid dendrite penetration into the solid electrolyte in the form of a dendritic crack that ultimately leads to short-circuit of the cell; and mode II degradation, which describes the gradual internal deposition into the solid electrolyte which does not form cracks.

Since mode II degradation is widely believed not to directly lead to short-circuit and cell failure, and with no consensus in the mechanism being reached even until today, this section will focus on the phenomena and mechanisms of mode I degradation, comparing various electro-chemo-mechanical models for a comprehensive understanding. As different short-circuiting phenomena have been found experimentally, the different models don't necessarily stand alone. Instead, the short-circuit in all-solid-state batteries might result from various factors that directly or indirectly lead to cell failure. The separation of the different models needs to take into account the fundamental differences between different models, and how different phenomena could be governed by a same model, due to the different properties and structure of the solid electrolyte.

Different short-circuiting phenomena in all-solid-state batteries can be categorised into four major types, as shown in **Fig. 1.12**: **a.** initiation and propagation of dendritic crack filled with lithium metal[131]. **b.** preferential growth of dendrite along grain boundaries[132]. **c.** directly lithium deposition in closed pores[133]. **d.** growth of lithium through interconnect pores[134].

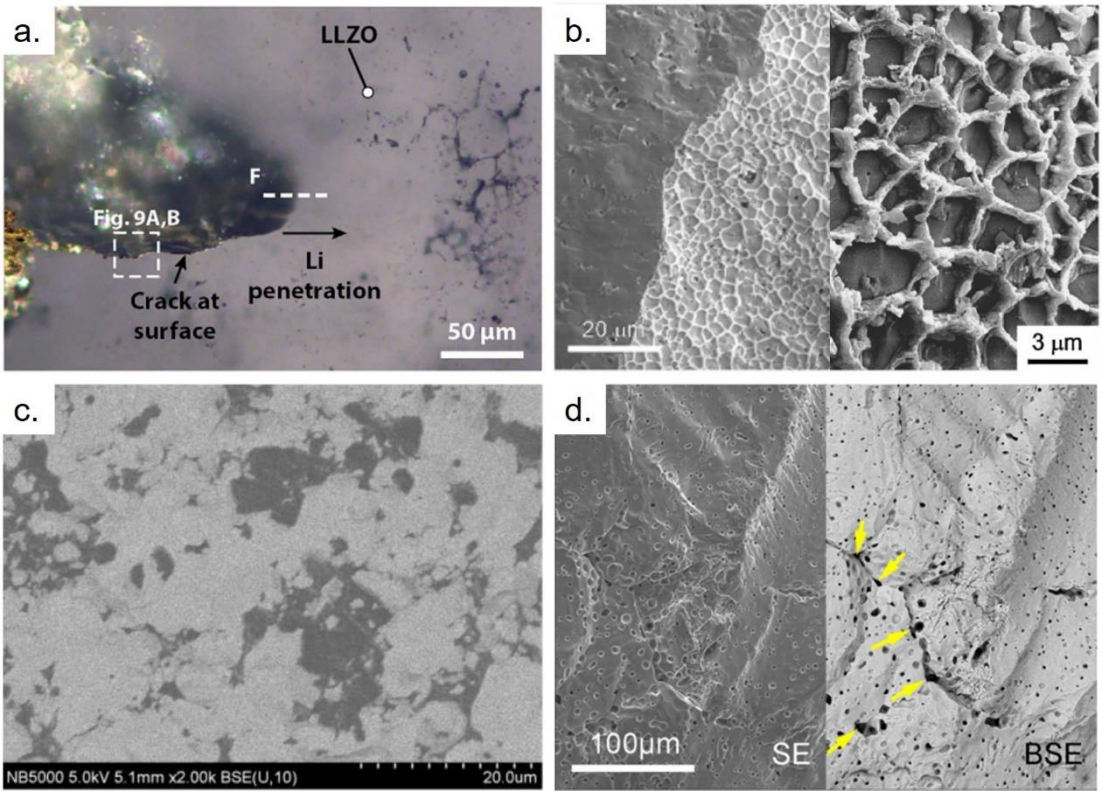

Fig. 1.12. Microscopically observed different modes of dendrites in Li/LLZO/Li cells. **a.** initiation and propagation of dendritic crack filled with lithium metal. **b.** preferential growth of dendrite along grain boundaries. **c.** directly lithium deposition in closed pores. **d.** growth of lithium through interconnect pores. (Adapted from Dasgupta et al[131], Sakamoto et al.[132], Wang et al.[133], Nan et al.[134])

Despite their distinctly different patterns in failure, they are not necessarily governed by intrinsically different processes. As almost all the characterisation of dendrites was conducted *ex-situ*, which does not necessarily reveal the whole lifetime of dendrite formation, researchers might observe only the most prominent correlation between an observed phenomenon and dendrite formation. For example, the listed four types of cell failure in **Fig. 1.12** were all found in the same type of solid electrolyte, LLZO, thus, presumably they should follow the same process of dendrite formation. The difference in their failure modes might simply come from their slight difference in solid electrolyte structure, their different stages of dendrite evolution, or different orientations of the dendrites that were shown. To be specific, while Sakamoto et al. reported dendrite growth along grain boundaries in LLZO, **Fig. 1.12b**, Dasgupta et al. observed

dendrite transgranular fracture in LLZO as well. This difference could come from the much larger grain size in Dasgupta's sample, which may lead to transgranular fracture as well-established in ceramic research, or from different conductivity of the grain boundaries. Dendrite growth along the grain boundary (**Fig. 1.12b**) might also follow the pre-existing pores inside the solid electrolyte (**Fig. 1.12d**), as grain boundaries are known to be pore-rich in ceramics, and different amounts of lithium remained after cross-sectioning. All the other observed failures might originate from direct deposition of lithium inside the closed pores, as **Fig. 1.12c** only shows the very early stage of dendrite initiation. In this regard, the dendrite models should focus more on the electro-chemo-mechanics, i.e. how the electrochemical potential can drive the soft lithium metal to break a tough ceramic.

For all-solid-state batteries with Li metal anode, the failure mechanism was first discussed by Chiang et al. on lithium penetration into single crystalline LLZO and glassy LPS[126]. The Griffith-like strain energy release rate failure model describes that the Poiseuille pressure resulting from continuous lithium plating into a surface flaw could generate sufficient hydrostatic stress and result in cracking of solid electrolyte, based on the assumption that stress relaxation via lithium extrusion might not be possible when the aspect ratio of the flaw is large enough. With knowledge of the fracture toughness of the solid electrolyte, and various plating overpotential, a critical surface flaw size could be determined, as shown in **Fig. 1.13a**.

While the model from Chiang et al. didn't take into account the inhomogeneity of lithium plating, a model recently derived by Bucci et al. quantified the interfacial stress with the consideration of interfacial kinetics, based on a mechanical effect modified Butler-Volmer equation[135]. This model predicts that dendrite propagation can be blocked at the crack tip due to the stress-driven increase of chemical potential of lithium that may block further lithium deposition. In accord to this, a diagram with critical crack length and critical interfacial resistance was proposed, as interfacial resistance can effectively increase the overpotential of lithium plating at a given current density, **Fig. 1.13b**.

A recent model by Ceder et al. demonstrated that such an effect of stress is not only relevant for interface kinetics, but also for the ionic transport inside the solid electrolyte[136]. This work derived a mathematical model for the pressure build up in a surface crack induced by the plastic flow of deposited lithium. The model takes lithium metal plastic flow, electrolyte fracture, and ion redistribution in the solid electrolyte into account, as competing ways of stress relaxation. With their quantitative analysis, the important role of a sufficient ionic conductivity of solid electrolyte to stabilise lithium deposition was revealed, **Fig. 1.13c**.

While most models focus on the stresses in the solid electrolyte, other efforts were made to better understand the mechanical properties of lithium metal. Hackney et al. recently proposed a comprehensive perturbation model with better consideration of the mechanical properties of lithium at different length scales[137]. The authors predicted a range of critical defect length, where the dimensions of surface cracks are too large for efficient diffusional creep while too small for effective dislocation glide, thus leading to a local stress concentration and crack propagation, **Fig. 1.13d**.

While most models are based on the simplification of a uniform microstructure, Srinivasan et al. demonstrated the effect of grain boundaries on crack initiation in polycrystalline LLZO[138]. By using a lattice-spring network, they showed preferred lithium deposition in grain boundaries that can lead to large strain energy, and eventually fracture of the solid electrolyte, **Fig. 1.13e**.

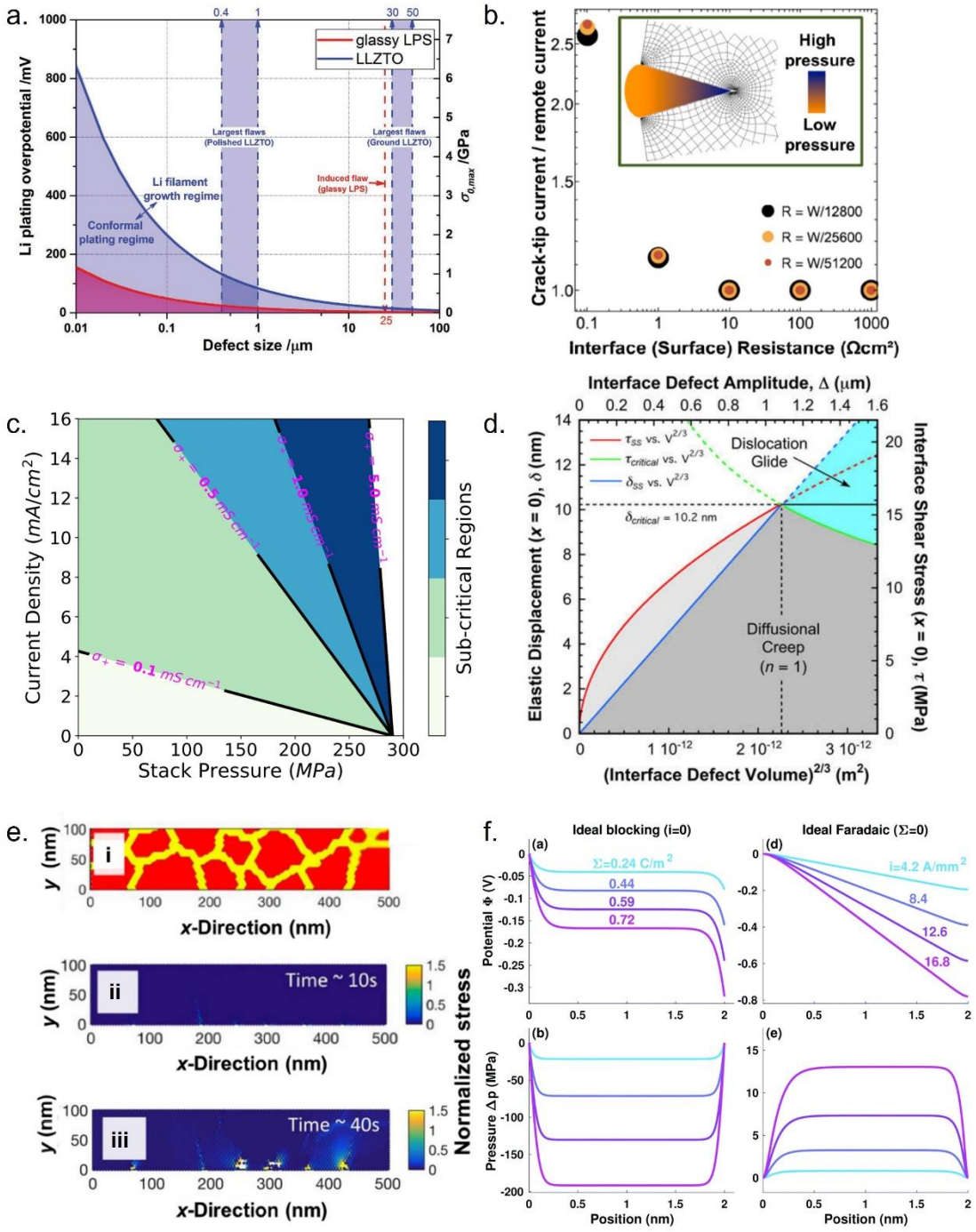

Fig. 1.13. Overview of the developed models to explain mode I dendrite failure in all-solid-state batteries. The models are categorised according to different considerations of fundamental mechanisms[136–141]. **a.** Griffith-like strain energy release rate model, showing the impacts of plating overpotential and defect size on dendrite formation. **b.** Crack propagation model with Butler-Volmer kinetics from mechanical stress taken into account, showing the impacts of crack-tip current and interfacial resistance on dendrite propagation. **c.** Crack propagation model

based on the plastic flow of Li and ion redistribution, showing the role of high ionic conductivity of the SE to stabilise electrodeposition. **d.** Perturbation model based on the mechanical properties of Li at different length scales, showing a range of critical defect length. **e.** Dendrite initiation model showing preferred Li deposition in grain boundary regions based on lattice-spring network. **f.** Dendrite initiation model based on space charging effects.

Apart from the majority of the models that are based on Poiseuille pressure and require a lithium-filled surface crack, Li and Monroe demonstrated that the fracture of solid electrolyte can be driven by the Maxwell stress from space charging effects[139]. The stress strongly depends on the reversible or capacitive nature of the Li/SE interface, which can be described by the interfacial characteristic frequency $f_{int} = i(2\pi \sum)^{-1}$, which is equated in impedance analysis $f_{int} = i(2\pi R_{int} C_{int})^{-1}$. The relative interfacial stress can be determined by the properties of the interface, with a compressive stress for an ideal blocking interface, and a tensile stress for an ideal Faradaic interface, whose level depends on the square of the current density, Fig, 1,13f. Based on experimental data of CCD values, a critical tensile pressure of 1 kPa was estimated by this model. The cell failure was ascribed to lithium nucleation in the grain boundaries rather than solid electrolyte fracture.

Overall, a critical point of many theoretical assessments is the Poiseuille pressure driven by lithium deposition, and the interfacial kinetics described by Butler-Volmer kinetics. However, the majority of the models end up requiring the existence of an impractically sized surface crack or interfacial flaw (~50 μm) to be filled with lithium to generate sufficient stress (30 ~ 100 MPa) in order to fracture the solid electrolyte. However, such a surface flaws were not observed in practical cases. The fact that lithium dendrites still form at a low level of current density even for a flawless interface suggests that such models are not yet sufficient to explain dendrite formation in all-solid-state batteries. In addition, the mechanical properties of lithium were not fully taken into account in most models. Recent studies demonstrate that the mechanical behaviour of lithium could vary significantly at small scale or high enough strain rate, and may

play an important role in dendrite formation[142,143]. Moreover, the proposed models do not explain the CCD difference between different solid electrolytes, i.e. why the oxide materials with much higher fracture toughness and shear moduli suffer from a lower CCD compared with most sulphide-based solid electrolytes. Since no consensus has been reached for a mechanistic understanding of dendrites in all-solid-state batteries, a comprehensive model, which includes proper descriptions of lithium behaviour, properties of solid electrolytes, dynamic process of dendrite evolution, etc. is highly desired, to guide future preventative strategies against lithium dendrites.

1.5 X-ray computed tomography to study cell failure

Owing to the buried nature of lithium dendrites in all-solid-state batteries, the characterisation of dendrite initiation and propagation remains a grand challenge. Ex-situ and destructive methods, involving sectioning the electrolyte and imaging the dendrite using techniques such as SEM have proved valuable. However, due to compliant and soft nature of lithium, it cannot be guaranteed that the morphology after sectioning remains representative of how the dendrite is in the cell. More importantly, *ex-situ* characterisations do not allow following of the development of cracks and penetration of dendrites during cell operation, which is critical to understand the dendrite growth mechanism in all-solid-state batteries. Optical microscopy has been used for *in-situ* studies. However, the in-plane cell set-up, which is widely used in optical imaging of dendrites, does not present the practical conditions in sandwich-structured all-solid-batteries. Moreover, it is challenging to characterise the full shape of dendrites buried inside the solid electrolyte. Due to the non-invasive and non-destructive nature, X-ray computed tomography has been extensively used to investigate failure processes of batteries, providing 3D analysis of structural changes over a large range of length scales. In this section, the applications of X-ray computed tomography to characterise battery failure will be briefly

reviewed, including previous works on dendrites in liquid electrolyte and solid polymer electrolyte, as well as recent investigations on failures of all-solid-state batteries.

Characterising lithium dendrites in liquid electrolyte is challenging, due to the weak attenuation contrast between lithium and the surrounding electrolyte, especially for lab-based X-ray microscopy. Synchrotron X-rays can deliver a high flux beam at low energies, optimising the contrast whilst minimising the required acquisition time. In 2015, Lee et al. employed phase-contrast synchrotron X-ray computed tomography to characterise the microstructures of electro-deposited lithium for the first time. With improved spatial resolution, and optimised contrast via phase-contrast imaging, the 3D microstructures of dendrites were clearly visualised[144]. Moreover, with the capability to electrochemically operate the cell, direct comparison between the structures of dendrites formed under galvanostatic plating and after cycling has been achieved, **Fig. 1.14**. Whilst the mossy dendritic structure formed after plating presents the same electron density as lithium metal, the mossy structure after cycling is more attenuating, suggesting the participation of electrolyte salts in the formation of such mossy structure during cycling. Although the microstructures of dendrites have been revealed in this work, a gap remains in understanding the whole evolution of dendrites, as the formation of dendrites was not followed *in-situ* with a time-resolved manner.

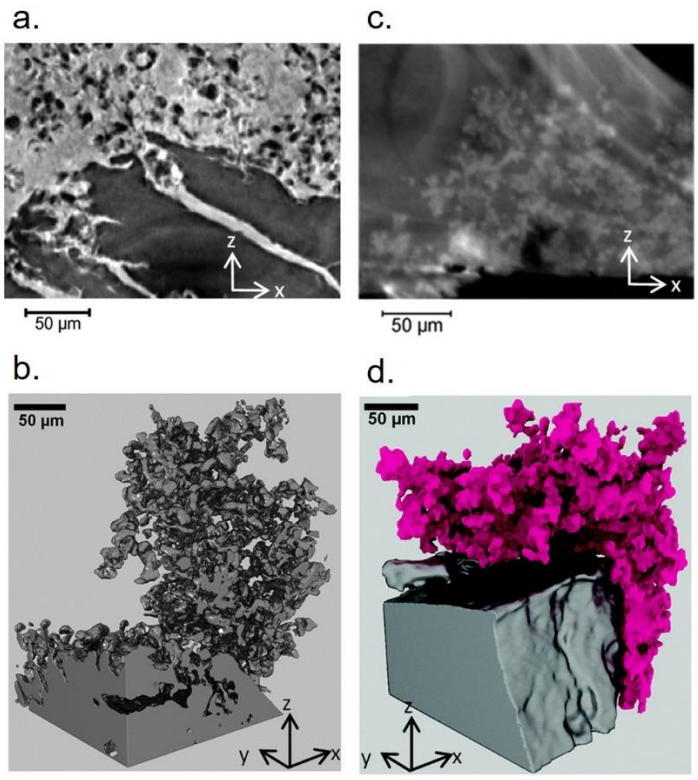

Fig. 1.14. Microstructures of lithium formed during galvanostatic cycling. **a.** & **b.** 2D slice and 3D rendering of the same metallic lithium microstructure formed after plating. **c.** & **d.** 2D slice and 3D rendering of the same metallic lithium microstructure formed after cycling. (Adapted from Lee et al.[144])

The most representative X-ray computed tomography characterisation of dendrites in solid polymer electrolyte is the work done by Balsara et al. in 2013[145]. The same technical challenge holds for the characterisation of lithium dendrites in solid polymer electrolytes. This is the weak contrast between the lithium dendrites and the surrounding electrolyte, although the contrast is inversed from the liquid electrolyte case, as the polymer electrolyte is slightly more attenuating than lithium metal, while the attenuation of the liquid electrolyte is less than that of lithium. While *in-situ* characterisation was again not achieved, the authors followed the whole process of dendrite formation by characterising a small punched-off portion of various cells that were arrested at different stages of dendrite formation. Due to the lack of distinguishable differences among the cells, the *ex-situ* results have been widely taken as a successful *in-situ* characterisation. Unlike the fractal dendrites in liquid electrolyte, the dendrites in solid polymer

electrolytes present a globular lithium protrusion at the interface, Fig. 1.15. Instead of directly imaging the lithium dendrite, the authors revealed the lithium/electrolyte interface, which was highlighted by Fresnel phase contrast. So, the whisker-like structures shown in Fig. 1.15h were in essence the filaments of solid polymer electrolyte surrounded by the lithium protrusion. A subsurface structure before further lithium protrusion into the electrolyte was observed for the first time, and was suggested as the key to inhibit cell failure with solid polymer electrolyte.

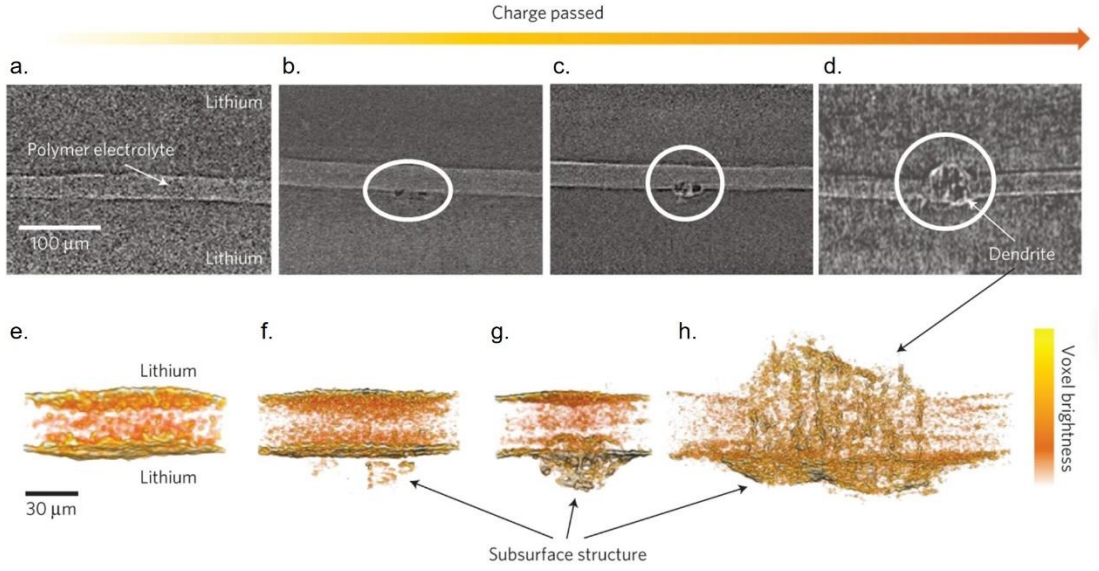

Fig. 1.15. Evolution of dendrite growth through solid polymer electrolyte. **a.** to **d.** X-ray tomography slices showing the cross-sections of symmetric lithium cells cycled to various stages with different amount of charge passed. **a.** 0 C cm^{-2}. **b.** 9 C cm^{-2}. **c.** 84 C cm^{-2}. **d.** shorted cell. **e.** to **h.** 3D reconstructed volumes of cells shown in **a.** to **d.** Dendritic structures that span the thickness of the polymer electrolyte are seen in the shorted cell. (Adapted from Balsara et al.[145])

Owing to the opaque nature of the inorganic solid electrolyte, and the dendrites being buried inside the solid electrolyte, direct *in-situ* observation of dendrites via TEM, SEM, and optical microscopy is more challenging in all-solid-state batteries than other battery systems. Therefore, non-destructive X-ray computed tomography would be expected to play a crucial role in revealing the whole process of cell failure in all-solid-state batteries. X-ray computed tomography has been extensively employed to investigate failure of all-solid-state batteries

since 2018. In 2018, Hatzell et al. examined the microstructural changes in LLZO solid electrolytes between pristine and failed samples via *ex-situ* synchrotron X-ray computed tomography[146]. Due to the overwhelming attenuation from LLZO electrolyte, and weak contrast between lithium and pores, direct observation of lithium dendrites was not achieved. Instead, the volume and connectivity of X-ray transparent regions (lithium and pores) were quantified before and after cycling, suggesting the short-circuit depended on the connectivity of pores, **Fig. 1.16**. However, as the scans were done ex-situ, with different samples for pristine and failed status, the sub-volumes selected for quantitative analysis may not be sufficiently representative, and cannot be directly compared. This might explain why a surprising conclusion that better sintering leads to greater porosity, pore connectivity and easier cell failure was reached by Hatzell et al, which is contrary to the well-established fact in ceramic science that sintering at higher temperature reduces porosity and pore connectivity[147].

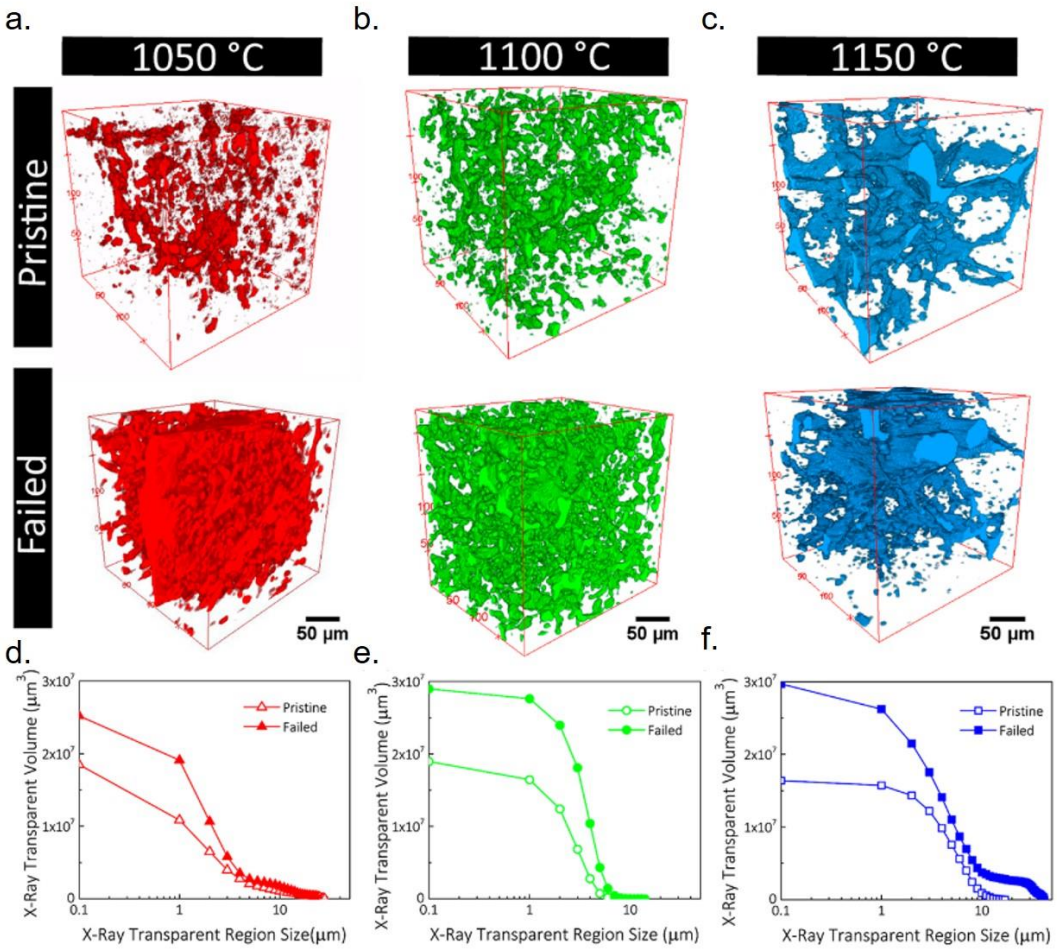

Fig. 1.16. Comparison of microstructure in LLZO solid electrolytes sintered at different conditions in pristine and after cell failure. 3D visualisation of pores in the LLZO electrolytes sintered at **a.** 1050 °C. **b.** 1100 °C. **c.** 1150 °C. The corresponding analyses of pore size distribution are shown in **d.** to **f.** (Adapted from Hatzell et al.[146])

The first *operando* characterisation of cell failure in all-solid-state batteries was achieved by Pylypenko et al. with the implementation of a self-designed *operando* sample holder[148]. By replacing the LLZO solid electrolyte with LPS, and reducing the sample diameter, fast imaging with improved contrast was achieved in their studies. However, *in-situ* tracking of lithium ingress in the sample was not possible due to the weak contrast between lithium and empty space in the tomograms. So, instead of tracking lithium dendrite formation, the authors tracked the expansion of pre-existing cracks in the sample as a result of lithium deposition. In addition to insufficient contrast, the Li/LPS/Li cell characterised in this study is far from being

representative of an acceptable pristine sample. Due to an imperfect cell design and sample preparation, the pristine sample contained many pre-existing cracks that had propagated across the whole thickness of the solid electrolyte. Such defects altered the behaviour of lithium deposition in creating electrolyte fracture to follow and expand the pre-existing cracks. The most important and meaningful part in the *operando* characterisation of dendrites was not achieved.

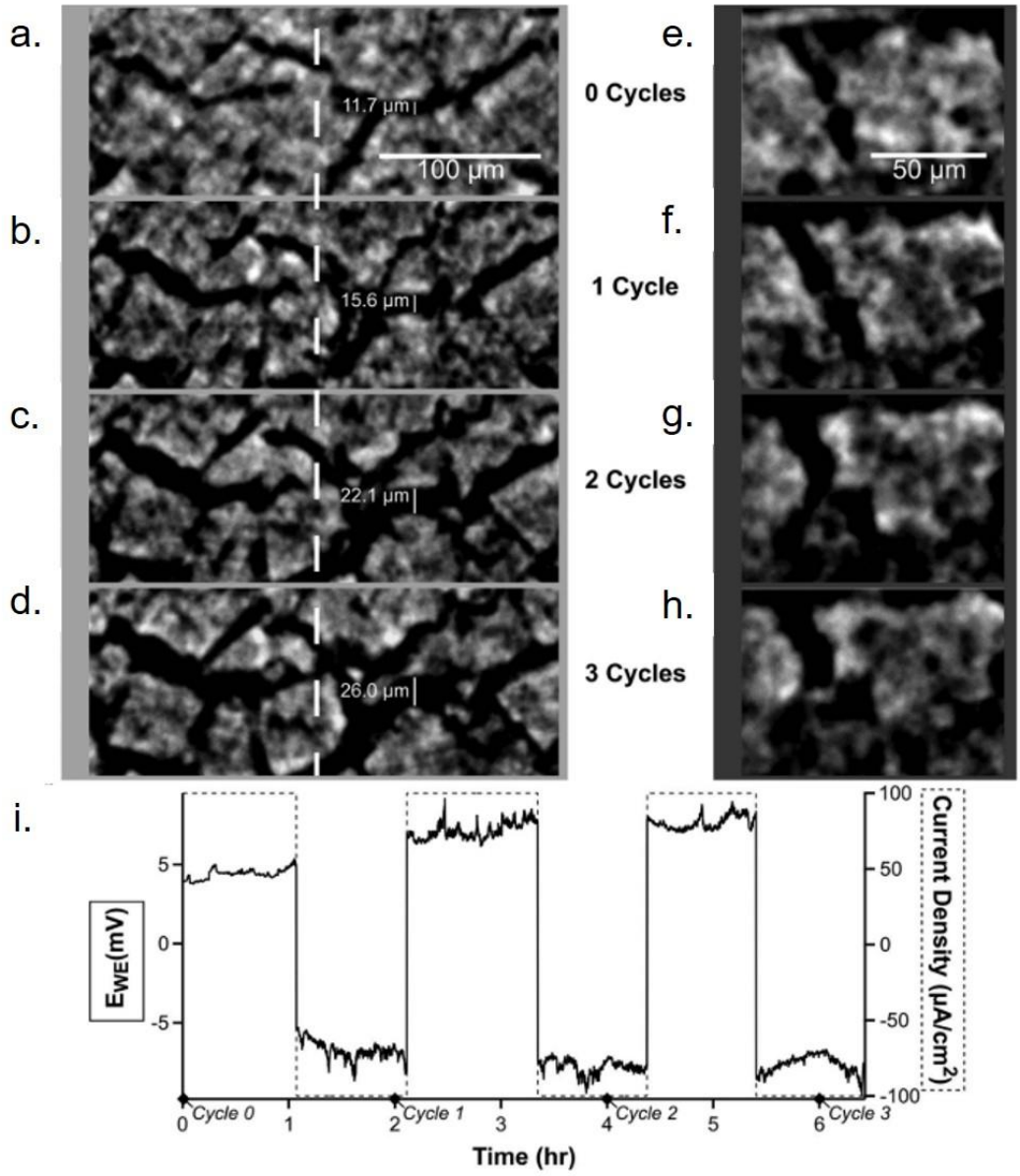

Fig. 1.17. X-ray tomography slices from *in-operando* study of Li/LPS/Li cell cycled at 100 µA/cm^2. **a.** to **d.** reconstructed and thresholded images of the same region after successive

cycles. **e.** to **h.** cross-sectional images of the slice marked by the dotted line shown in **a.** to **d.** Cycling data during the *in-operando* study is shown in i. (Adapted from Pylypenko et al.[148])

Later, Meng et al. employed lab-based X-ray computed tomography with a specially designed cell to conduct an *in-situ* characterisation of dendrite formation[149]. With identical samples preparation as normal batteries and proper stack pressure control, a satisfactory pristine sample was obtained, together with an intimate contact between lithium and Li_6PS_5Cl solid electrolyte at the interface. Comparing the tomograms at the pristine state and after cycling, a less attenuating phase was present inside the Li_6PS_5Cl solid electrolyte after cycling, which was in theory a mixture of lithium ingress and empty space. Whilst the imaging contrast was insufficient to reliably distinguish lithium from the empty space, the authors conducted X-ray diffraction in transmission mode to confirm the existence of lithium by detecting the additional peaks from multiple SEI phases inside the bulk electrolyte. This study provided a novel route of multi-modal characterisation for dendrite investigation.

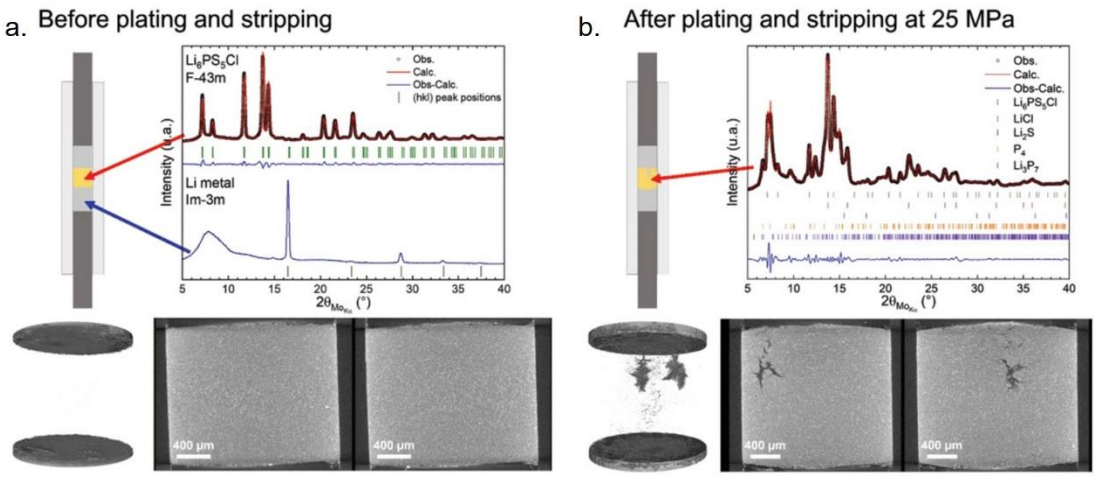

Fig. 1.18. Schematic of cell used for X-ray tomography and X-ray diffraction, X-ray diffraction pattern and fitting, and X-ray tomography slices of a Li/Li_6PS_5Cl/Li cell at a. pristine and b. after plating and stripping. (Adapted from Meng et al.[149])

Apart from characterising solid electrolyte fracture induced by mode I degradation, X-ray computed tomography has also been employed to characterise cell failure due to continuous interphase reaction. In 2019, McDowell et al. investigated the correlation between interphase

formation and chemomechanical degradation in a Li/LAGP/Li cell, where LAGP was known to continuously react with lithium metal, by forming a mixed-ion-electron conducting interphase, **Fig. 1.19**[150]. During the electrochemical cycling, cracking of the solid electrolyte, driven by the volume expansion of interphase layer, was found to significantly increase the impedance of cell. A good fit was established between the area of cracking and the increase in cell impedance.

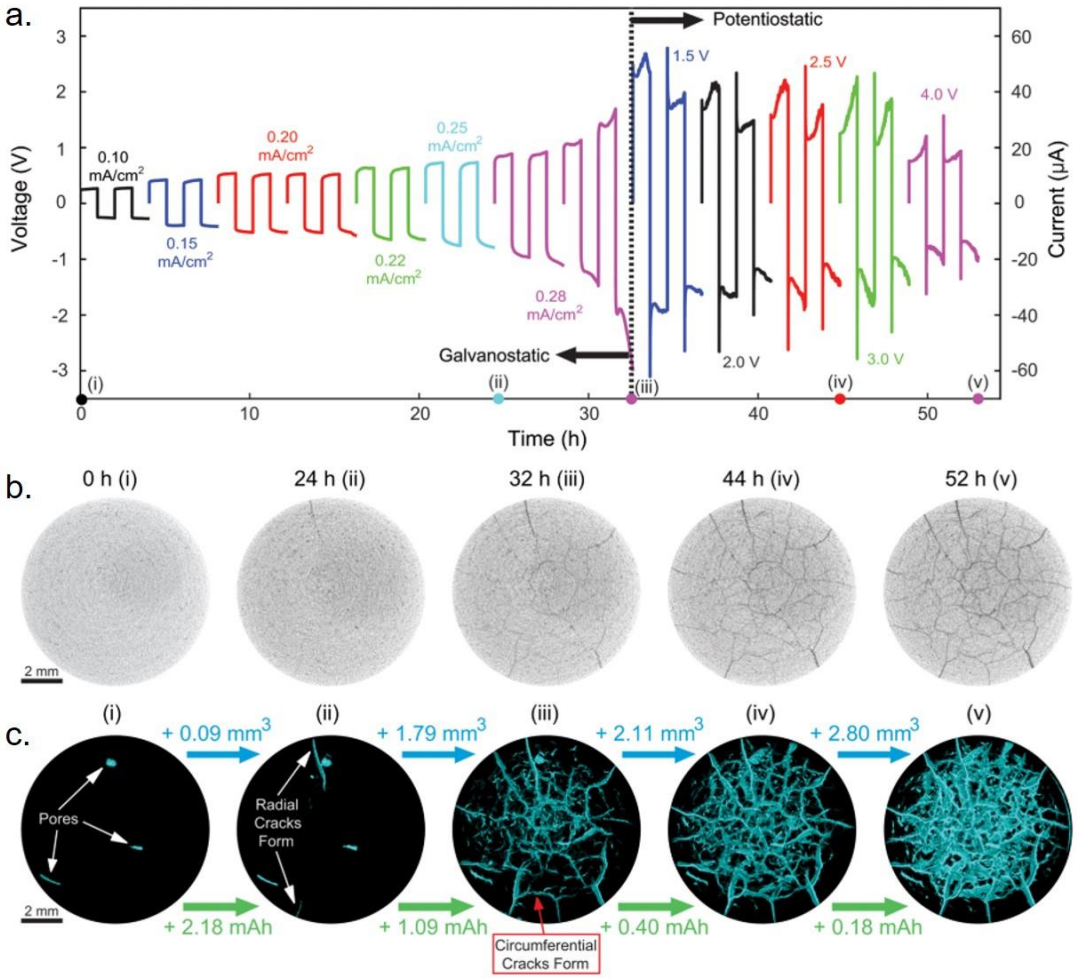

Fig. 1.19. Electrochemical data and X-ray tomography images showing the degradation of LAGP within a Li/LAGP/Li cell during cycling. **a.** In electrochemical measurement, galvanostatic cycling was conducted with increasing current densities for the first 32 h, and then potentiostatic cycling for the remaining time. **b.** & **c.** show the 2D slices of the LAGP pellet at different stages of cycling and the corresponding 3D volume rendering. (Adapted from McDowell et al.[150])

X-ray computed tomography has proved valuable in investigating the failure in all-solid-state batteries. With the capability of tracking electrolyte cracking, lithium ingress, and other microstructural changes under practical cycling conditions, such a technique could provide the unique insight necessary for a mechanistic understanding of dendrite formation. In the meantime, further optimisation of sample preparation, sample environment, and test methodology are required to make full use of this powerful technique. X-ray computed tomography with satisfactory spatial resolution, *operando* capability with fast temporal resolution, and sufficient contrast to differentiate lithium from other phases are necessary for future investigations of all-solid-state batteries.

1.6 Aim of this work

As described in this chapter, all-solid-state batteries could bring a step increase in energy density compare with current Li-ion batteries, only with the application of Li metal anode. While a variety of potential solid electrolytes with promising properties have been explored, little has been achieved in preventing the Li metal anode-related degradation on stripping and plating. To enable the reliable application of the Li metal anode, the mechanisms of cell degradation as a response to Li stripping/plating must be well understood.

In the first instance, this work aims to provide a fundamental understanding of interfacial degradation induced anodic dissolution (stripping) of alkali metal anode. Whilst the formation of voids has been suggested as the origin of voltage polarisation during stripping, this work aims to develop a methodology of *operando* X-ray computed tomography, to characterise the whole process of interfacial degradation. By characterising void accumulation in various battery systems, a quantitative analysis of voids is pursued, revealing the root causes of voltage increase. Other forms of interfacial degradation, apart from void accumulation, will also be discussed, addressing the importance of both morphological stability and chemical/electrochemical stability during cell cycling.

In a second instance, this work aims to mechanistically investigate the process of cell failure induced by lithium plating. Utilising phase-contrast synchrotron X-ray computed tomography combined with spatially mapped X-ray diffraction, the propagation of cracks and propagation of lithium dendrites through the solid electrolytes have been tracked *in-situ*, as a function of charge passed. With the beam conditions and experimental set-up fully optimised, this work aims to directly visualise lithium ingress in the dendritic cracks for the first time, revealing the precedence order of electrolyte cracking and lithium ingress (dry crack propagates ahead of lithium or lithium-filled crack drives a gradual propagation of dendrite). With the fracture behaviour of solid electrolyte clearly observed and understood, the findings are expected to guide a comprehensive model for dendrite formation in all-solid-state batteries, as well as effective preventative strategies in the future.

Finally, the methodology of tomographic characterisation has been further optimised to achieve the first *operando* characterisation of the full process of dendrite formation, with an unprecedentedly high temporal resolution. Combined with multi-scale characterisations, supported by chemical and electrochemical experiments, the mechanisms of dendrite initiation and propagation are discussed. This part of the work aims to propose a comprehensive model to explain the mechanisms of dendrite initiation and propagation, based on the obtained fundamental understandings of dendrites. With limiting factors of solid electrolyte and strategies to improve the performance of all-solid-state batteries suggested by the model, measures are taken to improve the CCD from the perspective of cycling conditions and solid electrolyte processing. The effects of relative density of solid electrolyte, mechanical properties on CCD for dendrite propagation are examined.

References

1. Zeng, X. *et al.* Commercialization of Lithium Battery Technologies for Electric Vehicles. *Advanced Energy Materials* **9**, (2019).

2. Yoshino, A. The Birth of the Lithium-Ion Battery. *Angew. Chemie Int. Ed.* **51**, 5798–5800 (2012).

3. Goodenough, J. B. How we made the Li-ion rechargeable battery: Progress in portable and ubiquitous electronics would not be possible without rechargeable batteries. John B. Goodenough recounts the history of the lithium-ion rechargeable battery. *Nature Electronics* **1**, 204 (2018).

4. Etacheri, V., Marom, R., Elazari, R., Salitra, G. & Aurbach, D. Challenges in the development of advanced Li-ion batteries: A review. *Energy and Environmental Science* **4**, 3243–3262 (2011).

5. Tarascon, J. M. & Armand, M. Issues and challenges facing rechargeable lithium batteries. *Nature* **414**, 359–367 (2001).

6. Whittingham, M. S. Electrical energy storage and intercalation chemistry. *Science (80-.).* **192**, 1126–1127 (1976).

7. Murphy, D. W. & Christian, P. A. Solid state electrodes for high energy batteries. *Science (80-.).* **205**, 651–656 (1979).

8. Thackeray, M. M., David, W. I. F., Bruce, P. G. & Goodenough, J. B. Lithium insertion into manganese spinels. *Mater. Res. Bull.* **18**, 461–472 (1983).

9. Mizushima, K., Jones, P. C., Wiseman, P. J. & Goodenough, J. B. Li_xCoO_2 (0<x<-1): A new cathode material for batteries of high energy density. *Mater. Res. Bull.* **15**, 783–789 (1980).

10. Armand, M. & Tarascon, J. M. Building better batteries. *Nature* **451**, 652–657 (2008).

11. Xu, K. Nonaqueous liquid electrolytes for lithium-based rechargeable batteries. *Chem. Rev.* **104**, 4303–4417 (2004).

12. Yoshino, A. Carbonaceous Material for Negative Electrode of Lithium Ion Battery. *TANSO* **1999**, 45–49 (1999).

13. Goriparti, S. *et al.* Review on recent progress of nanostructured anode materials for Li-ion batteries. *Journal of Power Sources* **257**, 421–443 (2014).

14. Larcher, D. & Tarascon, J. M. Towards greener and more sustainable batteries for electrical energy storage. *Nature Chemistry* **7**, 19–29 (2015).

15. Winter, M. & Besenhard, J. O. Electrochemical lithiation of tin and tin-based intermetallics and composites. *Electrochim. Acta* **45**, 31–50 (1999).

16. Idota, Y., Kubota, T., Matsufuji, A., Maekawa, Y. & Miyasaka, T. Tin-based amorphous oxide: A high-capacity lithium-ion-storage material. *Science (80-.).* **276**, 1395–1397 (1997).

17. Anani, A., Crouch-Baker, S. & Huggins, R. A. Kinetic and Thermodynamic Parameters of Several Binary Lithium Alloy Negative Electrode Materials at Ambient Temperature. *J. Electrochem. Soc.* **134**, 3098–3102 (1987).

18. Hong, Z. & Wei, M. Layered titanate nanostructures and their derivatives as negative electrode materials for lithium-ion batteries. *J. Mater. Chem. A* **1**, 4403–4414 (2013).

19. Nitta, N. & Yushin, G. High-capacity anode materials for lithium-ion batteries: Choice of elements and structures for active particles. *Part. Part. Syst. Charact.* **31**, 317–336 (2014).

20. Zhang, Y. *et al.* Towards better Li metal anodes: Challenges and strategies. *Materials Today* **33**, 56–74 (2020).

21. Wang, Y. *et al.* Lithium and lithium ion batteries for applications in microelectronic

devices: A review. *Journal of Power Sources* **286**, 330–345 (2015).

22. Pinson, M. B. & Bazant, M. Z. Theory of SEI Formation in Rechargeable Batteries: Capacity Fade, Accelerated Aging and Lifetime Prediction. *J. Electrochem. Soc.* **160**, A243–A250 (2013).

23. Verma, P., Maire, P. & Novák, P. A review of the features and analyses of the solid electrolyte interphase in Li-ion batteries. *Electrochimica Acta* **55**, 6332–6341 (2010).

24. Ploehn, H. J., Ramadass, P. & White, R. E. Solvent Diffusion Model for Aging of Lithium-Ion Battery Cells. *J. Electrochem. Soc.* **151**, A456 (2004).

25. Fang, C., Wang, X. & Meng, Y. S. Key Issues Hindering a Practical Lithium-Metal Anode. *Trends Chem.* **1**, 152–158 (2019).

26. Chen, K. H. *et al.* Dead lithium: Mass transport effects on voltage, capacity, and failure of lithium metal anodes. *J. Mater. Chem. A* **5**, 11671–11681 (2017).

27. Fang, C. *et al.* Quantifying inactive lithium in lithium metal batteries. *Nature* **572**, 511–515 (2019).

28. Lu, Y., Tu, Z. & Archer, L. A. Stable lithium electrodeposition in liquid and nanoporous solid electrolytes. *Nat. Mater.* **13**, 961–969 (2014).

29. Park, M. S. *et al.* A highly reversible lithium metal anode. *Sci. Rep.* **4**, 1–8 (2014).

30. Li, S. *et al.* Developing High-Performance Lithium Metal Anode in Liquid Electrolytes: Challenges and Progress. *Adv. Mater.* **30**, 1–29 (2018).

31. Kim, S. H., Choi, K. H., Cho, S. J., Kil, E. H. & Lee, S. Y. Mechanically compliant and lithium dendrite growth-suppressing composite polymer electrolytes for flexible lithium-ion batteries. *J. Mater. Chem. A* **1**, 4949–4955 (2013).

32. Janek, J. & Zeier, W. G. A solid future for battery development. *Nature Energy* **1**, 1–4 (2016).

33. Khurana, R., Schaefer, J. L., Archer, L. A. & Coates, G. W. Suppression of lithium dendrite growth using cross-linked polyethylene/poly(ethylene oxide) electrolytes: A new approach for practical lithium-metal polymer batteries. *J. Am. Chem. Soc.* **136**, 7395–7402 (2014).

34. Rosso, M., Gobron, T., Brissot, C., Chazalviel, J. N. & Lascaud, S. Onset of dendritic growth in lithium/polymer cells. in *Journal of Power Sources* **97**–**98**, 804–806 (Elsevier, 2001).

35. Masquelier, C. Solid electrolytes: Lithium ions on the fast track. *Nature Materials* **10**, 649–650 (2011).

36. Schnell, J. *et al.* All-solid-state lithium-ion and lithium metal batteries – paving the way to large-scale production. *J. Power Sources* **382**, 160–175 (2018).

37. Richards, W. D., Miara, L. J., Wang, Y., Kim, J. C. & Ceder, G. Interface Stability in Solid-State Batteries. *Chem. Mater.* **28**, 266–273 (2016).

38. Xiao, Y. *et al.* Understanding interface stability in solid-state batteries. *Nature Reviews Materials* **5**, 105–126 (2020).

39. Zhao, Q., Stalin, S., Zhao, C. Z. & Archer, L. A. Designing solid-state electrolytes for safe, energy-dense batteries. *Nature Reviews Materials* **5**, 229–252 (2020).

40. Xia, S., Wu, X., Zhang, Z., Cui, Y. & Liu, W. Practical Challenges and Future Perspectives of All-Solid-State Lithium-Metal Batteries. (2019). doi:10.1016/j.chempr.2018.11.013

41. Ogawa, M., Yoshida, K. & Harada, K. All-solid-state lithium batteries with wide operating temperature range. *SEI Tech. Rev.* 88–90 (2012).

42. Chen, L. *et al.* Progress and Perspective of All-Solid-State Lithium Batteries with High Performance at Room Temperature. *Energy and Fuels* **34**, 13456–13472 (2020).

43. Kato, Y. *et al.* All-Solid-State Batteries with Thick Electrode Configurations. *J. Phys. Chem. Lett.* **9**, 607–613 (2018).

44. Luntz, A. C., Voss, J. & Reuter, K. Interfacial Challenges in Solid-State Li Ion Batteries. *Journal of Physical Chemistry Letters* **6**, 4599–4604 (2015).

45. Monroe, C. & Newman, J. The Effect of Interfacial Deformation on Electrodeposition Kinetics. *J. Electrochem. Soc.* **151**, A880 (2004).

46. Monroe, C. & Newman, J. Dendrite Growth in Lithium/Polymer Systems. *J. Electrochem. Soc.* **150**, A1377 (2003).

47. Lou, S. *et al.* Interface Issues and Challenges in All-Solid-State Batteries: Lithium, Sodium, and Beyond. *Adv. Mater.* **33**, 2000721 (2021).

48. Zhang, F. *et al.* A review of mechanics-related material damages in all-solid-state batteries: Mechanisms, performance impacts and mitigation strategies. *Nano Energy* **70**, 104545 (2020).

49. Mo, F. *et al.* Inside or Outside: Origin of Lithium Dendrite Formation of All Solid-State Electrolytes. *Adv. Energy Mater.* **9**, 1902123 (2019).

50. Sharafi, A., Meyer, H. M., Nanda, J., Wolfenstine, J. & Sakamoto, J. Characterizing the Li-$Li_7La_3Zr_2O_{12}$ interface stability and kinetics as a function of temperature and current density. *J. Power Sources* **302**, 135–139 (2016).

51. Wenzel, S., Leichtweiss, T., Krüger, D., Sann, J. & Janek, J. Interphase formation on lithium solid electrolytes - An in situ approach to study interfacial reactions by photoelectron spectroscopy. *Solid State Ionics* **278**, 98–105 (2015).

52. Tang, H. *et al.* Probing Solid-Solid Interfacial Reactions in All-Solid-State Sodium-Ion Batteries with First-Principles Calculations. *Chem. Mater.* **30**, 163–173 (2018).

53. Tian, Y. *et al.* Compatibility issues between electrodes and electrolytes in solid-state

batteries. *Energy Environ. Sci.* **10**, 1150–1166 (2017).

54. Sakuda, A., Hayashi, A. & Tatsumisago, M. Interfacial observation between $LiCoO_2$ electrode and Li_2S-P_2S_5 solid electrolytes of all-solid-state lithium secondary batteries using transmission electron microscopy. *Chem. Mater.* **22**, 949–956 (2010).

55. McGrogan, F. P. *et al.* Compliant Yet Brittle Mechanical Behavior of Li_2S–P_2S_5 Lithium-Ion-Conducting Solid Electrolyte. *Adv. Energy Mater.* **7**, 1–5 (2017).

56. Bucci, G., Talamini, B., Renuka Balakrishna, A., Chiang, Y. M. & Carter, W. C. Mechanical instability of electrode-electrolyte interfaces in solid-state batteries. *Phys. Rev. Mater.* **2**, 105407 (2018).

57. Koerver, R. *et al.* Capacity Fade in Solid-State Batteries: Interphase Formation and Chemomechanical Processes in Nickel-Rich Layered Oxide Cathodes and Lithium Thiophosphate Solid Electrolytes. *Chem. Mater.* **29**, 5574–5582 (2017).

58. Koerver, R. *et al.* Chemo-mechanical expansion of lithium electrode materials-on the route to mechanically optimized all-solid-state batteries. *Energy Environ. Sci.* **11**, 2142–2158 (2018).

59. Spencer Jolly, D. *et al.* Sodium/Na β″ Alumina Interface: Effect of Pressure on Voids. *ACS Appl. Mater. Interfaces* **12**, 678–685 (2020).

60. Sakamoto, J. More pressure needed. *Nature Energy* **4**, 827–828 (2019).

61. Kasemchainan, J. *et al.* Critical stripping current leads to dendrite formation on plating in lithium anode solid electrolyte cells. *Nat. Mater.* **18**, 1105–1111 (2019).

62. Wu, Z. *et al.* Utmost limits of various solid electrolytes in all-solid-state lithium batteries: A critical review. *Renewable and Sustainable Energy Reviews* **109**, 367–385 (2019).

63. Kim, K. J., Balaish, M., Wadaguchi, M., Kong, L. & Rupp, J. L. M. Solid-State Li–Metal Batteries: Challenges and Horizons of Oxide and Sulfide Solid Electrolytes and

Their Interfaces. *Advanced Energy Materials* **11**, 2002689 (2021).

64. Afyon, S. *et al.* Building better all-solid-state batteries with Li-garnet solid electrolytes and metalloid anodes. *J. Mater. Chem. A* **7**, 21299–21308 (2019).

65. Sharafi, A. *et al.* Surface Chemistry Mechanism of Ultra-Low Interfacial Resistance in the Solid-State Electrolyte $Li_7La_3Zr_2O_{12}$. *Chem. Mater.* **29**, 7961–7968 (2017).

66. Wenzel, S., Sedlmaier, S. J., Dietrich, C., Zeier, W. G. & Janek, J. Interfacial reactivity and interphase growth of argyrodite solid electrolytes at lithium metal electrodes. *Solid State Ionics* **318**, 102–112 (2018).

67. Chen, B., Xu, C., Wang, H. & Zhou, J. Insights into interfacial stability of Li_6PS_5Cl solid electrolytes with buffer layers. *Curr. Appl. Phys.* **19**, 149–154 (2019).

68. Xu, R. *et al.* Interface engineering of sulfide electrolytes for all-solid-state lithium batteries. *Nano Energy* **53**, 958–966 (2018).

69. Okuno, Y., Haruyama, J. & Tateyama, Y. Comparative study on sulfide and oxide electrolyte interfaces with cathodes in all-solid-state battery via first-principles calculations. *ACS Appl. Energy Mater.* **3**, 11061–11072 (2020).

70. Kanno, R., Hata, T., Kawamoto, Y. & Irie, M. Synthesis of a new lithium ionic conductor, thio-LISICON-lithium germanium sulfide system. *Solid State Ionics* **130**, 97–104 (2000).

71. Kanno, R. & Murayama, M. Lithium Ionic Conductor Thio-LISICON: The Li_2S-GeS_2-P_2S_5 System. *J. Electrochem. Soc.* **148**, A742 (2001).

72. Kamaya, N. *et al.* A lithium superionic conductor. *Nat. Mater.* **10**, 682–686 (2011).

73. Ong, S. P. *et al.* Phase stability, electrochemical stability and ionic conductivity of the $Li_{10\pm1}MP_2X_{12}$ (M = Ge, Si, Sn, Al or P, and X = O, S or Se) family of superionic conductors. *Energy Environ. Sci.* **6**, 148–156 (2013).

74. Kato, Y. *et al.* High-power all-solid-state batteries using sulfide superionic conductors. *Nat. Energy* **1**, 1–7 (2016).

75. Wenzel, S. *et al.* Direct Observation of the Interfacial Instability of the Fast Ionic Conductor Li10GeP2S12 at the Lithium Metal Anode. *Chem. Mater.* **28**, 2400–2407 (2016).

76. Mizuno, F., Hayashi, A., Tadanaga, K. & Tatsumisago, M. New, highly ion-conductive crystals precipitated from Li_2S-P_2S_5 glasses. *Adv. Mater.* **17**, 918–921 (2005).

77. Hayashi, A., Hama, S., Morimoto, H., Tatsumisago, M. & Minami, T. Preparation of Li_2S–P_2S_5 amorphous solid electrolytes by mechanical milling. *J. Am. Ceram. Soc.* **84**, 477–479 (2001).

78. Hayashi, A., Hama, S., Morimoto, H., Tatsumisago, M. & Minami, T. High lithium ion conductivity of glass-ceramics derived from mechanically milled glassy powders. *Chem. Lett.* 872–873 (2001). doi:10.1246/cl.2001.872

79. Tatsumisago, M. & Hayashi, A. Sulfide Glass-Ceramic Electrolytes for All-Solid-State Lithium and Sodium Batteries. *Int. J. Appl. Glas. Sci.* **5**, 226–235 (2014).

80. Tatsumisago, M., Hama, S., Hayashi, A., Morimoto, H. & Minami, T. New lithium ion conducting glass-ceramics prepared from mechanochemical Li_2S-P_2S_5 glasses. *Solid State Ionics* **154**, 635–640 (2002).

81. Tachez, M., Malugani, J. P., Mercier, R. & Robert, G. Ionic conductivity of and phase transition in lithium thiophosphate Li_3PS_4. *Solid State Ionics* **14**, 181–185 (1984).

82. Yamane, H. *et al.* Crystal structure of a superionic conductor, $Li_7P_3S_{11}$. *Solid State Ionics* **178**, 1163–1167 (2007).

83. Seino, Y., Ota, T., Takada, K., Hayashi, A. & Tatsumisago, M. A sulphide lithium super ion conductor is superior to liquid ion conductors for use in rechargeable batteries. *Energy Environ. Sci.* **7**, 627–631 (2014).

84. Deiseroth, H. J. *et al.* Li_6PS_5X: A class of crystalline Li-rich solids with an unusually high Li+ mobility. *Angew. Chemie - Int. Ed.* **47**, 755–758 (2008).

85. Deng, Z., Zhu, Z., Chu, I. H. & Ong, S. P. Data-driven first-principles methods for the study and design of alkali superionic conductors. *Chem. Mater.* **29**, 281–288 (2017).

86. Rao, R. P., Sharma, N., Peterson, V. K. & Adams, S. Formation and conductivity studies of lithium argyrodite solid electrolytes using *in-situ* neutron diffraction. *Solid State Ionics* **230**, 72–76 (2013).

87. Rayavarapu, P. R., Sharma, N., Peterson, V. K. & Adams, S. Variation in structure and Li +-ion migration in argyrodite-type Li_6PS_5X (X = Cl, Br, I) solid electrolytes. *J. Solid State Electrochem.* **16**, 1807–1813 (2012).

88. Rao, R. P. & Adams, S. Studies of lithium argyrodite solid electrolytes for all-solid-state batteries. *Phys. Status Solidi Appl. Mater. Sci.* **208**, 1804–1807 (2011).

89. Chen, M., Yin, X., Reddy, M. V. & Adams, S. All-solid-state MoS_2/Li_6PS_5Br/In-Li batteries as a novel type of Li/S battery. *J. Mater. Chem. A* **3**, 10698–10702 (2015).

90. Yubuchi, S. *et al.* Preparation of high lithium-ion conducting Li_6PS_5Cl solid electrolyte from ethanol solution for all-solid-state lithium batteries. *J. Power Sources* **293**, 941–945 (2015).

91. Zhou, L. *et al.* Solvent-Engineered Design of Argyrodite Li_6PS_5X (X = Cl, Br, I) Solid Electrolytes with High Ionic Conductivity. *ACS Energy Lett.* **4**, 265–270 (2019).

92. Zhou, L., Assoud, A., Zhang, Q., Wu, X. & Nazar, L. F. New Family of Argyrodite Thioantimonate Lithium Superionic Conductors. *J. Am. Chem. Soc.* **141**, 19002–19013 (2019).

93. Wenzel, S., Sedlmaier, S. J., Dietrich, C., Zeier, W. G. & Janek, J. Interfacial reactivity and interphase growth of argyrodite solid electrolytes at lithium metal electrodes. *Solid State Ionics* **318**, 102–112 (2018).

94. Peljo, P. & Girault, H. H. Electrochemical potential window of battery electrolytes: The HOMO-LUMO misconception. *Energy Environ. Sci.* **11**, 2306–2309 (2018).

95. Lotsch, B. V. & Maier, J. Relevance of solid electrolytes for lithium-based batteries: A realistic view. *J. Electroceramics* **38**, 128–141 (2017).

96. Krauskopf, T., Richter, F. H., Zeier, W. G. & Janek, J. Physicochemical Concepts of the Lithium Metal Anode in Solid-State Batteries. *Chem. Rev.* **120**, 7745–7794 (2020).

97. Richards, W. D., Miara, L. J., Wang, Y., Kim, J. C. & Ceder, G. Interface Stability in Solid-State Batteries. *Chem. Mater.* **28**, 266–273 (2016).

98. Zhu, Y., He, X. & Mo, Y. First principles study on electrochemical and chemical stability of solid electrolyte-electrode interfaces in all-solid-state Li-ion batteries. *J. Mater. Chem. A* **4**, 3253–3266 (2016).

99. Zhu, Y., He, X. & Mo, Y. Origin of Outstanding Stability in the Lithium Solid Electrolyte Materials: Insights from Thermodynamic Analyses Based on First-Principles Calculations. *ACS Appl. Mater. Interfaces* **7**, 23685–23693 (2015).

100. Schwietert, T. K. *et al.* Clarifying the relationship between redox activity and electrochemical stability in solid electrolytes. *Nat. Mater.* **19**, 428–435 (2020).

101. Wenzel, S. *et al.* Direct Observation of the Interfacial Instability of the Fast Ionic Conductor $Li_{10}GeP_2S_{12}$ at the Lithium Metal Anode. *Chem. Mater.* **28**, 2400–2407 (2016).

102. Hartmann, P. *et al.* Degradation of NASICON-type materials in contact with lithium metal: Formation of mixed conducting interphases (MCI) on solid electrolytes. *J. Phys. Chem. C* **117**, 21064–21074 (2013).

103. Hoar, T. P. & Price, L. E. The electrochemical interpretation of Wagner's theory of tarnishing reactions. *Trans. Faraday Soc.* **34**, 867–872 (1938).

104. Ma, C. *et al.* Interfacial Stability of Li Metal-Solid Electrolyte Elucidated via in Situ Electron Microscopy. *Nano Lett.* **16**, 7030–7036 (2016).

105. Zhu, Y. *et al.* Dopant-Dependent Stability of Garnet Solid Electrolyte Interfaces with Lithium Metal. *Adv. Energy Mater.* **9**, 1803440 (2019).

106. Hesse, D., Werner, P., Mattheis, R. & Heydenreich, J. Interfacial reaction barriers during thin-film solid-state reactions: The crystallographic origin of kinetic barriers at the NiS_2/Si(111) interface. *Appl. Phys. A Solids Surfaces* **57**, 415–425 (1993).

107. Schmalzried, H. & Janek, J. Chemical kinetics of phase boundaries in solids. *Berichte der Bunsengesellschaft für Phys. Chemie* **102**, 127–143 (1998).

108. Krauskopf, T., Hartmann, H., Zeier, W. G. & Janek, J. Toward a Fundamental Understanding of the Lithium Metal Anode in Solid-State Batteries - An Electrochemo-Mechanical Study on the Garnet-Type Solid Electrolyte $Li_{6.25}Al_{0.25}La_3Zr_2O_{12}$. *ACS Appl. Mater. Interfaces* **11**, 14463–14477 (2019).

109. Meyer, M., Rickert, H. & Schwaitzer, U. Investigations on the kinetics of the anodic dissolution of lithium at the interface Li/Li3N. *Solid State Ionics* **9**–**10**, 689–693 (1983).

110. Jow, T. R. & Liang, C. C. Interface Between Solid Electrode and Solid Electrolyte—A Study of the Li/LiI (Al_2O_3) Solid-Electrolyte System. *J. Electrochem. Soc.* **130**, 737–740 (1983).

111. Yonemoto, F. *et al.* Temperature effects on cycling stability of Li plating/stripping on Ta-doped $Li_7La_3Zr_2O_{12}$. *J. Power Sources* **343**, 207–215 (2017).

112. Koshikawa, H. *et al.* Dynamic changes in charge-transfer resistance at Li metal/$Li_7La_3Zr_2O_{12}$ interfaces during electrochemical Li dissolution/deposition cycles. *J. Power Sources* **376**, 147–151 (2018).

113. Zheng, G. *et al.* Interconnected hollow carbon nanospheres for stable lithium metal anodes. *Nat. Nanotechnol.* **9**, 618–623 (2014).

114. Aurbach, D., Zinigrad, E., Teller, H. & Dan, P. Factors Which Limit the Cycle Life of Rechargeable Lithium (Metal) Batteries. *J. Electrochem. Soc.* **147**, 1274 (2000).

115. Qian, J. *et al.* High rate and stable cycling of lithium metal anode. *Nat. Commun.* **6**, 1–9 (2015).

116. Suo, L., Hu, Y. S., Li, H., Armand, M. & Chen, L. A new class of Solvent-in-Salt electrolyte for high-energy rechargeable metallic lithium batteries. *Nat. Commun.* **4**, 1–9 (2013).

117. Ryou, M.-H., Lee, Y. M., Lee, Y., Winter, M. & Bieker, P. Mechanical Surface Modification of Lithium Metal: Towards Improved Li Metal Anode Performance by Directed Li Plating. *Adv. Funct. Mater.* **25**, 834–841 (2015).

118. Witten, T. A. & Sander, L. M. Diffusion-limited aggregation, a kinetic critical phenomenon. *Phys. Rev. Lett.* **47**, 1400–1403 (1981).

119. Bai, P., Li, J., Brushett, F. R. & Bazant, M. Z. Transition of lithium growth mechanisms in liquid electrolytes. *Energy Environ. Sci.* **9**, 3221–3229 (2016).

120. Popovic, J. *et al.* High Lithium Transference Number Electrolytes Containing Tetratriflylpropene's Lithium Salt. *J. Phys. Chem. Lett.* **9**, 5116–5120 (2018).

121. Golozar, M. *et al.* In situ observation of solid electrolyte interphase evolution in a lithium metal battery. *Commun. Chem.* **2**, 1–9 (2019).

122. Barton, J. L. & Bockris, and J. O. The electrolytic growth of dendrites from ionic solutions. *Proc. R. Soc. London. Ser. A. Math. Phys. Sci.* **268**, 485–505 (1962).

123. Monroe, C. & Newman, J. The Impact of Elastic Deformation on Deposition Kinetics at Lithium/Polymer Interfaces. *J. Electrochem. Soc.* **152**, A396 (2005).

124. Aguesse, F. *et al.* Investigating the dendritic growth during full cell cycling of garnet electrolyte in direct contact with Li metal. *ACS Appl. Mater. Interfaces* **9**, 3808–3816

(2017).

125. Manalastas, W. *et al.* Mechanical failure of garnet electrolytes during Li electrodeposition observed by in-operando microscopy. *J. Power Sources* **412**, 287–293 (2019).

126. Porz, L. *et al.* Mechanism of Lithium Metal Penetration through Inorganic Solid Electrolytes. *Adv. Energy Mater.* **7**, 1–12 (2017).

127. Lu, X., Lemmon, J. P., Sprenkle, V. & Yang, Z. Sodium-beta alumina batteries: Status and challenges. *Jom* **62**, 31–36 (2010).

128. De Jonghe, L. C., Feldman, L. & Buechele, A. Failure modes of Na-beta alumina. *Solid State Ionics* **5**, 267–269 (1981).

129. De Jonghe, L. C., Feldman, L. & Beuchele, A. Slow degradation and electron conduction in sodium/beta-aluminas. *J. Mater. Sci.* **16**, 780–786 (1981).

130. Feldman, L. A. & De Jonghe, L. C. Initiation of mode I degradation in sodium-beta alumina electrolytes. *J. Mater. Sci.* **17**, 517–524 (1982).

131. Kazyak, E. *et al.* Li Penetration in Ceramic Solid Electrolytes: Operando Microscopy Analysis of Morphology, Propagation, and Reversibility. *Matter* **2**, 1–24 (2020).

132. Cheng, E. J., Sharafi, A. & Sakamoto, J. Intergranular Li metal propagation through polycrystalline $Li_{6.25}Al_{0.25}La_3Zr_2O_{12}$ ceramic electrolyte. *Electrochim. Acta* **223**, 85–91 (2017).

133. Han, F. *et al.* High electronic conductivity as the origin of lithium dendrite formation within solid electrolytes. *Nat. Energy* **4**, 187–196 (2019).

134. Ren, Y., Shen, Y., Lin, Y. & Nan, C. W. Direct observation of lithium dendrites inside garnet-type lithium-ion solid electrolyte. *Electrochem. commun.* **57**, 27–30 (2015).

135. Bucci, G. & Christensen, J. Modeling of lithium electrodeposition at the lithium/ceramic

electrolyte interface: The role of interfacial resistance and surface defects. *J. Power Sources* **441**, 227186 (2019).

136. Barroso-Luque, L., Tu, Q. & Ceder, G. An Analysis of Solid-State Electrodeposition-Induced Metal Plastic Flow and Predictions of Stress States in Solid Ionic Conductor Defects. *J. Electrochem. Soc.* **167**, 020534 (2020).

137. Herbert, E. G., Dudney, N. J., Rochow, M., Thole, V. & Hackney, S. A. On the mechanisms of stress relaxation and intensification at the lithium/solid-state electrolyte interface. *J. Mater. Res.* **34**, 3593–3616 (2019).

138. Barai, P., Higa, K., Ngo, A. T., Curtiss, L. A. & Srinivasan, V. Mechanical Stress Induced Current Focusing and Fracture in Grain Boundaries. *J. Electrochem. Soc.* **166**, A1752–A1762 (2019).

139. Li, G. & Monroe, C. W. Dendrite nucleation in lithium-conductive ceramics. *Phys. Chem. Chem. Phys.* **21**, 20354–20359 (2019).

140. Chiang, Y. M. Mechanism of Lithium Metal Penetration through Inorganic Solid Electrolytes. *Adv. Energy Mater.* **7**, 1–12 (2017).

141. Bucci, G. & Christensen, J. Modeling of lithium electrodeposition at the lithium/ceramic electrolyte interface: The role of interfacial resistance and surface defects. *J. Power Sources* **441**, (2019).

142. Xu, C., Ahmad, Z., Aryanfar, A., Viswanathan, V. & Greer, J. R. Enhanced strength and temperature dependence of mechanical properties of Li at small scales and its implications for Li metal anodes. *Proc. Natl. Acad. Sci.* **114**, 57–61 (2017).

143. Citrin, M. A. *et al.* From ion to atom to dendrite: Formation and nanomechanical behavior of electrodeposited lithium. *MRS Bull.* 1–14 (2020). doi:10.1557/mrs.2020.148

144. Eastwood, D. S. *et al.* Three-dimensional characterization of electrodeposited lithium

microstructures using synchrotron X-ray phase contrast imaging. *Chem. Commun.* **51**, 266–268 (2015).

145. Harry, K. J., Hallinan, D. T., Parkinson, D. Y., Macdowell, A. A. & Balsara, N. P. Detection of subsurface structures underneath dendrites formed on cycled lithium metal electrodes. *Nat. Mater.* **13**, (2013).

146. Shen, F., Dixit, M. B., Xiao, X. & Hatzell, K. B. Effect of Pore Connectivity on Li Dendrite Propagation within LLZO Electrolytes Observed with Synchrotron X-ray Tomography. *ACS Energy Lett.* **3**, 1056–1061 (2018).

147. Hu, Z. & Lu, K. Evolution of pores and tortuosity during sintering. *J. Am. Ceram. Soc.* **97**, 2383–2386 (2014).

148. Seitzman, N. *et al.* Toward all-solid-state lithium batteries: Three-dimensional visualization of lithium migration in β-Li3PS4 ceramic electrolyte. *J. Electrochem. Soc.* **165**, A3732–A3737 (2018).

149. Doux, J. *et al.* Stack Pressure Considerations for Room Temperature All-Solid-State Lithium Metal Batteries. *Adv. Energy Mater.* 1903253 (2019). doi:10.1002/aenm.201903253

150. Tippens, J. *et al.* Visualizing Chemomechanical Degradation of a Solid-State Battery Electrolyte. *ACS Energy Lett.* **4**, 1475–1483 (2019).

Chapter 2. Experimental Techniques

2.1 Introduction

This chapter aims to serve as an introduction to all the experimental techniques involved in this project and their related mechanisms. Experimental techniques are categorized into sample preparation techniques, characterisation techniques, electrochemical techniques, and mechanical test techniques according to their functions. First, ball milling and SPS are introduced as solid electrolyte preparation techniques. Then, a variety of characterisation techniques including XRD, SEM, EDX, FIB, DEMS, SIMS, XCT, and phase-contrast imaging are presented with their mechanisms and scope of characterisation. EIS, galvanostatic cycling, and rate test are introduced as three common methods of electrochemical tests. The fundamentals of nano-indentation and four-point bending test are also introduced in this chapter, which have been employed to measure the mechanical properties of solid electrolyte materials.

2.2 Sample preparation techniques

2.2.1 Ball milling

As a traditional technique of powder processing, ball milling is widely used for reducing the particle sizes and for the mixing of different materials. Ball milling is a shear-force dominant process, where the particles are breakdown by impact and attrition of the grinding media (normally Zirconia, steel, or agate balls).

In addition to controlling particle sizes, ball milling with high energy plays an important role in battery research to produce metastable materials, which cannot be produced using thermal equilibrium processes. With a faster rotation speed and heavier grinding balls, the impact energy of the high-energy ball milling is typically 1000 times higher than that of the

conventional ball milling[1]. The much-increased impact energy can activate chemical reactions which are normally only possible at higher temperatures. This is called reactive milling or mechano-chemistry. In this work, ball milling was employed to synthesise Li_6PS_5Cl solid electrolyte from precursors of Li_2S, P_2S_5, and LiCl. The energetic ball milling allowed formation of crystallised Li_6SP_5Cl, as well as the local disordering in the Li_6PS_5Cl lattice structure, which enhanced the ionic conductivity of the synthesised solid electrolyte[2].

2.2.2 Spark plasma sintering

Spark plasma sintering (SPS) is an advanced sintering technique used to achieve fast and effective densification of ceramics at lower temperature compared to conventional sintering techniques. SPS has been named alternatively as field-assisted sintering technique, pulsed-electric current sintering, plasma-activated sintering, and current-activated pressure-assisted densification.

The main characteristic of SPS is the pulsed or unpulsed AC or DC current that directly passes through the graphite/tungsten carbide die, as well as the conductive power compact during sintering. The SPS set-up and the sample environment are shown in **Fig. 2.1**.

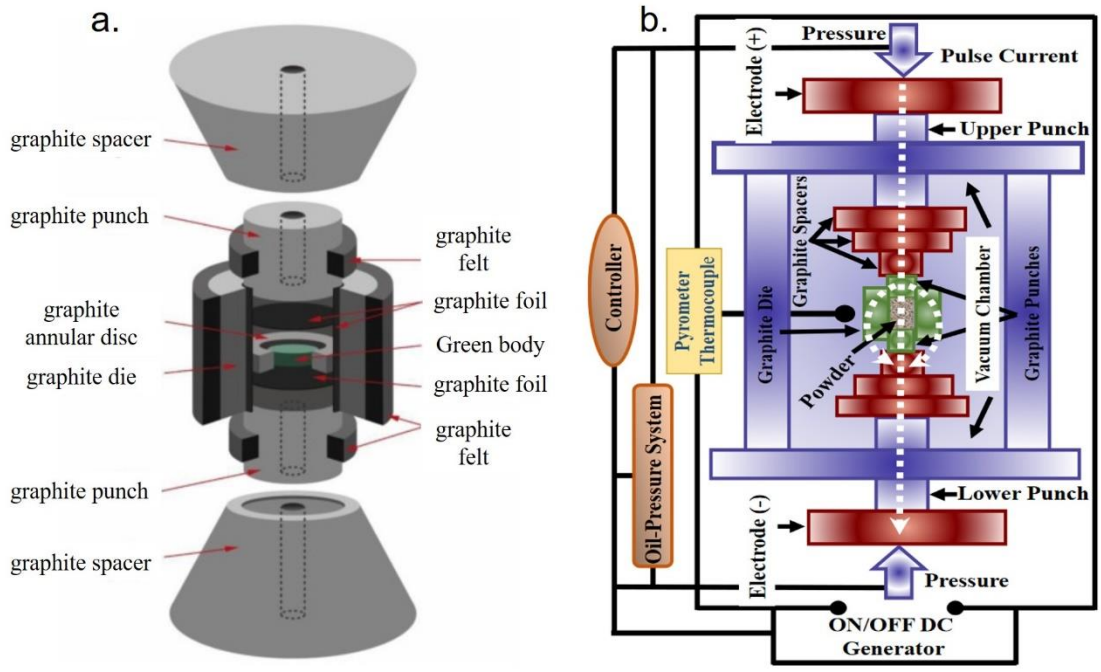

Fig. 2.1. Schematic illustrating **a.** the assembly of sample into the graphite tools used for SPS. **b.** the schematic of the SPS machine (Adapted from Arvind Agarwal, 2021[3]).

The SPS process is a combination of stress, heating, and electric fields. While their respective effects on the sintering mechanisms and sample densification are not well-established, the following aspects are recognised to play important roles during SPS[4]:

Plasma generation: with the pulsed current passing through the sample, sparks and even plasma discharges can be generated between the particle contacts. The ionisation at the particle contact develops the "impulsive pressure" which facilitates diffusion of the atoms at contacts, thus assists densification.

Electroplastic effect: metal powders could have a lower yield strength under an electric field due to the electroplastic effect.

Joule heating: due to the passage of huge electric current through particles, significant Joule heating is generated, which assists the welding of particles under uniaxial pressure.

Pulsed current: apart from Joule heating and generation of plasma, the passage of current also assists the densification via an electrical field diffusion effect. In conductive samples, the

applied electrical field leads to high-speed migration of ions, which eventually results in high-speed diffusion, and therefore accelerated densification.

Mechanical pressure: when a spark discharge is generated in a gap or at the contact point between powder particles, a local high temperature-state is achieved, which causes evaporation and melting on the surface of particles. With the uniaxial pressure applied, the surface of particles can be plastically deformed, which assists the densification of materials.

As the heat generation in SPS is internal, in contrast to conventional sintering or hot pressing where the heat is externally provided, the SPS is normally accompanied with an extremely high heating or cooling rate, and therefore a very short sintering time. The lower sintering temperature, extremely short sintering time, and outstanding densification of SPS offers vast possibilities for its application in the development of all-solid-state batteries, providing an effective way to optimise the structure of solid electrolyte via thermal processing. In this work, the SPS was employed to densify the Li_6PS_5Cl pellets, minimising the porosity of solid electrolyte pellets.

2.3 Characterisation techniques

2.3.1 X-ray diffraction

X-ray diffraction (XRD) is a widely-used technique to determine the crystallographic structure of a material. XRD relies on the nature of X-ray as an electromagnetic wave, with a wavelength in the order of nanometres. X-rays can interact with the electric fields of electrons in atoms and are therefore scattered by atoms in all directions, without the beam losing any energy. This interaction between the X-ray and the characterised materials is called coherent scattering or Thomson scattering.

Interference can take place, when waves are scattered by an ordered (i.e. periodic) lattice. The interference results in a pattern of higher or lower intensities, due to in-phase (constructive), or

out-of-phase (destructive) interference respectively. Constructive interference is observed when Bragg's Law is satisfied:

$$n\lambda = 2\, d_{hkl}\, sin\, \theta \qquad 2.1$$

Where n is an integer, λ is the wavelength of the incident X-ray, d_{hkl} is the d-spacing (the distance between two adjacent parallel (hkl) planes in the lattice structure, and θ is the half the scattering angle ($2\,\theta$), between the incoming and scattered outgoing beam directions. The process of forming constructive interference as described by the Bragg's Law is well illustrated in **Fig. 2.2**.

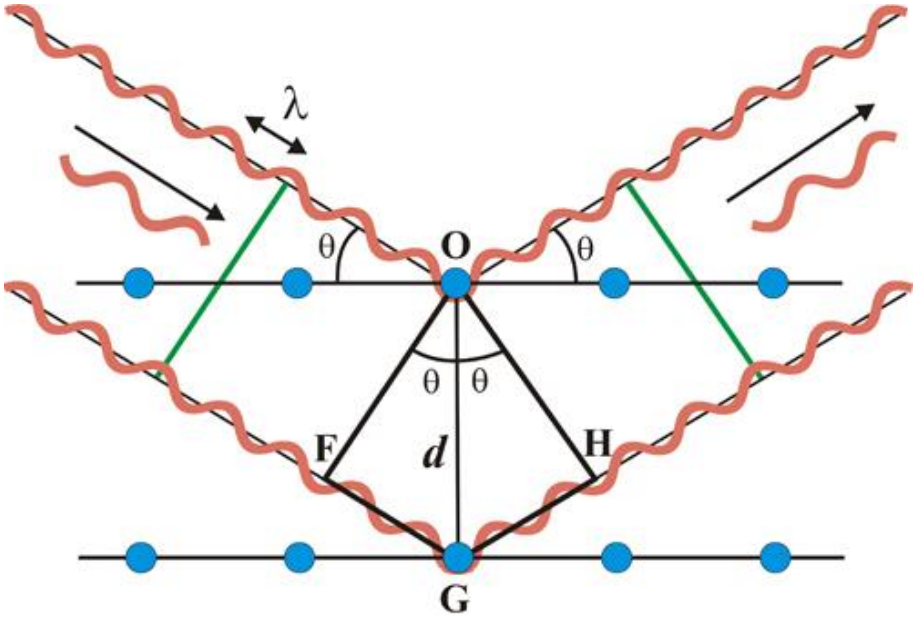

Fig. 2.2. Schematic outlining the Bragg's Law (adapted from Martínez-Ripoll, 1995[5])

Each peak at a specific angle θ corresponds to a set of parallel planes in the lattice structure. Using the Bragg's Law, the position of the peak in the diffraction pattern, and the beam energy of the X-ray, the distance between the corresponding planes can be determined. With the positions of various diffraction peaks, information about the present symmetry and lattice parameters of the unit cells can be determined. The intensity of diffraction peaks relies on the numbers and species of the present atoms. The ability of an atom to scatter the incident X-ray is described by the atom scattering factor f_j, which is proportional to the atomic number Z

(higher atomic number Z, stronger scattering). The intensity of a diffracted wave, I_{hkl} is proportional to the square of the structure fracture F_{hkl}, which is a sum of contributions from all the constituent atoms in the same (hkl) plane, as shown in the equation below:

$$I_{hkl} \propto |F_{hkl}|^2 \tag{2.2}$$

$$F_{hkl} = \sum_{j=1}^{j=n} f_j \cos 2\pi(hx_j + ky_j + lz_j) + i \sum_{j=1}^{j=n} f_j \sin 2\pi(hx_j + ky_j + lz_j) \tag{2.3}$$

where x_j, y_j, and z_j represents the coordinates of the atom j in the unit cell, and f_j is the atomic scattering factor of atom j.

In addition to the reflection diffraction geometry, which has been widely used for powder X-ray diffraction (PXRD), the transmission geometry of X-ray diffraction also plays an important role in characterising small samples or organic crystals. Instead of measuring the intensity of the outcoming X-ray at various angles for the reflection geometry, a 2D detector needs to be equipped to detect the Debye-Scherrer rings from X-ray diffraction in the transmission mode. The Debye-Scherrer rings, which result from the constructive interference, can then be recognised and analysed for the lattice information of the characterised materials, **Fig. 2.3**.

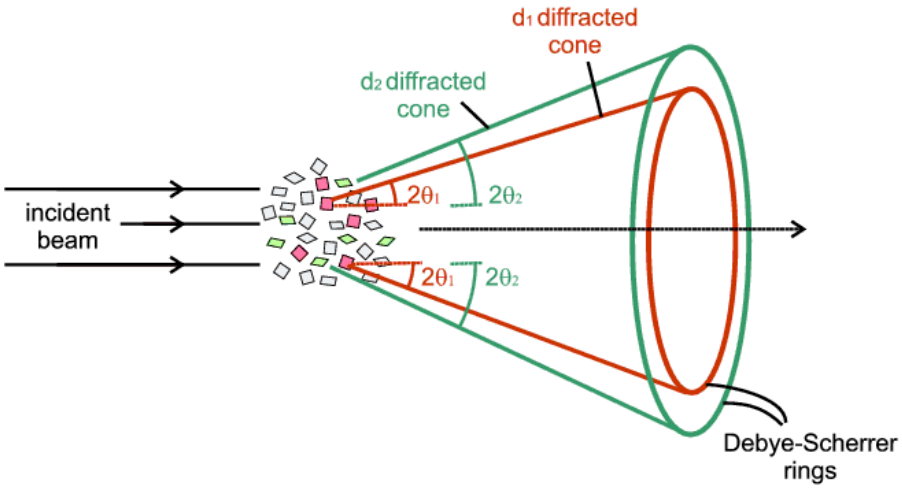

Fig. 2.3. Schematic showing the process of transmission-mode X-ray diffraction.

While transmission-mode X-ray diffraction are more sensitive in capturing low-angle peaks , the tested samples need to be sufficiently transparent to the incident X-ray[6]. With recent development of high-energy X-ray, the requirement of sample for transmission-mode X-ray diffraction is less pronounced. With a shorter wavelength of the high-energy X-ray, a better resolution can also be achieved for X-ray diffraction.

Apart from providing the chemical footprint of materials, X-ray diffraction is also a powerful tool in mechanical characterisation[7,8]. By detecting the shift in diffraction peaks, resulting from the slight change in lattice structure, the elastic strain in the crystals of the sample can be precisely determined. The elastic strain also leads to the broadening of diffraction peak, suggesting the stress state inside the sample. Therefore, the time-resolved X-ray diffraction is widely employed to investigate strain evolution in mechanical tests of materials

2.3.2 Scanning electron microscopy

Scanning electron microscopy (SEM) is an imaging technique which uses a focused electron beam that is rastered over the sample surface to obtain information about the surface topography and composition of the sample. Due to its capability to characterise the sample at very high magnification down to the nanometre scale, SEM has been widely used in battery research, investigating the morphological changes of battery components.

The outstanding resolution of electron microscopy comes from the short wavelength of electrons, as described by Abbe's equation[9]:

$$d = 0.612\,\lambda/n\sin\alpha \qquad 2.4$$

where d = resolution, λ = wavelength of imaging radiation, n = index of refraction of medium between point source and lens, relative to free space, α = half the angle of the cone of light from specimen plane accepted by the objective.

In SEM, electrons are generated from an electron gun on the top of the column structure. The diameter of the produced electron beam is generally too large for high-resolution imaging.

Therefore, the generated beam is later focused and defined to form a small electron spot on the specimen, using the electromagnetic lenses and apertures. A high-vacuum environment is typically maintained for the whole process, which allows electrons to travel without scattering by the air.

Upon interactions between the incident electron beam and the specimen, various signals are released from the specimen surface: backscattering electrons (BSE), secondary electrons (SE), Auger electrons (AE), and characteristic X-ray, **Fig. 2.4**. These signals are captured by respective detectors to provide morphological or composition information[10].

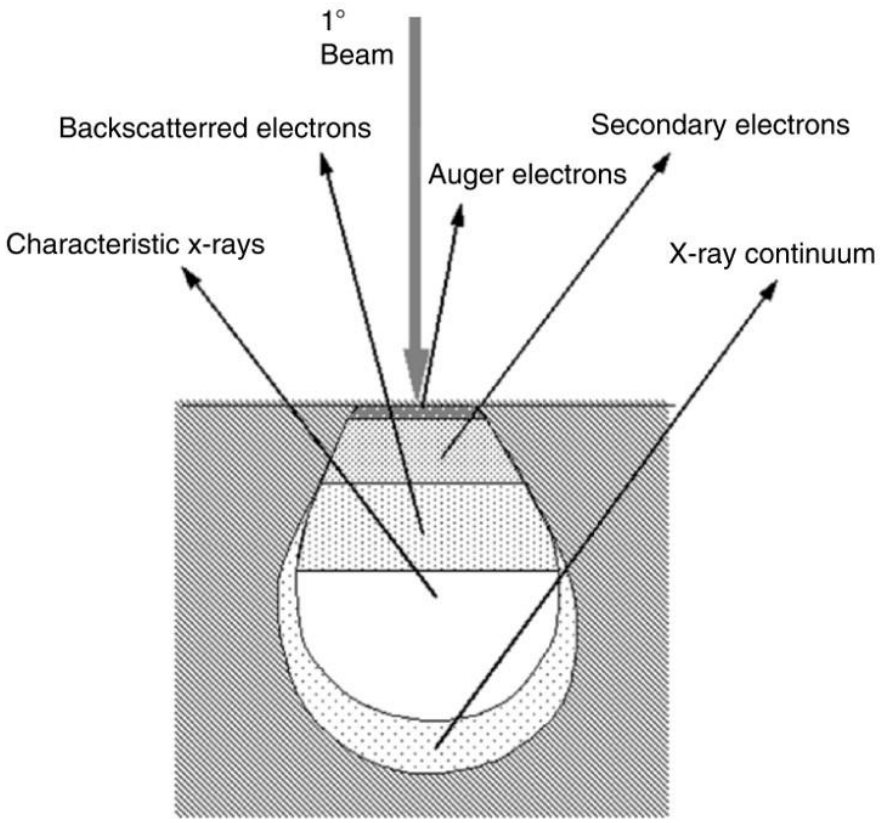

Fig. 2.4. Illustration of various signals generated by the interaction between the electron beam and specimen, and the regions where different signals can be detected (adapted from Joy et al., 2007[10]).

The most widely used signal among all is the secondary electron emission signal. When the incident electron beam strikes the surface of specimen, it causes the ionization of specimen

atoms. Due to the ionization, loosely bound electrons may be emitted, and they are referred to as the secondary ions. With a low energy, typically around 3 ~ 5 eV, secondary electrons can only escape from the specimen surface for a few nanometres, thus can accurately mark the position of the beam and provide high-resolution topographic information of the specimen. In the regions which are not in proximity to the detector, shadows will be generated in the ultimate image, as the secondary electrons cannot reach the detector.

Another powerful method of imaging in SEM is based on the detection of backscattering electrons, which could provide both compositional and topographic information of the specimen. A BSE is defined as an electron which underwent a single or multiple scattering, escaped from the surface, and so has an energy greater than 50 eV. The amount of reemitted BSE depends on the composition of the specimen, with atoms of higher atomic number contributing a larger count of BSEs. Hence, BSE provides an atomic number contrast image of the specimen's surface.

SEM, as a powerful imaging technique, plays an important role in battery study, providing the morphological information of specimens. It is important to make sure the specimen is conductive enough to avoid any build-up of charge on the surface. For solid electrolytes, which are not conductive enough, this issue can be avoided by coating the specimen with conductive metal (Au coating), or reducing the accelerating voltage of electrons to very low levels. Most comprehensive characterisation of batteries materials can be done by combining SEM with energy dispersive X-ray spectroscopy, for additional compositional formation.

2.3.3 Energy dispersive X-ray spectroscopy

Energy dispersive X-ray spectroscopy (EDX) is an analytical technique used for the elemental analysis of specimen, based on the detection of emitted characteristic X-rays from the specimen. EDX is normally performed in conjunction with SEM or TEM. When the incident electron strikes the surface of the specimen, energy exchange occurs between the incident electron and the electrons of the surface atoms. When the incident electron is inelastically scattered, the

electrons of the surface atoms gain some energy, and are ejected out of their orbital. The process of filling the vacant shell with an electron from an outer shell, to maintain charge neutrality, generates X-rays, as shown in **Fig. 2.5**. The energy difference between the two orbitals is unique and intrinsically determined by the elemental composition[11]. By mapping the detected characteristic X-ray signals onto the SEM, the compositional distribution on the surface of the specimen is provided. By quantifying the accumulative signals, quantitative analysis of elemental distribution on the surface is also possible.

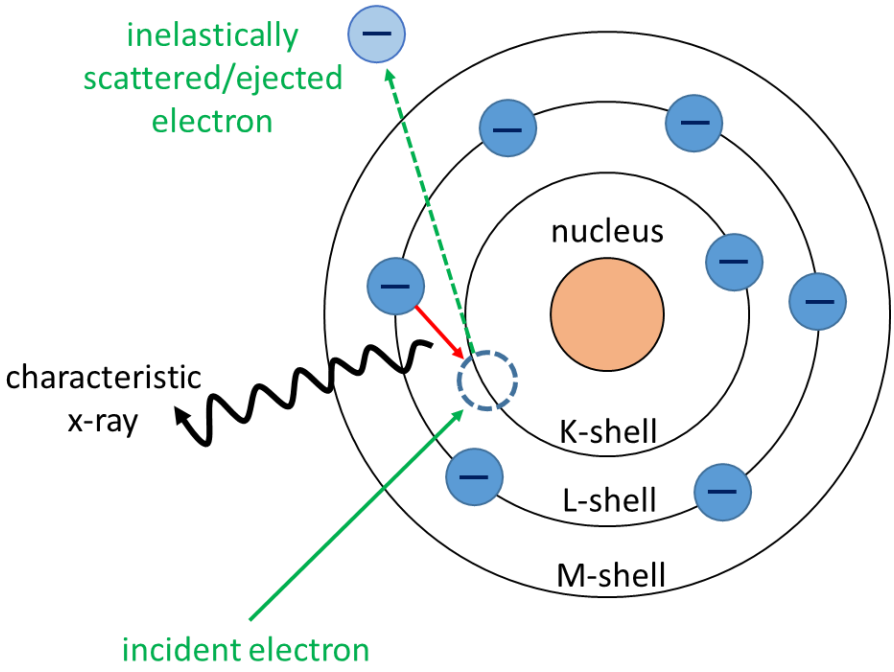

Fig. 2.5. Schematic of EDX mechanism (adapted from Hitachi High-Tech., 2008[12]).

2.3.4 Focused ion beam

While SEM can reveal the morphology of the sample surface, a way of sectioning is desired to uncover the structures buried inside the sample. Mechanical machining has proved valuable in efficiently sectioning the sample, but for fragile materials and sensitive structures, a finer way of exposing the inner structure of sample to SEM is needed. While the accelerated electrons interact with the specimen non-destructively, providing imaging signals, accelerated ions, with a massive mass compared with electrons can modify the morphology of the specimen, **Fig. 2.6**.

The focused ion beam (FIB) can mill the specimen surface, via the sputtering process, and this process can be controlled with nanometre precision by focusing the ion beam[13]. With the energy and intensity of the ion beam carefully controlled, it is also possible to remove unwanted material on the surface, and also to assist deposition of material, with a nanometre thickness on the surface of the specimen.

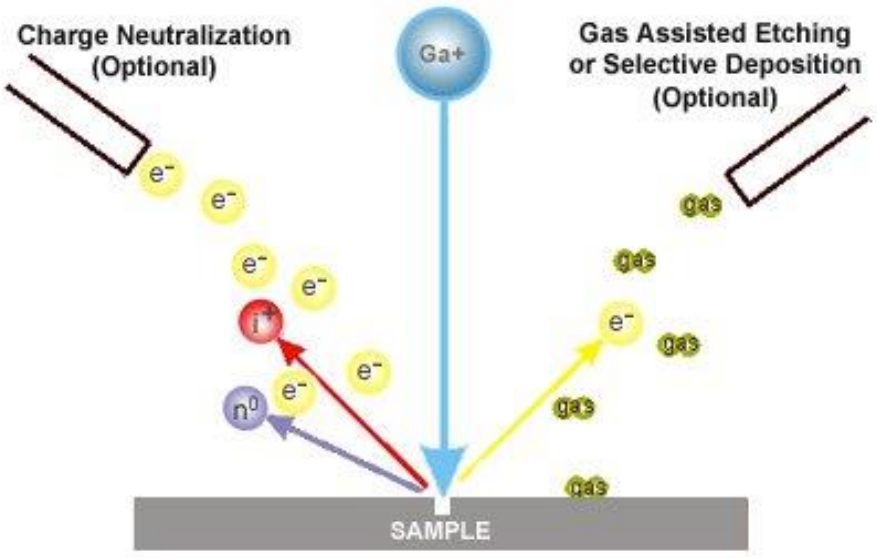

Fig. 2.6. Schematic outlining how FIB works.

FIB is even more powerful when combined with SEM, as the FIBed surface can be immediately characterised by SEM to monitor and control the process precisely. For light and fragile materials, such as lithium, which are sensitive to ion beam damage, pioneering work has been done to employ cryo-FIB to cross-section the sample, to keep the virgin morphology of the sample[14].

2.3.5 Differential electrochemical mass spectrometry

Differential electrochemical mass spectroscopy (DEMS) is a technique that combines electrochemical measurements with mass spectrometry, detecting the gas consumption and production during the chemical/electrochemical process. By quantifying the gas evolution, the corresponding components in the samples can be accordingly quantified[15].

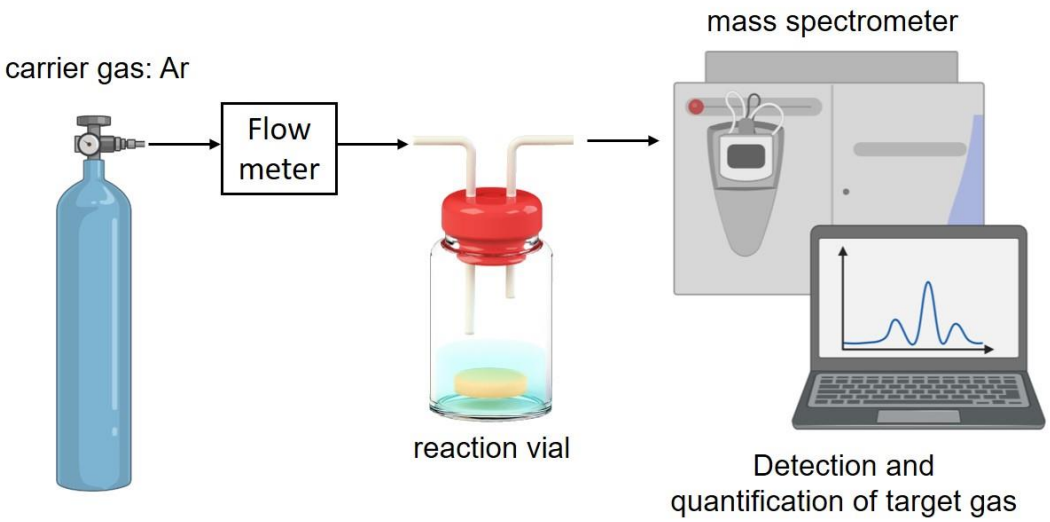

Fig. 2.7. Schematic outlining the set-up of DEMS test, which is used to quantify the deposited lithium inside the pores in this work.

During the experiments, a carrier gas flow (pure Ar) will pass a flowmeter, then the analysis vial, and eventually the mass spectrometer, **Fig. 2.7**. The set-up was first calibrated for common gases including Ar, O_2, CO_2, H_2 and N_2 by calibration gases. Calibration gases of different known amounts were applied considering the nonlinearity and cross-sensitivity of gas mixtures. With the carrier gas flowing, and reaction products generated *in-situ* in the analysis vial, the reaction products will be delivered to the mass spectrometer for quantitative analysis. Different gas molecules are first ionised by electrons in the ion source chamber, and then separated by the electric and magnetic fields based on different mass-to-charge ratio[16]. The gas molecules are then recognised and quantified by Faraday detectors, which records the number of molecules and their mass/charge. By calculating the integrated amount of gas detected, normalised to carrier gas flow, the amount of reaction products can be precisely determined. In this work, DEMS was employed to quantify the deposited lithium inside the solid electrolyte after lithium plating, providing elemental evidence of direct lithium deposition during cell cycling.

2.3.6 Secondary ion mass spectrometry

Also based on the mass spectrometer, secondary ion mass spectrometry (SIMS) is a powerful tool to characterise the elemental distribution on the surface of samples with sub-micron spatial resolution, and precise quantification. Inside SIMS, a primary beam of ions will be generated and emitted to interact with the surface of sample. With sufficient energy from the primary ion beam, a collision cascade is induced in the surface layer, and as a consequence of such energy dissipation, bonds are broken and secondary particles are emitted. While most of the emitted particles remain charge-neutral, a small percentage of particles will be positively or negatively charged. Those ions are then accelerated, focused, and quantitatively analysed by a mass spectrometer[17].

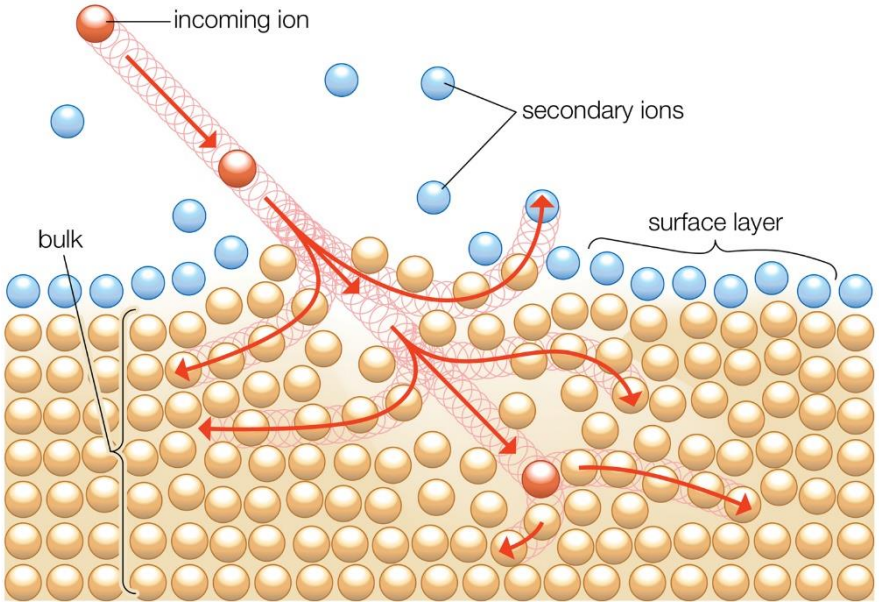

Fig. 2.8. Schematic illustrating the interaction between primary ion beam and sample surface to produce secondary ions (adapted from Hercules et al.[18]).

Imaging via ion intensity maps is achieved by scanning the primary ion beam over a region of interest of the sample. A 3D distribution of elements can be obtained by combining the surface elemental mapping with a depth profiling. With a sputter source, the surface layer of the sample

can be etched off, and the freshly exposed layer can be consecutively analysed with the primary ion beam.

Compared with other forms of elemental characterisation techniques, SIMS present outstanding sensitivity in detection. With the capability of conducting *in-situ* analysis with FIB, and a good sensitivity in detecting lithium, SIMS has proved valuable in providing composition information for battery materials. In this work, SIMS was employed to map the lithium distribution in the pores inside the solid electrolyte after lithium deposition.

2.3.7 X-ray computed tomography

X-ray computed tomography (XCT) is a non-destructive 3D imaging technique widely employed to visualise the interior features of samples. For different types of XCT, and with different optics applied, an imaging resolution of sub-micron, or even down to tens of nanometres can be achieved. Most tomography methods provide a 3D map of the X-ray attenuation Typically, the sample is located in the X-ray beam on a sample stage which can rotate through 180º or 360º. Then a projection image, which is a radiograph taken at one fixed angle of the rotation stage, is obtained to provide information about the total absorption of the sample in a specific orientation. Projections are later equiangularly taken in the whole range of rotation (0º ~ 180º or 0º ~ 360º). The whole set of projections are processed via a tomographic reconstruction algorithm (usually back-projection) into a tomogram, which represents a 3D matrix of attenuation data for each point in the imaged 3D volume. The 3D data can be presented as virtual slices, or using 3D visualisation tools. Based on the different X-ray attenuation from each phase, the boundaries between different phases are distinguished, and therefore the internal structure of the sample is visible.

In attenuation contrast imaging, with the collection of a projection image (radiograph), a parallel beam X-ray transmits through the sample at each rotation angle. The transmitted X-ray is transformed into visible light linearly via a scintillator, and then recorded as an image by a detector. By collecting the dark and flat references (projections taken when there is 0% and

100% X-ray transmission, respectively), the X-ray transmission through the sample is determined using **Eq. 2.5**:

$$\frac{I_\theta}{I_0} = \frac{I - I_D}{I_F - I_D} \tag{2.5}$$

Where $\frac{I_\theta}{I_0}$ = the transmission of X-ray at a specific orientation, I, I_D, I_F are intensities measured by the detector for X-ray across the sample, dark reference, and flat reference, respectively. The X-ray intensity along the propagation direction of the X-ray can be best described using the Beer-Lambert Law[19]:

$$I_\theta = I_0 e^{-\int_{-\infty}^{+\infty} \mu(x,y)ds} \tag{2.6}$$

Where μ(x,y) gives the attenuation coefficient distribution at a specific incident angle of θ. The total attenuation P at a specific angle is given by:

$$P_\theta(r) = \int_{-\infty}^{\infty}\int_{-\infty}^{\infty} f(x,y)\delta(xcos\theta + ysin\theta - r)dxdy \tag{2.7}$$

where $xcos\theta + ysin\theta = r$, and $\delta(\,)$ is the Dirac delta function. With a complete set of projections, the function $P_\theta(r)$ contains the attenuation information of all projections, and is known as the sinogram of the XCT scan. According to the Fourier slice theorem, the 1D Fourier transform of a projection $P_\theta(r)$ is equal to the 2D Fourier transform of the attenuation coefficient distribution $\mu(x,y)$ evaluated along the slice through the origin that is orthogonal to the beam direction. So, the attenuation coefficient distribution inside the sample can be obtained via the 1D Fourier transform followed by the 2D inverse Fourier transform of the set $P_\theta(r)$. The X-ray attenuation coefficient distribution is then represented in normalised grayscale in the generated tomograms, which depends on the electron density of the constituent atoms in the corresponding voxel. By assembling all the XCT slices and their grayscale together, a virtual 3D model of the sample is generated, which enables the visualisation of features with different compositions and densities hidden inside the sample. As the visualisation of the

structure describes the transmission of X-ray through the sample with negligible beam damage to all-solid-state batteries, *in-situ* characterisations can therefore be achieved.

2.3.8 Phase-contrast imaging

Phase-contrast can assist the differentiation between phases with similar attenuation coefficients. The propagation-based phase-contrast is achieved with highly coherent X-ray and by placing the detector in some distance to the sample, so the radiation refracted by the sample can interfere with the unchanged be am. The process of an X-ray wave passing through a sample is outlined in **Fig. 2.9** below[20].

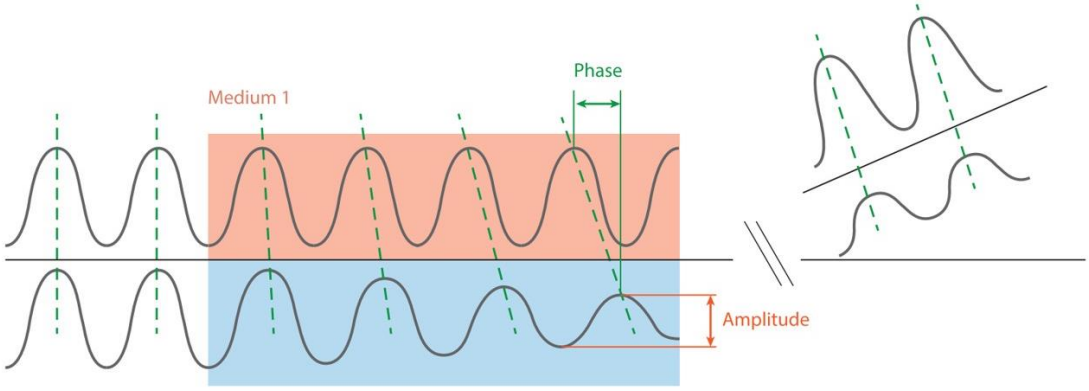

Fig. 2.9. Schematic outlining the change of X-ray wave when passing through a sample (adapted from Wood et al.[20]).

Every material has its intrinsic X-ray complex refractive index n = 1 – δ + iβ. The imaginary part, β, describes the change in amplitude of X-ray when passing through a sample, which is related to the X-ray attenuation coefficient μ through $\mu = \frac{4\pi\beta}{\lambda}$, where λ is the wavelength of X-ray. The real part (1 – δ) describes the change in X-ray wavelength as it propagates through a material. The differences in δ between different materials lead to phase shifts, as shown in **Fig. 2.9**. Any X-ray imaging would simultaneously probe both the real and imaginary parts of the complex refractive index, especially for a coherent beam. So, whether an X-ray computed tomography is attenuation-contrast or phase-contrast depends on to what extent the contrast is dominated by the attenuation effect from the imaginary part or the interference effects

stemming from the real part in reconstruction. In newly developed reconstruction algorithms, it is possible to combine the information from attenuation contrast and phase contrast. Without use of these special algorithms, the interference pattern is observed as bright and dark fringes at the interfaces between different materials, superimposed onto the attenuation-based image. While it remains technically complex to retrieve the phase shifts for quantitative analysis, the phase contrast reconstruction can be employed to qualitatively enhance the contrast among different weakly attenuating materials[21]. Such combination of phase information and attenuation information has proved valuable in battery, especially dendrite-related study, allowing reliable segmentation of lithium domain from other weakly attenuating phases[22].

2.4 Electrochemical techniques

2.4.1 Electrochemical impedance spectroscopy

Electrochemical impedance spectroscopy (EIS) is a technique which enables the measurement of resistance, capacitance, and ultimately ionic conductivity of ionic conductive systems, such as a solid electrolyte. In EIS measurements, an AC voltage perturbation is applied to the electrochemical cell, which generates an AC current signal response with the same frequency and a phase shift as a response. Both the applied voltage and the generated current are sinusoidal, which ensures no directional charge transfer during the EIS measurement. The voltage and the current response can be described by the following equations[23]:

$$V_t = V_0 \, sin(\omega t) \tag{2.8}$$

$$I_t = I_0 \, sin(\omega t + \varphi) \tag{2.9}$$

where V_t = voltage at time t, V_0 = voltage at time zero, I_t = current response at time t, I_0 = current response at time zero, t = the time, ω = the angular frequency of voltage and current, which can also be expressed by the frequency in Hertz, f, through $\omega = 2\pi f$.

Using the Ohm's law, the impedance Z of the electrochemical cell can be derived as:

$$R = \frac{v}{I} \tag{2.10}$$

$$z = \frac{V_t}{I_t} = \frac{V_0\, sin(\omega t)}{I_0\, sin(\omega t + \varphi)} = \frac{Z_0\, sin(\omega t)}{sin(\omega t + \varphi)} \tag{2.11}$$

Using the Euler relationship:

$$e^{i\varphi} = cos\,\varphi + i\, sin\,\varphi \tag{2.12}$$

The impedance of the cell can be represented in a complex form:

$$Z(\omega) = \frac{V}{I} = Z_0 e^{i\varphi} = Z_0(cos\,\varphi + i\, sin\,\varphi) \tag{2.13}$$

With $cos\,\varphi$ as the real part and $i\, sin\,\varphi$ as the imaginary part, the impedance Z of the electrochemical cell can be represented as a function of frequency using a Nyquist plot, as shown in **Eq. 2.13**, **Fig. 2.10**.

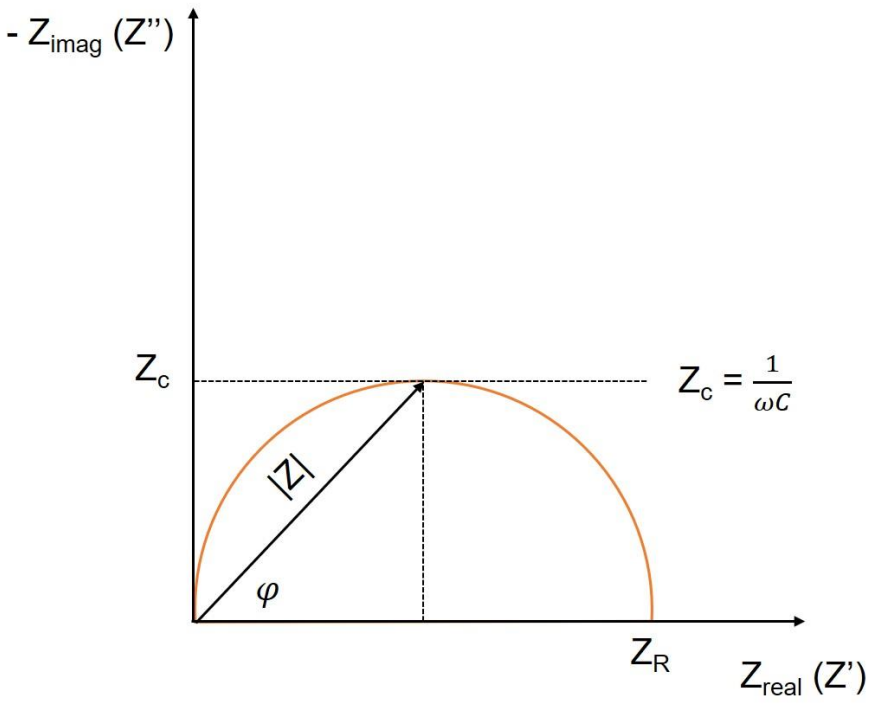

Fig. 2.10. Nyquist plot showing a representation of the Z in complex form.

Each point of the characteristic semicircle of a Nyquist plot corresponds to an impedance value at a specific frequency. The impedance is either represented as a vector |Z| with a magnitude and a phase angle (arg Z) or as a complex quantity:

$$Z_{total} = Z_{real} + Z_{imag} \qquad 2.14$$

In a practical electrochemical system, there are commonly multiple resistance and capacitance contributions from different stages of ion migration. The individual impedance contributions of the cell can be better understood by fitting with combinations of several equivalent circuits. The equivalent circuits normally consist of resistors and capacitors in series or in parallel[24]. The EIS can be measured with non-blocking electrodes, where the charge can pass the electrode/SE interfaces, therefore the resistance from the interfaces can be quantified, **Fig. 2.11a**. The EIS can also be measured with blocking-electrodes, which cannot host ions from the solid electrolyte, and serve as perfect capacitors, **Fig. 2.11b**.

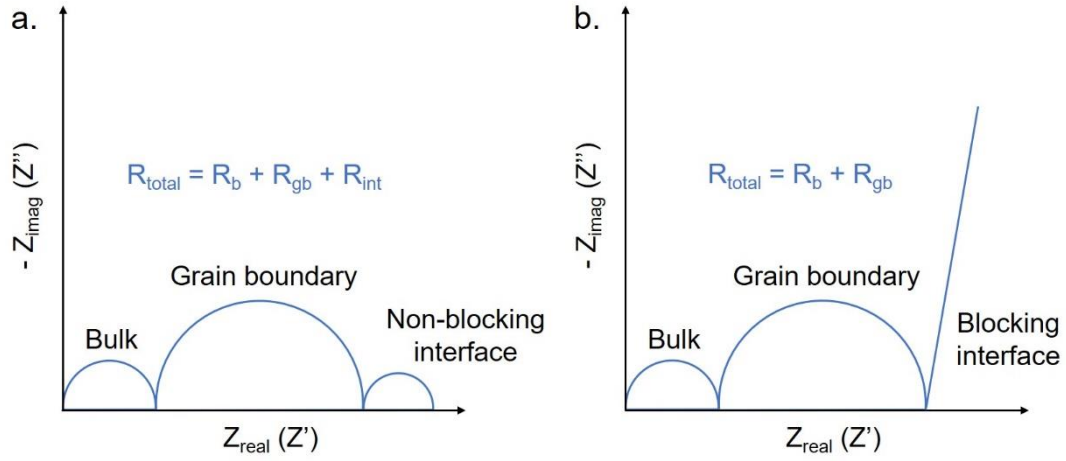

Fig. 2.11. Expected Nyquist plot of a solid electrolyte, **a.** measured with non-blocking electrodes, and **b.** measured with blocking electrodes.

2.4.2 Galvanostatic cycling

Galvanostatic cycling is a technique widely used in battery research to test the performance and lifetime of cells. During the test, cells are subjected to a series of cycles of electrochemical charge and discharge, with a constant current applied to the cell, and the cell voltage or potential

simultaneously measured. In this work, galvanostatic cycling was performed on symmetric Li/SE/Li cells. As the degradation of the cell is normally rate-dependent, by monitoring voltage response in galvanostatic cycling at various current densities, the current density above which the degradation occurs can be drawn. The data is usually plotted with the cell voltage as a function of the charge passed or time. The stability of cycling is represented by the stability of cell voltage. According to the Ohm's law, **Eq. 2.15**, when the electrochemical process of the cell is stable, a constant voltage would be expected with a constant current applied. Therefore, the fluctuation of cell voltage during cycling suggests changes taking place during the electrochemical operation.

$$V = IR \tag{2.15}$$

EIS measurements are commonly incorporated into the galvanostatic cycling, after each step of charge or discharge, suggesting the effect of charge or discharge on the impedance of the cell. To ensure the accuracy of EIS measurement, a cell relaxation of a few minutes with the open circuit voltage (OCV) measured is employed before each EIS measurement. By comparing the EIS measured at the intervals of charge or discharge with the EIS measured before galvanostatic cycling, the degradation of cell can be quantified.

2.4.3 Rate test

The rate test is an electrochemical test widely employed to determine the critical current density (CCD) of all-solid-state batteries, above which dendrite formation and cell failure occurs. The rate test is in essence a series of galvanostatic cycles, with the current density increased by a certain amount after every specific number of cycles passed. The capacity of every charge or discharge normally remains the same through the rate test, in spite of the varying current density. When the current density of the cell is increased, according to the Ohm's law, the voltage of the cell should increase proportionally, as the resistance of the cell remains the same. Therefore, a sudden drop in voltage suggests the drop in cell impedance, originating from the dendrite

penetration inside the cell. The current density, above which such a drop in voltage occurs, is determined as the CCD, **Fig. 2.12**.

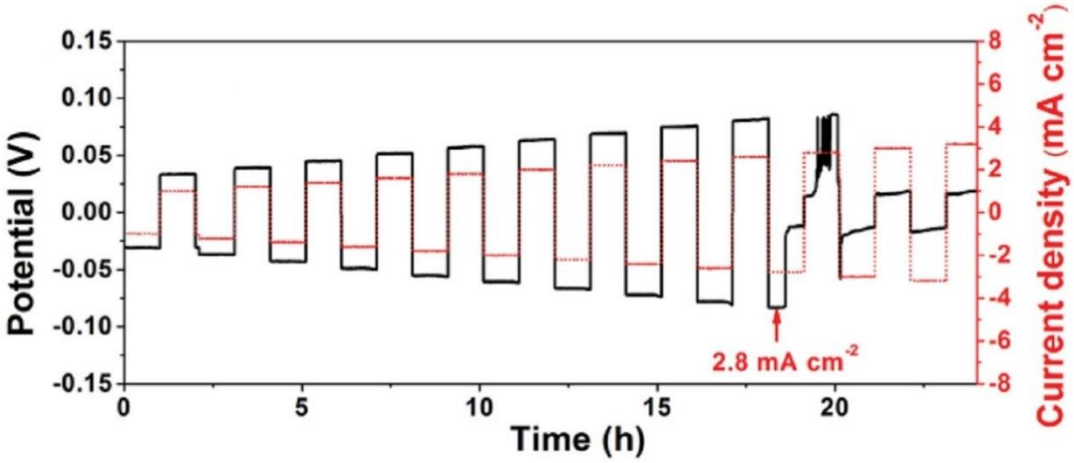

Fig. 2.12. An example of rate test widely used to determine the CCD of all-solid-state batteries. (adapted from Sun et al.[25])

While the rate test is a traditional way of determining the CCD for all-solid-state batteries, there is no established benchmark of its method in research. Due to various factors that could affect the cell failure, the accuracy of a rate test largely depends on its electrochemical settings. For example, a rate test with too low a capacity for each charge/discharge might lead to a huge delayed detection of dendrite formation, as the amount of charge passed is insufficient to form a long enough dendrite that propagates through the whole thickness of the sample. Other drawbacks of the traditional rate test include: the interfacial degradation on stripping will lead to the increase in cell voltage, and delay the detection of cell failure; the voiding on stripping will enhance local current density to a varying extent, which adds to randomness of the rate test result; due to Joule effect of current passing along the dendrite, the dendrite could melt before reaching the other electrode, a subtle voltage drop followed by a bounce back to its original voltage level will be detected under such a circumstance, which could be attributed to a disturbance to the cell during the test, thus covering up the detection of dendrites. For an accurate and reproducible determination of CCD, the methodology of rate test needs to be optimised.

2.5 Mechanical test techniques

2.5.1 Nano-indentation

Nanoindentation is a mechanical testing technique widely used to measure the elastic modulus and hardness of materials. During the nanoindentation test, a hard tip with known geometry and mechanical properties is pressed into the surface of a specimen up to a certain depth into the surface. Typically, the load placed on the indenter tip is increased as the tip further penetrates into the specimen until a user-defined load is reached. Here, the load on the indenter can be either kept constant for a period or immediately released. A load-displacement curve can be obtained during the measurement, and together with post-test observation to obtain the dimension of indent left on the specimen, multiple mechanical properties of the specimen can be extracted. A typical load-displacement curve obtained from nanoindentation is shown in **Fig. 2.13a** below, with a schematic outlining the concepts of different depths of indentation in **Fig. 2.13b**.

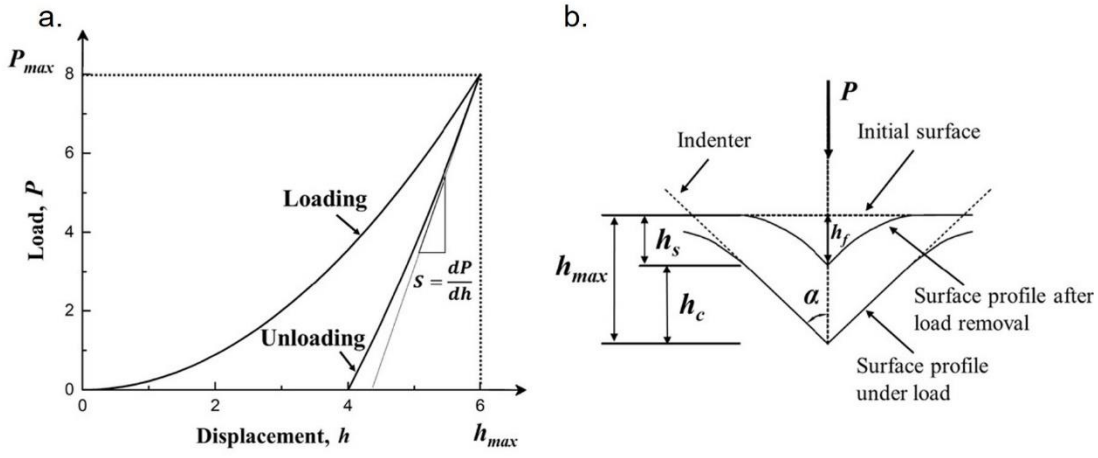

Fig. 2.13. a. A load-displacement curve of a typical nanoindentation measurement. **b.** Schematic diagram outlining different depths after unloading. (adapted from Xia et al.[26])

With the impression area of the indenter tip precisely measured (or inferred from the indentation depth and indented geometry), along with the maximum load (P_{max}) applied during indentation, the indentation hardness (H) of the specimen can be calculated using:

$$H = \frac{P_{max}}{A} \tag{2.16}$$

For a Berkovich indenter, the impression area can be calculated using:

$$A = 3\sqrt{3}h_c^2 \, tan^2 \, \theta = 24.494h_c^2 \tag{2.17}$$

With the indenter face angle θ known to be 65.27°, the hardness of the specimen can be directly calculated based on the depth of indent[27].

One major advantage of nanoindentation over conventional micro-indentation is the ability to measure the elastic modulus (E) from the contact stiffness (S) during unloading. The elastic modulus is related to the stiffness during unloading via the following equation:

$$S = \frac{2}{\sqrt{\pi}} E_r \sqrt{A} \tag{2.18}$$

where A is the contact area and E_r is the reduced modulus of the tip and sample as given by:

$$\frac{1}{E_r} = \frac{(1 - \nu_t^2)}{E_t} + \frac{(1 - \nu_s^2)}{E_s} \tag{2.19}$$

where E_t, ν_t, and E_s, ν_s are the elastic modulus and Poisson's ratio of the tip and sample respectively. So, with the load-displacement curve, the measured impression area, and the known mechanical properties of the indentation tip, the Young's modulus of the sample can be extracted. It is noteworthy that as most solid electrolyte materials are air-sensitive, battery samples are typically immersed in a solution to prevent their direction exposure to air and moisture. However, the solution around the sample could significantly impact the accuracy of nanoindentation measurement[26]. To better determine the mechanical properties of battery materials, indentation conducted in an inert atmosphere is desired.

2.5.2 Four-point bending test

Four-point bending test, also called four-point flexural test, is a mechanical test used to measure the flexural properties of a material (e.g. strength). With the addition of a fourth contact point , a central portion of the sample surface is under a uniform and maximum tensile stress, different from the three-point bending, where only the small region at the central contact is under maximum stress. Such a difference is important in studying brittle inorganic solid electrolytes, whose flexural strength and fracture toughness is directly related to the number and severity of flaws exposed to the maximum stress by Weibull statistics, for instance **Fig. 2.14**.

During the four-point bending, a beam-shaped sample with the suitable length, width, and thickness is inserted into the four-point bending jig, between the loading span and the support span with four loading pins. A load (P) is applied to the loading pins at a constant loading rate, while the displacement (D) is recorded until sample fracture.

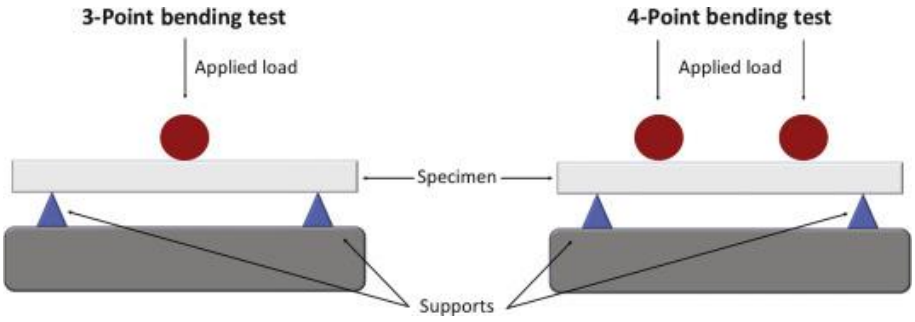

Fig. 2.14. Schematic showing the set-up comparison between three-point bending and four-point bending. (adapted from Kfan et al.[28])

With the known geometry of the four-point bending set-up, the known geometry of the sample, and the recorded load-displacement curve, flexural properties such as flexural strength can be calculated using the following equation[29,30]:

$$\sigma_{f,max} = \frac{3PL}{4bd^2} \qquad 2.20$$

where $\sigma_{f,max}$ is the flexural strength (in MPa), P is the maximum load before the fracture of specimen (in N), L is the length of the support span (in mm), and b and d are the width of thickness of the sample (in mm).

With a sharp crack with known geometry (notch) introduced to the centre of the beam, the fracture toughness of the material can also be measured using four-point bending. Given a straight-through crack with a length of a as the notch, the fracture toughness can be determined using[31]:

$$K_{Ic} = \frac{P}{b\sqrt{d}}Y = \frac{P}{b\sqrt{d}}\frac{L_s - L_l}{d}\frac{3\,\Gamma_M\sqrt{\alpha}}{2(1-\alpha)^{\frac{3}{2}}} \tag{2.21}$$

$$\Gamma_M = 1.9887 - 1.326\alpha - \frac{(3.49 - 0.68\alpha + 1.35\alpha^2)\alpha(1-\alpha)}{(1+\alpha)^2} \tag{2.22}$$

$$\alpha = \frac{a}{d} \tag{2.23}$$

where P is the maximum load before fracture, L_s and L_l are the lengths of support and loading spans, b and d are the width and thickness of the specimen.

The precise measurement of the flexural properties of solid electrolyte is critical to a fundamental understanding of cell failure, as the dendrite initiation and propagation are in essence fracture and crack propagation driven by the electrochemical process. Methodology development is required to accurately measure the flexural properties of highly sensitive solid electrolyte materials.

References

1. Chen, Y. Solid-state formation of carbon nanotubes. in *Carbon Nanotechnology* 53–80 (Elsevier, 2006). doi:10.1016/B978-044451855-2/50006-1

2. Boulineau, S., Courty, M., Tarascon, J. M. & Viallet, V. Mechanochemical synthesis of Li-argyrodite Li_6PS_5X (X = Cl, Br, I) as sulfur-based solid electrolytes for all solid state batteries application. *Solid State Ionics* **221**, 1–5 (2012).

3. Nisar, A., Zhang, C., Boesl, B. & Agarwal, A. Unconventional Materials Processing Using Spark Plasma Sintering. *Ceramics* **4**, 20–39 (2021).

4. Suarez, M. *et al.* Challenges and Opportunities for Spark Plasma Sintering: A Key Technology for a New Generation of Materials. in *Sintering Applications* (InTech, 2013). doi:10.5772/53706

5. Cano, Félix Hernández, Concepción Foces-Foces, and M. M.-R. *Cristalografía*. (Editorial CSIC-CSIC Press, 1995).

6. He, B. B. Introduction to two-dimensional X-ray diffraction. *Powder Diffr.* **18**, 71–85 (2003).

7. Korsunsky, A. M. *et al.* Measurement of Residual Elastic Strains in a Titanium Alloy Using High Energy Synchrotron X-Ray Diffraction. *Exp. Mech.* **46**, 519–529 (2006).

8. Wanner, A. & Dunand, D. C. Synchrotron X-ray study of bulk lattice strains in externally loaded Cu-Mo composites. *Metall. Mater. Trans. A Phys. Metall. Mater. Sci.* **31**, 2949–2962 (2000).

9. Köhler, H. On Abbe's theory of image formation in the microscope. *Opt. Acta (Lond).* **28**, 1691–1701 (1981).

10. Zhou, W., Apkarian, R., Wang, Z. L. & Joy, D. Fundamentals of scanning electron microscopy (SEM). in *Scanning Microscopy for Nanotechnology: Techniques and*

Applications 1–40 (2007). doi:10.1007/978-0-387-39620-0_1

11. *Energy Dispersive X-ray Spectroscopy*. (2002).

12. Hitachi High-Tech. Introduction to SEM (Application Note). (2008).

13. Melngailis, J. Focused ion beam technology and applications. *J. Vac. Sci. Technol. B Microelectron. Nanom. Struct.* **5**, 469 (1987).

14. Lee, J. Z. *et al.* Cryogenic Focused Ion Beam Characterization of Lithium Metal Anodes. *ACS Energy Lett.* **4**, 489–493 (2019).

15. Abd-El-Latif, A. A. *et al.* Insights into electrochemical reactions by differential electrochemical mass spectrometry. *TrAC - Trends in Analytical Chemistry* **70**, 4–13 (2015).

16. Baltruschat, H. Differential electrochemical mass spectrometry. *J. Am. Soc. Mass Spectrom.* **15**, 1693–1706 (2004).

17. Schaepe, K. *et al.* Secondary ion mass spectrometry. in *Characterization of Nanoparticles: Measurement Processes for Nanoparticles* 481–509 (Elsevier, 2019). doi:10.1016/B978-0-12-814182-3.00025-0

18. Encyclopædia Britannica. Surface Analysis: Secondary ion mass spectroscopy and ion scattering spectroscopy.

19. Als-Nielsen, J. & McMorrow, D. *Elements of Modern X-ray Physics*. *Elements of Modern X-ray Physics: Second Edition* (Wiley, 2011). doi:10.1002/9781119998365

20. Pietsch, P. & Wood, V. X-Ray Tomography for Lithium Ion Battery Research: A Practical Guide. *Annu. Rev. Mater. Res* **471229**, 1–12 (2017).

21. Paganin, D., Mayo, S. C., Gureyev, T. E., Miller, P. R. & Wilkins, S. W. Simultaneous phase and amplitude extraction from a single defocused image of a homogeneous object. *J. Microsc.* **206**, 33–40 (2002).

22. Eastwood, D. S. *et al.* The application of phase contrast X-ray techniques for imaging Li-ion battery electrodes. *Nucl. Instruments Methods Phys. Res. Sect. B Beam Interact. with Mater. Atoms* **324**, 118–123 (2014).

23. Barsoukov, E. & Macdonald, J. R. *Impedance Spectroscopy: Theory, Experiment, and Applications*. *Impedance Spectroscopy: Theory, Experiment, and Applications* (Wiley-Interscience, 2005). doi:10.1002/0471716243

24. Larfaillou, S., Guy-Bouyssou, D., Le Cras, F. & Franger, S. Comprehensive characterization of all-solid-state thin films commercial microbatteries by Electrochemical Impedance Spectroscopy. *J. Power Sources* **319**, 139–146 (2016).

25. Mo, F. *et al.* Inside or Outside: Origin of Lithium Dendrite Formation of All Solid-State Electrolytes. *Adv. Energy Mater.* **9**, 1902123 (2019).

26. Seo, M., Kawamata, D. & Chiba, M. Differences in Mechanical Properties of the Passive Metal Surfaces Obtained in Solution and Air. in *Passivation of Metals and Semiconductors, and Properties of Thin Oxide Layers* 439–449 (Elsevier, 2006). doi:10.1016/B978-044452224-5/50069-X

27. Mann, A. Nanoindentation. in *Surfaces and Interfaces for Biomaterials* 225–247 (Elsevier Ltd., 2005). doi:10.1533/9781845690809.2.225

28. Khan, Y. Characterizing the properties of tissue constructs for regenerative engineering. in *Encyclopedia of Biomedical Engineering* **1**–**3**, 537–545 (Elsevier, 2019).

29. Yin, Y., Qiao, Y. & Hu, S. Four-point bending tests for the fracture properties of concrete. *Eng. Fract. Mech.* **211**, 371–381 (2019).

30. Gogotsi, G. A. Fracture toughness of ceramics and ceramic composites. *Ceram. Int.* **29**, 777–784 (2003).

31. MUNZ, D., BUBSEY, R. T. & SHANNON, J. L. Fracture Toughness Determination

of $A1_2O_3$ Using Four-Point-Bend Specimens with Straight-Through and Chevron Notches. *J. Am. Ceram. Soc.* **63**, 300–305 (1980).

Chapter 3. *In-Situ* Characterisations of Interfacial Degradation in All-Solid-State Batteries

Abstract

While dendrite formation on plating has been long taken as the only cause of cell failure in all-solid-state batteries, the effect of interfacial degradation from stripping has been widely ignored. The degradation on stripping can lead to voltage polarisation and trigger dendrite initiation at a current density considerably below the critical current density for plating. However, little is known about the origin of such failure. In this chapter, a critical stripping current density (CCS) is identified that results in dendrite formation on plating and cell failure. By using scanning electron microscopy and X-ray computed tomography, void formation and accumulation, when stripped above the critical stripping current density, has been revealed as the form of interfacial degradation. The CCS has been investigated in various cell systems, as a function of stack pressure and current density, revealing the dominant role of metal creep in preventing contact loss and cell failure. The combined effects of stack pressure and temperature have been studied to better eliminate void formation on stripping. By developing *in-situ* X-ray computed tomography, void formation and accumulation have been tracked and quantitatively analysed along with cycling for the first time. The dynamics of void formation and interfacial degradation have been observed with synchrotron X-ray computed tomography, unveiling the origin of void formation and voltage polarisation.

3.1 Introduction

All-solid-state batteries could deliver a step change in energy density and improved safety via the use of an alkali metal anode and a ceramic electrolyte. However, dendrite formation at the anode that penetrate the ceramic electrolyte is one of the greatest challenges facing all-solid-

state batteries. While dendrite formation on charging directly leads to short-circuit and cell failure[1–4], the interfacial contact between alkali metal anode and solid electrolyte can be lost on discharging, leading to enhanced local current density, and triggering dendrite initiation on subsequent charging[5–9].

In general, interfacial contact loss is reflected by cell polarisation during cycling[10]. AC impedance spectroscopy is also widely employed before and after charge/discharge on all-solid-state batteries to investigate dynamic changes of interfacial impedance[11,12]. The increasing interfacial impedance during cycling is attributed to the deterioration of interfacial contact. However, for Li/SE/Li symmetric cells, which are predominantly used to investigate the behaviour of Li plating/stripping, Li plating on one electrode is coupled with simultaneous Li stripping on the other electrode. Therefore, it is difficult to separate the effect of Li stripping from Li plating in Li/SE/Li cells. Contrary to two-electrode cells, by introducing a reference electrode (RE), the three-electrode cells allow separate investigation of Li plating/stripping, as the voltage is now measured between the working electrode (WE) and reference electrode (RE), and is only dependent on the changes of WE/SE interface[13,14].

By using a three-electrode set-up, it is demonstrated that there is a critical current density on stripping (which we denote as CCS), above which voids will form at the interface, voltage polarisation will increase, leading eventually to dendrite formation[15,16]. Unlike the critical current density for plating (CCD or CCP), above which the dendrite forms and short-circuit occurs, Li stripping above the CCS deteriorates the interfacial contact and creates current density hot spots, but not necessarily to such a level in a single stripping that dendrites must form in the subsequent plating. Instead, stripping above CCS induces contact loss and void formation. Those voids are partially eliminated on subsequent plating, but grow in the following stripping, and hence the voids accumulate on cycling, reducing the contact and gradually increasing the local current density until a dendrite is triggered.

In this study, a Li/Li_6PS_5Cl/Li cell, which forms a kinetically stable interphase between Li and

SE[17,18], has been investigated with a three-electrode cell to determine its CCS with different stack pressures to force the Li metal anode to creep and occlude the voids. The dependence of the CCS on cycling temperature has then been studied with Li/Li_6PS_5Cl/Li cell, as higher temperature enhances the rate of creep and Li diffusivity, resulting in increased CCS. Na/Na-beta''-Alumina/Na cell, which forms no interphase between Na and SE[19], has also be investigated due to the inherent similarity between Li and Na, whilst their melting point and mechanical properties remain different. Li/Li_3N/Li cell has also been studied with the same methodology as an interphase-free system for Li metal anode, as Li and Li_3N are believed to be thermodynamically stable[20].

Though the voltage behaviour of cells has been observed during cell cycling, it remains a great challenge to confirm the formation of voids on stripping, and the occlusion of voids on plating. Scanning electron microscopy (SEM) has been utilised to characterise the voids and interface by cross-sectioning the cell. However, the destructive nature of cross-sectioning and the compliant nature of Li makes it impossible to maintain the original morphology of voids in Li metal, and importantly, the evolution of voids during cycling can never be tracked. Therefore, *in-situ* X-ray computed tomography has been applied to reveal the evolution of voids during cycling in practical conditions and in various cell systems. The *in-situ* X-ray computed tomography has been optimised for lab-based XCT and then synchrotron XCT for better image quality, capability of quantitative analysis, and better temporal resolution.

3.2 Protocol

3.2.1 Electrolyte preparation

Li_6PS_5Cl: Li_2S, P_2S_5, and LiCl (Sigma-Aldrich) were ground together in the ratio corresponding to the stoichiometry of Li_6PS_5Cl. 1g of ground power was then loaded into a ZrO_2 ball-mill jar with 50g of 10-mm-diameter ZrO_2 balls. Two such sealed jars were then placed into a Fritsch PULVERISETTE 7 premium line Planetary Micro Mill, and ball-milled at 600 r.p.m. for 14 h. The ball-milled powder was loaded into a 5-mm-diameter stainless steel

die set (Specac) under a uniaxial pressure of 500 MPa. The disc was then surrounded by graphite foil, sealed in an evacuated quartz tube, and placed inside a preheated muffle furnace at 600 ℃ for 15 min, and left to cool to room temperature inside the furnace. The surface of the disc was polished to remove any residual graphite, and ground into powder with a mortar and pestle. The powder was again pressed into a 5-mm-diameter disc at the pressure of 500 MPa, sealed in a quartz tube, heated to 300 ℃ at 10 ℃/min inside a furnace, and then at 300 ℃ for 15 min. The phase purity of powder from the sintered pellet was then examined with powder XRD, **Fig. 3.1**. The sintered disc was cooled to room temperature and used as solid electrolyte pellet.

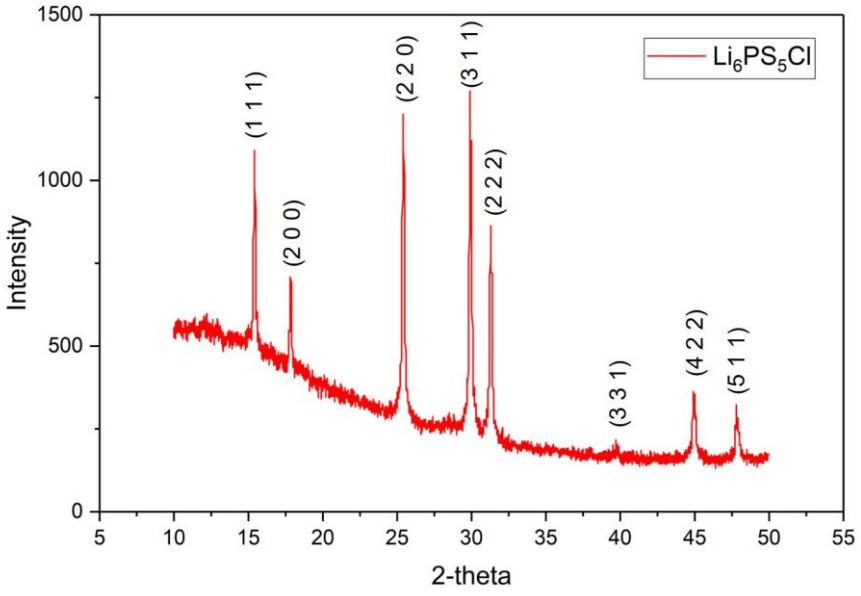

Fig. 3.1. Powder XRD pattern of Li_6PS_5Cl powder as synthesised.

Na-beta”-Alumina: Na-beta”-Alumina discs with a diameter of 10 mm and thickness of 0.7 mm were purchased from Ionotec. The discs were polished in deionised water on successively finer grits of the SiC paper (400, 600, 800, 1200, and 2500). They were dried and transferred into a muffle furnace inside an Ar-filled glovebox, and heated at 400 ℃ in a platinum crucible to remove surface contaminant. The heat-treated discs were used as solid electrolyte pellets. The Na-beta”-Alumina discs were prepared by Dominic Spencer Jolly.

Li_3N: Li_3N powder (Sigma-Aldrich) was loaded into a 5-mm-diameter stainless steel die set (Specac) and pressed under a uniaxial pressure of 500 MPa into a disc. The disc was transferred to a muffle furnace inside an Ar-filled glovebox, heated at 600 °C on a graphite foil for 1 h for densification, and cooled to room temperature at 10 °C/min. The sintered discs were sequentially polished with 250, 400, 600, 800, 1200, 2500, and 4000 grit SiC papers until the surface of the discs had a mirror-shine. The polished discs were used as solid electrolyte pellets. The Li_3N discs were prepared by Gareth Hartley.

3.2.2 Three-electrode cell assembly

Li/Li_6PS_5Cl/Li and Li/Li_3N/Li cells: Inside an Ar-filled glovebox, metallic Li foil with a thickness of 200 µm was scratched with a scalpel to remove its surface layer. A 5.4-mm-diameter Li disc was punched out and pressed at 100 kN to a resultant thickness of 50 µm. Two 2-mm-diameter Li discs were cut from the pressed Li foil, and concentrically pressed onto both sides of a solid electrolyte pellet (Li_6PS_5Cl/Li_3N). A 0.5-mm-diamter Li foil was additionally placed beside the working electrode as the reference electrode. The solid electrolyte pellets with Li electrodes were then assembled into pouch cells and sealed under vacuum, with Cu foils serving as current collectors. The configuration of a three-electrode cell is shown in the figure below, **Fig. 3.2**.

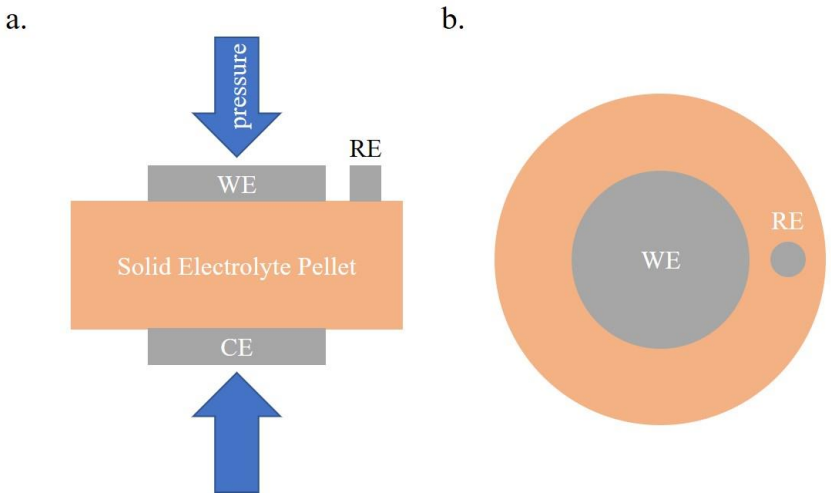

Fig. 3.2. Three-electrode cell configuration for electrochemical tests: three-electrode cell at **a.**

side-view **b.** top-view configuration, respectively. WE, CE and RE denote working, counter, and reference electrodes, respectively, which are the corresponding alkali metal for each test.

Na/Na-beta”-Alumina/Na: Within an Ar-filled glovebox, the Na metal was cut from the ingot and the surface layer carefully removed with a scalpel. The Na metal was then pressed to a 100 μm thick foil. Two 5-mm-diameter Na discs were cut from the pressed Na foil, and pressed onto both sides of a Na-beta”-Alumina pellet as working and counter electrodes. A 1-mm-diameter Na foil was additionally pressed beside the working electrode as the reference electrode. Solid electrolyte pellets with Na electrodes were then assembled and sealed under vacuum into pouch cells, with Al foils serving as current collectors.

3.2.3 Three-electrode cell cycling and EIS

Constant pressure galvanostatic cycling was carried out using a Gamry Interface-1010E potentiostat. The cycling capacity for each plating and stripping was fixed at 1.0 mAh cm^{-2}. Electrochemical impedance spectroscopy was performed on cells with a voltage perturbation of 5 mV (for Li_6PS_5Cl and Li_3N) and 10 mV for Na-beta”-Alumina in a frequency range from 1 MHz to 1 Hz. The data were analysed using the ZView software.

3.2.4 Cross-sectional scanning electron microscopy

Pristine and cycled cells were cross-sectioned using a tungsten carbide blade ultrasonic cutter (SONOTEC) to minimise the effect of cross-sectioning on the interface. The cross-sectioned cells were mounted onto a customised holder with Cu adhesive tape and transferred into a Zeiss Merlin scanning electron microscope using an airtight transfer holder (Gatan). The cross-sectional SEM was conducted by Dominic Spencer Jolly and Stefanie Zekoll.

3.2.5 *In-situ* X-ray computed tomography imaging and reconstruction

The Li/Li_6PS_5Cl/Li and Na/Na-beta”-Alumina/Na cells were assembled and sealed under vacuum into miniature pouch cells (3 cm × 3 cm) with Cu-coated (100 nm) Al foil (for Li)/ Al

foil (for Na) serving as current collectors to avoid any shadowing effect in X-ray imaging, **Fig. 3.3b** & **c**. The cell was then located within the chamber of a Zeiss Xradia Versa 510 X-ray computed tomography microscope. A Deben CT5000 loading rig was used to apply the pressure required for battery cycling. The cell was charged and discharged using a Gamry Interface-1010E inside the Xradia between scans, **Fig. 3.3a**.

The reference image for radiographs was taken after the *in-situ* scans (for reconstruction of the tomograms), with the cell removed from the loading rig, and rig placed at the same position as *in-situ* scans. The reference image was obtained by taking 10 Flat images in acquisition mode, and averaging them, with identical scan settings of the *in-situ* scans. The reference image was manually applied to all *in-situ* scans in XRMDataExplorer. The *in-situ* scans were then reconstructed with identical settings using ZEISS XMReconstructor. The settings of various X-ray computed tomography scans are shown in the table below.

Battery	Accelerating Voltage	Exposure Time (sec)	No. of Projections	Voxel Size (μm/voxel)	Rotation Angle
$Li/Li_6PS_5Cl/Li$ (*in-situ* study)	80 kV	24	1601	3.63	360º
Na/Na-β''-Alumina/Na	120 kV	30	1601	2.20	360º
$Li/Li_6PS_5Cl/Li$ (temperature study)	80 kV	22	2401	1.99	360º

Table 1. Scan settings of all lab-based XCT scans involved in this chapter.

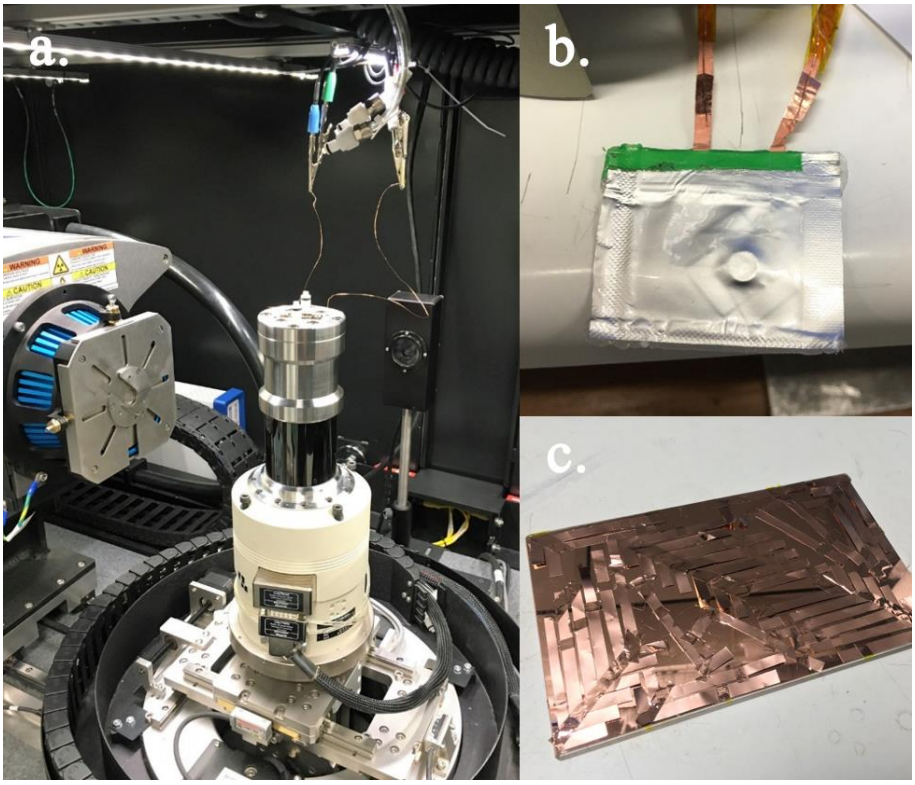

Fig. 3.3. Photos of *in-situ* X-ray computed tomography set-up with miniature pouch cell compressed by Deben loading rig, located within the chamber of Xradia Versa 510. **a.** Pouch cell placed inside the loading rig, connected to Gamry potentiostat with Cu wires fitting through the top of the loading rig. **b.** Miniature pouch cell (3 cm × 3 cm), evacuated and sealed with a cell inside the pouch. Enamelled Cu wires were soldered to the current collectors, with insulative coating scratched off, and wrapped with Kapton tape to avoid short-circuit. **c.** Current collectors made from Al foil were cut off into the right shape, taped to a glass board, and coated with 100 nm thick Cu via thermal evaporation.

3.2.6 Synchrotron X-ray computed tomography imaging and reconstruction

The Li/Li_3N/Li cell was assembled into a self-designed tube-cell, which applied stack pressure to electrodes and maintained air-tightness (Ar atmosphere). The tube-cell was then mounted to a levelled sample stage at the I13-2 beamline at Diamond Light Source to avoid any shadowing from current collecting pin on imaging (Experiment No. MG23980-1). The cell was charged and discharged using a Gamry Interface-1010E, connected to the cell from the top and bottom,

Fig. 3.4.

Pink beam (8-30 keV) was used for imaging to maximise the temporal resolution. Images were collected with a PCO Edge 5.5. sCMOS camera combined with an optical microscope with a 2× magnification, leading to a pixel size of 1.625 µm and a field of view of 4.7 × 4.4 mm^2. The conversion from X-ray to visible light was achieved with a LuAG 500 µm thick scintillator. Exposure time was set to 30 ms. For each tomogram, 3001 equiangularly distributed projections were taken over 180º. Tomograms were obtained continuously during the cycling of the cell, with an extra tomogram taken before and after charge/discharge as static status. The projections were reconstructed using the algorithm developed at the beamline.

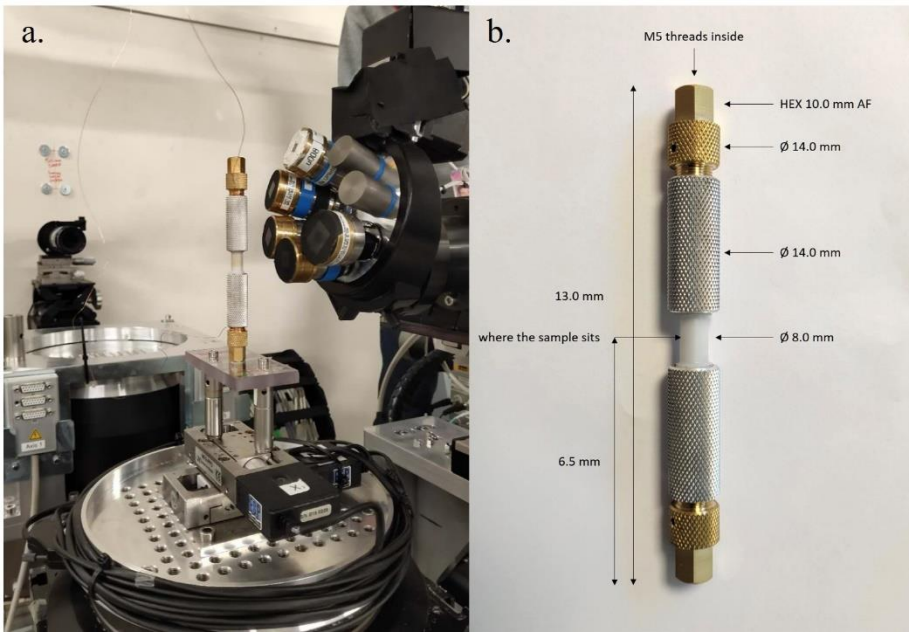

Fig. 3.4. Photos of *in-operando* set up with tube-cell at the beamline, and specifications of the tube-cell. **a.** The tube-cell was mounted onto a levelled sample stage to ensure the Li/SE interface is parallel to the beam. The tube-cell was connected to the potentiostat via Cu wires connected to the top and bottom. **b.** Specifications of the tube-cell. The cell was placed to the middle of the tube-cell, surrounded by Delrin (Polyoxymethylene) to maximise the X-ray transmission.

3.2.7 Data processing, visualisation, and quantitative analysis

The tomograms were reconstructed into stacks of images. Each image sequence was then opened with ImageJ, with the brightness/contrast properly adjusted. Different image sequences from an *in-situ* test were identically modified. The image sequence was then resliced perpendicular to the interface to reveal interfacial contact and voiding. The regions with features of interest were then cropped out as the region of interest (ROI). The cropped-out volume image was further processed with Avizo Fire (ThermoFisher Scientific), to have the serial images from an *in-situ* test registered (feature position matched). Orthoslices were used to reveal the voiding at the interface in 2D, with the colourmap adjusted. Volume rendering with appropriate colourmaps was utilised to present features of different grayscale values (anode, voids, electrolyte) in Avizo. Segmentation and label analysis tool were used to segment the voids out and quantitatively analyse the void volume distribution. The same processing was applied to a serial of volume images from a whole *in-situ* test, the change in total volume of voids, and distribution of voids at different size range were plotted out to unveil the evolution of voids during cell cycling.

3.3 Results and Discussions

3.3.1 Li/Li_6PS_5Cl/Li voltage polarisation, voiding, and the first *in-situ* X-ray computed tomography of void evolution at the interface

A three-electrode cell was cycled under a stack pressure of 3 MPa, at a current density of 1.0 mA cm^{-2} with a capacity of 1.0 mAh cm^{-2} for every charge/discharge (capacity corresponds to ~5 μm thick layer of Li), representing realistic current densities and capacities. During the cycling, a large variation of the working electrode potential with charge passed is shown in **Fig. 3.5a**. It reveals a voltage asymmetry of the working electrode between stripping and plating that could not be identified from two-electrode cell studies. The cycling commenced with

plating on the working electrode, which ensured intimate contact at the WE/SE interface by filling any pre-existing voids with the deposited lithium. The polarisation remains constant at 12 mV for the first plating. Subsequent stripping begins with the same polarisation as the end of plating, but the polarisation then increased modestly and continuously with more charge passed, reaching 19 mV at the end of stripping. As cycling continues, the stripping polarisation increases along with the cycle number, reaching a polarisation of 130 mV at the end of the seventh stripping, **Fig. 3.5a**. It is worth noting whilst the polarisation at the end of stripping after several cycles is significant, the polarisation on plating, even at the onset of plating, is considerably lower than that of stripping. Such asymmetry in cell polarisation suggests that the interfacial contact loss can be rapidly recovered with a small capacity. The cell short-circuits on the eighth plating of the working electrode. The three-electrode cell cycling was performed by Jitti Kasemchainan.

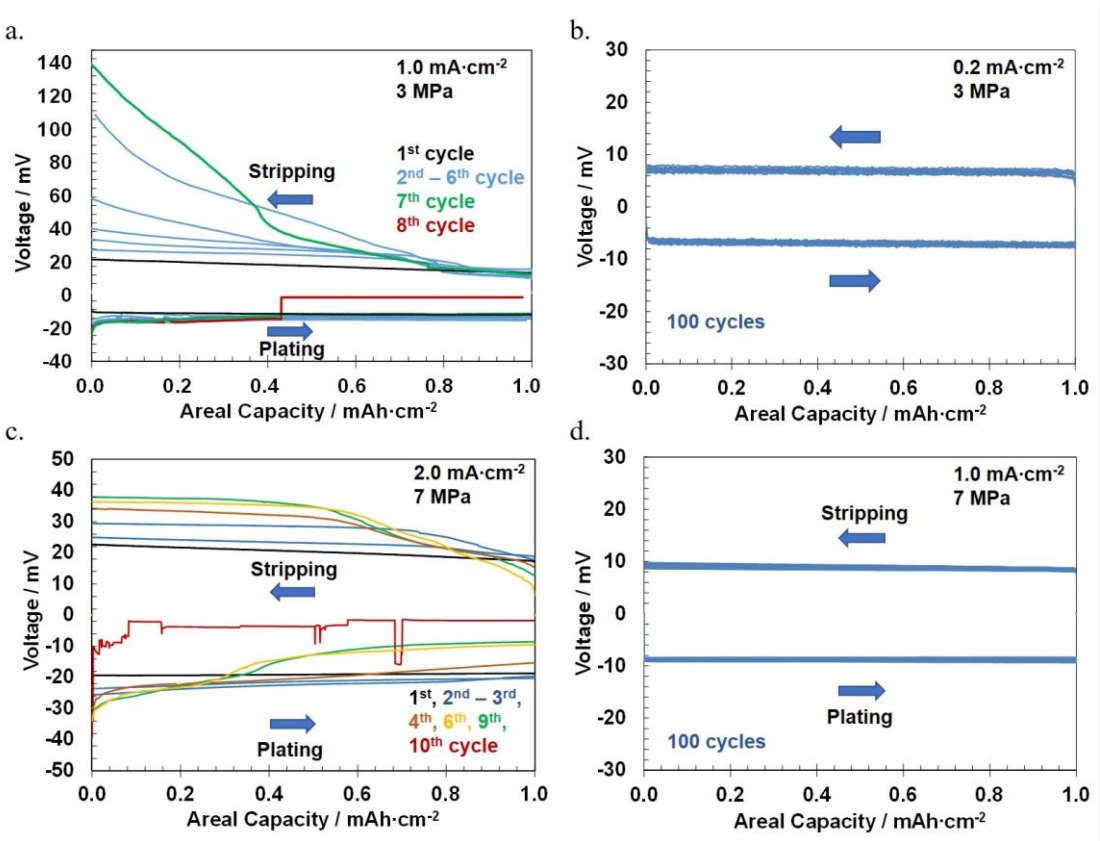

Fig. 3.5. Voltage versus charge passed for three-electrode cells on Li metal plating and stripping at the Li/Li_6PS_5Cl/Li interface. **a.** 3 MPa-1.0 mA cm^{-2}. **b.** 3 MPa-0.2 mA cm^{-2}. **c.** 7 MPa-2.0

mA cm^{-2}. **d.** 7 MPa-1.0 mA cm^{-2}. (Figure produced by Jitti Kasemchainan).

In order to confirm how the variation of cell polarisation is related to the interfacial deterioration, cross-sectional SEM was utilised to characterise the interface of cells at different stages of cycling, under the same current and pressure conditions. The SEM images of the pristine WE/SE interface as well as that after the first plating show that there is intimate contact between the Li metal and the solid electrolyte, **Fig. 3.6a** & **b**. Small void (size ~ 6 μm) formation is evidenced after the first stripping of working electrode, in accord with the small rise in polarisation, **Fig. 3.6c**. In stark contrast, the SEM image at the end of the sixth stripping shows remarkable detachment of the Li metal electrode from the solid electrolyte, **Fig. 3.6d**. Sizable voids (size ~ 40 μm) can be seen at the interface. The reduction of contact area between the Li metal and solid electrolyte results in an increase in local current density, and total interfacial resistance for the same constant overall current density (1.0 mA cm^{-2}), and is in accord with the increasing polarisation on stripping. Interestingly, the SEM image after the seventh plating shows an occluded void inside the Li metal. A thin film of deposited Li cuts the void off from the interface, and restores the interfacial contact. It therefore requires only a relatively limited amount of charge passed on plating to cover WE/SE interface such that the area of contact is very similar to the pristine interface. Such observation explains the rapid drop in polarisation at the very early stages of plating, in agreement with the voltage behaviour shown in **Fig. 3.5a**. The existence of such occluded voids also explains why low polarisation is shown in the early stages of all stripping. As stripping commences, the WE/SE contact is the same as at the end of previous plating, which is similar to a pristine cell, as the existing voids are covered with a thin layer of Li. Only when the layer of Li in contact with the solid electrolyte is removed, do the occluded voids become exposed to the solid electrolyte surface again, returning to high polarisation. Notably, Li penetration into the solid electrolyte was also observed in proximity to the occluded void in the SEM taken after the seventh plating. It is expected that the dendrite penetration results from the enhanced local current density near the void at the interface, which exceeds critical plating current density.

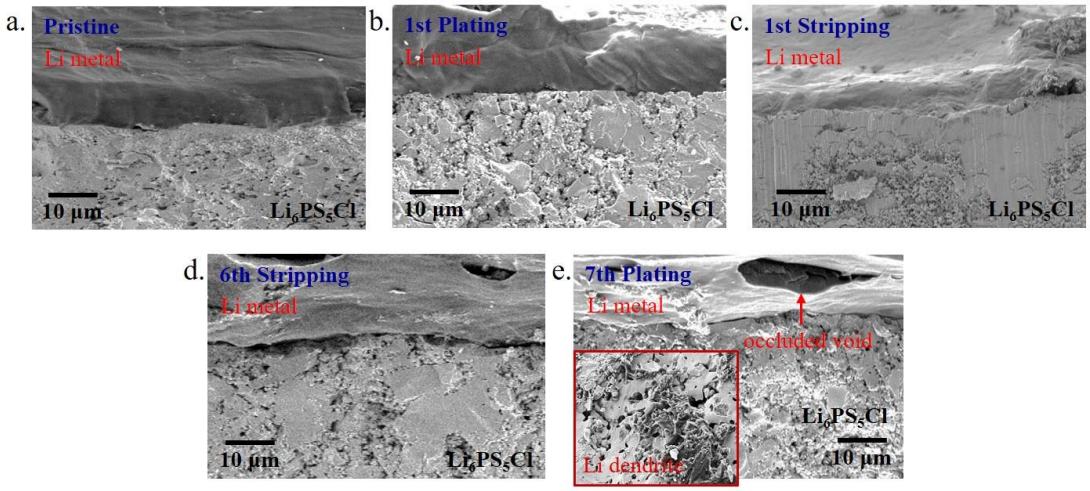

Fig. 3.6. Cross-sectional SEM images of the Li metal/Li_6PS_5Cl interface at different stages of cycling, 3 MPa, 1.0 mA cm^{-2}. **a.** pristine. and after **b.** 1st plating. **c.** 1st stripping. **d.** 6th stripping. **e.** 7th plating. A dendrite that penetrates into solid electrolyte in proximity to the void is magnified and shown in e.

The whole process of interface evolution, when cycled at an overall current density above the critical stripping current density is shown below in **Fig. 3.7**.

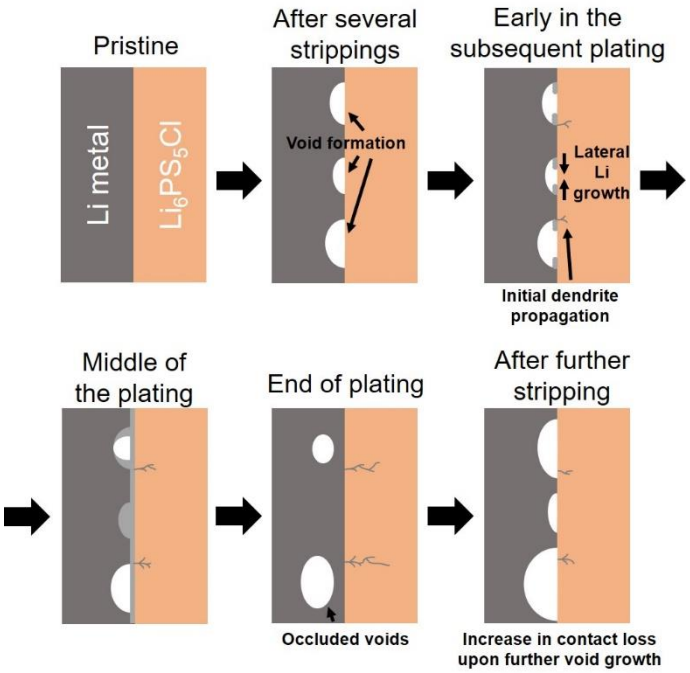

Fig. 3.7. Schematic of the Li metal/Li_6PS_5Cl interface cycled at an overall current density above

the CCS. Sequence from pristine to after several strippings and platings of Li metal: voids form on stripping; lateral growth of a thin Li film across the electrolyte surface occludes the void and reduces cell polarisation. Some voids are eliminated on plating, but the occluded voids reopen on subsequent stripping, leading to accumulation of voiding, and increasing loss of contact with cycling. This increases stripping polarisation and results in high local current density in subsequent plating, and consequentially dendrites on plating.

The generation of voids will occur when the stripping current removes Li from the interface faster than it can be replenished. $J_{\text{Li diffusion}} + J_{\text{Li creep}} < J_{\text{Li}^+ \text{ migration}}$, where J is the flux. The rate of Li replenished to the interface depends on the diffusion of Li atoms within Li metal and Li metal creep. The pressure-dependent measurements of critical stripping current density were therefore conducted, to determine the effect of stack pressure on maintaining the interface via creep of the Li metal. By decreasing the overall current density to 0.2 mA cm^{-2}, a low and constant polarisation can be achieved without changing the capacity and stack pressure, **Fig. 3.5b**. Whilst the CCS at 3 MPa is limited to 0.2 mA cm^{-2}, plating and stripping can proceed with almost no change in polarisation at a current density of 1.0 mA cm^{-2} when increasing the stack pressure to 7 MPa. Higher stack pressure enhances the creep rate of Li metal, which enables Li to be replenished at the interface at a faster rate, thus Li atoms can be stripped away at a higher rate without deteriorating the interfacial contact, **Eq. 3.1**, where σ is the stack pressure, $\dot{\varepsilon}$ is the creep rate, A_c is a materials-specific creep parameter, m is the power-law creep exponent, Q_c is the activation energy for dislocation climb, $\bar{R}$ is the molar gas constant, and T is the temperature[21]. However, such enhancement is not limitless. When cycled at 2.0 mA cm^{-2} with a stack pressure of 7 MPa, a gradual increase in cell polarisation as the number of cycles increased was also observed in a similar way to those cycled at 3 MPa and a current density of 1.0 mA cm^{-2}, as the rate of stripping exceeds the creep rate of Li metal driven by a stack pressure of 7 MPa. The short-circuit occurs after the 10$^{\text{th}}$ cycle as the local current density exceeds the CCP, as the interfacial contact has greatly deteriorated during cycling.

$$\dot{\varepsilon} = A_c \sigma^m \exp\left(\frac{-Q_c}{\bar{R}T}\right) \quad 3.1$$

Although the morphology of the voids at the interface has been characterised with cross-sectional SEM, showing voids of bigger sizes as the number of cycles increases, the destructive nature does not allow tracking of void growth and accumulation during cycling. Moreover, the cells were cross-sectioned with the ultrasonic cutter, though better than laser cutting and FIB, as it generates less heat, the cutting can still dramatically change the morphology of the interface, especially the soft Li metal. Hence, it is hard to ensure the morphology of voids observed by cross-sectional SEM is representative of their original shapes. A non-destructive and *in-situ* characterisation technique is indeed required to confirm the void formation and track the dynamic growth of voids during cell cycling. *In-situ* X-ray computed tomography of Li/Li_6PS_5Cl/Li cells was therefore conducted to evidence the accumulation of voids. The *in-situ* X-ray computed tomography was obtained as described in the Protocol section with the lab-based XCT. The Li/Li_6PS_5Cl/Li cell of the same dimension as in the three-electrode cell cycling test was assembled into a miniature pouch cell to ensure identical cycling conditions. The Deben loading rig was employed to precisely control the pressure applied to the cell, whilst reamaining X-ray transparent around the cell.

Virtual cross-sectional image slice from the *in-situ* XCT taken after the 1st stripping shows good interfacial contact between Li metal and Li_6PS_5Cl electrolyte with only a few small-sized voids, in accord to the modest voltage polarisation observed in the first stripping, **Fig. 3.8a**. After the 3rd stripping, void accumulation becomes apparent, several flat and wide voids (black pixels) can be seen at the interface, which are highlighted by dashed yellow circle in **Fig. 3.8b**. After the 5th stripping, it is noteworthy that the sizable voids observed after the 3rd stripping aren't recovered by plating; instead, those voids grow further in the 4th and 5th stripping, forming a big gap (size ~ 45 μm) at the interface, and largely detaches the Li metal from the Li_6PS_5Cl electrolyte, **Fig. 3.8c**.

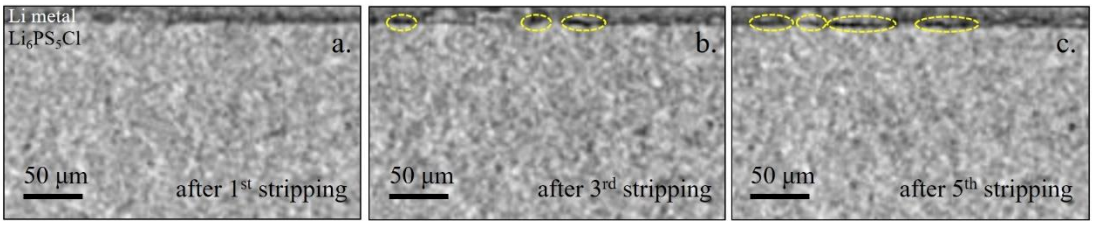

Fig. 3.8. Virtual cross-sectional image slices from *in-situ* X-ray computed tomography of the Li metal/Li_6PS_5Cl interface of a cycled Li/Li_6PS_5Cl/Li cell. Current density of 1.0 mA cm^{-2} and capacity of 1.0 mAh cm^{-2} (3 MPa). **a.** after the 1st stripping. **b.** after the 3rd stripping. and **c.** after the 5th stripping. The black pixels at the Li/Li_6PS_5Cl interface reveal the accumulation of voids (low X-ray attenuation) with increasing cycle number.

While the empty void represents zero attenuation in the X-ray computed tomography image, Li metal, as a low attenuating material, also shows a low grayscale in the image. It makes it harder to clearly distinguish all the voids, but only the big ones which have sufficiently accumulated. A different colourmap is therefore employed to improve the visual contrast between void, Li metal, and Li_6PS_5Cl electrolyte. At the interface, pixels with grayscale below a certain threshold (half of pure Li metal), are segmented out and highlighted in white. This allows the voids with sizes above the imaging pixel size (3.63 µm/pixel) to be clearly distinguished, **Fig. 3.9**.

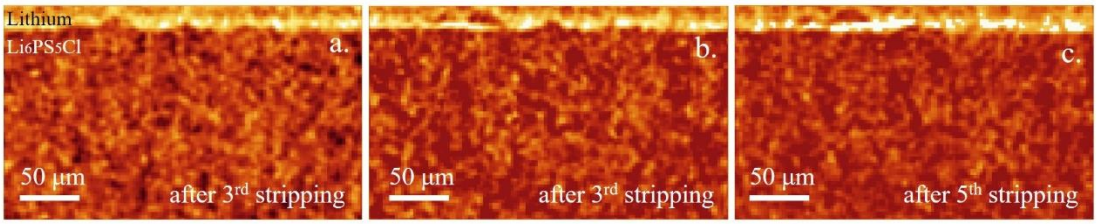

Fig. 3.9. Virtual cross-sectional image slices from in-situ X-ray computed tomography of the Li metal/Li_6PS_5Cl interface of a cycled Li/Li_6PS_5Cl/Li cell, in a colourmap with voids highlighted in white to show the void accumulation with increasing cycle number.

While the gradual void accumulation during cell cycling has been revealed, to better comprehend void growth and accumulation, *in-situ* X-ray computed tomography with higher spatial resolution, better temporal resolution, and ideally a more coherent beam at lower energy

(better contrast between Li metal and void) is required in further study.

3.3.2 Dependence of critical stripping current density and voiding on temperature in Li/Li_6PS_5Cl/Li cell

As void formation at the interface is dominated by, $J_{\text{Li diffusion}} + J_{\text{Li creep}} < J_{\text{Li}^+ \text{ migration}}$, an increase in temperature may be expected to effectively improve the cell performance, as high temperatures not only increase the rate of self-diffusion within Li metal, but also the rate of deformation by power-law creep. In addition, operating a cell with very high stack pressure is unlikely to be viable in practice, as maintaining a high pressure for the cell pack is technically challenging and costly. In this regard, the stack pressure applied to cell has been reduced to 1 MPa in this study, for commercial relevance in practical usage. Three-electrode cell cycling combined with X-ray computed tomography are employed to examine the morphological stability of the Li/SE interface during discharge over a temperature range of 25 ℃ to 80 ℃. By studying temperature-dependent electrode kinetics, the extent to which cycling above room temperature increases the rate of reversible lithium stripping is quantified.

Three-electrode cells were constructed and cycled under 1 MPa stack pressure at 25 ℃, 60 ℃, and 80 ℃, respectively, **Fig. 3.10a**. At each temperature, cycling began at 0.25 mA cm^{-2} with a capacity of 1.0 mAh cm^{-2} for 5 cycles. Then the current density was increased in steps of 0.25 mA cm^{-2} every 5 cycles until cell failure. Due to the aforementioned inherent advantage of the three-electrode cell, it allowed separation of the effects from stripping and plating processes at the Li/SE interface, and any increase in polarisation during stripping could then be attributed to the contact loss at the Li/SE interface due to voiding. Therefore, the critical current density for voiding is determined to be exceeded at the current density at which voltage polarisation of the cell increases during stripping. The three-electrode cells were assembled and tested by Dominic Spencer Jolly.

For the cell cycled at 25 ℃, a modest polarisation increase of 26 mV is observed during the

first stripping of the working electrode at 0.25 mA cm^{-2}. After the 4th stripping, a polarisation of almost 200 mV is observed, which triggers cell short-circuit in the subsequent plating on the working electrode, due to too high local current density. At 25 °C and under a low stack pressure of 1 MPa, 0.25 mA cm^{-2} already exceeds the critical stripping current density, **Fig. 3.10b**.

In contrast, at the increased temperature of 60 °C, cycling at 0.25 mA cm^{-2} leads to very similar polarisation on each cycle of 4 ~ 8 mV, **Fig. 3.10c**. The small increase in voltage at the early stages of stripping on each cycle is attributed to minor voiding that is filled on the subsequent plating. The absence of an abrupt change in cell polarisation but rather a transition region where small and shallow voids form on stripping and reversibly on plating confirms that viable cycling can be achieved at 0.25 mA cm^{-2} and low stack pressure, by increasing the temperature (red). On increasing the current density to 0.5 mA cm^{-2}, increasing polarisation is observed on each successive stripping (increasing from 7.7 mV to 24.4 mV in the first cycle, to 27.1 mV in the second cycle and to 33.17 mV in the third cycle), followed by sudden cell failure due to dendrite growth in the fourth cycle (blue). The critical stripping current density at 60 °C is therefore greater than 0.25 mA cm^{-2}, but is exceeded at 0.5 mA cm^{-2}.

Finally, when cycling at 80 °C, with a current density of 0.25 mA cm^{-2}, it again shows no increase in polarisation on stripping, maintaining a stable voltage of approximately 2 mV (red), **Fig. 3.10d**. Upon increasing the current density to 0.5 mA cm^{-2-}, the cell polarisation remains highly stable at about 4 mV (blue). However, when increasing the current density to 0.75 mA cm^{-2}, the reversible stripping and plating can no longer be maintained. The cell shows signs of severe void formation on stripping (yellow), with voltage increasing from ~6 mV to 61 mV during the first stripping, and reaching a polarisation of 248 mV during the fifth stripping. The voltage spikes on the fifth stripping clearly suggest dendrite penetration into the solid electrolyte on the plating of the counter electrode. Therefore, at 80 °C, whilst 0.5 mA cm^{-2} is below the critical stripping current density, 0.75 mA cm^{-2} clearly exceeds such critical value.

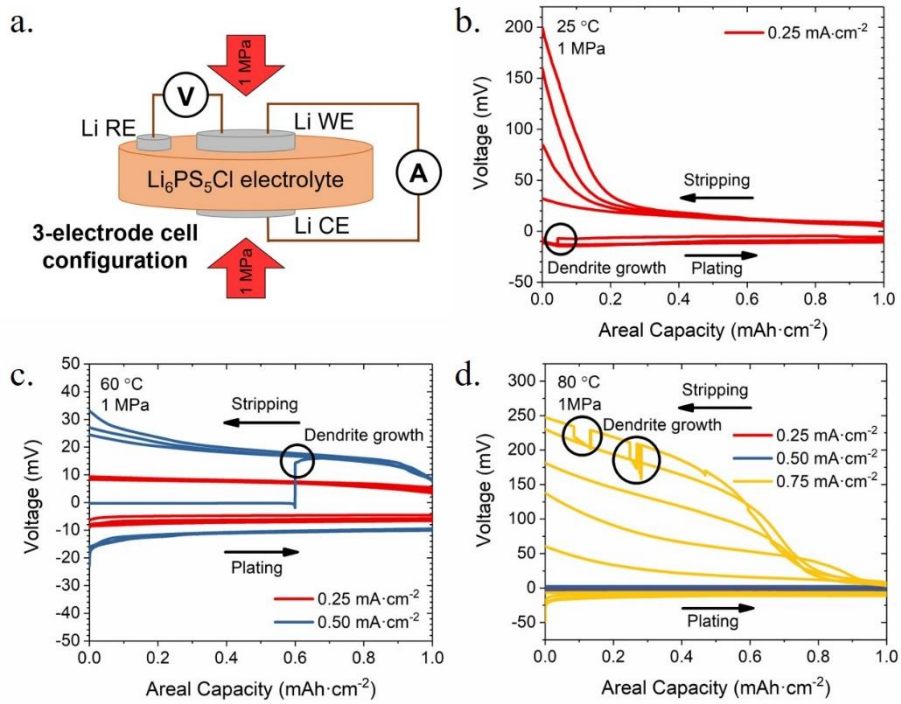

Fig. 3.10. a. Configuration of a three-electrode cell; WE, CE, and RE stand for the working, counter, and reference electrodes, respectively. Three-electrode cycling plots under 1 MPa stack pressure, moving capacity of 1.0 mAh cm^{-2}, at **b.** 25 °C, **c.** 60 °C, and **d.** 80 °C. For each cell, plating occurs first on the working electrode. (Figure produced by Dominic Spencer Jolly).

In order to compare the morphological changes at the Li/SE interface on cycling with current densities in different range in relation to the critical stripping current densities, X-ray computed tomography was conducted to characterise the Li/SE interface with lab-based XCT. Two-electrode cells were cycled at 80 °C under 1 MPa pressure in a temperature-controlled chamber inside the glovebox at 0.5 mA cm^{-2} and 0.75 mA cm^{-2}, i.e. below and above the critical stripping current density determined in **Fig. 3.10d**. X-ray computed tomography scans were taken after 25 cycles, or cell failure. A pristine two-electrode cell, rested with 1 MPa at the same temperature was also scanned for comparison. In line with the three-electrode cycling results, the two-electrode cell cycled at 0.5 mA cm^{-2} under 1 MPa stack pressure at 80 °C showed highly reversible cycling with little change in polarisation, which suggests intimate contact at the interface throughout cycling, (**Fig. 3.11a**). This result was supported by XCT imaging, which showed negligible difference between the Li/Li_6PS_5Cl interface at pristine (**Fig. 3.11c**), and

after 25th stripping at the above conditions (**Fig. 3.11d**). Good contact can be seen between the Li electrode (green) and the solid electrolyte (yellow) in both. The one area of blue indicative of a void, represents only ~3% of the electrode/electrolyte interface. In comparison, for the cell cycled at 0.75 mA cm^{-2} under the same conditions, increasing polarisation is observed over 12 cycles, (**Fig. 3.11b**) and voids (blue) are apparent across the entire interface between the Li electrode and the solid electrolyte (**Fig. 3.11e**). The corresponding grayscale images of **Fig. 3.11c-e** from XCT are shown in **Fig. 3.11f-h**.

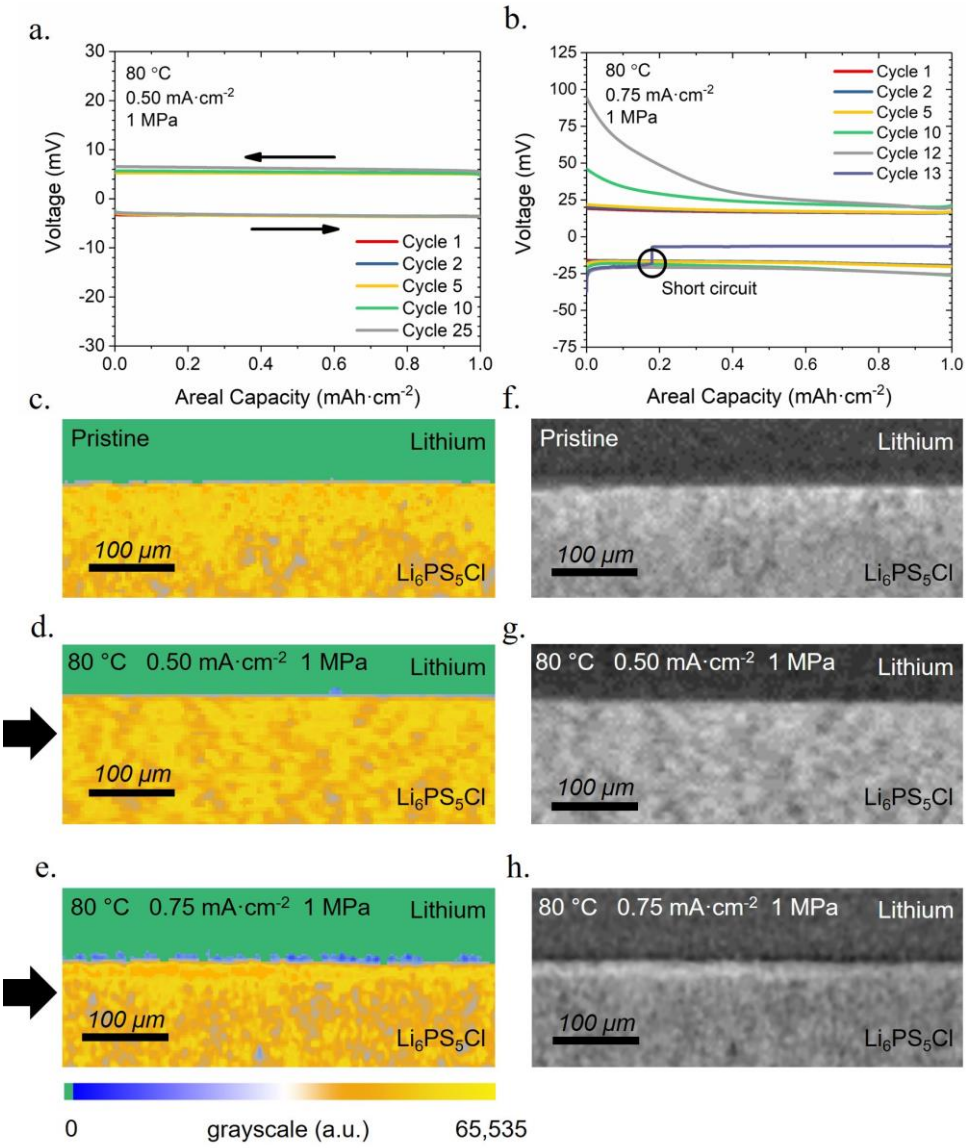

Fig. 3.11. Cycling plots of two-electrode cells cycled at 80 °C under 1MPa at **a.** 0.5 mA cm^{-2}, **b.** 0.75 mA cm^{-2}. Virtual cross-sectional images from X-ray computed tomography showing

Li/Li_6PS_5Cl interface when **c.** at pristine, and after cycling at **d.** 0.5 mA cm^{-2} corresponding to **a.**, and **e.** 0.75 mA cm^{-2} corresponding to **b.** Green, blue and yellow represents lithium, voids, and Li_6PS_5Cl, respectively. The grayscale images of **c**-**e** are shown in **f**-**h**.

In this study, three-electrode electrochemical techniques coupled with direct imaging of the interface by X-ray computed tomography reveal that operating an all-solid-state battery above room temperature can increase the critical current density at which voids form at the Li/SE interface during stripping, and therefore increase the rate at which it is possible to discharge the battery whilst maintaining interfacial stability. This finding builds on previous work showing that operating batteries at high stack-pressure can enable higher rates of discharge and is indeed based on the same concept; that operating a SSB under conditions that favour high rates of creep in the Li metal prevents voiding at the Li/SE interface. However, as 80 °C is already challenging to maintain, whilst far from the melting point of lithium, the strategy of increasing the discharge rate by increasing the cycling temperature is not as effective as increasing stack pressure. A combination of modestly increased temperature and a small amount of stack pressure might be a feasible and cost-effective way to improve the rate performance of all-solid-state batteries.

3.3.3 First quantitative analysis of voiding in Na/Na-beta”-Alumina/Na cell

In comparison to Li metal anode, all-solid-state batteries with Na anode have received less attention due to their comparatively lower theoretical capacity (1166 mAh g^{-1}), despite still offering a significant improvement over hard carbon anodes used in Na-ion cell. As it has been shown in previous studies the process of formed voids being replenished by Li is dominated by the pressure-driven power-law creep of Li. It is suggested that the mechanical properties of the alkali metal that serves as the anode would play a critical role in determining the critical stripping current density in cell cycling. Na metal anode, with a much lower melting point, thus a much larger creep rate at room temperature than Li metal under the same pressure, would be expected to offer a great improvement in high-rate stripping.

In addition, the higher X-ray scattering of Na versus Li makes *in-situ* tomographic studies of the evolving interface more tractable than Li[22]. Such improvement in contrast allows the first quantitative analysis of void evolution during cycling, and offer the prospect of better understanding the general aspects of alkali metal anodes in contact with ceramic electrolytes.

In this study, Na-beta''-Alumina has been selected as the solid electrolyte based on its high conductivity (2 mS cm^{-1}) and its complete interfacial stability against Na anode. Here, it is demonstrated that void accumulation on cycling in Na cells is similar to the Li/SE interface. In addition, the coalescence and replenishment of voids on cycling has been directly imaged for the first time via *in-situ* X-ray computed tomography. The functionality of interfacial contact loss with pressure has also been determined, showing that the critical pressure above which voids do not form, and hence cells do not die, varies linearly with the current density of cell operation.

Alkali-rich oxides invariably have hydroxides and carbonates present on their surfaces, which have a significant effect on the interfacial impedance. Discs of Na-beta''-Alumina, 10 mm diameter and 0.7 mm thick, were subjected to a similar procedure as reported by Sakamoto and co-workers for the removal of hydroxide and carbonate surface species from $La_7La_3Zr_2O_{12}$ (LLZO) discs, involving a polishing and heating protocol[23]. The surface treatment was found to reduce greatly the interfacial impedance of Na/Na-beta''-Alumina cells.

Three-electrode cells of Na/Na-beta''-Alumina were assembled with the voltage measured between the working electrode and an added reference electrode to reflect the degradation of WE/SE interface, with a constant current passing between the working and counter electrodes. Cell cycling began by plating on the working electrode to maximise the interfacial contact (and stripping the counter electrode), followed by stripping the working electrode (and plating the counter electrode). A capacity of 0.5 mAh cm^{-2} was cycled, equivalent to stripping/plating approximately 5 μm of Na. The Na/Na-beta''-Alumina cells were assembled and tested by Dominic Spencer Jolly.

The assembled cell was cycled under a pressure of 4 MPa at a current density of 1.5 mA cm^{-2}, results in a marked asymmetry between plating and stripping. The former exhibits a low and constant polarisation (12 mV) with charge passed in every cycle, whereas for the latter, the polarisation increases with charged passed and with the cycle number, from 0.23 V in cycle 1 to 0.42 V in cycle 10, (**Fig. 3.12a**). Such polarisation asymmetry caused by interfacial deterioration (void formation) on stripping, is in good accord with the previous study on the Li/Li_6PS_5Cl interface. The inability to replenish all the voids in the subsequent plating, leads to the continuously increasing polarisation with the cycle number, which is also in good agreement with the Li anode studies.

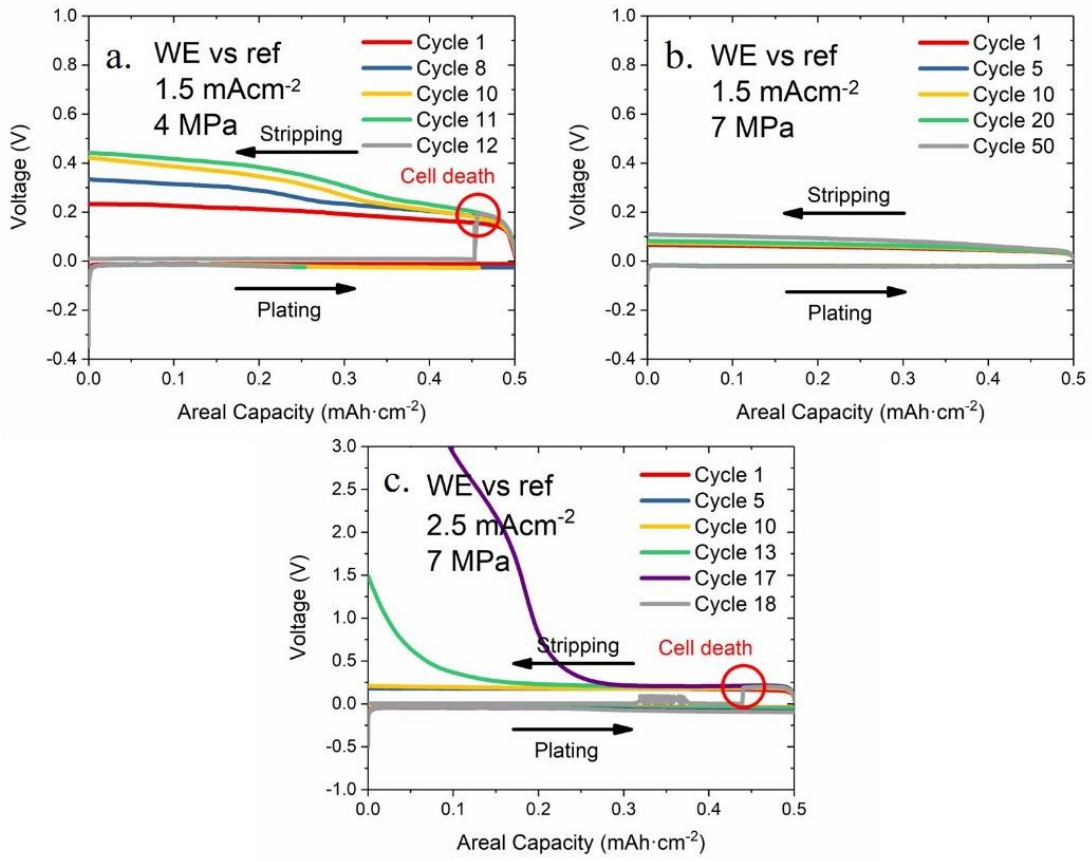

Fig. 3.12. Voltage measured between the working and reference electrodes when cycling at **a.** 4 MPa and 1.5 mA cm^{-2}, **b.** 7 MPa and 1.5 mA cm^{-2}, **c.** 7 MPa and 2.5 mA cm^{-2}. WE and ref are the working, and reference electrodes, respectively. (Figure produced by Dominic Spencer Jolly).

Three-electrode cells cycled under the same described conditions were disassembled, cross-sectioned, and characterised by SEM to reveal interfacial contact at different stages of cell cycling, (**Fig. 3.13**). After the first plating (**Fig. 3.13b**), the interfacial morphology looks much like the pristine cell (**Fig. 3.13a**) with no voiding evident. However, after the first stripping, small voids are present at the interface (**Fig. 3.13c**). Such observation is consistent with the three-electrode cycling data (**Fig. 3.12a**), as well as previous studies that voids form on stripping[7,24,25]. A comparison between the interfaces after the first stripping and the eleventh stripping (**Fig. 3.13d**) clearly shows that voids can grow significantly in size over multiple cycles, resulting in severe interfacial contact loss, and the polarisation increase observed in **Fig. 3.12a**. As the critical stripping current density has been defined in previous studies, it is clear that for a Na/Na-beta''-Alumina cell under a 4 MPa pressure, 1.5 mA cm^{-2} is above the critical stripping current density, leading to the development of voids on stripping and eventual cell death.

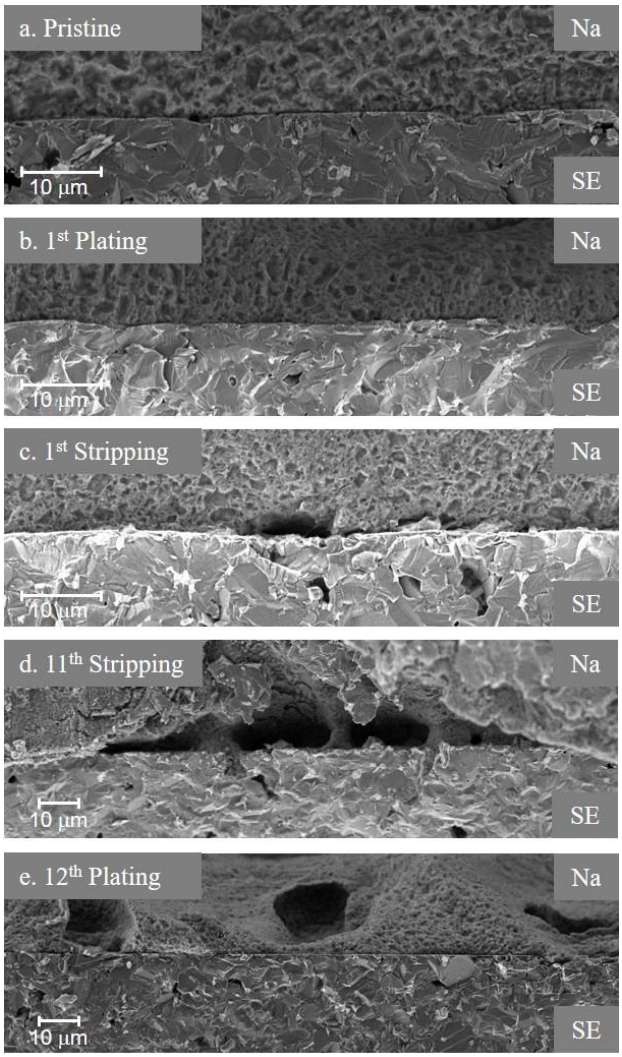

Fig. 3.13. Cross-sectional SEM images of the Na/Na-beta''-Alumina interface when **a.** pristine and after **b.** 1st plating, **c.** 1st stripping, **d.** 11th stripping, and **e.** 12th plating after cycling under 4 MPa pressure at 1.5 mA cm^{-2}. (Figure produced by Dominic Spencer Jolly).

On the plating side, while the voltage polarisation suggests the reformation of a conformal interface with each plating, the cross-sectional SEM showing the final plating offers some insight (**Fig. 3.13e**), clearly shows not only a conformal interface but also occluded voids in the Na, which are set back from the interface. Similar to plating Li, the deposited Na will nucleate at the most energetically favourable point. When there is a pre-existing void at the interface, the preferred point of nucleation will be the triple contact point between Na, SE, and void, since the deposited Na does not have to push against the stack pressure to create volume in order to

grow. In this criterion, the growth of Na will occur across the solid electrolyte interface forming a thin film with a small capacity to occlude the void, explaining the low and consistent polarisation on plating, similar to a pristine cell.

Though the formation and accumulation of voids have been confirmed by post-mortem techniques, such as cross-sectional SEM, the dynamics of void growth and occlusion remains unknown. Are all the voids only occluded by a thin layer of Na on plating, or some of the voids can be fully filled? Does the wide and flat void at the interface originate from merge of voids or continuous growth of a single one? As the cycle number increases, will small-sized voids remain the most populated or big voids will dominate the contact loss? At the end of stripping, what percent of interface contact can be lost? Without answering all such questions, the key fundamentals of void evolution may never be completely unveiled.

In-situ X-ray computed tomography was therefore performed to observe how the voids grow and evolve on cycling. A two-electrode cell of Na/Na-beta''-Alumina was assembled, cycled at a current density of 1.5 mA cm^{-2} for a capacity of 0.75 mAh cm^{-2}, under 2 MPa pressure, and characterised by lab-based X-ray computed tomography at pristine and after every plating/stripping. A combination of low pressure and moderate current density was selected to ensure severe contact loss at the end of cycling.

A series of registered virtual cross-sectional image slices (images at the same location) from the *in-situ* X-ray computed tomography scans show the evolution of interfacial contact after every plating and stripping, and the reversibility of void formation, **Fig. 3.14**. Intimate contact between the Na metal anode and Na-beta''-Alumina electrolyte can be seen in the pristine cell, with a few small-sized voids, **Fig. 3.14a**. The interfacial contact remains largely unchanged during in the 1st cycle, in agreement with the low voltage polarisation widely observed in electrochemical test, **Fig. 3.14b** & **c**. Formation of small-sized voids can be carefully observed at the interface at the 2nd stripping, in accord with a modest polarisation increase since the 2nd cycle, **Fig. 3.14d**. However, most of such voids are replenished completely in the 2nd plating,

as small-sized voids only require a small amount of capacity to be fully filled, **Fig. 3.14e**. In the scan after the 3rd stripping, severe interfacial deterioration is apparent. Instead of populated, small-sized voids observed after the 2nd stripping, bigger voids with clear semi-elliptical shape are observed on the 3rd stripping, completely separating the Na metal anode from Na-beta''-Alumina electrolyte, leading to further interfacial deterioration, **Fig. 3.14f**. In the subsequent plating, it is noteworthy that most of the voids can be replenished completely by the deposited Na, except a few voids on the left-hand side remains largely unchanged, which could be occluded with only a thin layer of Na, **Fig. 3.14g**. In the 4th stripping, even bigger voids are observed at the interface, in accord with the further increased voltage polarisation. Importantly, while there are new voids emerging at the interface, most of the voids are present on the 3rd stripping, **Fig. 3.14h**. Such observation suggests that though voids can be filled in the plating, they are not completely diminished; instead, they continue to serve as current hot spots in the subsequent cycles, evolve to voids of bigger dimensions on stripping, leading to further Na anode detachment as the cycle number increases. Though remarkable voids are observed, the interfacial contact can be largely recovered by plating again as shown in **Fig. 3.14i**.

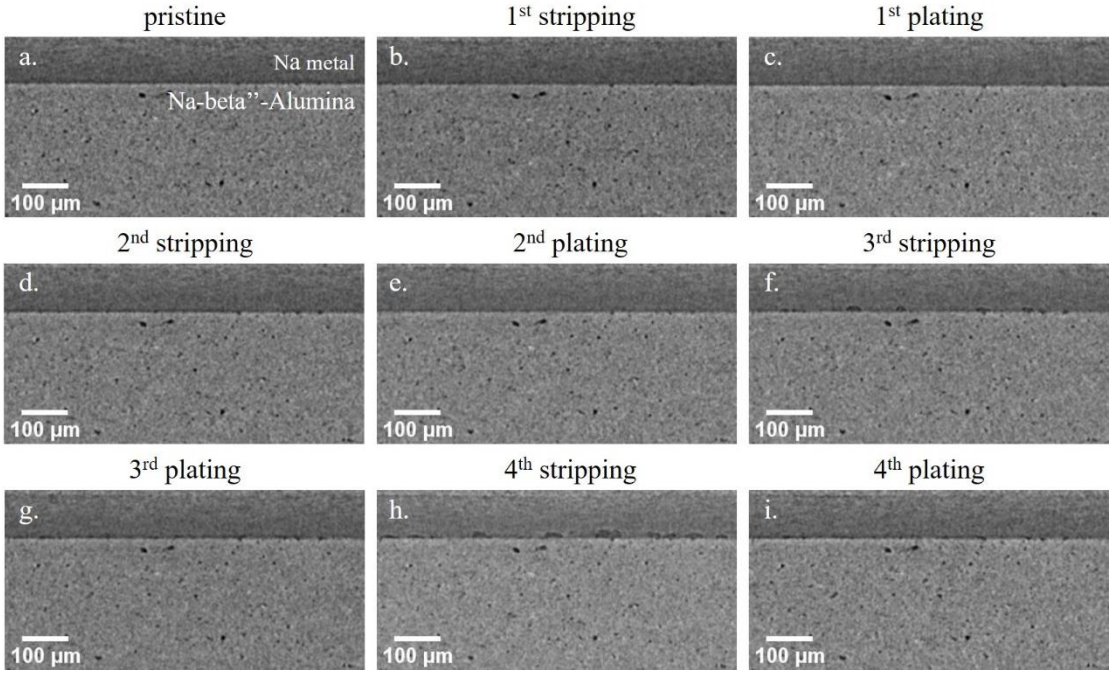

Fig. 3.14. Virtual cross-sectional images slices from *in-situ* X-ray computed tomography sans

of the Na/Na-beta''-Alumina cells showing the interface **a.** at pristine and after **b.** 1st stripping **c.** 1st plating **d.** 2nd stripping **e.** 2nd plating **f.** 3rd stripping **g.** 3rd plating **h.** 4th stripping **i.** 4th plating. The cell was cycled at a pressure of 2 MPa, and a current density of 1.5 mA cm^{-2} with a capacity of 0.75 mAh cm^{-2}.

While virtual cross-sectional image slices show direct comparison of interfaces along cycling at a specific cross-section, the whole picture of void development can be better revealed via the rendering of a volume image. A series registered volume images are shown in **Fig. 3.15**, with the electrolyte shown in red, voids in blue, and Na metal anode above the electrolyte set to be transparent.

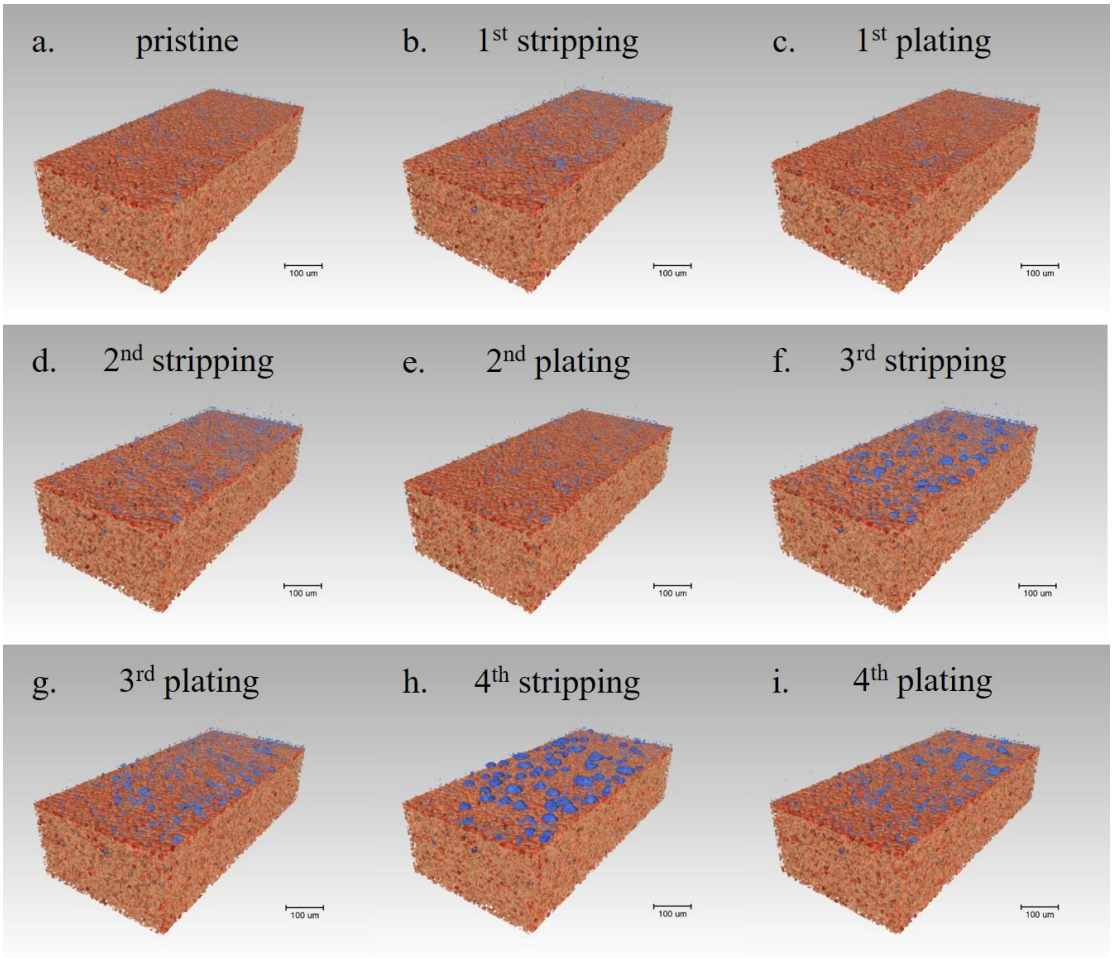

Fig. 3.15. Volume rendered images from *in-situ* X-ray computed tomography scans of Na/Na-

beta''-Alumina cell when **a.** pristine and after **b.** 1st stripping **c.** 1st plating **d.** 2nd stripping **e.** 2nd plating **f.** 3rd stripping **g.** 3rd plating **h.** 4th stripping **i.** 4th plating. The cell was cycled at a pressure of 2 MPa, and a current density of 1.5 mA cm^{-2} with a capacity of 0.75 mAh cm^{-2}.

While in agreement with the virtual cross-sectional images, the volume rendered images reveal the following key insights of void development more clearly:

1. Small voids are present even at the pristine interface, indicative of some porosity in the Na metal.
2. Voids increase in number and size on stripping and diminish in number and size on the subsequent plating.
3. Voiding at the interface increases as a function of cycle number, following memory effect to some extent, i.e. although voids are replenished by plating, where voids formed served as preferred void accumulation sites in the follow stripping.

The tomographic results, as it contains a large volume of the sample, can be analysed quantitatively by determining the number and volume of voids, and how this evolves on cycling to represent the evolution of the whole sample. Voids are separated based on connectivity, with volume measured as described in the Protocol section, **Fig. 3.16**. For accuracy of the quantitative analysis, only voids larger than 3 × 3 × 3 voxels (6.6144 × 6.6144 × 6.6144 μm^3) are taken into account.

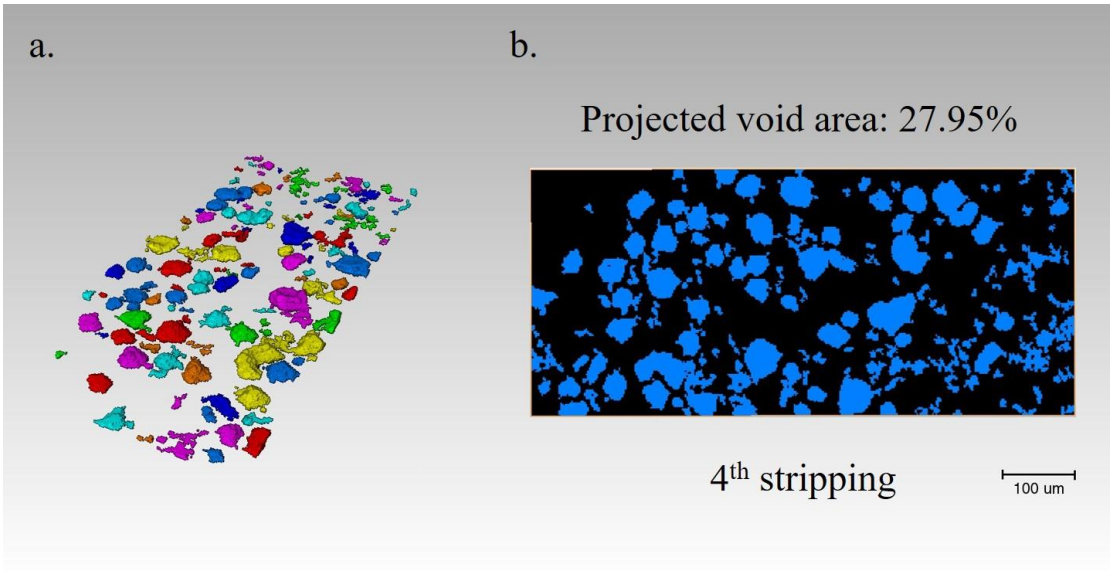

Fig. 3.16. a. Volume rendering of voids touching the Na/ Na-beta''-Alumina interface after the 4th stripping, with voids separated and coloured based on connectivity. **b.** Projection of voids onto the interface, showing a total ratio of 27.95% contact loss from voiding after the 4th stripping.

An analysis of the total volume of voids at different stages of cycling is presented in **Fig. 3.17a**. The volume of voids at the end of each stripping increases as a function of cycle number, consistent with increasing detachment. This is particularly clear from the 3rd stripping. The voids are only partially filled on subsequent plating, as is evident from the 3rd cycle onward. The void volume at the end of each plating also increases on cycling, in accord with the increasing volume of occluded voids.

Fig. 3.17b shows the number of voids in three different size regions. It is evident that larger voids become more apparent at higher cycle number. The small voids (1000 – 2500 μm^3) dominate on the 2nd stripping. Interestingly, despite the emergence of the medium (2500 – 10000 μm^3) and large voids (>10000 μm^3) at higher cycle numbers, the small voids persist on stripping and crucially also on plating. This implies that as the larger voids are filled in on plating, such filling is not complete in many cases, resulting in smaller voids remaining at the end of plating. This is also reflected from the 3rd stripping to the 3rd plating, where the number

of medium voids decreases as being filled by deposited Na. Correspondingly, the number of small voids increases on plating as the medium voids are not filled completely but diminish in size and fall into the range of small voids.

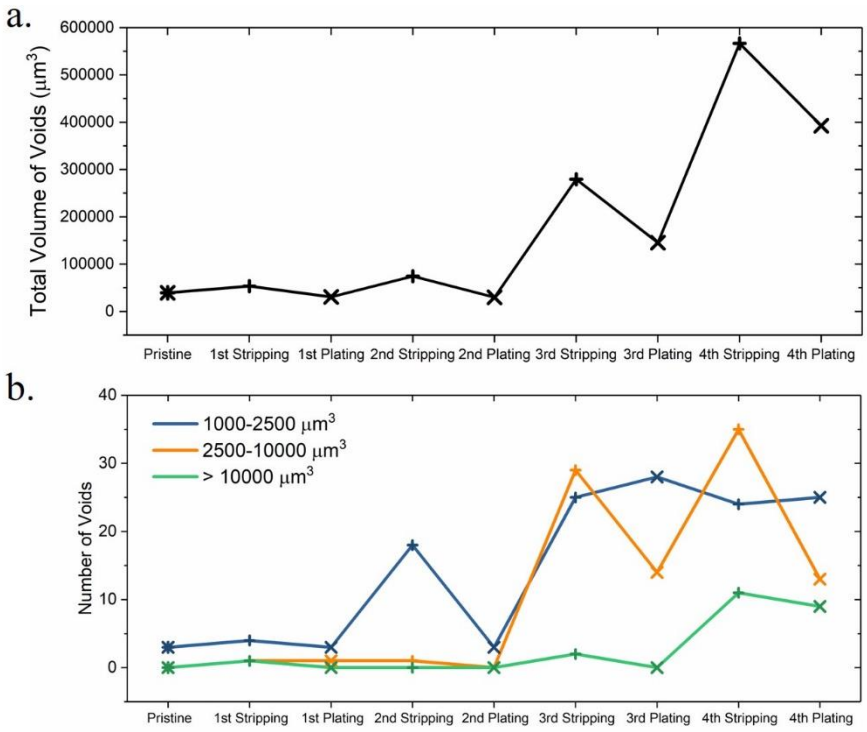

Fig. 3.17. Plots showing **a.** the total volume of voids in the Na anode and **b.** the number of voids in the range 1000 – 2500 µm^3 (blue), 2500 – 10000 µm^3 (orange), and >10000 µm^3 (green). The analysis was performed on a 6.58 × 10^{-2} mm^3 of the cell interface.

To examine the extent of contact loss at the end of cycling, voids present after the 4th stripping are projected on the interface, for a total ratio of contact loss, **Fig. 3.16b**. Though remarkable voids are present throughout the interface, only 27.95% of the interface is covered by voiding. If the voltage polarisation is only related to the increase in interfacial impedance due to contact loss, the cell polarisation should follow the formula below:

$$V_{measured} = V_{full\ contact} \times (\frac{A_o}{A})$$

Where $V_{measured}$ is the measured voltage during cell cycling, $V_{full\ contact}$ contact is voltage

measured at 100% contact when passing the same overall current density, A_o is the contact area at 100% contact, and A is the true contact area. Apparently, a contact loss of 27.95% would not result in the observed significant polarisation in cell voltage. This suggests that the current constriction due to contact loss is not the only factor that contributes to increase in interfacial impedance; the limited diffusion of Na in Na anode might also play a key role. As the stripping rate exceeds a certain level, the rate of Na being replenished to the interface by diffusion is not sufficient, which results in a Na-depleted region near the interface and increases the interfacial impedance.

And when plating, the local current density varies with the true area of contact between the electrode and electrolyte as below:

$$I_{local} = I_o/(\frac{A}{A_o})$$

Where I_{local} is the local current density, I_o is the applied current density (100% contact), A is the true contact area, and A_o is the area given 100% contact. As plating commences, the plated Na immediately fills the Na-depleted region near the interface, leaving current constriction the only cause of voltage polarisation. Thus, the cell voltage drops for a great extent immediately as plating commences, and gradually decreases as the true contact area increases due to Na deposition. However, when cycling above CCS, contact loss will become great enough that there are high local plating currents, which exceeds the critical plating current density. This will result in dendrite growth and cell death as observed in the 12th cycle of **Fig. 3.12a**.

As it has been done for Li anode in previous studies, the effect of pressure was examined by increasing the stack pressure to 7 MPa with the current density remaining at 1.5 mA cm^{-2}. While the polarisation on plating remains unchanged, a much smaller increase in polarisation is observed on stripping, remaining low over 50 cycles, **Fig. 3.12b**. Increasing the current density to 2.5 mA cm^{-2} at the pressure of 7 MPa again showed polarisation on stripping that increases significantly with cycle number, reaching 3.0 V in cycle 17 before the cell failure, **Fig. 3.12c**.

The cycling data showed similarities to that at a current density of 1.5 mA cm^{-2} under a 4 MPa pressure, suggesting the formation and accumulation of voids until cell failure. Thus, at a pressure of 7 MPa, the critical stripping current density is above 1.5 mA cm^{-2}, but below 2.5 mA cm^{-2}.

To investigate the functional relationship between stack pressure and void formation at different current densities, five three electrode cells were assembled and the polarisation increase with pressure on stripping at different current densities measured, **Fig. 3.18**. The tests were performed by Dominic Spencer Jolly and James E. Darnbrough. The pressure was controlled by a Deben loading rig, and the potential increase was measured following 0.1 mAh cm^{-2} charge passed. Following this, the cells were compressed under a high pressure (15 MPa) to reform the interface before being tested at a lower pressure to remove any remaining voids, and the potential increase at different current densities was determined again. This was repeated, reducing the pressure in steps of approximately 1 MPa until the increase in potential exceeded 3V. These data show that the dependence of voltage increase on pressure has the same functionality regardless of current density, with the curves being displaced to higher pressures for higher current densities. Each curve shows a severe variation of polarisation with an increase in pressure, **Fig. 3.18**.

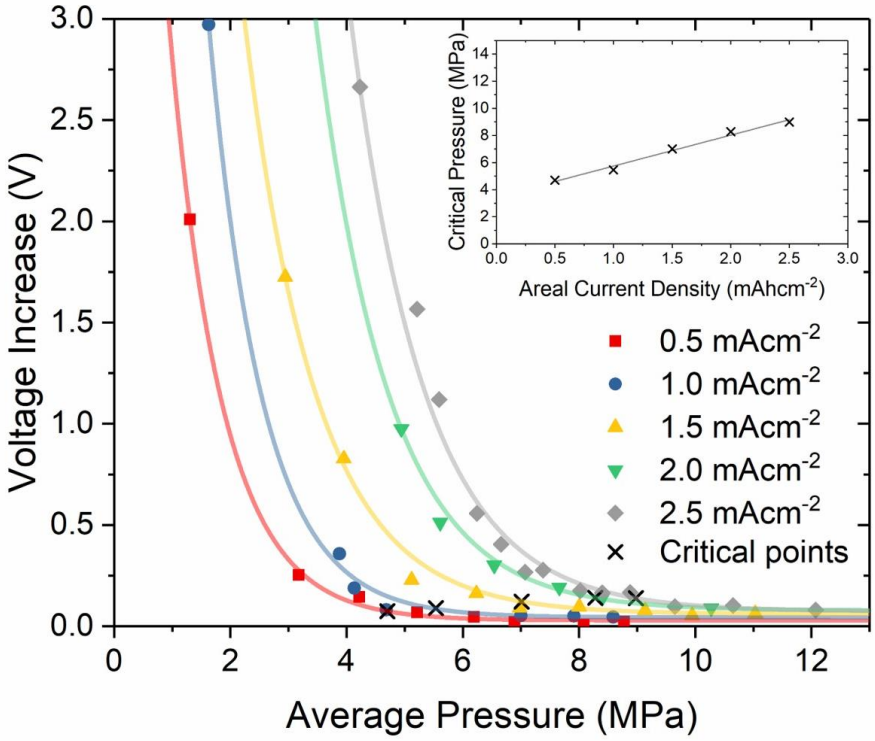

Fig. 3.18. Figure showing the relation between average pressure and voltage increase at 0.5, 1.0, 1.5, 2.0, and 2.5 mA cm^{-2} areal current densities. The inset shows how the critical pressure varies with areal current density. (Figure produced by Dominic Spencer Jolly).

Voids form when the flux of Na^+ ions away from the interface exceeds the flux of Na to the interface due to Na diffusion and creep. The dependence of critical stripping current density on pressure suggests that creep (stress-driven deformation) is the major mechanism of Na transport to the interface. For each current density, the critical pressure required to maintain the contact was estimated by finding the point in the fitted curve, where the $dV/dP = -0.05$. The critical pressures at different current densities were plotted in the inset of **Fig. 3.18**, showing that the critical pressure required for the suppression of voids increases linearly with current density, i.e. the flux of Na to the interface is linearly dependent on the pressure. Based on the comparison of Na/Na-beta''-Alumina and Li/Li_6PS_5Cl cells, it appears that higher current densities are possible with Na anode, likely due to greater creep rate of Na.

In the study of Na/Na-beta''-Alumina cells, the electrochemical data showed similarities to

previous studies on Li/Li_6PS_5Cl cells[15], suggesting that void formation above critical stripping current density is a general phenomenon for all-solid-state batteries with metal anode, regardless of the species of electrolyte, and alkali metal. By investigating the functional relationship between critical pressure with current density, it has been confirmed that creep of the metal anode is the dominant way to maintain the interfacial contact. Thanks to the improved contrast between void and Na metal, the development of void formation during cycling has been revealed and quantitatively analysed. Deviated from the previous theory, void occlusion with a thin layer of Na is not the dominant way of Na deposition. Instead, plating was found to be able to fill most of the voids. However, the existing voids, though filled, will continue to serve as current hot-spots in the subsequent stripping, forming bigger voids, leading to more severe interfacial deterioration. By quantifying the areal ratio of contact loss at the interface, it is suggested that current constriction due to contact loss is the not the key factor in voltage polarisation. The Na-depletion inside the Na anode near the interface would be expected to play a role, as this would hinder the diffusion of Na to the interface, and in consequence increase the interfacial impedance.

3.3.4 Dynamic voiding and interfacial protrusion in Li/Li_3N/Li cell

Whilst *in-situ* lab-based X-ray computed tomography scans have been used to track of the evolution of void formation during plating and stripping, the dynamics of void initiation and growth has never been revealed, as it required a much higher temporal resolution to track the changes within a single stripping. Moreover, while Na anode could provide better contrast with voids, allowing quantitative analysis, Li anode is always preferred against Na anode, for the inherent advantage of much greater capacity. To ensure sufficient contrast between Li anode and voids, as well as sufficient time resolution to conduct *operando* characterisation, synchrotron X-ray radiation with highly coherent beam and greater X-ray flux was employed for imaging. An experimental set-up based on a self-designed tube-cell was developed to optimise the imaging quality, as described in the Protocol section.

To avoid any potential effect from interfacial instability, Li_6PS_5Cl, which was widely used in previous studies as it forms a self-limiting interphase of a few nm with Li, has been replaced with Li_3N electrolyte, which is believed to be stable against Li metal as it forms no interphase. Li_3N pellets were prepared as described in the Protocol section, with both surfaces of the pellet polished to maximise the contact. In addition, due to the poor wettability between Li and Li_3N, thin Li metal layers of 500 nm were deposited to each side of the pellet using thermal evaporation to ensure interfacial contact, before a 50 μm thick Li anode was pressed onto the pellet as the anode.

Three-electrode electrochemical test was conducted, as for Li/Li_6PS_5Cl/Li and Na/Na-beta''-Alumina/Na cells, to test if the same voltage polarisation response to plating/stripping due to voiding applies to Li/Li_3N/Li cells. Due to the low conductivity of Li_3N electrolyte and rather poor wettability with Li metal, Li/Li_3N/Li cells only allow for cycling with much lower current density and capacity. Three-electrodes cells were assembled and cycled with the voltage measured between the working and reference electrodes, at current densities of 0.1, 0.2 mA cm^{-2}, capacity of 0.1 mAh cm^{-2}, under 3 MPa pressure, and at 0.2, 0.5 mA cm^{-2}, capacity of 0.1 mAh cm^{-2}, under 7 MPa, **Fig. 3.19**. The cells were assembled and tested by Gareth Hartley.

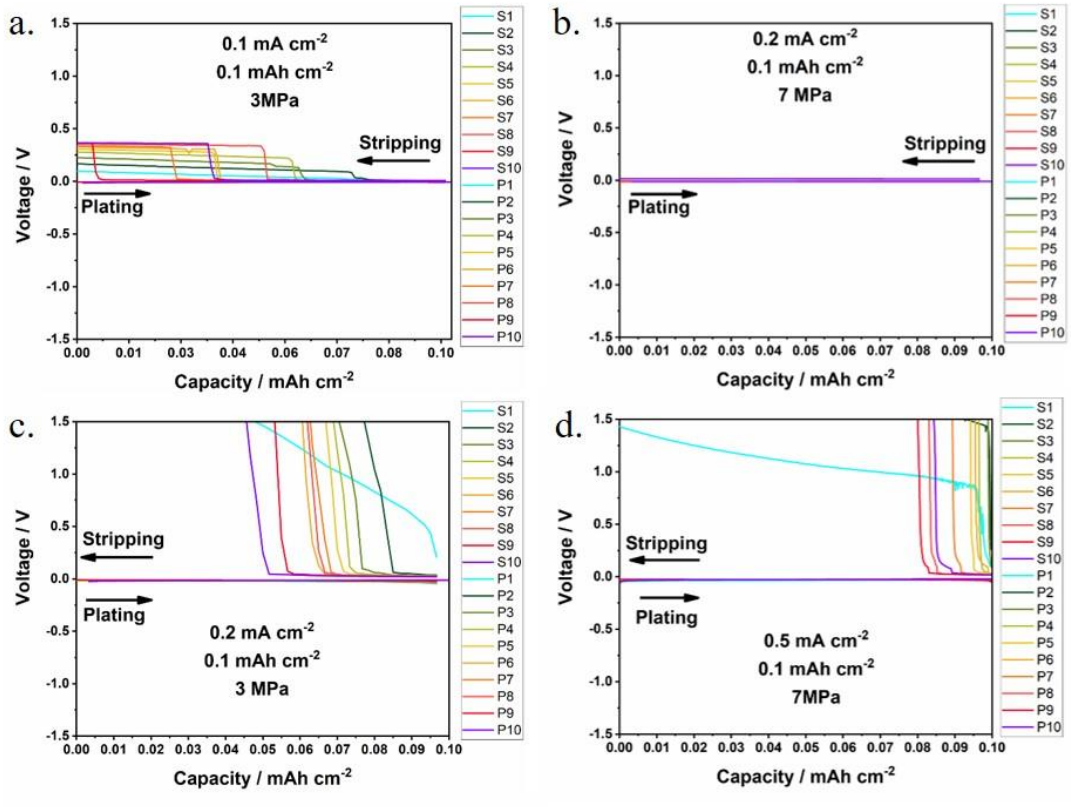

Fig. 3.19. Voltage measured between the working and reference electrodes when cycling at **a.** 3 MPa and 0.1 mA cm^{-2}, **b.** 7 MPa and 0.2 mA cm^{-2}, **c.** 3 MPa and 0.2 mA cm^{-2}, **d.** 7 MPa and 0.5 mA cm^{-2}. A capacity of 0.1 mAh cm^{-2} was passed for each plating/stripping. Cycling commenced with plating on the working electrode to maximise the interfacial contact. (Figure produced by Gareth Hartley).

Similar to previous studies on Li/Li_6PS_5Cl and Na/Na-beta''-Alumina cells, voltage polarisation during plating remains low and consistent and it recovers the interfacial contact by depositing lithium. Also, in good accord with previous studies, the voltage polarisation increases during stripping, as stripping creates voids at the interface, under insufficient stack pressure. The critical stripping current densities were also found to increase with stack pressure. However, due to the aforementioned drawbacks of Li_3N electrolyte, the CCS is much lower compared with Li_6PS_5Cl even with a reduced capacity (CCS $<$ 0.1 mA cm^{-2} at 3 MPa, and 0.2 mA cm^{-2} $<$ CCS $<$ 0.5 mA cm^{-2} at 7 MPa).

Despite all the similarities in voltage response, how voltage polarisation evolves in Li/Li_3N cells is different from Li/Li_6PS_5Cl and Na/Na-beta''-Alumina cells. As shown in **Fig. 3.19b** & **d**, stripping at a current density above the CCS results in a remarkable increase in voltage polarisation since the 1st stripping. In the subsequent cycles, a low-voltage plateau can always be observed at the start of each stripping, as the voids are occluded during plating, and therefore, it requires a small amount of capacity to strip off the thin layer of Li that occludes the void and expose the void to the interface. As cycling continues, the voids grow in size, leading to more severe interfacial deterioration, thus less capacity is needed to expose the voids, so a shorter low-voltage plateau is expected as the number of cycles increases. However, the opposite was observed in Li/Li_3N cells, i.e. the low-voltage plateaus were extended as the number of cycles increased.

To unveil the origin of such difference, synchrotron X-ray computed tomography was employed to characterise the plated interface and stripped interface of a Li/Li_3N/Li before and after half a cycle, with a high current density of 1.2 mA cm^{-2}, and a low pressure of 3 MPa to ensure the formation of voids. Before cycling, intimate interfacial contact can be seen at both interfaces, in accord with a low cell impedance at pristine, **Fig. 3.20c** & **d**. After half a cycle, virtual cross-sectional image slices from the same places are compared to nail down the effect of plating and stripping on interfacial morphology. As it is shown in **Fig. 3.20e**, the plated interface remains unchanged from pristine. As an intimate contact has been obtained by thermal evaporating Li at pristine, no further interfacial recovery takes place. However, considerable interfacial contact loss due to the formation of voids is observed on the stripped electrode, **Fig. 3.20f**, leading to a significant increase in cell impedance, **Fig. 3.20b**. Protrusion of a secondary phase is also observed underneath the voids, which is not present at the pristine state.

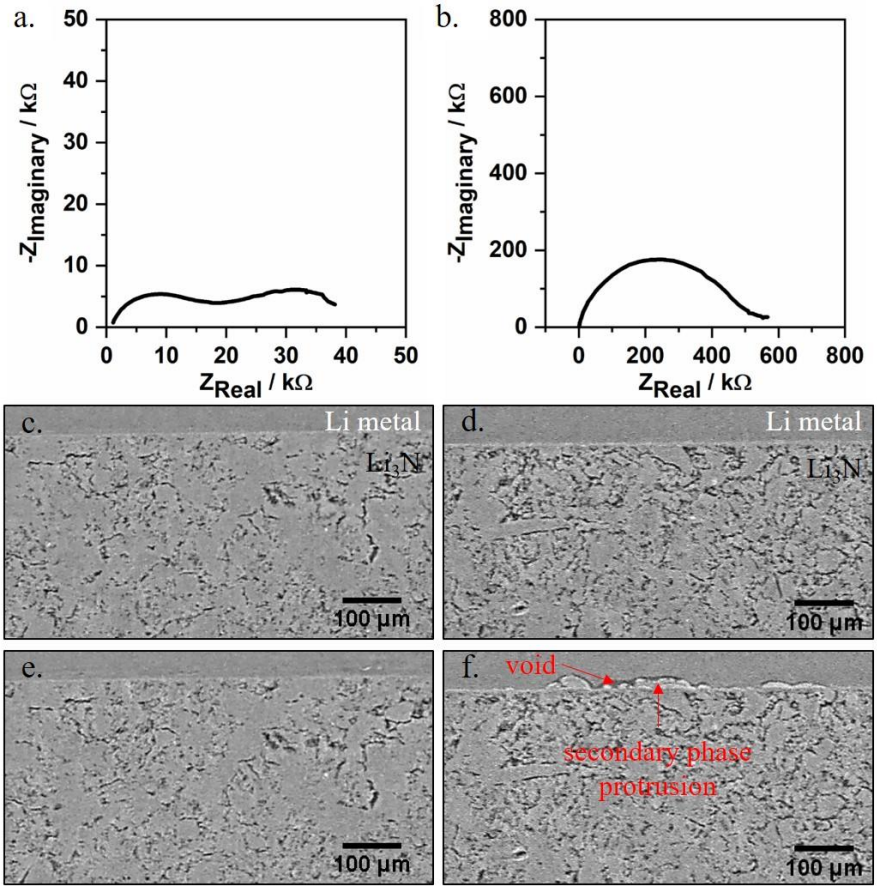

Fig. 3.20. Nyquist EIS plot of Li/Li_3N/Li cells **a.** at pristine **b.** after galvanostatic charge at 1.2 mA cm^{-2}, for 1.5 mAh cm^{-2} under 3 MPa pressure. Corresponding virtual cross-sectional images from X-ray computed tomography perpendicular to the Li/Li_3N interfaces, showing **c.** pristine interface before plating, **d.** pristine interface before stripping, **e.** plated interface after plating, **f.** stripped interface after stripping.

Given that all the interfacial changes are affiliated with stripping, the dynamic changes occurring at the interface undergoing stripping were imaged in real-time with *in-operando* X-ray computed tomography. X-ray computed tomography scans were taken at the pristine state and during the charge of the cell, resulting in a temporal resolution of 2.5 min/scan (0.05 mAh cm^{-2} of charge passed between every two scans). The voltage response during charge and the corresponding XCT scans are shown below in **Fig. 3.21**. As the interface shown in the image remained largely unchanged after 1.10 mAh cm^{-2} of charge passed, scans taken from 1.10 mAh cm^{-2} to 1.50 mAh cm^{-2} are removed.

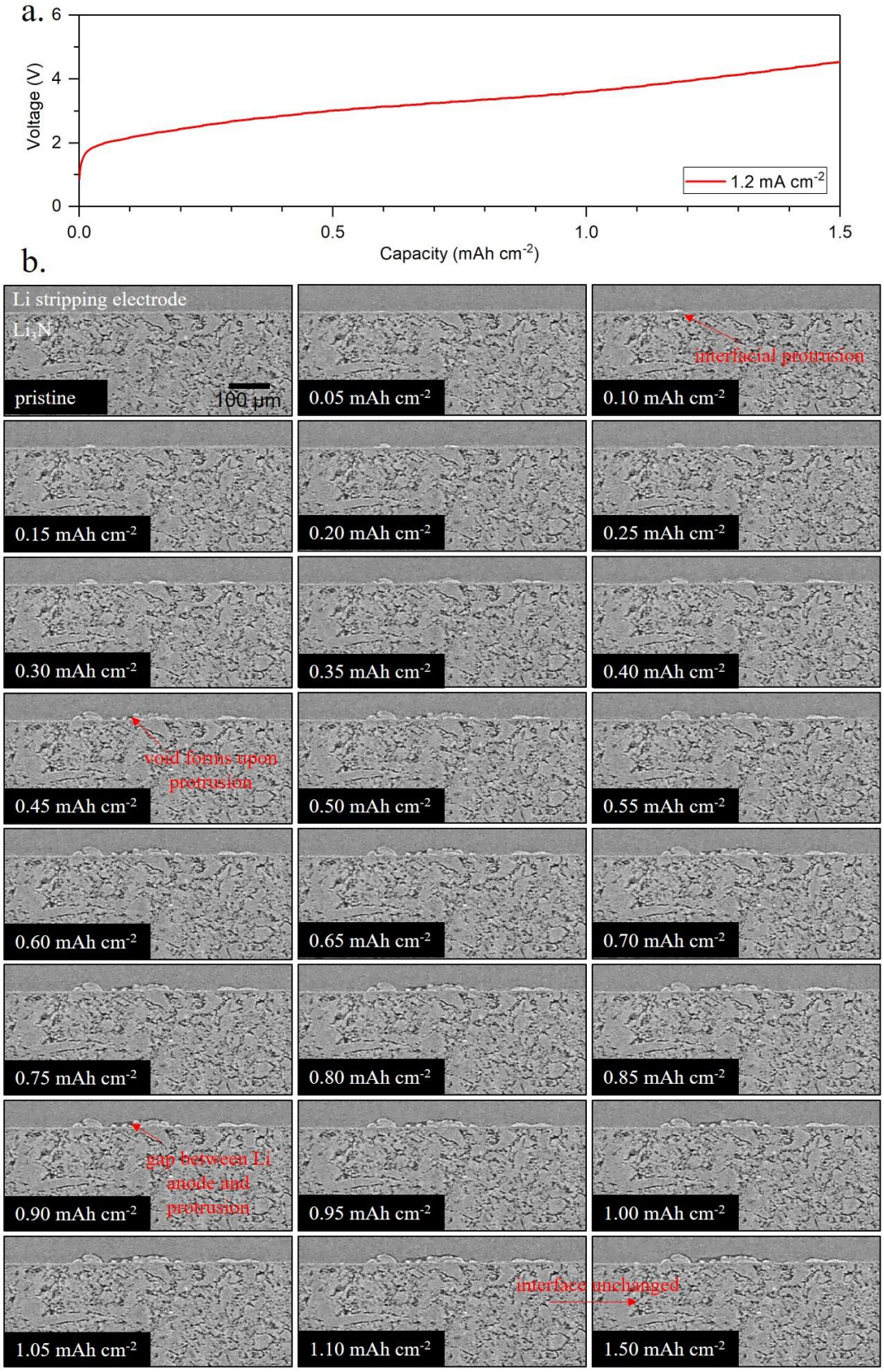

Fig. 3.21. *Operando* X-ray computed tomography of a Li/Li_3N/Li during galvanostatic charge at a current density of 1.2 mA cm^{-2} and a capacity of 1.5 mAh cm^{-2}. **a.** Voltage versus charge

passed for the galvanostatic operation. **b.** Virtual cross-sectional image slices from operando XCT scans showing the evolution of stripping interface with charge passed.

Due to the low conductivity of Li_3N electrolyte, a voltage bias of 0.87 V was generated as soon as passing a large current of 1.2 mA cm^{-2}. The voltage polarisation then gradually increased with charge from 0.87 V to 4.53 V, due to the interfacial deterioration. Interestingly, at the beginning of polarisation increase (pristine to 0.05 mAh cm^{-2}), no void formation was observed at the interface in our region of interest, suggesting the polarisation originated either from voiding in other regions, or from the Li-depletion in the Li anode near the interface. As more charge passed, and voltage polarisation increased, instead of voiding, an interfacial protrusion of a secondary phase, which presented similar grayscale to Li_3N (similar electron density to Li_3N) was revealed at the interphase. A continuous growth of the interfacial protrusion can be observed with more charge passed (0.10 mAh cm^{-2} to 0.45 mAh cm^{-2}). The shape of the interfacial protrusion remained constant after 0.45 mAh cm^{-2} of charge passed, instead, voiding started to occur preferentially between the interfacial protrusion and Li anode. The voids thickened and widened as more charge passed, leading to complete contact loss between the interfacial protrusion and Li anode, in accord with the continuous increase in voltage polarisation (0.45 mAh cm^{-2} to 1.10 mAh cm^{-2}). Later, despite the continuous increase in voltage polarisation, the interface in the region of interest remained unchanged.

It is worth noting that voids were hardly observed in regions without interfacial protrusion; instead, voiding preferentially occurs upon interfacial protrusion, suggesting different properties of the secondary phase from the bulk Li_3N electrolyte, **Fig. 3.21b**. As Li was stripped at a higher rate in proximity to the secondary phase, it is proposed that the secondary phase might have higher ionic conductivity than Li_3N, or worse wettability against Li metal, so the formation of voids required lower energy compared with the Li/Li_3N interface. In addition, while Li_3N was believed to be stable against Li, as no product could be formed, Li_3N was predicted to be stable against Li only in the electrochemical potential range from 0 V to 0.66 V[20], where the product of potential reaction was not discussed or examined. Further

characterisation, such as glancing incidence XRD needs to be conducted in the future to figure out the composition of interfacial protrusion.

The phenomenon of interfacial protrusion is not limited to Li/Li_3N/Li cells due to any unique property of Li_3N; instead, it has also been observed in the *in-situ* lab-based X-ray computed tomography scans of Li/Li_6PS_5Cl/Li cells, **Fig. 3.22**. While intimate contact with the flat interface can be seen at pristine, interfacial protrusion was clearly observed after the 3rd stripping. After the 5th stripping, remarkable contact loss was shown between the Li anode and the interfacial protrusion, suggesting similar properties of the interfacial protrusion to the secondary phase observed in Li/Li_3N/Li cells. Li_6PS_5Cl was reported to be kinetically stable against Li anode, by forming a self-limiting interphase of only a few nm. Nevertheless, the observed interfacial protrusion was formed with a much greater thickness than a few nm. It is hypothesised that the interfacial protrusion is in essence a meta-stable phase formed between Li and Li_6PS_5Cl, which is more Li-rich than Li_6PS_5Cl, thus more conductive, and more favoured by Li stripping. Therefore, once the interfacial protrusion formed, it served as the hot-spots of current densities, and helped initiate voiding during stripping, leading to interfacial deterioration.

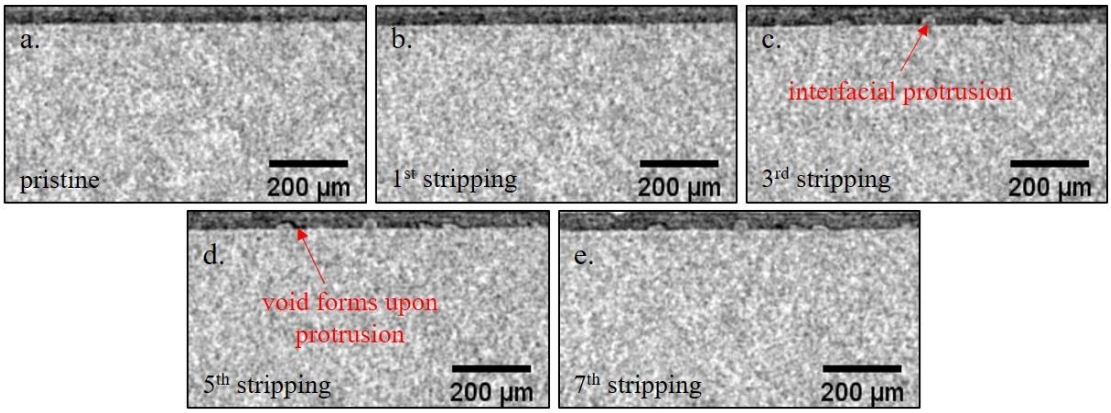

Fig. 3.22. Virtual cross-section image slices from *in-situ* lab-based XCT scans of a Li/Li_6PS_5Cl/Li cell **a.** at pristine, **b.** after the 1st stripping, **c.** after the 3rd stripping, **d.** after the 5th stripping, and **e.** after the 7th stripping.

To better illustrate the role of interfacial protrusion and its relation to void formation, a modified model of interfacial protrusion and voiding is proposed as shown in **Fig. 3.23**. Instead of attributing the formation of voids merely to the flux of Li replenished to the interface being overwhelmed by Li stripping, interfacial protrusion of a secondary phase has been introduced in this model to reform the current density distribution. Secondary phase forms due to the pre-existing current density hot-spots, thus higher electrochemical potential, and leads to preferred Li stripping and eventually voiding due to its different property from the bulk electrolyte. Once the void forms and accumulates, local contact loss can lead to enhanced local current density and in consequence dendrite initiation, in the same way as mentioned in the previously proposed model.

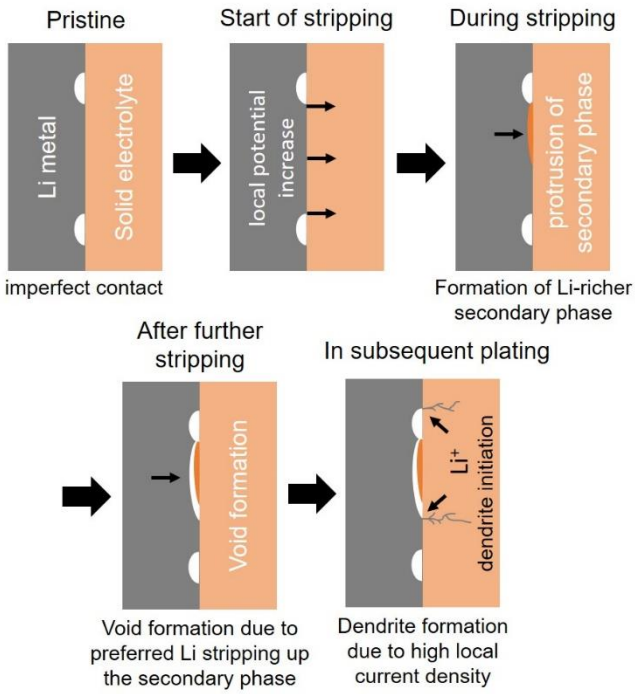

Fig. 3.23. Schematic of the Li metal/SE interface cycled at an overall current density above the CCS. Sequence from pristine to after stripping and plating of Li metal: imperfect contact at pristine leads to interfacial protrusion forms on stripping, due to higher local potential. Due to the different property of interfacial protrusion, voids preferentially form and accumulate upon the interfacial protrusion. The contact loss on stripping results in high local current density in subsequent plating, and consequentially dendrites on plating.

The findings of interfacial protrusion in Li/Li_3N/Li and Li/Li_6PS_5Cl/Li cells highlight the importance of interfacial chemistry in viable electrochemical cycling. While Li_3N and Li_6PS_5Cl were both considered to be promising electrolyte materials for Li anode due to their stability, decompositions of both electrolytes were observed on stripping. Moreover, the product of decomposition was found to serve as preferential sites for voiding, which directly leads to further interfacial deterioration of the cell. As the properties of the decomposition product could be different from the bulk electrolyte, it is not necessary for the interfacial protrusion to be as thick as being observed in order to serve as a current density hot-spot. It is likely that interfacial protrusion of much smaller thickness exists throughout the stripping interface, which are the underlying origin of current density hot-spots even if the physical contact between Li and SE was ideal. In this regard, all promising solid electrolyte materials should be carefully investigated for their stability against Li anode during electrochemical operation. As interfacial decomposition leads to voiding, thus increase local current density, and eventually reduce the critical current density that the cell could be operated at, for any successful all-solid-state batteries, such interfacial degradation must be avoided.

3.4 Conclusions

The investigation on the process of stripping unveils the existence of a critical stripping current density, above which cycling leads to evolving interfacial deterioration and enhancement in local current density, and consequentially dendrite formation. These studies suggest that apart from Li plating, which directly leads to cell failure, interfacial degradation on stripping is equally important and needs to be fundamentally understood to enable the use of an energy dense alkali metal anode.

In these studies, the critical stripping current density has been systematically investigated based on three-electrode cells which can separate the effects of plating and stripping. While plating replenishes the voids, recover the interfacial contact, and reduce the cell polarisation, stripping above critical stripping current density leads to void formation, thus interfacial contact loss,

voltage polarisation, and eventually trigger dendrite formation in subsequent plating. The critical stripping current densities have been determined under various stack pressures and cycling temperature, suggesting effective strategies to improve the rate performance of all-solid-state batteries.

The formation of voids has been firstly confirmed by cross-sectional SEM, where impact from sectioning is unavoidable, given the compliant nature of alkali metal anode. Therefore, X-ray computed tomography has been employed to characterise voiding. Based on the self-developed *in-situ* set-up the void evolution and accumulation during cell cycling has been revealed for the first time. Then X-ray computed tomography has been optimised to provide further fundamental insights of Li stripping. With better spatial resolution and contrast from Na anode, the void evolution after every plating/stripping has been tracked and quantitatively analysed. Further development based on a customised tube-cell and synchrotron X-ray enables *operando* characterisation of void formation with improved spatial (1.625 μm/pixel) and temporal (2.5 min/scan) resolution. Interfacial protrusion, which leads to voiding and contact loss, has been visualised, highlighting the significant role of interfacial chemistry in stripping-related degradation.

Enabled by the *in-situ* characterisation of interfacial degradation in all-solid-state batteries, the importance of stripping-induced degradation in cell failure has been addressed. Void formation has been confirmed by characterisation as the origin of cell voltage polarisation, and form of interfacial degradation. With the effect of cycling conditions on voiding investigated, and role of interfacial chemistry unveiled, these studies suggest promising strategies to achieve sustainable stripping, leaving dendrite formation on plating the only challenge remaining in utilising alkali metal anode in all-solid-state batteries.

3.5 References

1. Albertus, P., Babinec, S., Litzelman, S. & Newman, A. Status and challenges in enabling the lithium metal electrode for high-energy and low-cost rechargeable batteries. *Nat. Energy* **3**, 16–21 (2018).

2. Tsai, C. L. *et al.* $Li_7La_3Zr_2O_{12}$ Interface Modification for Li Dendrite Prevention. *ACS Appl. Mater. Interfaces* **8**, 10617–10626 (2016).

3. Ren, Y., Shen, Y., Lin, Y. & Nan, C. W. Direct observation of lithium dendrites inside garnet-type lithium-ion solid electrolyte. *Electrochem. commun.* **57**, 27–30 (2015).

4. Masias, A. *et al.* Fundamentals of Inorganic Solid State Electrolytes for Batteries. *Adv. Energy Mater.* **166**, 1–14 (2019).

5. Jow, T. R. & Liang, C. C. Interface Between Solid Electrode and Solid Electrolyte—A Study of the Li/LiI (Al_2O_3) Solid-Electrolyte System. *J. Electrochem. Soc.* **130**, 737–740 (1983).

6. Hongahally Basappa, R., Ito, T. & Yamada, H. Contact between Garnet-Type Solid Electrolyte and Lithium Metal Anode: Influence on Charge Transfer Resistance and Short Circuit Prevention. *J. Electrochem. Soc.* **164**, 666–671 (2017).

7. Koshikawa, H. *et al.* Dynamic changes in charge-transfer resistance at Li metal/$Li_7La_3Zr_2O_{12}$ interfaces during electrochemical Li dissolution/deposition cycles. *J. Power Sources* **376**, 147–151 (2018).

8. Manalastas, W. *et al.* Mechanical failure of garnet electrolytes during Li electrodeposition observed by in-operando microscopy. *J. Power Sources* **412**, 287–293 (2019).

9. Yonemoto, F. *et al.* Temperature effects on cycling stability of Li plating/stripping on Ta-doped $Li_7La_3Zr_2O_{12}$. *J. Power Sources* **343**, 207–215 (2017).

10. Krauskopf, T., Hartmann, H., Zeier, W. G. & Janek, J. Toward a Fundamental Understanding of the Lithium Metal Anode in Solid-State Batteries - An Electrochemo-Mechanical Study on the Garnet-Type Solid Electrolyte $Li_{6.25}Al_{0.25}La_3Zr_2O_{12}$. *ACS Appl. Mater. Interfaces* **11**, 14463–14477 (2019).

11. Krauskopf, T. *et al.* Lithium Metal Growth Kinetics on LLZO Garnet Type Solid Electrolytes – Operando Study of Lithium Deposition and Dendrite Growth. *Joule* **3**, 1–20 (2019).

12. Wang, M. J., Choudhury, R. & Sakamoto, J. Characterizing the Li-Solid-Electrolyte Interface Dynamics as a Function of Stack Pressure and Current Density. *Joule* **3**, 2165–2178 (2019).

13. Wu, M.-S., Chiang, P.-C. J. & Lin, J.-C. Electrochemical Investigations on Advanced Lithium-Ion Batteries by Three-Electrode Measurements. *J. Electrochem. Soc.* **152**, A47 (2005).

14. Ender, M., Illig, J. & Ivers-Tiffée, E. Three-Electrode Setups for Lithium-Ion Batteries. *J. Electrochem. Soc.* **164**, A71–A79 (2017).

15. Kasemchainan, J. *et al.* Critical stripping current leads to dendrite formation on plating in lithium anode solid electrolyte cells. *Nat. Mater.* **18**, 1105–1111 (2019).

16. Spencer Jolly, D. *et al.* Sodium/Na-β″-Alumina Interface: Effect of Pressure on Voids. *ACS Appl. Mater. Interfaces* **12**, 678–685 (2020).

17. Yu, C., van Eijck, L., Ganapathy, S. & Wagemaker, M. Synthesis, structure and electrochemical performance of the argyrodite Li_6PS_5Cl solid electrolyte for Li-ion solid state batteries. *Electrochim. Acta* **215**, 93–99 (2016).

18. Wenzel, S., Sedlmaier, S. J., Dietrich, C., Zeier, W. G. & Janek, J. Interfacial reactivity and interphase growth of argyrodite solid electrolytes at lithium metal electrodes. *Solid State Ionics* **318**, 102–112 (2018).

19. Wenzel, S. *et al.* Interfacial Reactivity Benchmarking of the Sodium Ion Conductors Na_3PS_4 and Sodium β-Alumina for Protected Sodium Metal Anodes and Sodium All-Solid-State Batteries. *ACS Appl. Mater. Interfaces* **8**, 28216–28224 (2016).

20. Zhu, Y., He, X. & Mo, Y. Origin of Outstanding Stability in the Lithium Solid Electrolyte Materials: Insights from Thermodynamic Analyses Based on First-Principles Calculations. *ACS Appl. Mater. Interfaces* **7**, 23685–23693 (2015).

21. LePage, W. S. *et al.* Lithium mechanics: Roles of strain rate and temperature and implications for lithium metal batteries. *J. Electrochem. Soc.* **166**, A89–A97 (2019).

22. Haas, R. *et al.* Practical Implications of Using a Solid Electrolyte in Batteries with a Sodium Anode: A Combined X-Ray Tomography and Model-Based Study. *Energy Technol.* **7**, 1801146 (2019).

23. Sharafi, A. *et al.* Surface Chemistry Mechanism of Ultra-Low Interfacial Resistance in the Solid-State Electrolyte $Li_7La_3Zr_2O_{12}$. *Chem. Mater* **29**, 20 (2017).

24. Yonemoto, F. *et al.* Temperature effects on cycling stability of Li plating/stripping on Ta-doped $Li_7La_3Zr_2O_{12}$. *J. Power Sources* **343**, 207–215 (2017).

25. Krauskopf, T., Hartmann, H., Zeier, W. G. & Janek, J. Toward a Fundamental Understanding of the Lithium Metal Anode in Solid-State Batteries - An Electrochemo-Mechanical Study on the Garnet-Type Solid Electrolyte $Li_{6.25}Al_{0.25}La_3Zr_2O_{12}$. *ACS Appl. Mater. Interfaces* **11**, 14463–14477 (2019).

Chapter 4. Visualising Plating-Induced Cracking in All-Solid-State Batteries

Abstract

Lithium dendrite (filament) propagation through ceramic electrolytes, leading to short-circuits at high rates of charge, is one of the greatest barriers to realising high energy density all-solid-state lithium anode batteries. Utilising *in-situ* X-ray computed tomography coupled with spatially mapped X-ray diffraction, the propagation of cracks and the propagation of lithium dendrites through the solid electrolyte have been tracked in a Li/Li_6PS_5Cl/Li cell as a function of the charge passed. On plating, cracking initiates with spallation, conical "pothole"-like cracks that form in the ceramic electrolyte near the surface with the plated electrode. The spallations form predominantly at the lithium electrode edges where local fields are high. Transverse cracks then propagate from the spallations across the electrolyte from the plated to the stripped electrode. Lithium ingress drives the propagation of the spallation and transverse cracks by widening the crack from the rear, i.e. the crack front propagates ahead of the Li. As a result, cracks traverse the entire electrolyte before the Li arrives at the other electrode and therefore before a short-circuit occurs.

4.1 Introduction

The inability to plate lithium metal on charging at practical current densities without the metal penetrating the ceramic electrolyte and leading to a short-circuit is one of the greatest barriers to progress for all-solid-state batteries[1–15]. Previous work has shown that dendrite growth through polymer electrolytes is suppressed if the electrolyte has a sufficiently high shear modulus[16,17]. However, ceramics with orders of magnitude higher shear moduli than lithium do

not suppress dendrite growth, demonstrating that the mechanism for dendrite penetration through ceramics is different from that through polymers and is as yet not well understood.

While *Ex-situ* and destructive methods such as scanning electron microscopy have proved valuable in demonstrating the problem[18–21], it is important to follow the development of cracks and the ingress of lithium metal into the ceramic during operation of the cell in order to understand the mechanism of dendrite penetration and cell failure. Optical microscopy has been used for *in-situ* studies. However, it is challenging to characterise dendrites buried inside the solid electrolyte[22–24]. X-ray computed tomography (XCT) carried out during all-solid-state battery operation has imaged the evolution of interfacial voids and has been used to follow the growth of reactive interphase layers when Li is contacted with $Li_{1+x}Al_xGe_{2-x}(PO4)_3$ (LAGP), where the growing interphase results in electrolyte cracking[25–30].

In this study, *in-situ* XCT with high spatial resolution and phase-contrast was used combined with spatially mapped X-ray diffraction, which enables the following of progression of cracks and the progression of the lithium ingress as a function of charge passed in cells composed of argyrodite solid electrolyte (Li_6PS_5Cl) sandwiched between two lithium metal electrodes. This sulphur-based electrolyte is a strong candidate for all-solid-state batteries and is a useful model system because it combines high conductivity with the ability to form a stabilising solid electrolyte interface (SEI) of a few nm in contact with lithium metal[31–35].

By tracking *in-situ* both lithium ingress and crack propagation into the ceramic, it is shown that the crack front propagates well ahead of metallic lithium in the crack. On plating lithium, spallations (conical “pothole”-like cracks) form in the electrolyte adjacent to the plated electrode. The spallation crack propagates towards the plated electrode surface along a path where porosity is above the average of the ceramic. They are also more prevalent at the edges of the lithium electrode due to higher local field and current density. Transverse cracks emanate from the spallations and propagate across the electrolyte, forming a path between the plated and stripped electrodes. Lithium ingress drives the propagation of the spallation and transverse

cracks by widening the crack from the rear, i.e. the crack front propagates ahead of the Li and Li is not at the crack tip. Only later when lithium plates along the entire crack does the cell finally short circuit.

4.2 Protocol

4.2.1 Electrolyte preparation

All procedures were performed inside an Ar-filled glovebox (O_2 and H_2O levels < 1 ppm). Li_2S, P_2S_5, and LiCl (Sigma-Aldrich) were ground together in the ratio corresponding to the stoichiometry of Li_6PS_5Cl. 1 g of such powder was then loaded into a ZrO_2 ball-mill jar with 50 g of 10-mm-diameter ZrO_2 balls. Two such sealed jars were removed from the glove box and placed in a Fritsch PULVERISETTE 7 premium line Planetary Micro Mill and ball-milled at 600 r.p.m. for 14 h. The ball-milled powder was returned to the glove box and pressed into a disc with a 5-mm-diameter stainless steel die set under a uniaxial load of 1 t. The disc was placed onto graphite foil inside a preheated furnace at 600 °C (also in the glove box), then left to cool to room temperature at 5 °C/min. The disc was ground with a mortar and pestle, pressed into a 5-mm-diameter disc at a uniaxial load of 1 t, and heated inside the furnace at 300 °C for 15 min. The sintered electrolyte disc was cooled to room temperature and used to assemble the cells.

4.2.2 Powder X-ray diffraction

Powder X-ray diffraction was carried out using a Rigaku Miniflex X-ray diffractometer with Cu $K_{\alpha 1}$ radiation inside an N_2-filled glovebox, with O_2 and H_2O levels < 1 ppm.

4.2.3 Li/Li_6PS_5Cl/Li symmetric cell assembly and cycling

Metallic lithium foil of 50 µm thick was punched into two 2-mm-diameter disc-shaped lithium electrodes, and pressed onto both sides of a sintered Li_6PS_5Cl disc. An insulating polymer ring was placed around the lithium to constrain and define the footprint of the lithium electrodes. All galvanostatic cycling was performed using a Gamry Reference 600+ potentiostat, with cells controlled under a defined stack-pressure. High current densities and resultant high overpotentials were used to initiate dendrite growth and electrolyte cracking.

4.2.4 Cross-sectional SEM

The two-electrode cells were cross-sectioned using an ultrasonic cutter with a tungsten carbide blade (SONOTEC) inside an Ar-filled glovebox. The cross-sectioned cells were mounted onto a custom-made holder with Cu adhesive tape and transferred into a Zeiss Merlin scanning electron microscope using an airtight transfer device (Gatan).

4.2.5 *In-situ* phase-contrast synchrotron X-ray CT

X-ray tomograms were recorded at the TOMCAT beamline at the Swiss Light Source, Paul Scherrer Institute. The beam was monochromatized to 35 keV. Images were collected with a PCO Edge 5.5 sCMOS camera combined with an optical microscope with a x4 magnification, leading to a pixel size of 1.63 µm and a field of view of 4.2 × 3.5 mm^2. The conversion from X-ray to visible light was achieved with a LuAG:CE 100 µm thick scintillator. The detector was placed at 350 mm from the sample, in order to work in propagation-based phase contrast. Exposure time was set to 200 ms. For each tomogram, 3570 equiangularly distributed projections were taken over 180° as well as 30 darks and 50 flats before and after the tomography scan. The projections were reconstructed using the Paganin phase retrieval method[36] and Gridrec reconstruction routines developed at the beamline[37].

X-ray tomograms were obtained at pristine, and after each step of electrochemical operation, where the electrochemical charge/discharge was paused to avoid possible image blurring due to morphological changes during tomogram collection.

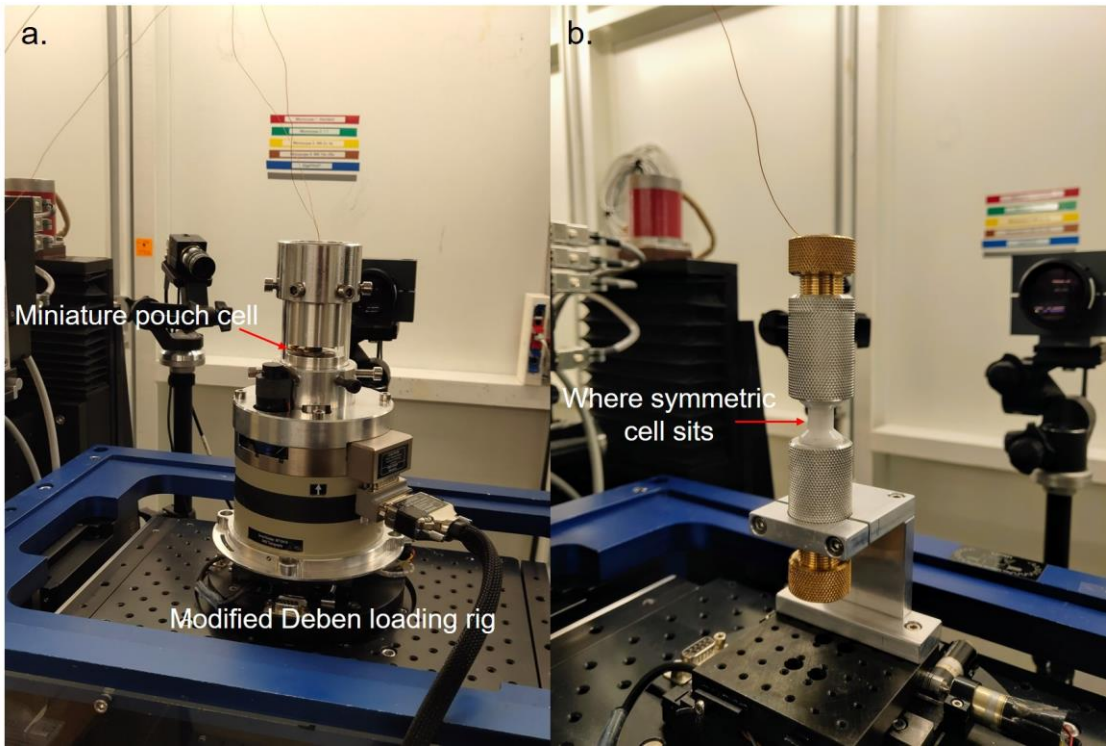

Fig. 4.1. Two types of experimental set-up for phase-contrast synchrotron X-ray computed tomography. a. Miniature pouch cell with static pressure applied by modified Deben loading rig. **b.** Customised tube-cell mounted on the sample stage in TOMCAT.

For X-ray CT scans to reveal the spallation and electrolyte cracking after every charge/discharge, a miniature two-electrode pouch cell was assembled and placed inside a modified Deben loading rig for the precise control of stack pressure, **Fig. 4.1a**. The modification of the Deben rig is for easier sample mounting and weight reduction of the whole set-up, so it is compatible with the sample stage in TOMCAT. For X-ray CT scans to reveal the evolution of electrolyte cracking and dendrite penetration, a customised tube-cell was employed for cell cycling, which maintained air-tightness and pressure control, **Fig. 4.1b**. The sample was fixed at the middle of the Acetal(polyoxymethylene) tube, which allowed X-ray to transmit through, and optimised the imaging quality of phase-contrast X-ray computed tomography.

4.2.6 *In-situ* Synchrotron X-ray CT-diffraction mapping

The *in-situ* Synchrotron X-ray CT-diffraction mapping measurements were conducted at the I12 X-ray imaging and diffraction beamline, at the Diamond Light Source. The sample was mounted onto the sample stage with the incident X-ray perpendicular to the electrode. The tomogram was recorded at a monochromatic beam energy of 54 keV. For the tomogram, 2900 equiangularly distributed projections were taken over 180°, with the resulting voxel size of 3.24 μm and field of view of 8.0 × 7.0 mm^2. After the CT scan, the imaging detector was exchanged for a 2D area diffraction detector without moving the sample. Diffraction in transmission was then performed with the same monochromatic 54 keV beam, reduced by slits to a spot size of 100 × 100 μm^2 to map an area of 4 × 4 mm^2 with no overlap (a 40 × 40 matrix centred at the centre of lithium electrode). The diffraction data were analysed using the DAWN platform.

4.2.7 Analysis of grayscale in the crack

The grayscale values across the cracks were measured along a line perpendicular to the crack to confirm a continuous grayscale. Grayscale analysis was only taken where the crack is sufficiently wide (narrowest > 7 voxels) (1.63 μm/voxel and resolution 2× voxel size), to avoid potential effects from the surrounding electrolyte, and to ensure reliable detection of lithium.

The grayscale values inside the crack at different regions (**Fig. 4.11f**) were measured and averaged along a 15-pixel line at the centre of the crack, parallel to the edge of the crack. The standard deviations of the grayscale values are given as error bars in the figure.

4.2.8 Electrochemical impedance spectroscopy measurements

Electrochemical impedance spectroscopy (EIS) was performed on two-electrode cells at a voltage perturbation of 10 mV, in a frequency range from 0.1 MHz to 0.1 Hz using a Gamry Reference 600+ potentiostat. The data were analysed using the ZView software package.

4.2.9 Analysis of Pore Volumetric Density

The analysis of pore volumetric density was conducted using Avizo Fire (ThermoFisher Scientific). The pore volumetric density of bulk electrolyte was calculated by greyscale segmentation of the pores in a cube of 500 × 500 × 500 voxels (815 × 815 × 815 μm^3), with the pores below 3 × 3 × 3 voxels (4.89 × 4.89 × 4.89 μm^3) filtered out, and dividing the total volume of pores by the volume of the 500 × 500 × 500 voxel cube. The pore volumetric density along the spallation crack was calculated by segmenting out the pores which pre-existed in the pristine electrolyte and were crossed by the spallation crack after 1st plating, with the pores below 3 × 3 × 3 voxels filtered out, and dividing the total volume of pores by the volume of the spallation cracking region.

4.2.10 *Ex-Situ* X-ray CT

The *ex-situ* X-ray CT scans on a cycled Na/Na-beta''-alumina symmetric cell (**Fig. 4.4**) and a cycled Li/Li_3N symmetric cell (**Fig. 4.5**) were obtained with a Zeiss Xradia Versa 510 X-ray computed tomography microscope. For the Na/Na-beta''-alumina symmetric cell, the tomogram was recorded at 120 kV accelerating voltage (current of 84 µA), with 3201 equiangularly distributed projections over 360°, resulting in a voxel size of 4.67 µm and field of view of 9.37 × 9.56 mm^2. For the Li/Li_3N symmetric cell, the tomogram was recorded at 40 kV accelerating voltage (current of 74 µA), with 1601 equiangularly distributed projections over 360°, resulting in a voxel size of 3.85 µm and field of view of 3.81 × 3.89 mm^2.

4.2.11 Digital volume correlation analysis

The DVC analysis was conducted via DaVis (LaVision) on the *in-situ* X-ray computed tomograms to reveal the displacement and strain change in the Li_6PS_5Cl during cycling. A rectangular region at the centre of the pellet has been cropped out for DVC analysis. A multi-pass scheme was used for direct correlation by sub-volumes of 128^3, 64^3, 32^3, 24^3 and 16^3 voxels, with a 75% overlap. Strains were calculated based on the local gradient of displacement, and

shown in the colour scale based on their magnitude. Displacement profile along the red arrow was obtained by collecting X-direction component of the displacement along the arrow, and processed in MATLAB.

4.3 Results and Discussions

4.3.1 Spallation in the ceramic electrolyte at the interface with the plated lithium electrode

A two-electrode symmetric Li/Li_6PS_5Cl/Li cell was assembled without exposure to air and was mounted in the synchrotron XCT beamline with the stack pressure controlled by a Deben loading rig. Galvanostatic cycling was performed under a compression of 7 MPa at a current density of 1.25 mA cm^{-2} for a capacity of 0.5 mAh cm^{-2}, **Fig. 4.2**. High current density was used to ensure Li dendrite formation and electrolyte cracking during cycling. XCT image slices were acquired along planes parallel to, and 5 pixels (8.15 μm) from, the two Li/solid electrolyte interfaces, **Fig. 4.2b**; the positions of the image slices in **Fig. 4.2b** are indicated by the red and blue arrows on the virtual cross-sectional image slice in **Fig. 4.2c(i)**. The light grey discs at the centre of the XCT scans in **Fig. 4.2b** are manually superimposed onto the image slices to mark the position of the lithium electrodes. Images were collected before cycling, after the first half cycle and after successive full cycles. The cycling commenced with plating (lithium deposition) occurring at the interface shown in **Fig. 4.2b(i)** and with stripping occurring at the interface shown in **Fig. 4.2b(ii)**. Before cycling, there was no evidence of cracks pre-existing in the electrolyte in the proximity of either interface with lithium, **Fig. 4.2b (i)** & **(ii)**. After one half cycle, the interface that underwent stripping remained largely unchanged, **Fig. 4.2b(iv)**; whereas cracks were clearly observed in the solid electrolyte adjacent to the electrode interface which underwent plating, **Fig. 4.2b(iii)**. The cracks observed in the ceramic, in the proximity of the plated electrode, were more prevalent close to the edge of the lithium electrode as

compared with the central region. As the formation of these cracks was observed to be a plating-induced phenomenon, the study is focused on the first-plated electrode for observation of the evolution of the process during subsequent cycles. Image slices, adjacent to the electrode which was plated first, are shown in **Fig. 4.2b** after the **(v)** 2nd, **(vi)** 3rd, **(vii)**, 4th, and **(viii)** 5th plating steps. Similar cracks of larger quantity and dimensions were observed to arise with each successive cycle, while the edge-preferred distribution of the cracks remained apparent. A gradual decrease in the magnitude of cell polarization, starting from the second cycle, was seen during cycling, **Fig. 4.2a**, and voltage spikes were detected on the 2nd and 3rd charge, indicating lithium ingress into ceramic electrolytes[38,39].

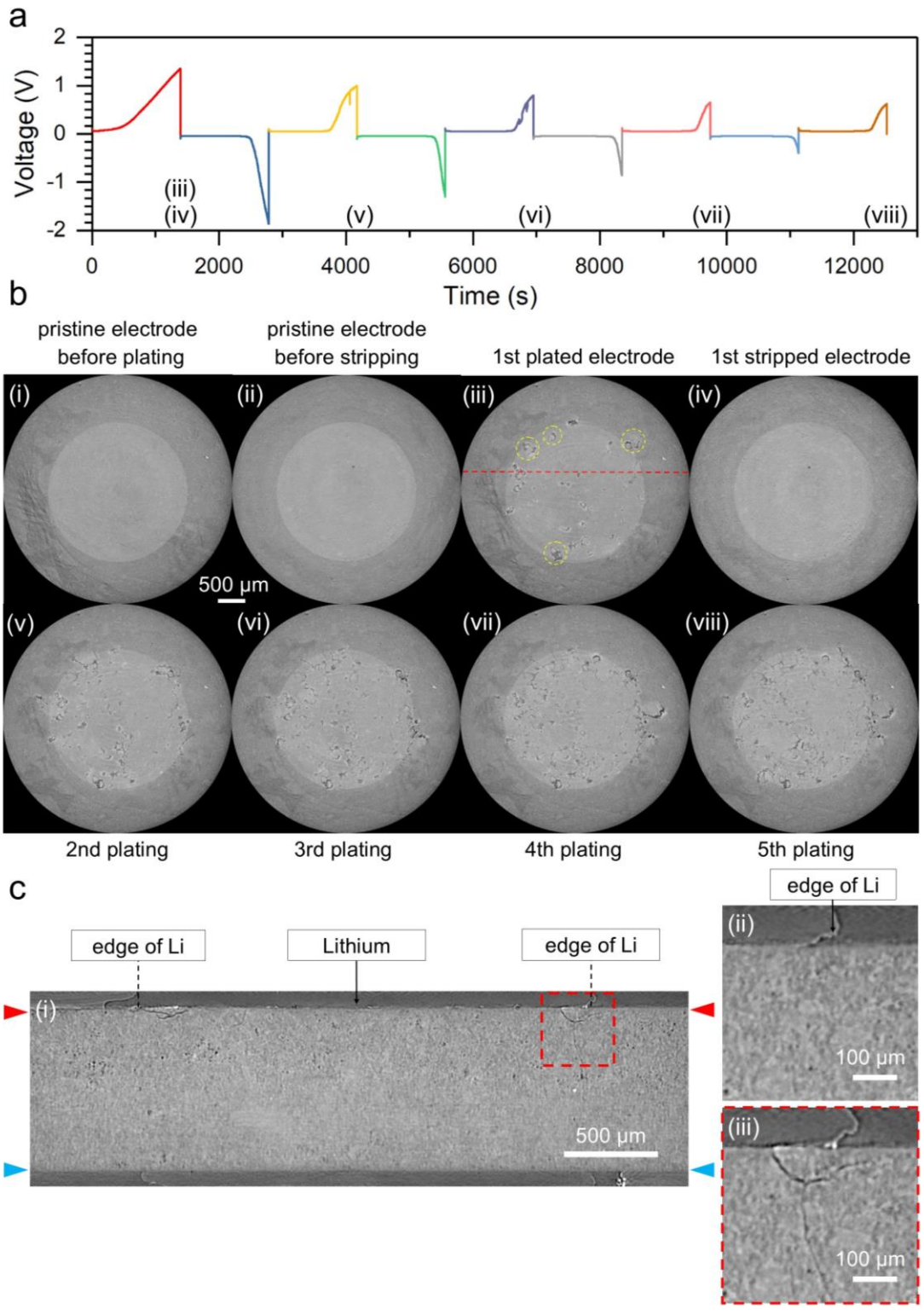

Fig. 4.2. *In-situ* phase-contrast X-ray CT of a Li/Li_6PS_5Cl/Li cell showing lithium plating-induced spallation. a. voltage versus time for the symmetric Li/Li_6PS_5Cl/Li cell cycled at 7 MPa, 1.25 mA cm^{-2}, with a capacity of 0.5 mAh cm^{-2}. Each colour represents half a cycle. The numbers correspond to the different stages of cycling at which X-ray CT scans shown in **b (iii)**

to **(viii)** were collected. **b**. virtual image slices taken along planes parallel to and at 5 pixels (8.15 μm) beneath each lithium electrode (positions indicated by red and blue arrows in c.). **(i)** and **(ii)** are slices taken at the electrodes to be **(i)** plated and **(ii)** stripped, before passing a current; **(iii)** plated interface and **(iv)** stripped interface, after the first half cycle; **(v)** to **(viii)** show the evolution of the 1st interface to be plated, after successive cycles. Light grey discs were manually superimposed onto the virtual image slices to mark the position of lithium electrodes. **c**. **(i)** cross-sectional image slice along the red dashed line in **b(iii)** reveals the spallations at the edge of the lithium electrode. **(ii)** A magnified image from the cross-sectional image slice of the pristine cell at the position of **c(iii)**, showing no pre-existing defects. **(iii)** A magnified image shows a vertical crack under spallation, indicating correlation between spallation and vertical cracking. The wave like feature on the right-hand side of the Li electrode corresponds to the edge of Li metal where it contacts with the polymer insulating ring used to constrain and define the footprint of the Li electrode.

To understand how these cracks affect the impedance of the cell, electrochemical impedance spectroscopy (EIS) was conducted on the pristine cell and after every plating of the first plated electrode, **Fig. 4.3**. The EIS data demonstrates a gradual decrease in cell impedance as the number of these cracks increases, providing evidence that lithium ingresses into these cracks, increasing the contact area between lithium and the ceramic electrolyte.

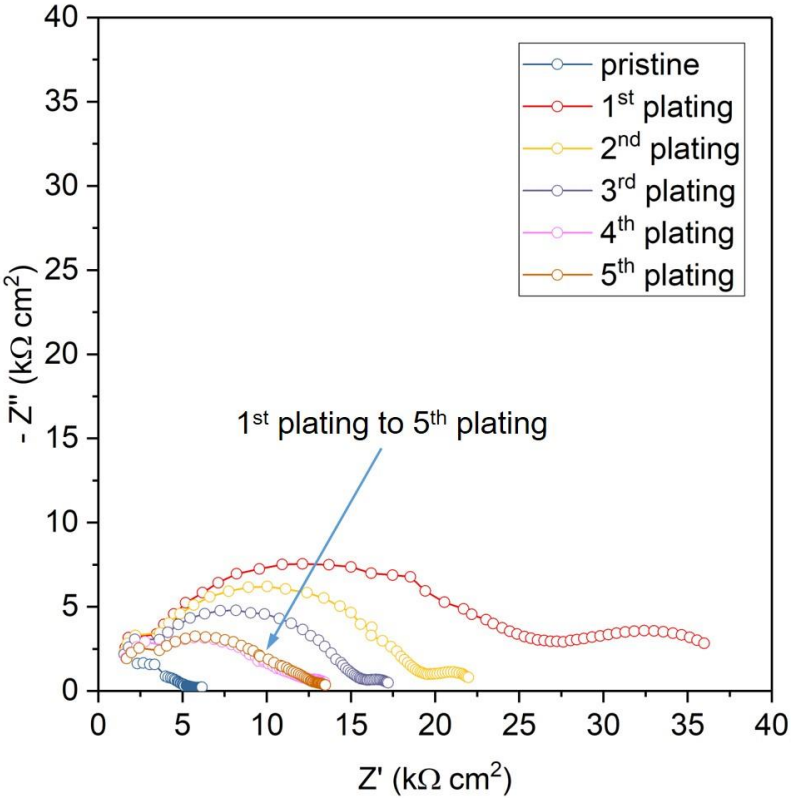

Fig. 4.3. The impedance of the cell measured at pristine, and after the 1st, 2nd, 3rd, 4th, and 5th plating of the initially plated electrode. The impedance increases significantly after 1st plating due to void formation at the initially stripped electrode; and decreases gradually in the subsequent cycles as the number of spallations increases, until reaching a steady state after the 4th plating.

A virtual cross-sectional image slice of the cell, **Fig. 4.2c(i)**, was taken orthogonal to the Li/Li_6PS_5Cl interface at the position indicated by the dashed red line in **Fig. 4.2b(iii)**. The virtual cross-sectional image shows that the cracks near the plated electrode are cone-shaped sections of electrolyte that have become largely detached from the bulk electrolyte. In the case of the crack highlighted in **Fig. 4.2c** it is in the region of 100 microns into the electrolyte. Due to their geometric similarity to pothole-like spallation cracks observed in surface damage of concrete and other brittle ceramics, the features formed are termed, *spallations*. The virtual cross-sectional images in **Fig. 4.2c(i)** and **(iii)**, reinforce the preference for spallations at the edges of the lithium electrode. On the virtual cross-sectional slice, **Fig. 4.2c(iii)**, a vertical crack

can be seen to propagate from underneath the spallation, which suggests a correlation between spallation and vertical cracking. A magnified image from the cross-sectional image slice of the pristine cell was taken at the same position of **c(iii)**, showing no pre-existing defects, **Fig. 4.2c(ii)**.

It should be noted that spallations are not limited to Li/Li_6PS_5Cl cells; they are also observed in cycled Na/Na-beta''-Alumina cells, **Fig. 4.4**, and in cycled Li/Li_3N cells, **Fig. 4.5**. Li_3N and Na-beta''-Alumina have been shown to be chemically unreactive with their respective anodes, thus the formation of spallation and vertical cracks do not rely on the formation of an interphase layer[40,41].

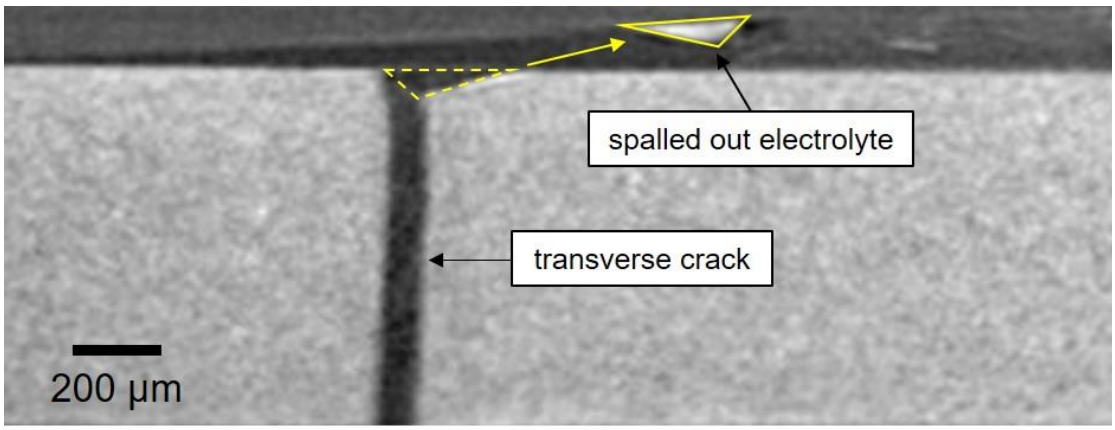

Fig. 4.4. Virtual cross-sectional image slice from *ex-situ* X-ray CT on a cycled Na/Na-beta''-Alumina/Na symmetric cell. It clearly reveals a piece of electrolyte (cone-shaped piece) completely spalled out from the bulk electrolyte, and a transverse crack propagation underneath the spallation.

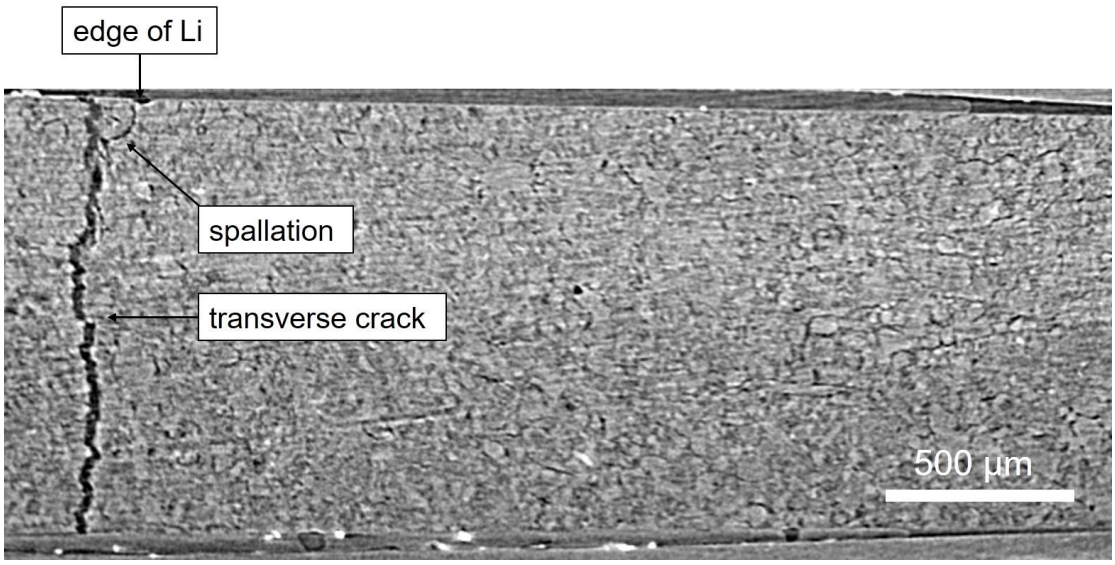

Fig. 4.5. Virtual cross-sectional image slice from *ex-situ* XCT scan of a cycled Li/Li_3N/Li symmetric cell. A spallation and associated transverse crack propagation were observed at the edge of the lithium electrode.

Furthermore, virtual cross-sectional images of a different spallation show cracking initiating in the Li_6PS_5Cl electrolyte ~20 µm below the surface with the plated electrode (**Fig. 4.6**). The SEI layer that forms at the Li/ Li_6PS_5Cl interface self-limits at a few nm[33], a very different length scale from the spallations. These cracks are therefore unlike those observed in LAGP, where the interphase layer grows continuously across the electrolyte and cracking has been attributed to the associated strain. Li_6PS_5Cl, Li_3N and Na-beta''-Alumina are very different electrolytes and yet share the same behaviour, suggesting that spallation is a general phenomenon in solid-state batteries with metallic electrodes. *Ex-situ* SEM carried out on a (physically) cross-sectioned, cycled Li/Li_6PS_5Cl/Li cell confirmed the presence of spallation features (**Fig. 4.7.**).

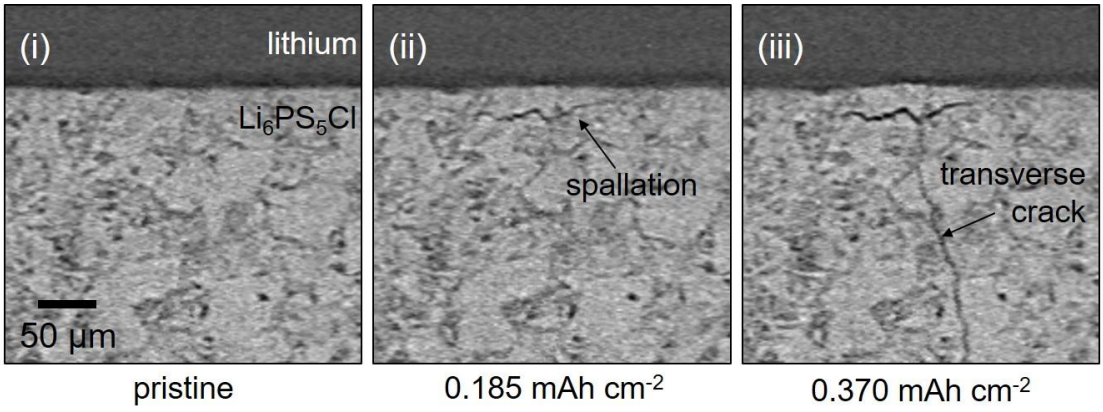

Fig. 4.6. ***In-situ*** **X-ray CT virtual cross-sections from a different region during a single plating of a Li/Li_6PS_5Cl/Li cell showing the early stages of spallation formation.** Virtual cross-sectional image slices of **(i)** the pristine cell and after **(ii)** 0.185 mAh cm^{-2}, **(iii)** 0.370 mAh cm^{-2} of charge passed.

Further PFIB-SEM has been conducted with Junfu Bu's assistance to better reveal the morphology of spallation, avoiding any damage on fracture surface from ultrasonic sectioning, **Fig. 4.8**. Apart from showing the clear shape of spallation, the PFIB-SEM also clearly shows the deposited lithium inside the spallation crack, and lithium extrusion from the spallation crack to the interface.

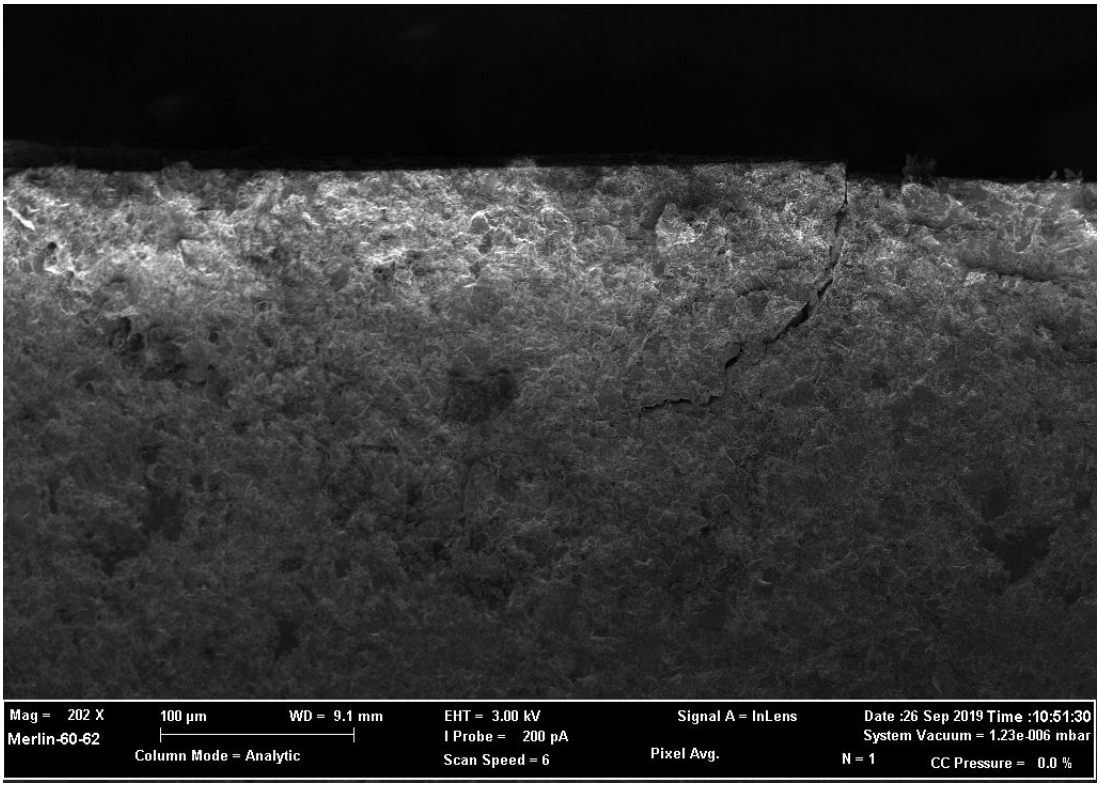

Fig. 4.7. SEM cross-section showing spallation within Li_6PS_5Cl electrolyte.

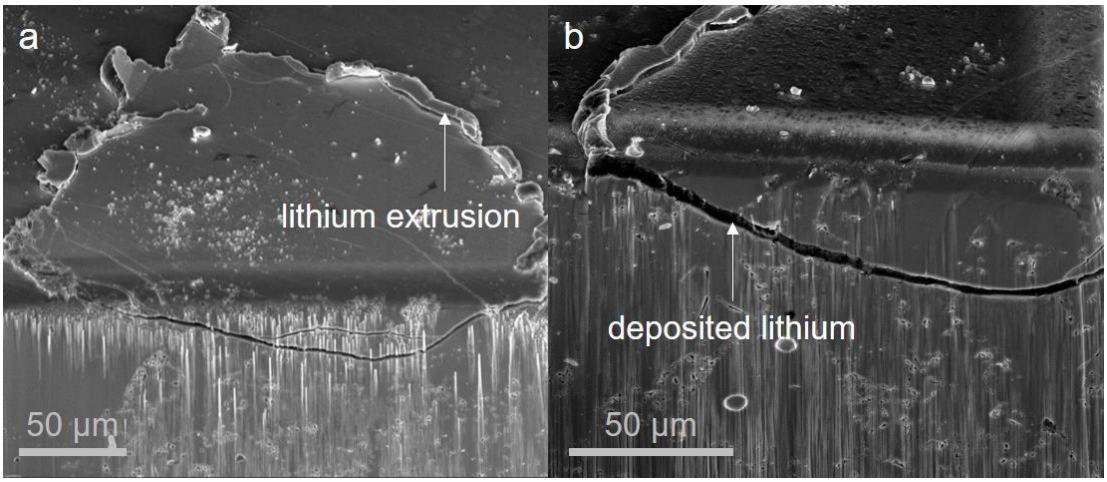

Fig. 4.8. PFIB-SEM cross-section showing spallation and Li within Li_6PS_5Cl electrolyte. **a.** SEM showing the shape and dimension of spallation, lithium metal extrusion can be seen near the edge of spallation. **b.** SEM showing lithium deposition inside the spallation crack.

The spallation crack formation and in particular the response of the crack to plating and stripping, was followed in more detail by digital volume correlation (DVC). DVC tracks the

changes in the position of sub-volumes of the images by comparing the *in-situ* phase-contrast XCT scans of the pristine and cycled cells. The DVC generates a 3D displacement field from the movement of the sub-volumes. A strain field is then obtained by calculating the gradient of the displacement field[42].

The maximum 3D strain at each point on the image slice adjacent and parallel to the plated electrode is shown in **Fig. 4.9**, the colour represents the intensity of the strain at each point. Hot spots of positive strain are seen as lithium deposition results in the spalling-out (detachment) of the electrolyte and the spallation crack widens. Positive strains are most prevalent around the edge of electrode after plating in areas where spallations exist or newly emerge. Such positive strains reduced as lithium was stripped back. With cycling there is a net accumulation of strain and spallation cracks, **Fig. 4.9**.

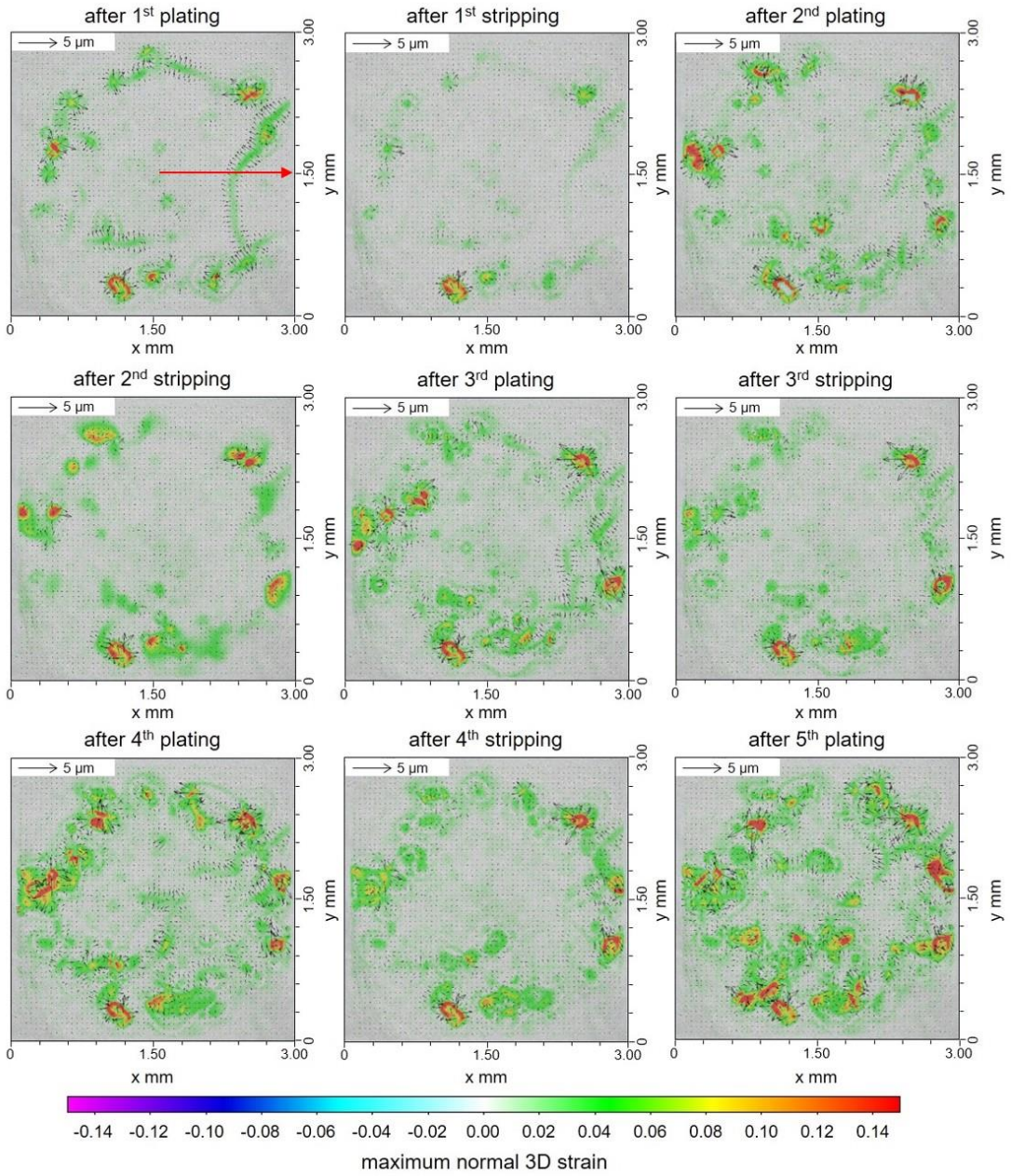

Fig. 4.9. Images from a plane parallel and adjacent to the plated electrode showing the maps of maximum normal 3D strain at each point on the plane (colour map) and displacement (arrows) of the electrolyte at different stages of cycling, obtained from digital volume correlation (DVC) analysis of the *in-situ* synchrotron X-ray CT scans.

In order to quantify the displacement change inside the electrolyte that is induced by lithium plating and stripping, the displacement profiles in X direction along the line of the red arrow (shown in 1st plating in **Fig. 4.9**) and the corresponding virtual cross-sectional image slices from

X-ray CT along the arrow are presented in **Fig. 4.10**. When spallation or transverse cracking occurs inside the electrolyte, a step change in displacement at the corresponding position can be seen in the displacement profile. Apart from the formation of new cracks, the plot also shows how the displacements change across the existing crack during Li plating and stripping i.e. displacement increases with Li plating and decreases with Li stripping. This is due to the crack opening, which widens with Li deposition, and crack narrowing when the deposited lithium is stripped out. Lithium deposition can also be clearly observed inside the crack, which pushes the spalled-out electrolyte upwards. This suggests that existing cracks inside the sample remain active during cell cycling, and can develop or propagate further with further Li deposition. Apart from tracking the morphological changes of solid electrolyte during cycling, it is also important to track how a dendrite forms and develops during the process of charge. Phase-contrast X-ray CT is therefore conducted to track the crack propagation and Li penetration within the process of a single charge.

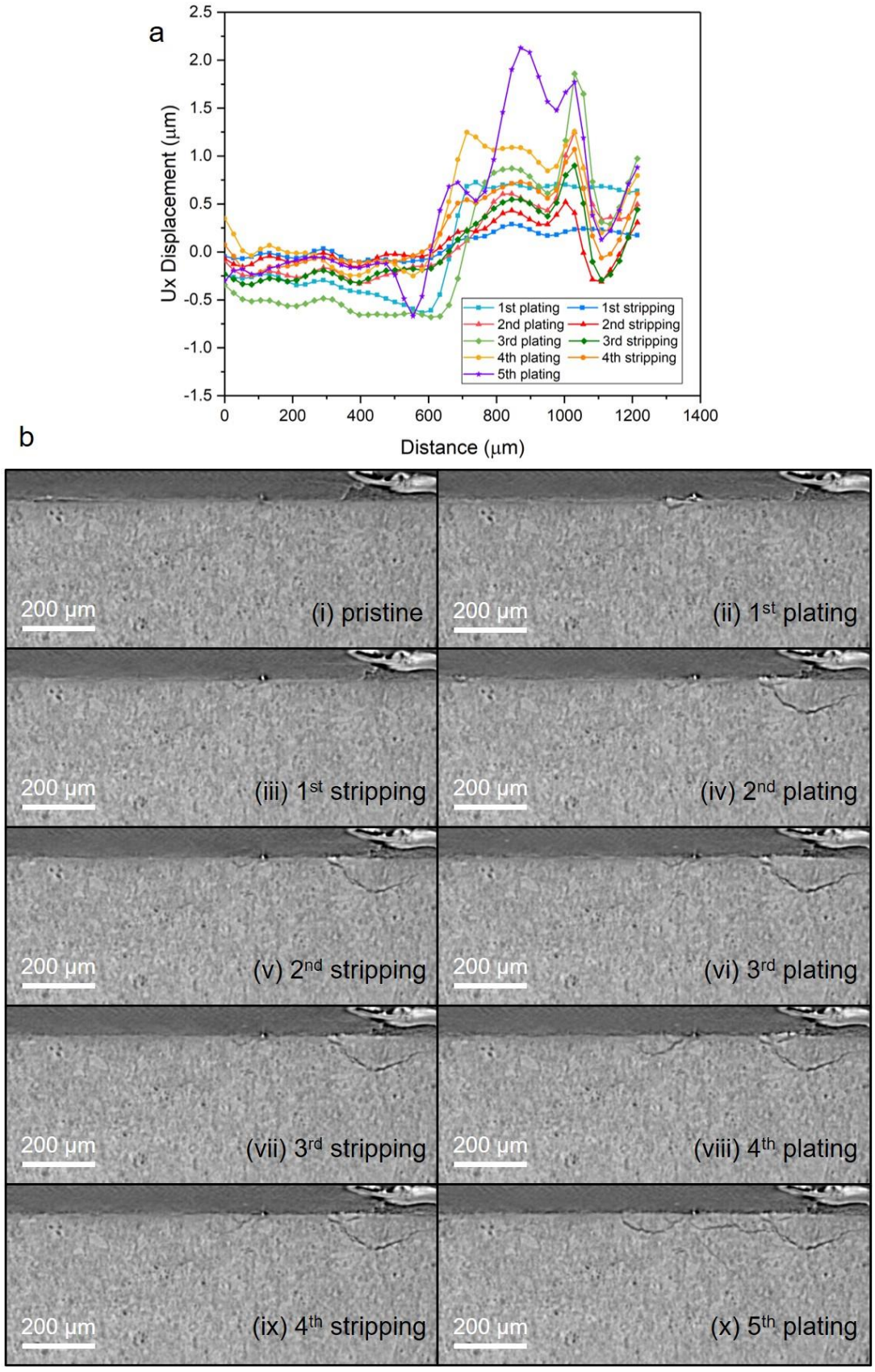

Fig. 4.10. Displacement profiles along the red arrow shown in Fig. 4.9 and corresponding virtual cross-sectional images slices from XCT at the along the red arrow. a. Displacement

profiles at different stages of cycling labelled with different colours, with each step change in displacement suggesting a new crack formation or crack widening. **b.** Virtual cross-sectional image slices from XCT at **(i)** pristine, and after **(ii)**1st plating, **(iii)**1st stripping, **(iv)**2nd plating, **(v)** 2nd stripping, **(vi)**3rd plating, **(vii)**3rd stripping, **(viii)**4th plating, **(ix)**4th stripping, **(x)**5th plating.

4.3.2 Crack propagation and lithium penetration into the electrolyte during plating

As phase-contrast imaging with a highly coherent beam can effectively enhance the contrast of weakly attenuating materials[43,44], i.e. lithium, the deposited lithium can be reliably distinguished from the empty space created by crack propagation. In order to track the propagation of cracks and their relation to lithium propagation into the solid electrolyte during plating, further *in-situ* XCT was performed on a Li/Li_6PS_5Cl/Li cell as a function of the charge passed, **Fig. 4.11**. **Fig. 4.11a** shows a series of virtual cross-sectional image slices, taken from the same position in the cell: **(i)** before passing a current, and after plating with **(ii)** 0.2 mAh cm^{-2}, **(iii)** 0.4 mAh cm^{-2}, **(iv)** 0.6 mAh cm^{-2}, **(v)** 0.8 mAh cm^{-2}, and **(vi)** 1.0 mAh cm^{-2} of lithium. The greyscale intensity in the tomographic images depends on the electron density of the constituent atoms[45]; here, lighter grey corresponds to heavier atoms and black corresponds to empty space. **Fig. 4.11b** shows magnified images of the electrolyte region near the plated electrode where the crack develops. After passing 0.2 mAh cm^{-2} of charge, a crack forms in the solid electrolyte underneath the electrode (as can be seen in the top right of the image in **Fig. 4.11b(ii)**). After 0.4 mAh cm^{-2} of charge, a spallation becomes apparent. In addition, the formation of a crack perpendicular to the electrode is observed (vertical crack), which with increasing charge passed, advances towards the stripped (bottom) electrode. Both the spallation crack and the vertical crack lengthen and widen with increasing charge passed, **Fig. 4.11a** and **b (iii)** to **(vi)**. After 0.8 mAh cm^{-2}, the vertical crack propagates through the entire thickness of the Li_6PS_5Cl disc and reaches the stripped electrode at the bottom. The voltage of the cell as a function of charge passed is shown in **Fig. 4.11c**. There is no evidence of a short-circuit. The

absence of a short-circuit, even after the passage of 1.0 mAh cm^{-2} of charge, implies that lithium did not propagate across the solid electrolyte, despite the crack having done so.

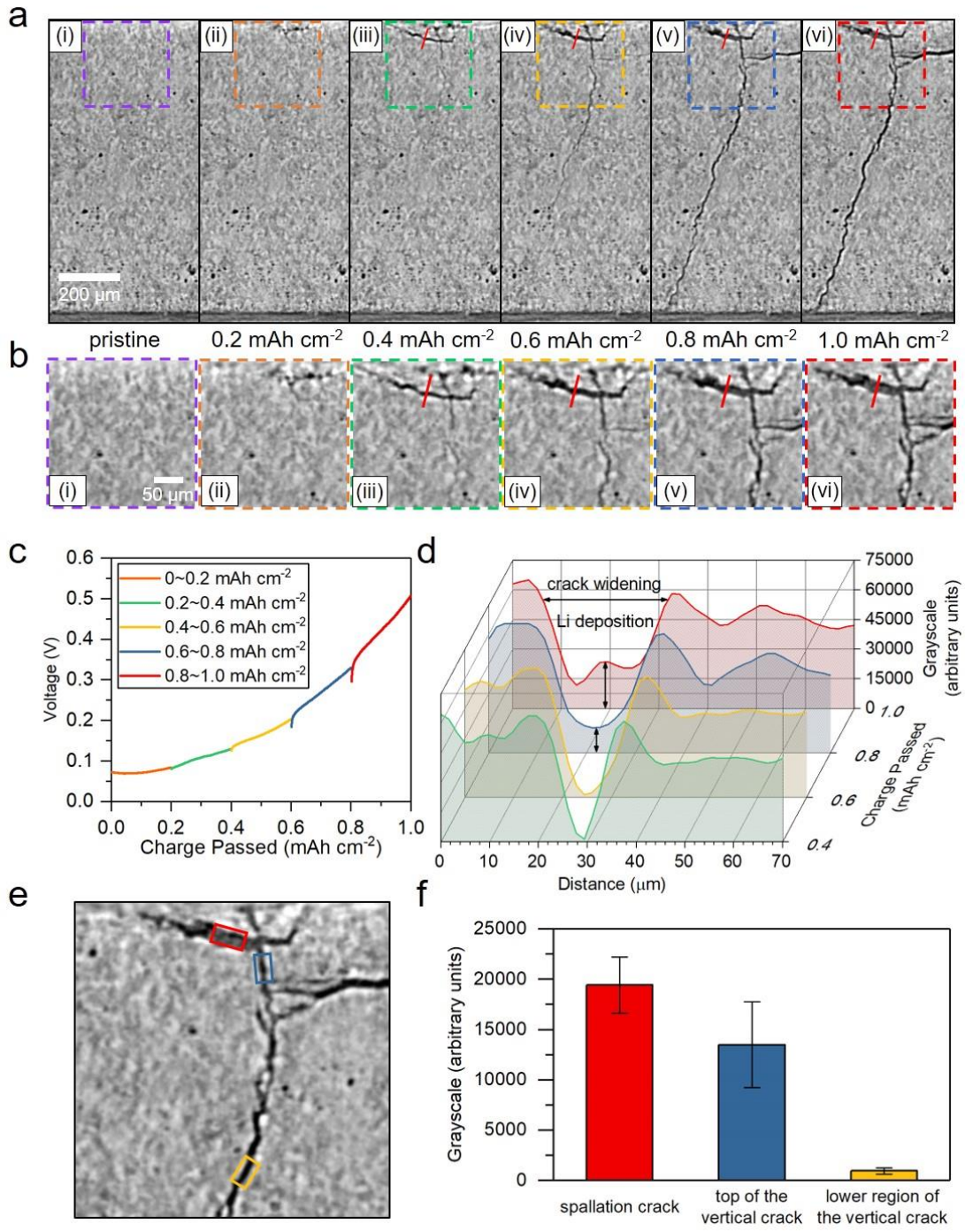

Fig. 4.11. *In-situ* phase-contrast X-ray CT virtual cross-sections during a single plating of a Li/Li_6PS_5Cl/Li cell and analysis of lithium deposition in the cracks showing that cracks propagate ahead of Li a. virtual cross-sectional image slices of **(i)** the pristine cell and after

(ii) 0.2 mAh cm^{-2}, **(iii)** 0.4 mAh cm^{-2}, **(iv)** 0.6 mAh cm^{-2}, **(v)** 0.8 mAh cm^{-2} and **(vi)** 1.0 mAh cm^{-2} of charge passed, plated electrode at the top. **b**. magnified images of the regions defined by the boxes in **a(i)** to **(vi)**. **c**. voltage versus charge passed showing increasing polarisation and no short-circuit (no sudden drop in voltage) even when the crack has propagated across the entire electrolyte. **d**. measured grayscale profiles across the crack at the region indicated by the red line in b. showing the accumulation of lithium inside the spallation crack during Li plating. **e**. magnified image from **a(vi)** showing where the grayscale values were determined for the spallation crack (red box) and different parts of the vertical crack (blue and yellow boxes) after passage of 1.0 mAh cm^{-2}. **f**. grayscale analysis showing the amount of lithium in the regions of the crack identified by the boxes after passage of 1.0 mAh cm^{-2}. The colours in the histogram plot correspond to the colours of the boxes in e. The error bars are determined as described in the Methods. There is no lithium in the lower region of the vertical crack (yellow) even after passage of 1.0 mAh cm^{-2} when the crack has formed across the entire electrolyte from plated to stripped electrode. Current density 1 mA cm^{-2}, cell pressure 1.5 MPa. The combination of a relatively low pressure and 1 mA cm^{-2} was employed because it was found to induce lithium penetration even in the 1st plating[29].

To study the propagation of lithium into the electrolyte, the grayscale intensity was examined in both the spallation and vertical cracks. As an empty crack presents near zero X-ray attenuation, the grayscale value increases with the amount of lithium within the image voxels that are in the crack. First, the extent of lithium ingress into the spallation crack was assessed by analysing the grayscale across the crack along the red line in **Fig. 4.11a** and **b (iii)** to **(vi)**. These results are shown in Fig. **4.11d**. With the passage of charge a gradual increase of attenuation is observed, which corresponds to increasing lithium deposition in the crack. The continuous grayscale inside the crack and the dynamic growth as more charge is passed excludes the possibility that the attenuating phase inside the crack is fragmented ceramic electrolyte, showing that it is indeed lithium deposition being observed. To examine lithium propagation along the vertical crack, the grayscale values were determined at the two regions

of the crack shown with blue and yellow boxes, and were compared with that of the spallation crack shown with the red box, **Fig. 4.11e**. The attenuation near the top of the vertical crack (blue box) and the lack of attenuation lower down the crack (yellow box), confirm that although the crack has propagated across the whole electrolyte after passage of 1.0 mAh cm^{-2}, only the top of the vertical crack, close to the plated electrode, is occupied by lithium, **Fig. 4.11f**. In addition, continuous grayscale analysis was conducted from inside the vertical crack to inside the spallation crack, showing a continuous increase in the average attenuation coefficient towards the plated electrode, showing that lithium is propagating along the crack, **Fig. 4.12**.

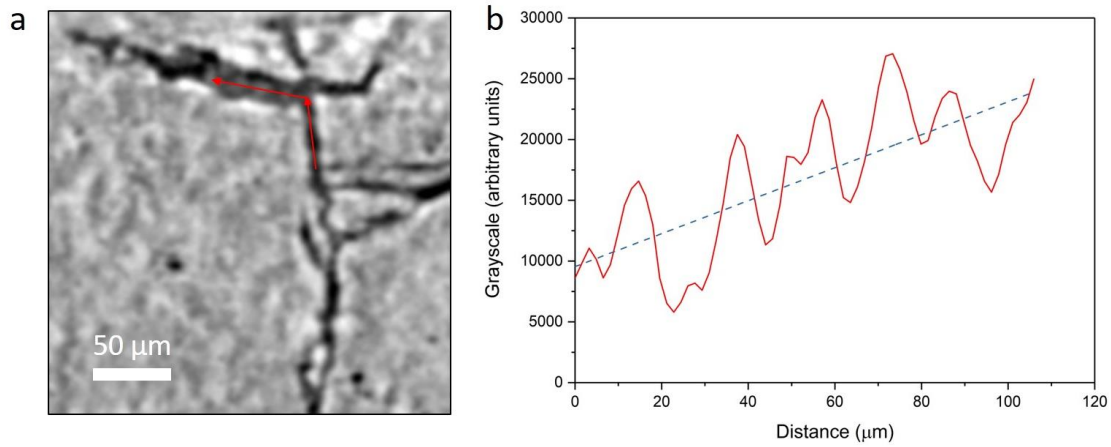

Fig. 4.12. Continuous grayscale line profile of lithium from inside the vertical crack to inside the spallation crack, showing an increase in the average attenuation coefficient when moving towards the plated electrode. a. magnified virtual cross-sectional image slice of the cell, after 1.0 mAh cm^{-2} of charge passed. The position and direction of the grayscale line profile are shown (red arrows). **b.** measured grayscale profile of lithium inside the crack along the red arrows (red curve), linear fitting of the grayscale profile (blue dashed line), showing the average attenuation coefficient increases vertically towards the plated electrode.

Overall, the grayscale analysis shows that after 0.8 mAh cm^{-2} lithium is filling the spallation crack and that after 1.0 mAh cm^{-2} there is lithium only at the top of the vertical crack, yet the crack has traversed the entire electrolyte between the two electrodes. Lithium ingress (dendrites)

drives the formation and propagation of spallation and transverse cracking in the solid electrolyte, and crucially from far behind the crack tip. Lithium ingress partially fills the crack widening it and leading to crack propagation ahead of the Li. In other words, Li drives crack propagation from the rear not at the crack tip. The transverse crack reached the other electrode before the Li, only later does the Li arrive and causes short-circuit.

3D image rendering was employed to visualise the crack propagation and lithium ingress in all directions as charge was passed, **Fig. 4.13**. The results are presented by mapping the colour scale from grey to green, where grey represents regions with low X-ray attenuation (empty crack) and green lithium. Li ingress into the solid electrolyte leads to the formation of spallations near the top of the image (plated electrode) after the passage of 0.2 mAh cm^{-2} of charge, **Fig. 4.13a**. After 0.4 mAh cm^{-2} of charge, spallations proliferate and cracks propagate perpendicular to the plated electrode, emanating from below the spallation, **Fig. 4.13b**. After 0.4 mAh cm^{-2} of charge Li is confined to the top of the cracks. **Fig. 4.13c** shows that after 0.6 mAh cm^{-2} of charge, the vertical cracks propagate further and there is increased deposition of lithium inside the spallation cracks. **Fig. 4.13d** and **e** demonstrate that after 0.8 and 1.0 mAh cm^{-2} the vertical crack propagates all the way to the stripped (bottom) electrode but there is no evidence of lithium at or near the crack tip, the Li is still confined to the rear (top) of the crack even after 1.0 mAh cm^{-2}. These results show that both the spallation and the subsequent vertical crack that propagates across the electrolyte propagate well ahead of the lithium ingress. This observation is contrary to the predictions of most modelling work that cracks only propagate when fully filled with lithium metal[46–50]. As such, these findings considerably narrow the possible mechanisms for dendrite growth through ceramic electrolytes.

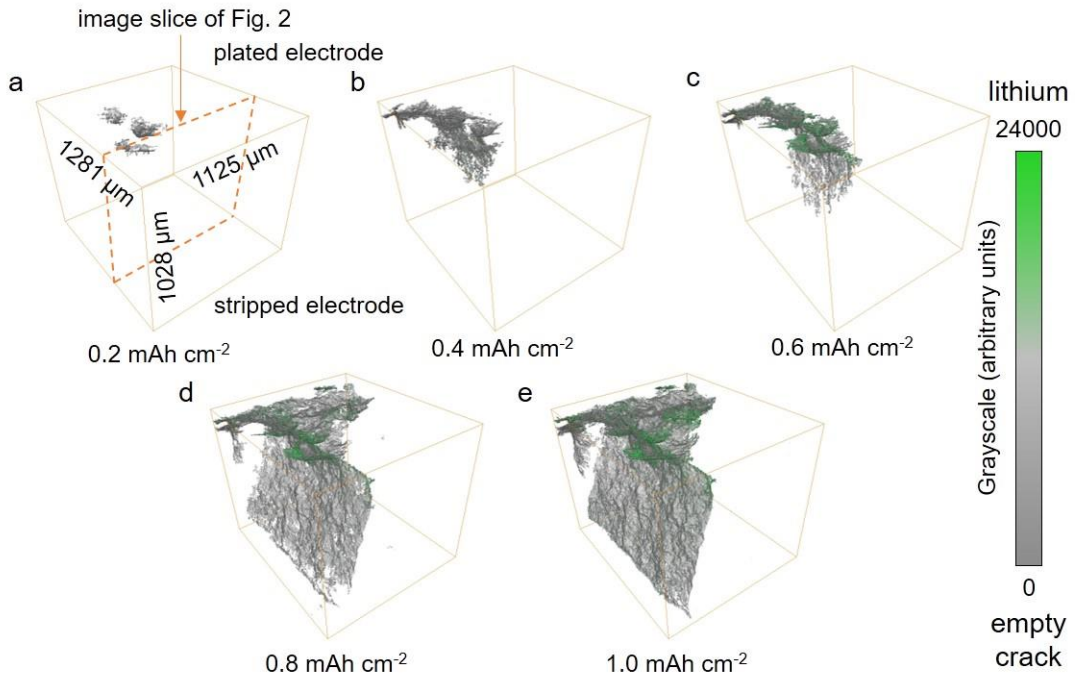

Fig. 4.13. 3D volume rendered images from the *in-situ* X-ray CT of cracks and deposited lithium inside the crack upon lithium plating, showing crack propagation ahead of lithium penetration. Rendering of a segment of the cell (approx., 1x1x1 mm^3) after: **a.** 0.2 mAh cm^{-2}, **b.** 0.4 mAh cm^{-2}, **c.** 0.6 mAh cm^{-2}, **d.** 0.8 mAh cm^{-2} and **e.** 1.0 mAh cm^{-2} of charge passed. In this case grey represents the empty crack and green the lithium. The location of the virtual cross-section in **Fig. 4.11a** is shown by the orange dashed line in **Fig. 4.13a**. The crack formed across the entire electrolyte from plated (top surface) to stripped (bottom surface) electrode before being fully filled with Li. Crack propagation ahead of Li ingress is in accord with absence of a short-circuit even when the crack reaches the stripped electrode.

4.3.3 Dendrite distribution in a cycled cell

Previous studies have suggested dendrites may be found most frequently at the electrode edges[22]. Given the above results, that show more spallations occur near the edge than within the central region of the electrode, that vertical cracks propagate from spallations across the electrolyte, it is interesting to map the location of the spallations and dendrites. To investigate this, synchrotron X-ray diffraction mapping was employed, **Fig. 4.14**. A Li/Li_6PS_5Cl/Li cell

was cycled galvanostatically at a current density of 1.5 mA cm^{-2} and with a capacity of 1.0 mAh cm^{-2} until a short-circuit was observed after 5 cycles. The cell was then aligned such that the incident monochromatic X-ray beam was perpendicular to the Li/Li_6PS_5Cl interface, i.e. along a line between the two electrodes. Diffraction mapping was carried out by collecting diffraction patterns from each segment of a 40 × 40 grid, centred on the electrode, with a grid size of 100 × 100 μm^2 and no overlap, as shown in **Fig. 4.14a**. Diffraction patterns of the sample, collected from each segment of the grid along the path of the transmitted beam through the electrode and electrolyte, are sensitive to dendrite formation along the beam path.

Diffraction patterns collected from the edge and centre of the electrode, marked as the red and blue squares respectively in **Fig. 4.14a**, are presented in **Fig. 4.14b (i)** and **(ii)**. The position of the most intense peak of lithium metal (the {110} peak) is identified with a ✦. Whereas the peak is negligible in the pattern from the centre, it is strong at the edge of the electrode. Taking this peak intensity from each XRD pattern and plotting it as a function of the position across the cell permits mapping of the lithium dendrite distribution, **Fig. 4.14c**. It is apparent that most of the dendrites are distributed along the electrode edge, with a single long dendrite (the longest spike) leading to the short-circuit of the cell.

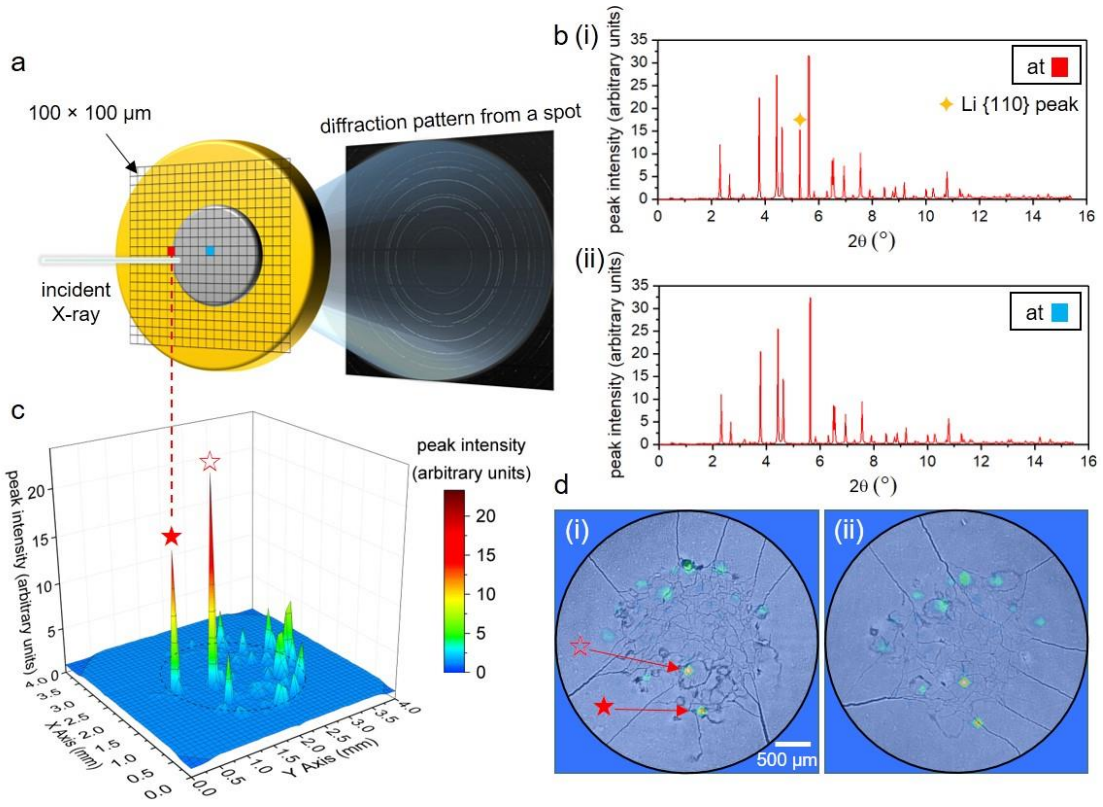

Fig. 4.14. Diffraction mapping showing distribution of lithium dendrites preferentially at the electrode edges and their association with the spallation cracks. Data collected on the Li/Li_6PS_5Cl/Li cell cycled at 1.5 mA cm^{-2} and capacity of 1 mAh cm^{-2} at 7 MPa pressure for 5 cycles until a short circuit occurred. **a**. schematic of X-ray diffraction mapping employing a 40 x 40 grid, with each grid segment being 100 x 100 μm^2 and no overlap. **b**. X-ray diffraction data collected at **(i)** the edge and **(ii)** the centre of the electrode. ✦ identifies the lithium {110} peak, which is strong at the electrode edge (from grid segment shown in red) and not detectable at the centre (grid segment shown in blue). **c**. diffraction intensity of lithium {110} peak plotted at each grid position revealing the distribution of lithium dendrites. The dashed black circle marks the position of the electrodes in the cell. **d**. XCT image slices from planes in the electrolyte parallel and adjacent to the two electrodes. The location of the dendrites from the diffraction mapping have been superposed on these images (highlighted in green and yellow where green represents low intensity as in **Fig. 4.14c**). The two most intense lithium peaks are marked with ★ and ☆.

To correlate the location of the lithium dendrites that propagate across the electrolyte with the spallations, synchrotron XCT was performed on the same cell. **Fig. 4.14d (i)** and **(ii)** show the image slices taken from the electrolyte along planes parallel and adjacent to the two Li/Li_6PS_5Cl interfaces. To compare the dendrite distribution in **Fig. 4.14c** with the location of the spallations, the results of the diffraction mapping from **Fig. 4.14c** were superposed in 2D onto the XCT image slices in **Fig. 4.14d**. The colour scale is the same as in **Fig. 4.14c**, i.e. green represents low lithium intensity. ★ and ☆ mark the positions of the most intense peaks of lithium. **Fig. 4.14d** shows that although not all spallations are associated with lithium dendrites that propagate far into the electrolyte, but all such dendrites are associated with spallations. These results demonstrate that the observations in **Fig. 4.11** and **Fig. 4.13** are typical of how lithium dendrites penetrate the ceramic electrolyte and form short-circuits, i.e. Li ingress forms spallations at the plated electrode predominantly at the edges and lead to transverse cracks across the electrolyte that are increasingly filled with Li. The prevalence of spallations and dendrites at the edges of the electrode may be associated with enhanced electric fields and current densities at electrode edges, as reported in previous modelling and observations[22,51]. In addition, some spallations and lithium dendrites are also observed to form away from the edges of electrode, **Fig. 4.14d**. This is attributed to the regions of inferior contact (voids) between the lithium electrode and the electrolyte, which also results in enhanced electric fields and current densities. The higher current density at the edges and around voids is confirmed by the finite element analysis of current density across the cell in **Fig. 4.15**. The calculations are described in the Appendix.

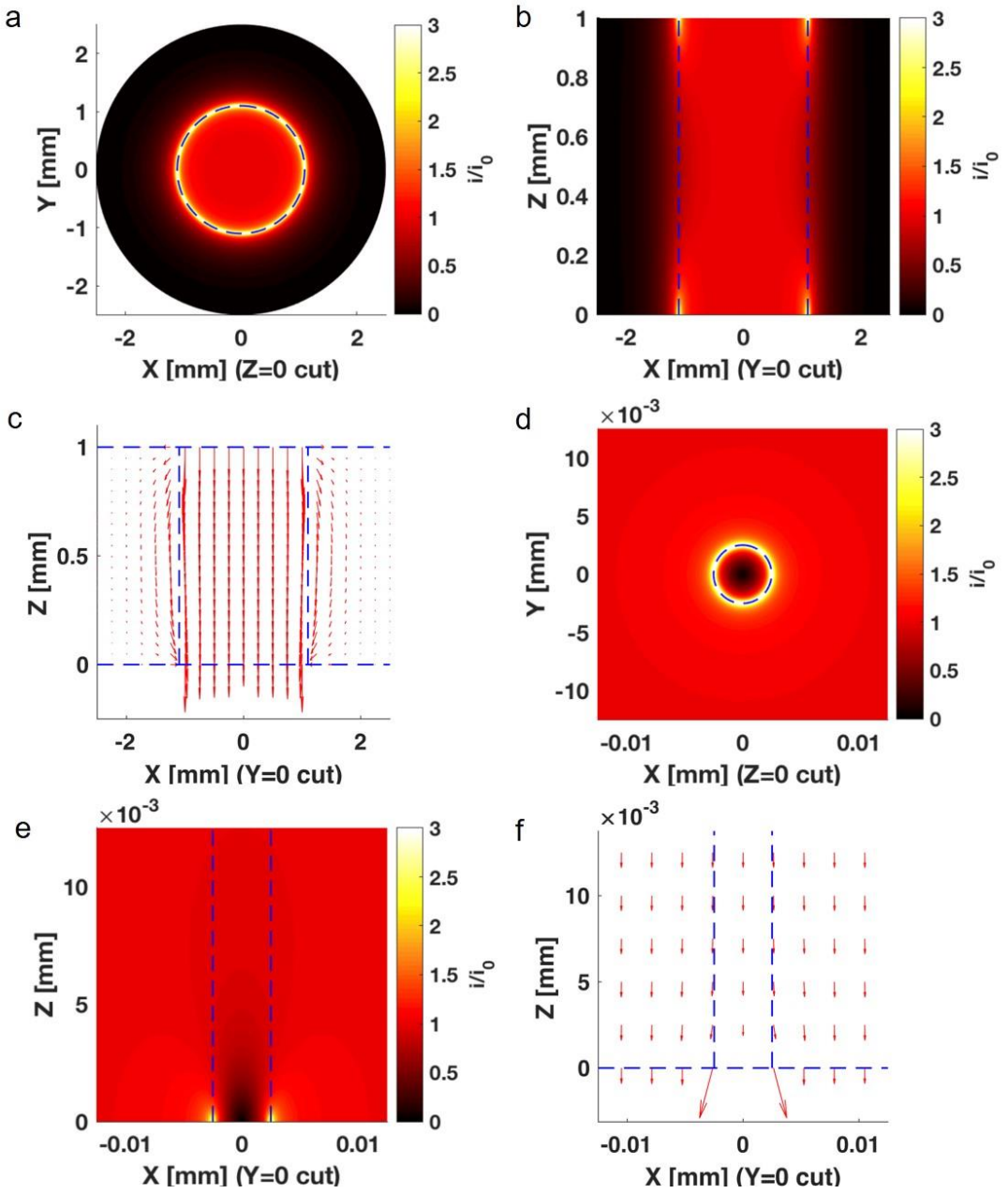

Fig. 4.15. Current density contour plots for a symmetric Li/Li_6PS_5Cl/Li cell with a lithium electrode diameter 2 mm, electrolyte diameter 5 mm, and thickness 1 mm, representing our practical cell dimensions. A void is introduced to the Li/Li_6PS_5Cl interface at the centre of electrode to simulate the effect of poor local contact on current flux distribution. **a**. current density distribution inside the electrolyte viewed perpendicular to the Li/Li_6PS_5Cl interface. **b**. current density distribution viewed in cross-section. **c**. distribution of electric field lines with the plated electrode shown at the bottom and stripped electrode at the top. **d**. current density distribution inside the electrolyte around the void at the Li/Li_6PS_5Cl interface viewed

perpendicular to the interface. **e.** current density distribution viewed in cross-section around the void at the Li/Li_6PS_5Cl interface. **f.** distribution of electric field lines around the void with the plated electrode on the bottom.

4.3.4 Correlation between spallation cracking and local porosity

Recent modelling work has postulated that porosity may have a role in dendrite growth and cross-sectional SEM images have shown lithium dendrites growing through pores[50,52,53]. Since the results presented here show that the formation of spallations leads to cracking that propagates across the electrolyte, it is interesting to examine the relationship between the spallations and the pre-existing porosity in the electrolyte.

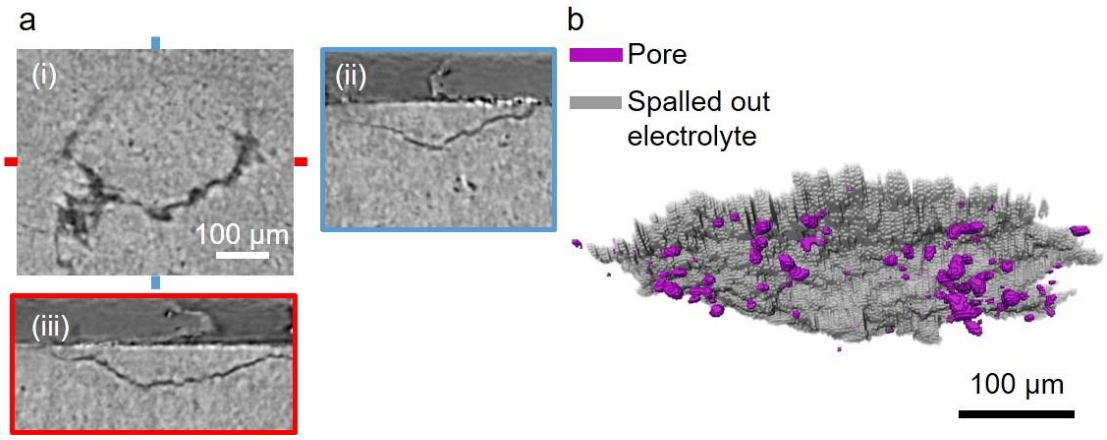

Fig. 4.16. Slices and volume rendered image from *in-situ* X-ray CT revealing the correlation between spallation and pre-existing pores inside the electrolyte. a. spallation imaged by XCT **(i)** parallel and adjacent to the plated electrode and **(ii)** and **(iii)** two virtual cross-sectional views. **b**. the spalled electrolyte is segmented out, rendered and shown in grey, with the pores present in the pristine electrolyte within the cracking region shown in purple.

A large spallation at the Li/Li_6PS_5Cl interface after plating is shown in **Fig. 4.16a**, with virtual slices taken in the electrolyte **(i)** parallel and adjacent to the plated lithium electrode and **(ii)** and **(iii)** two virtual cross-sectional views taken along the blue and red lines in **(i)**. The spalled electrolyte was segmented out and rendered as shown in **Fig. 4.16b**. By superimposing the pore

distribution in the pristine electrolyte onto the volume rendered image of the spalled electrolyte, it is apparent that there is significant porosity along the crack surface. The pore volumetric density is 4.12 % in the cracking region compared with 1.55 % for the bulk electrolyte, confirming the propensity for spallation to propagate along pre-existing pores. The volumetric porosities derived from tomographic analysis excludes pores smaller than 3 × 3 × 3 voxels (voxel size 1.63 μm) because they cannot be identified with certainty. As a result, the total pore density in the region of the spallation will be higher than is seen in **Fig. 4.16b**.

4.4 Conclusions

In-situ phase-contrast X-ray CT combined with spatially mapped X-ray diffraction on Li/ Li_6PS_5Cl/Li cells, has been employed to investigate the propagation of cracks and the propagation of lithium through the solid electrolyte during plating. It is shown that cracks propagate through the electrolyte far ahead of the lithium dendrites, rather than lithium metal driving the crack tip forward. It is demonstrated that Li ingress on plating results in the formation of spallation cracks (pot holes) adjacent to the interface with the plated electrode. Such cracks form because crack propagation to the nearest surface (the plated electrode) relieves the stress. The spallation crack propagates along a path where porosity is above the average of the ceramic. Spallations are more prevalent around the edge of the lithium electrode, where the field is greater, than elsewhere. Transverse cracks then form from the spallations and propagate across the electrolyte to the stripped electrode. Continued Li ingress widens the cracks and drives their propagation, but from the rear not the crack tip. The absence of short-circuits even when a crack traverses the entire electrolyte, linking the plated and stripped electrodes, supports the observation that lithium only later fills the crack completely.

The findings in this chapter provide important insights into electrolyte cracking and lithium dendrite growth and hence the process of failure in all-solid-state batteries. As the dendritic

crack forms as a dry crack, mechanically driven by Li deposition at the rear, more attention needs to be focused on blocking dry crack propagation to block dendrite propagation. Ceramic toughening and crack blocking strategies, which have been well developed in engineering ceramic research, such as fibre reinforcement and transformation toughening are expected to effectively improve the resistance of solid electrolyte to dendrite formation.

4.5 References

1. Janek, J. & Zeier, W. G. A solid future for battery development. *Nature Energy* **1**, 1–4 (2016).

2. Pellegrini, V., Bodoardo, S., Brandell, D. & Edström, K. Challenges and perspectives for new material solutions in batteries. *Solid State Commun.* **303**–**304**, 113733 (2019).

3. Palacín, M. R. Recent advances in rechargeable battery materials: A chemist's perspective. *Chem. Soc. Rev.* **38**, 2565–2575 (2009).

4. Famprikis, T., Canepa, P., Dawson, J. A., Islam, M. S. & Masquelier, C. Fundamentals of inorganic solid-state electrolytes for batteries. *Nature Materials* **18**, 1278–1291 (2019).

5. Fincher, C. D., Ojeda, D., Zhang, Y., Pharr, G. M. & Pharr, M. Mechanical properties of metallic lithium: from nano to bulk scales. *Acta Mater.* **186**, 215–222 (2020).

6. Yang, C. *et al*. Continuous plating/stripping behavior of solid-state lithium metal anode in a 3D ion-conductive framework. *Proc. Natl. Acad. Sci. U. S. A.* **115**, 3770–3775 (2018).

7. Masias, A., Felten, N., Garcia-Mendez, R., Wolfenstine, J. & Sakamoto, J. Elastic, plastic, and creep mechanical properties of lithium metal. *J. Mater. Sci.* **54**, 2585–2600 (2019).

8. Han, F., Yue, J., Zhu, X. & Wang, C. Suppressing Li Dendrite Formation in Li2S-P2S5 Solid Electrolyte by LiI Incorporation. *Adv. Energy Mater.* **8**, 1703644 (2018).

9. Porz, L. *et al.* Mechanism of Lithium Metal Penetration through Inorganic Solid Electrolytes. *Adv. Energy Mater.* **7**, 1–12 (2017).

10. Lotsch, B. V. & Maier, J. Relevance of solid electrolytes for lithium-based batteries: A realistic view. *J. Electroceramics* **38**, 128–141 (2017).

11. Pang, Q., Liang, X., Shyamsunder, A. & Nazar, L. F. An In Vivo Formed Solid

Electrolyte Surface Layer Enables Stable Plating of Li Metal. *Joule* **1**, 871–886 (2017).

12. Kerman, K., Luntz, A., Viswanathan, V., Chiang, Y.-M. & Chen, Z. Review—Practical Challenges Hindering the Development of Solid State Li Ion Batteries. *J. Electrochem. Soc.* **164**, A1731–A1744 (2017).

13. LePage, W. S. *et al.* Lithium Mechanics: Roles of Strain Rate and Temperature and Implications for Lithium Metal Batteries. *J. Electrochem. Soc.* **166**, A89–A97 (2019).

14. Chen, Y. *et al.* Li metal deposition and stripping in a solid-state battery via Coble creep. *Nature* **578**, 251–255 (2020).

15. van den Broek, J., Afyon, S. & Rupp, J. L. M. Interface-Engineered All-Solid-State Li-Ion Batteries Based on Garnet-Type Fast Li+ Conductors. *Adv. Energy Mater.* **6**, 1600736 (2016).

16. Monroe, C. & Newman, J. The Effect of Interfacial Deformation on Electrodeposition Kinetics. *J. Electrochem. Soc.* **151**, A880 (2004).

17. Monroe, C. & Newman, J. The Impact of Elastic Deformation on Deposition Kinetics at Lithium/Polymer Interfaces. *J. Electrochem. Soc.* **152**, A396 (2005).

18. Sharafi, A., Meyer, H. M., Nanda, J., Wolfenstine, J. & Sakamoto, J. Characterizing the Li-$Li_7La_3Zr_2O_{12}$ interface stability and kinetics as a function of temperature and current density. *J. Power Sources* **302**, 135–139 (2016).

19. Marbella, L. E. *et al.* 7 Li NMR Chemical Shift Imaging to Detect Microstructural Growth of Lithium in All-Solid-State Batteries. *Chem. Mater.* **31**, 2762–2769 (2019).

20. Aguesse, F. *et al.* Investigating the dendritic growth during full cell cycling of garnet electrolyte in direct contact with Li metal. *ACS Appl. Mater. Interfaces* **9**, 3808–3816 (2017).

21. Wu, B. *et al.* The role of the solid electrolyte interphase layer in preventing Li dendrite

growth in solid-state batteries †. *Enegy Environ. Sci.* 1803–1810 (2018). doi:10.1039/c8ee00540k

22. Swamy, T. *et al.* Lithium metal penetration induced by electrodeposition through solid electrolytes: Example in single-crystal $Li_6La_3ZrTaO_{12}$ garnet. *J. Electrochem. Soc.* **165**, A3648–A3655 (2018).

23. Kazyak, E. *et al.* Li Penetration in Ceramic Solid Electrolytes: Operando Microscopy Analysis of Morphology, Propagation, and Reversibility. *Matter* **2**, 1–24 (2020).

24. Manalastas, W. *et al.* Mechanical failure of garnet electrolytes during Li electrodeposition observed by in-operando microscopy. *J. Power Sources* **412**, 287–293 (2019).

25. Tippens, J. *et al.* Visualizing Chemomechanical Degradation of a Solid-State Battery Electrolyte. *ACS Energy Lett.* **4**, 1475–1483 (2019).

26. Seitzman, N. *et al.* Toward all-solid-state lithium batteries: Three-dimensional visualization of lithium migration in β-Li3PS4 ceramic electrolyte. *J. Electrochem. Soc.* **165**, A3732–A3737 (2018).

27. Doux, J. *et al.* Stack Pressure Considerations for Room Temperature All-Solid-State Lithium Metal Batteries. *Adv. Energy Mater.* 1903253 (2019). doi:10.1002/aenm.201903253

28. Spencer Jolly, D. *et al.* Sodium/Na β″ Alumina Interface: Effect of Pressure on Voids. *ACS Appl. Mater. Interfaces* **12**, 678–685 (2020).

29. Kasemchainan, J. *et al.* Critical stripping current leads to dendrite formation on plating in lithium anode solid electrolyte cells. *Nat. Mater.* **18**, 1105–1111 (2019).

30. Cao, C. *et al.* Emerging X-ray imaging technologies for energy materials. *Materials Today* (2019). doi:10.1016/j.mattod.2019.08.011

31. Boulineau, S., Courty, M., Tarascon, J. M. & Viallet, V. Mechanochemical synthesis

of Li-argyrodite Li_6PS_5X (X = Cl, Br, I) as sulfur-based solid electrolytes for all solid state batteries application. *Solid State Ionics* **221**, 1–5 (2012).

32. Zhou, L. *et al.* Solvent-Engineered Design of Argyrodite Li_6PS_5X (X = Cl, Br, I) Solid Electrolytes with High Ionic Conductivity. *ACS Energy Lett.* **4**, 265–270 (2019).

33. Wenzel, S., Sedlmaier, S. J., Dietrich, C., Zeier, W. G. & Janek, J. Interfacial reactivity and interphase growth of argyrodite solid electrolytes at lithium metal electrodes. *Solid State Ionics* **318**, 102–112 (2018).

34. Yu, C., van Eijck, L., Ganapathy, S. & Wagemaker, M. Synthesis, structure and electrochemical performance of the argyrodite Li6PS5Cl solid electrolyte for Li-ion solid state batteries. *Electrochim. Acta* **215**, 93–99 (2016).

35. Lee, H. *et al.* Advances and Prospects of Sulfide All-Solid-State Lithium Batteries via One-to-One Comparison with Conventional Liquid Lithium Ion Batteries. *Advanced Materials* **31**, 1900376 (2019).

36. Paganin, D., Mayo, S. C., Gureyev, T. E., Miller, P. R. & Wilkins, S. W. Simultaneous phase and amplitude extraction from a single defocused image of a homogeneous object. *J. Microsc.* **206**, 33–40 (2002).

37. Marone, F. & Stampanoni, M. Regridding reconstruction algorithm for real-time tomographic imaging. *J. Synchrotron Radiat.* **19**, 1029–1037 (2012).

38. Krauskopf, T. *et al.* Lithium-Metal Growth Kinetics on LLZO Garnet-Type Solid Electrolytes. *Joule* **3**, 2030–2049 (2019).

39. Albertus, P., Babinec, S., Litzelman, S. & Newman, A. Status and challenges in enabling the lithium metal electrode for high-energy and low-cost rechargeable batteries. *Nat. Energy* **3**, 16–21 (2018).

40. Wenzel, S. *et al.* Interfacial Reactivity Benchmarking of the Sodium Ion Conductors Na_3PS_4 and Sodium β-Alumina for Protected Sodium Metal Anodes and Sodium All-Solid-State Batteries. *ACS Appl. Mater. Interfaces* **8**, 28216–28224 (2016).

41. Zhu, Y., He, X. & Mo, Y. Origin of Outstanding Stability in the Lithium Solid Electrolyte Materials: Insights from Thermodynamic Analyses Based on First-Principles Calculations. *ACS Appl. Mater. Interfaces* **7**, 23685–23693 (2015).

42. Bay, B. K., Smith, T. S., Fyhrie, D. P. & Saad, M. Digital volume correlation: Three-dimensional strain mapping using x-ray tomography. *Exp. Mech.* **39**, 217–226 (1999).

43. Eastwood, D. S. *et al.* Lithiation-induced dilation mapping in a lithium-ion battery electrode by 3D X-ray microscopy and digital volume correlation. *Adv. Energy Mater.* **4**, 1300506 (2014).

44. Pietsch, P. & Wood, V. X-Ray Tomography for Lithium Ion Battery Research: A Practical Guide. *Annu. Rev. Mater. Res* **471229**, 1–12 (2017).

45. Baruchel, J., Buffière, J. Y., Maire, E., Merle, P. & Peix, G. X-ray tomography in material science. *Hermes Sci. Publ.* **31**, 1–209 (2000).

46. Porz, L. *et al.* Mechanism of Lithium Metal Penetration through Inorganic Solid Electrolytes. *Adv. Energy Mater.* **7**, 1701003 (2017).

47. Athanasiou, C. E., Jin, M. Y., Ramirez, C., Padture, N. P. & Sheldon, B. W. High-Toughness Inorganic Solid Electrolytes via the Use of Reduced Graphene Oxide. *Matter* **3**, 212–229 (2020).

48. Klinsmann, M., Hildebrand, F. E., Ganser, M. & McMeeking, R. M. Dendritic cracking in solid electrolytes driven by lithium insertion. *J. Power Sources* **442**, 227226 (2019).

49. Bucci, G. & Christensen, J. Modeling of lithium electrodeposition at the

lithium/ceramic electrolyte interface: The role of interfacial resistance and surface defects. *J. Power Sources* **441**, 227186 (2019).

50. Barroso-Luque, L., Tu, Q. & Ceder, G. An Analysis of Solid-State Electrodeposition-Induced Metal Plastic Flow and Predictions of Stress States in Solid Ionic Conductor Defects. *J. Electrochem. Soc.* **167**, 020534 (2020).

51. Tang, M., Albertus, P. & Newman, J. Two-Dimensional Modeling of Lithium Deposition during Cell Charging. *J. Electrochem. Soc.* **156**, A390 (2009).

52. Ren, Y., Shen, Y., Lin, Y. & Nan, C. W. Microstructure Manipulation for Enhancing the Resistance of Garnet-Type Solid Electrolytes to 'short Circuit' by Li Metal Anodes. *ACS Appl. Mater. Interfaces* **11**, 5928–5937 (2019).

53. Shen, F., Dixit, M. B., Xiao, X. & Hatzell, K. B. Effect of Pore Connectivity on Li Dendrite Propagation within LLZO Electrolytes Observed with Synchrotron X-ray Tomography. *ACS Energy Lett.* **3**, 1056–1061 (2018).

4.6 Appendix

Fig. 4.13 shows the current density contour plots and the distribution of electric field lines within a cylindrical solid electrolyte, sandwiched between two voltage-biased concentric lithium electrodes whose diameters are smaller than the electrolyte. To model the effect of voids on the current-density distribution, a void of 5 μm in diameter was introduced at the centre of plated electrode. Electric potential in the electrolyte F is governed by Laplace's equation $\nabla^2 F = 0$. Dirichlet boundary conditions (constant potential) are imposed on the surface in contact with electrodes. Surfaces not in contact with the electrode take no-flux Neumann conditions ($\vec{\nabla}\Phi = 0$). The current density is proportional to the gradient of electric potential

according to Ohm's law $\vec{i} = \sigma\vec{\nabla}\Phi$. **Fig. 4.15a** shows the distribution of current density across the top (adjacent to stripped electrode) or bottom (adjacent to plated electrode) surface of the electrolyte (these are the same due to symmetry). Due to the sharp change between constant-potential and insulting behaviour at the outer edge of the lithium electrode, the current density near the electrode edge is significantly greater (> 3 fold) than that at its centre (i_0). **Fig. 4.15b** shows that the current distribution is also non-uniform in the axial direction. Traversing the electrolyte axially from one of the high-current areas at the electrolyte edge, the current density decays rapidly. The current density at the edge becomes comparable to the current density at the centre at a depth of about 100 μm into the electrolyte and away from the interface, which suggests that spallations are unlikely to form far away from the interface. **Fig. 4.15c** shows the distribution of electric field lines in cross-section. The electric field lines spread out in the middle of the electrolyte and incline away from the axial near the electrode's edges. Consequently, lithium plating near the electrode edge may create inclined cracks and form inclined filaments, which would be favourable for forming spallations. **Fig. 4.15d** shows the current density distribution near a void. The edge of a surface void has a high local current density much like the electrode edge, but the influence is more limited due to the small void size. Spallations induced by surface voids would be expected to be smaller than those induced by the electrode edge. **Fig. 4.15e** indicates that the distortion of the current density near the void is also restricted to a shallow surface region, not deep into the bulk of the electrolyte (~5 μm). **Fig. 4.15f** plots the distribution of electric field lines near the central void. Due to the insulating nature of the void, electric field lines have to incline to bypass it, a possible cause of the inclined edges of spallations. The calculation and finite element modelling were performed by Guanchen Li and Charles Monroe.

Chapter 5. Mechanistic Investigation of Dendrite Initiation and Propagation in All-Solid-State Batteries

Abstract

The inability of solid electrolyte to prevent dendrite formation remains one of the biggest challenges for the practical application of all-solid-state batteries. While cell failures due to lithium dendrites propagating through the solid electrolyte have been widely observed, the mechanism of how a soft metal, such as lithium, can break the ceramic electrolyte is not understood. By employing operando X-ray computed tomography with unprecedentedly high time resolution, the whole process of the dendrite formation was followed in detail, from the very initiation to a complete short-circuit. Based on the observation, the dendrite formation was divided into two stages of dendrite initiation and propagation, with two comprehensive models proposed to explain the mechanism behind the behaviour of lithium. While dendrite initiation was attributed to the hydrostatic stress build-up by the deposition of lithium from a pore, and evidenced by experiments, the dendrite propagation was ascribed to the wedge-opening induced by the deposition kinetics of lithium. Predictions were made based on the mechanistic understanding, with which sustainable cell cycling at a satisfactory current density (4.0 mA/cm^2) was achieved. Based on the model, an advanced sintering method was also introduced to enhance the resistance to dendrite formation of solid electrolytes. The CCD of Li_6PS_5Cl was doubled by eliminating the open pores and enhancing the mechanical properties with spark plasma sintering.

5.1 Introduction

The Li dendrite formation that penetrates through the solid electrolytes and leads to cell failure remains a grand challenge for all-solid-state batteries with Li metal anode. While extensive efforts have been made to reveal the process of cell failure in all-solid-state batteries, the key question remains: why Li as such a soft matter can break and penetrate through the stiff ceramic electrolyte?

For the mechanistic investigations of dendrites, it is important to follow the very initiation and subsequent propagation of dendrites [1–4]. Optical microscopy has then been extensively used to track the development of dendrites with advantaged time resolution[5–7]. However, as dendrites are buried inside the solid electrolyte, it is challenging to reveal the whole picture of Li dendrites with optical microscopy. With a special set-up employed, such as in-plane cells, the dendrites could be restricted to form on the solid electrolyte surface, that is exposed to the optical microscope[6]. At the same time, due to intrinsically different electric fields, such observations might not be representative of how dendrites form in all-solid-state batteries under practice-relevant conditions[8].

While XCT was widely used for dendrite studies, previous experiments were conducted either *ex-situ* or *in-situ* with considerable electrochemical pauses for scans to be taken[9–16]. Recent studies suggest that pausing the applied galvanostatic current could remarkably change the stress status of lithium deposited in the dendritic crack, leading to extrusion of lithium from inside the crack, and a mismatch with continuous Li dendrite growth that is observed in the normal operation situation[5,6]. Therefore, an *operando* XCT with satisfactory spatial resolution (< 2 µm/pixel) and sufficiently high time resolution (< 5 min/scan) is desired to uncover the whole process of dendrite formation, from dendrite initiation to short circuit, without any disturbance to the electrochemical operation.

Extensive efforts have also been made to explain the dendrites formation in all-solid-state batteries from a theoretical perspective[17–21]. By referring to the mechanistic studies of Na

dendrites in Na/Na-beta''-Alumina cells in the past, models based on Griffith flaws have been proposed to account for the dendrite formation in all-solid-state batteries, where the local overpotential of Li deposition was directly converted to a mechanical driving force based on thermodynamic consideration[7,22–24]. However, the extrusion of Li from inside the surface flaw as a way of stress relaxation that has been experimentally observed was rarely addressed in such models[5,8]. Such extrusion should be not ignored by simply assuming the deposited Li is perfectly constrained inside the flaw, given the low yield strength of Li metal. In addition, such models rely on a pre-existing crack-like Griffith flaw on the surface with considerable aspect ratio, which are invalid in practice-relevant conditions.

More importantly, while all such models require the flaw or crack to be fully filled with Li in order to build up stresses, the recent discovery is clearly shown in **Chapter 4**. that the dendritic crack in all-solid-state batteries propagates as a dry crack far ahead of Li dendrite tip. Li dendrite propagation is driven by Li deposition from the rear rather than crack tip. The absence of Li at the crack tip forces a radical rethink of the mechanism that holds for dendrite initiation and propagation in all-solid-state batteries. A comprehensive model that adheres to experimental observation is needed to pave way towards the practical application of all-solid-state batteries.

In this work, *operando* X-ray computed tomography based on pink beam synchrotron X-ray has been conducted with an unprecedentedly high time resolution of 3 min 40 s per scan. Allowed by the satisfactory time and spatial resolution, the whole evolution of a dendrite has been tracked from the very initiation to a complete short circuit. Based on the observation, two comprehensive models were proposed for dendrite initiation and propagation, respectively. Multi-faceted experiments were conducted to evidence the models and testify the predictions made based on the models. The concept of critical current density for dendrite propagation has been defined, which guided a reliable cycling with a plating current density up to 4.0 mA/cm^2 to be achieved with the reduction of stack pressure. Finally, spark plasma sintering (SPS) was introduced to improve the performance of solid electrolyte, as suggested by the initiation model.

The performance of the resultant sample suggests further strategies to optimise the cell resistance to dendrite formation.

5.2 Protocol

5.2.1 Electrolyte preparation and cell assembly

Li_6PS_5Cl solid electrolyte powder with a particle size of D50 ~ 10 μm was purchased from MSE Supplies. The powder was pressed into a pellet with a 5-mm-diameter stainless stell die set under a uniaxial pressure of 400 MPa. The pellet was then transferred without exposure to air to a furnace inside an Ar-filled glovebox with O_2 and H_2O levels < 1 ppm, and sintered at 300 ℃ for 20 min. The sintered electrolyte pellet was then cooled to room temperature and used for cell assembly.

Metallic lithium 100 μm thick was punched into 2-mm-diameter diameter disc-shaped lithium electrodes, and pressed onto both sides of the sintered Li_6PS_5Cl pellet for two-electrode cell. Cells for *operando* XCT characterisation was then assembled into a customised tube-cell, which maintained air-tightness and stack pressure control. The tube-cell is shown in **Fig. 3.4** in **Chapter 3**. For a three-electrode cell, two disc-shaped lithium electrodes of 1 mm diameter were pressed onto the same side of the pellet as the working and reference electrodes, with a 1 mm gap between them. A 5 mm lithium disc was pressed onto the other side as the counter electrode. The working and reference electrode were separated by a 1 mm-wide polymer insulating tape mask. The cell was then assembled into a pouch cell with Cu current collectors, and sealed under a high-level of vacuum (~ 10^{-3} bar). The schematic of the three-electrode cell is shown below in **Fig. 5.1**.

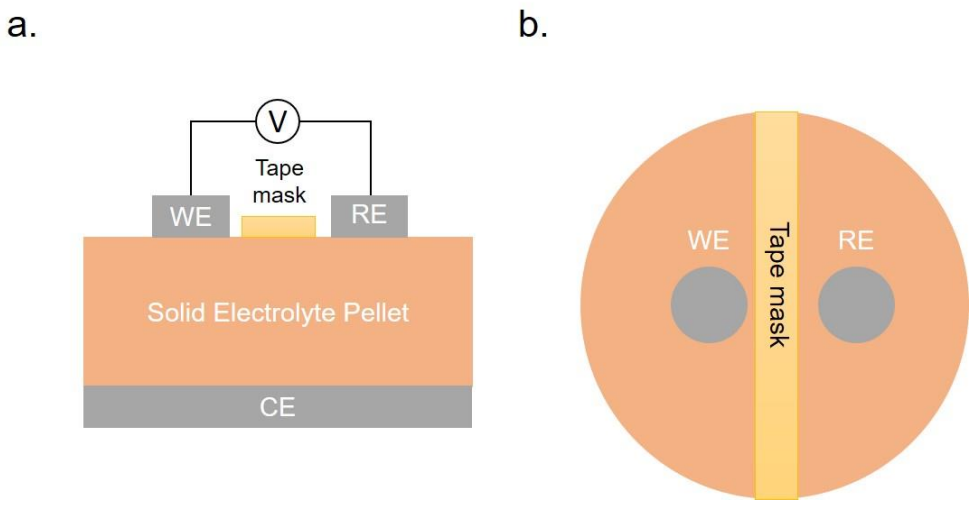

Fig. 5.1. Three-electrode cell configuration for pressureless galvanostatic cycling at **a.** side-view **b.** top view, respectively. WE, CE, and RE denote working, counter, and reference electrodes, respectively, which are lithium metal. No stack pressure is applied to the cell during cycling.

5.2.2 Powder X-ray diffraction

PXRD was conducted to confirm the phase purity of SPS samples after sintering at various temperatures. The electrolyte pellets after SPS were sufficiently polished to remove any graphite remaining on the surface, until a clean and smooth surface was obtained. The pellet was then ground into powder with a mortar and pestle for PXRD characterisation. The powder was transferred to a Rigaku Miniflex XRD inside a N_2-filled glovebox without exposure to air for PXRD measurements.

5.2.3 Plasma FIB-SEM

SPS Li_6PS_5Cl pellet of 5 mm diameter was adopted for PFIB-SEM characterisation for its pores of smaller quantity but bigger dimensions. Two 2-mm-diameter lithium electrodes were pressed on the both sides of the pellet, and then assembled into a pouch cell. The cell was then galvanostatically charged with an areal current density of 0.05 mA/cm^2 for a capacity of 2 mAh/cm^2 under no stack pressure. A combination of low current density and zero stack pressure

was employed to ensure no formation of lithium dendrites. A large areal capacity was applied to ensure sufficient lithium deposition in pre-existing pores inside the solid electrolyte. The PFIB-SEM was performed with the assistance from Junfu Bu.

5.2.4 *Operando* X-ray computed tomography

X-ray tomograms were recorded at I13-2 beamline at the Diamond Light Source (Experiment No. 23980-1). A pink beam with beam energy ranging from 8 keV to 30 keV was employed to maximise the X-ray beam flux and so improve the time resolution. Projections were collected with a PCO Edge 5.5 sCMOS camera combined with an optical microscope with a ×4 magnification, resulting in a pixel size of 1.625 μm and a field of view of 4.7 × 4.4 mm^2. A 500-μm-thick LuAG scintillator was used to convert X-rays to visible light. The exposure time was set to 100 ms. For each tomogram, 1801 equiangularly distributed projections were taken over 180º as well as 50 dark and 50 flat references before and after the whole *operando* experiment. X-ray tomograms were obtained at the pristine state, and were then collected continuously as soon as the galvanostatic charge started. A final tomogram was collected after the whole electrochemical charge for the steady state.

5.2.5 Differential electrochemical mass spectrometry

DEMS measurement was conducted on pristine and charged Li_6PS_5Cl to verify the direct lithium deposition into pores with the detection of H_2. Sintered Li_6PS_5Cl pellets were assembled into pouch cells with 2-mm-diameter lithium electrodes pressed onto both sides of the pellets. One pouch cell was galvanostatically charged at a current density of 0.05 mA/cm^2 and a capacity of 2 mAh/cm^2 under no stack pressure to ensure no formation of dendrite. The other pouch cell was rested under identical conditions with no current passed. The cells were then disassembled from the pouches and with the lithium electrode finely polished off with 4000-grid polishing papers in an Ar-filled glovebox. The pellet to be tested by DEMS was then transferred into a well-sealed vial along with a magnetic stirrer. After the vial was connected to the DEMS, the Ar carrier gas was flowing from the vial to the mass spectrometer remove the

remaining gas inside the vial, until a 100% argon flow was detected. The excess degassed LiOH solution was then injected into the vial, dissolving the Li_6PS_5Cl electrolyte and reacting with any Li metal inside the sample to form H_2. The released H_2 was detected and quantified by the mass spectrometer (Prima BT, Thermo Fisher Scientific) as a percentage of the total gas flow. A reaction time of 30 min was controlled for both the charged and pristine samples, to allow a complete reaction between the samples and solution.

The carrier gas flow rate (r) was controlled at 1 mL/min by a digital flow meter (Bronkhorst), so the detected amount of target gas in moles (n) can be calculated by the following equation, **Eq. 5.1**:

$$n = \frac{r \times P}{V_m} \tag{5.1}$$

More set-up details can be found in previous works[25,26].

5.2.6 Pressureless galvanostatic cycling

The pressureless galvanostatic cycling was conducted based on a three-electrode cell set-up as described in the method of cell assembly. No stack pressure was applied to the cell to avoid any mechanical effect on dendrite propagation, apart from the ambient pressure on the cell due to the vacuum inside the pouch cell. The galvanostatic cycling was conducted by repeating cycles of galvanostatic discharge and charge for the same capacity. While the discharge current density (plating on WE) varies for different samples, the same low current density of 0.05 mA/cm^2 was used on charge (stripping on WE) to ensure no void formation at the WE/SE interface. All galvanostatic measurements were performed using a Gamry Interface 1010 potentiostat.

5.2.7 Electrochemical impedance spectroscopy measurement

The SPS Li_6PS_5Cl and sintered Li_6PS_5Cl pellets were polished with 4000-grid polishing papers until mirror-shine surfaces were obtained. The polished pellets were then coated with 500nm Ni on both sides via magnetron sputtering, with the coated area controlled by pre-punched

Kapton tape masks with 3 mm holes. The Ni-coated pellets were then assembled into pouch cells under vacuum. The electrochemical impedance spectroscopy (EIS) was performed on the cells at a voltage perturbation of 10 mV, in a frequency range from 1 MHz to 10 Hz using a Gamry Interface 1010 potentiostat. The data were analysed using the ZView software package.

5.2.8 Electronic conductivity measurement

Electronic conductivity measurements were performed on the same samples for EIS measurements. The electronic conductivity was conducted by current response of the cell under a voltage bias of 0.1 V using a Gamry Interface 1010 potentiostat. The current response gradually comes to a constant value after the fast decay at the start due to space charge effects. The measured current after 30 min was used to calculate the electronic conductivity of the sample based on the Ohm's law.

5.2.9 Spark plasma sintering

Spark plasma sintering (SPS) was employed in this work as an advanced tool to densify the solid electrolyte, to minimise the porosity and improve ionic conductivity. Li_6PS_5Cl powder was loaded into a 20 mm graphite die set, and mounted onto the SPS sample stage. With a preload of 2 MPa, the SPS was evacuated to vacuum. The sample was then rapidly heated to various temperature (250 ℃ to 550 ℃) with a heating rate of 100 ℃/min for fast sintering, followed by 5 min of peak temperature holding and a slow cooling. The stack pressure on the die set was gradually increased from 2 MPa to 50 MPa as temperature increased. After cooling to room temperature, the sintered pellet was pushed out from the die set. Polishing and sectioning were then performed to finely remove the remained graphite on the surface, and cut the pellets into suitable dimensions. All procedures were performed in an Ar-filled glovebox, with O_2 and H_2O levels < 1 ppm

5.3 Results and Discussions

5.3.1 *Operando* X-ray computed tomography revealing the whole evolution of dendrite in all-solid-state batteries

A two-electrode symmetric Li/Li_6PS_5Cl/Li cell was assembled into a customised tube-cell, which maintained air-tightness and a stack pressure of 7 MPa, and was mounted in the I13-2 synchrotron XCT beamline to perform *operando* XCT scans. Galvanostatic charge was performed at a current density of 3 mA/cm^2 for a capacity of 3 mAh/cm^2, with XCT scans collected simultaneously at pristine and after every 220 s, **Fig. 5.2**. Such high current density was selected to ensure dendrite formation and cell failure in half a cycle, as it was known to be above the critical current density under given conditions. As suggested by previous studies that dendrites in all-solid-state batteries emanate from spallations, a series of virtual cross-sectional images slices orthogonal to the Li/Li_6PS_5Cl interface, along a same plane across a spallation, throughout the *operando* XCT scans are presented in **Fig. 5.2b**.

With the galvanostatic current passing, lithium plating takes place at the interface of the top electrode. Consistent with previous observations shown in **Chapter 4**, the lithium plating creates a spallation at the edge of electrode due to the current flux enhancement, **Fig. 5.2b (ii)** & **(iii)**. With more charge passed, the spalled-out electrolyte was further detached from the bulk as it was lifted by deposited lithium into the spallation crack. As deposited lithium reached the bottom of spallation crack, transverse cracking emanated from underneath the spallation, and propagated towards the other electrode, **Fig. 5.2b (iv)**. The initiation of the dendrite happened within the first 11 min of charge, followed by a longer process of dendrite propagation. With more lithium deposited into the dendritic crack, apparent widening and lengthening of the transverse crack were observed, **Fig. 5.2b (iv)** to **(vii)**. With another 11 min of charge, the initiated transverse crack propagated and reached the other electrode. The absence of a drop in cell voltage while the two electrodes were connected by the transverse crack is also consistent with the previous observation shown in **Chapter 4**. that lithium dendrites propagate far behind

the crack tip. The process from the complete crack propagation till the short circuit was also noteworthy, as it took considerable capacity (~ 0.73 mAh/cm^2) for lithium to fill the dry crack and bridge the two electrodes, even without any disturbance to the electrochemical process. More importantly, while the deposited lithium might rapidly coat the surface of the dry crack and lead to a short circuit as there was no longer any mechanical resistance, it still remarkably widened the crack as the dendrite propagated. The crack widening only stopped when a complete short circuit was reached. The morphology of the crack remained unchanged after short-circuit, as an electron path was built, and no further lithium deposition occurred inside the crack, **Fig. 5.2b (xi)** & **(xii)**. The distribution of lithium at the rear of the crack, the coupled lengthening and widening of the crack during propagation, and the continuous crack widening after complete crack propagation suggests a wedge-opening nature of dendrite propagation, which might originate from the deposition kinetics, and will be discussed in detail in section **5.3.3**.

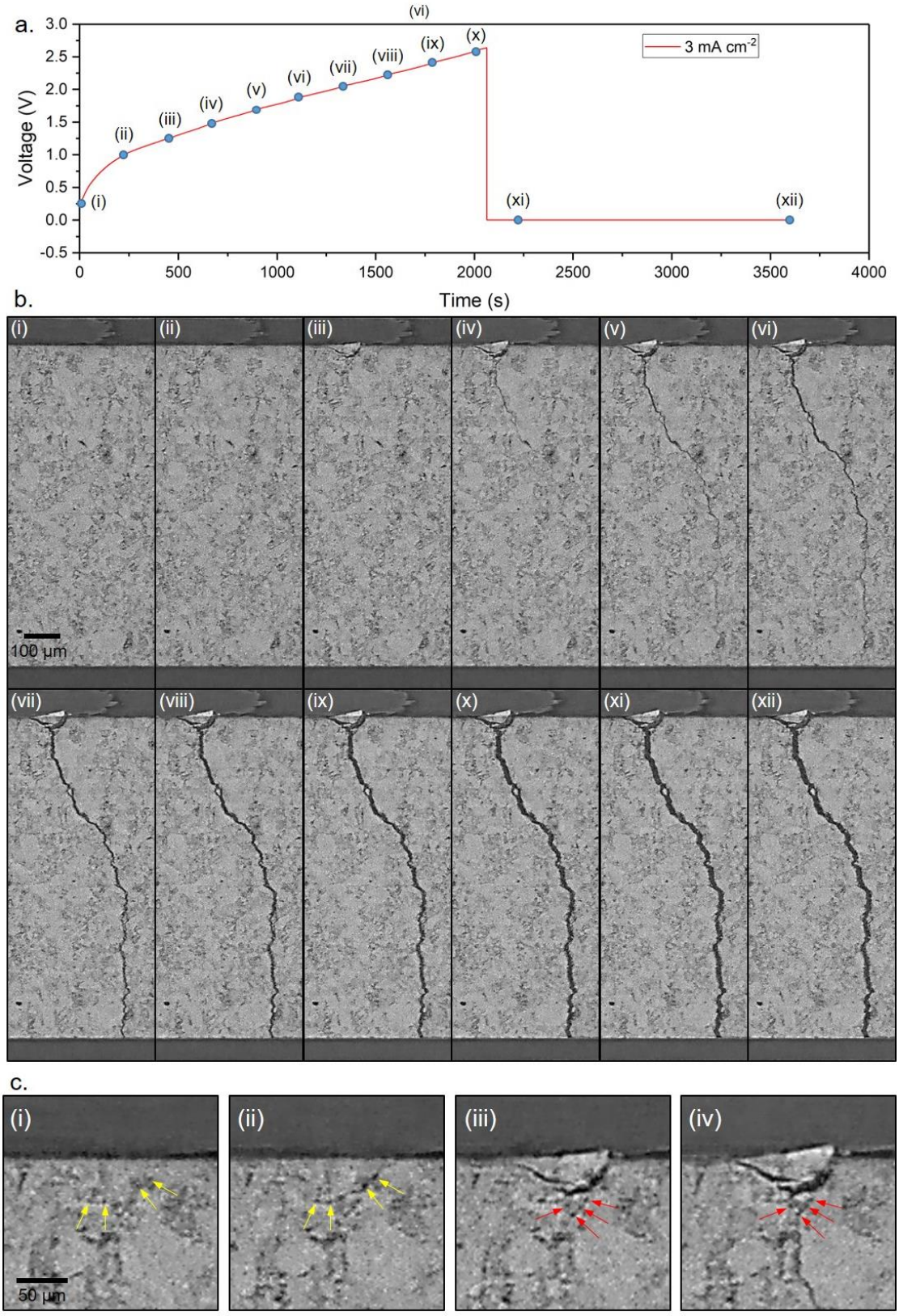

Fig. 5.2. *Operando* synchrotron X-ray CT virtual cross-sections showing the time-resolved evolution of dendrites from early initiation to a complete short-circuit. a. cell voltage versus time, showing no drop in voltage as the dendrite and crack propagated, and complete

short-circuit (voltage drop to zero) when the morphology of the electrolyte remained unchanged. **b.** virtual cross-sectional image slices from *operando* XCT scans with their states of charge marked in a. with the corresponding numbers. The time gap between adjacent scans (i) to (xi) are 3 min 40 s. **c.** magnified images of the regions where spallation and transverse cracks initiate from **b (i)** to **(iv)**. The pre-existing pores involved in the dendrite initiation were highlighted with arrows.

Allowed by the satisfactory time resolution, it was possible to examine the very initiation of dendrites, which is crucial to a mechanistic understanding, **Fig. 5.2c**. Magnified images of the region where spallation and transverse crack initiated from **Fig. 5.2b (i)** to **(iv)** are shown in **Fig. 5.2c (i)** to **(iv)**, revealing the morphological changes of solid electrolyte at the very beginning. No apparent defects or cracks were found in the pristine sample, except a few pre-existing pores, **Fig. 5.2c (i)**. After the first step of charge for 3 min 40 s, some of the pre-existing pores, 10 to 30 μm from the interface, were apparently enlarged, creating cracks that connected the pores, sketching the outline of the eventual spallation crack (**Fig. 5.2c (i)** & **(ii)**, pores highlighted by yellow arrows). The spallation crack became more apparent when the created crack was filled by the subsequent lithium deposition, **Fig. 5.2c (iii)**. A similar process was also observed for the initiation of the transverse crack. A few pores were observed in proximity to the spallation, **Fig. 5.2c (iii)**. After one more step of charge passed, the pre-existing pores became part of the crack, with the transverse crack clearly initiated from the lowest pre-existing pore (**Fig. 5.2c (iii)** & **(iv)**, pores highlighted by red arrows). These observations suggested that dendrite initiation, for both spallation and transverse cracks, emanated with lithium deposition in pores which were close to the plating interface. Referring to the reported modelling works, and the crucial role of pores in dendrite initiation, a dendrite initiation model based on pore-filling is herein proposed, and discussed in detail in the next section.

5.3.2 Dendrite Initiation from lithium deposition in pores

Extensive efforts have been made to explain the dendrite formation in all-solid-state batteries with a Griffith flaw present at the interface[7,18,22,24,27]. However, two dendrite characteristics of paramount importance have been ignored in most models: (i) the rate-dependent nature of dendrite initiation, which means stable deposition must be allowed under a critical current density without damaging the solid electrolyte (ii) the extrusion of lithium from inside the Griffith flaw to the interface, which is inevitable once the low yield strength of lithium metal is exceeded by the build-up stress. The models based on the Poseuille pressure, where the extrusion of lithium is allowed, requires the presence of surface flaws with impractical length and aspect ratio, given the low measured critical current density in all-solid-state batteries with Li metal anode. A model to explain the dendrite initiation in practice-relevant conditions is still required.

Here, a dendrite initiation model based on experimental observations is proposed by me with supporting calculations by Guanchen Li and Charles Monroe. A pre-existing pore in the solid electrolyte can be found in proximity to the Li/SE interface to be plated. The pore is connected to the interface through a grain boundary serving as a pipe. At the pristine state, no lithium is present inside the pore or the pipe. As plating commences, lithium will be gradually deposited along the grain boundary, as it is thermodynamically preferred[18]. On reaching the pore, lithium is deposited to coat the surface of pore and thickens in the meantime due to its self-diffusion, as the interface between the deposited lithium and surface of pore is the only region where Li^+ ions and electrons can both reach. Eventually, the pore is fully filled with lithium, and the subsequent lithium deposition into the pore forces the lithium to be extruded back to the interface or grow along new grain boundaries to accommodate the freshly deposited lithium. As the deposition along another grain boundary is slow in kinetics, the back extrusion of lithium to the interface is dominant. The whole process of pore-filling is illustrated with a schematic shown in **Fig. 5.3a**.

Due to large surface area of the pore, and its position deep into the solid electrolyte, considerable flux enhancement is expected for lithium insertion, while the back extrusion rate of lithium is limited due to the small radius of the grain boundary pipe. An equilibrium can be achieved below the critical current density, when the deposited lithium can be sufficiently extruded via the pipe while the stress build-up is sustainable for the solid electrolyte (i.e. below the local fracture strength along a grain boundary of the solid electrolyte). Once the critical level of current density is exceeded, the deposited lithium will force faster plastic flow from the pore to interface, leading to severe hydrostatic stress build-up, and fracture of solid electrolyte. The magnitude of the hydrostatic stress when the pore is filled and lithium continues to plate is investigated as below.

As shown in **Fig. 5.3b**, a pore of radius R connected to the interface via a pipe with the length of L and radius of a is inside the solid electrolyte. The pore and the pipe are both filled with lithium metal. As the radius of curvature of the pipe is much smaller than that of the pore, the lithium plating over-potential on the pipe surface will be much greater than that on the surface of the pore. The concentrated flux on the surface of the pore will extrude via creep or plastic flow out via the pipe to accommodate the freshly deposited lithium. Assuming creep dominates, the plastic property of lithium relates the shear stress with the creep speed in the tube v_z, **Eq. 5.2**:

$$\tau_{rz} = -K\left|\frac{\partial v_z}{\partial r}\right|^{n-1}\frac{\partial v_z}{\partial r} \qquad 5.2$$

where the creep properties K and n have been measured via nano-indentation on lithium metal experimentally. The lithium flow out of the pore Q_{out} is controlled by the pressure difference Δp between inside the pore and the Li/SE interface, **Eq. 5.3**.

$$Q_{out} = \frac{n\pi a^3}{1+3n}\left[\frac{a\Delta p}{2KL}\right]^{\frac{1}{n}} \qquad 5.3$$

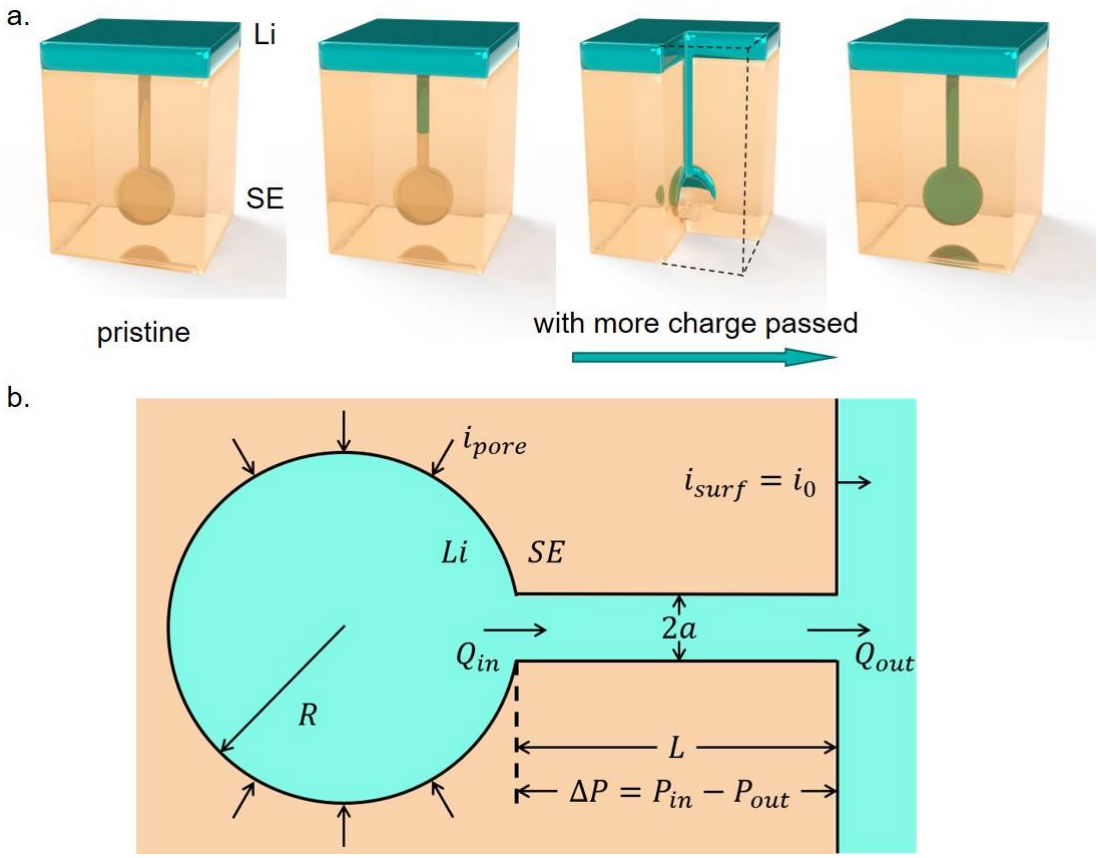

Fig. 5.3. The process of filling a pre-existing pore connected to the Li/SE interface through a grain boundary, and geometry of the dendrite initiation model. **a.** With more charge passed, the deposited lithium will grow along the grain boundary, partially fill the pore along the surface, until the pore is completed filled and deposited lithium starts to be extruded from the pore to interface. **b.** The geometry and dimensions related to the dendrite initiation model. Due to the enhanced current flux reaching the surface of the pore, lithium must be extruded out through the grain boundary to accommodate the freshly deposited lithium. With the grain boundary limiting the extrusion flux as a bottleneck, considerable hydrostatic stress is built-up in lithium.

The plating current density is assumed to be uniform throughout the surface of the pore. The plating over-potential difference between the surface of pore and the Li/SE interface follows, **Eq. 5.4**:

$$\Delta\mu_{e^-} = -\left(\frac{\bar{V}_{Li}^{M} + \bar{V}_{Li^+}^{SE}}{2z_+}\right)\frac{2\gamma}{R} - \left(\frac{\bar{V}_{Li}^{M} - \bar{V}_{Li^+}^{SE}}{z_+}\right)\Delta p + \frac{F z_{e^-} i_0 L}{\kappa} \qquad 5.4$$

where i_0 is the areal current density applied to the cell, κ is the conductivity of solid electrolyte, γ is the adhesion energy of lithium/solid electrolyte interface, $\bar{V}_{Li^+}^{SE}$ and $\bar{V}_{Li}^{M}$ are the partial molar volume of lithium in the solid electrolyte and lithium metal, respectively. With the over-potential, the total flow of lithium insertion Q_{in} can be defined by **Eq. 5.5**:

$$Q_{in} = \frac{4}{3}\pi R^3 \frac{\bar{V}_{Li}^{M}}{F z_+} i_0 \exp\left(\frac{\Delta\mu_{e^-}}{RT}\right) \quad 5.5$$

Due to the mass balance the Q_{in} and Q_{out} defined by **Eq. 5.5** and **Eq. 5.3** must be equal, so Δp can be expressed as a function of i_0, **Eq. 5.6**.

$$\Delta p \propto {i_0}^n R^{3n} a^{-3n-1} L \quad 5.6$$

So the pressure difference between the pore and the interface depend on the applied current density, the diameter of the pore, the width and length of the grain boundary. The only pressures applied to the Li/SE interface are ambient pressure and stack pressure, so the hydrostatic pressure build-up inside the pore due to lithium deposition can be estimated given certain current density, and the dimensions of pore and grain boundary. The dependence of pressure on the applied current density is plotted in **Fig. 5.4**. using two sets of geometrical parameters.

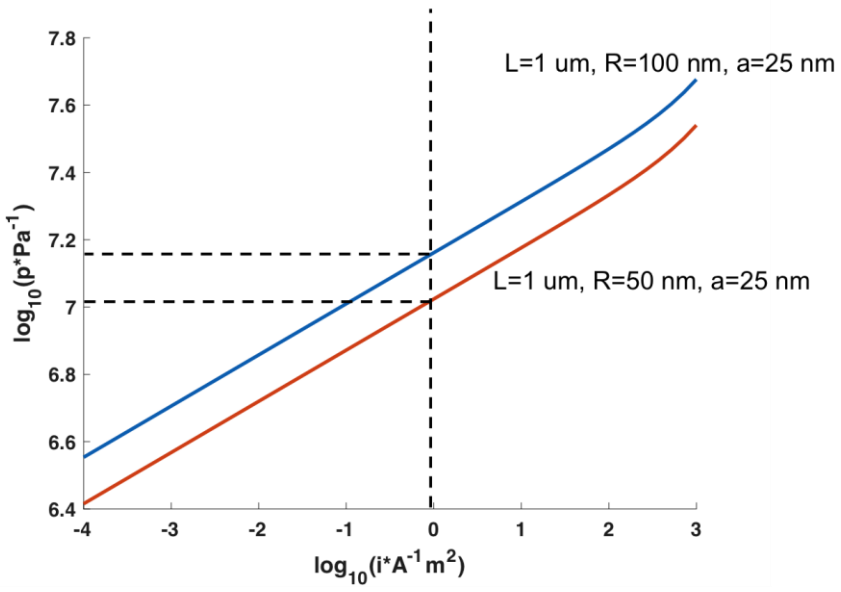

Fig. 5.4. Δp as a function of applied current density with two sets of geometrical parameters. (Figure produced by Guanchen Li).

With L=1 um, R=100 nm, and a = 25 nm, a pressure about 15 MPa can be built inside the pore at a current density of 0.1 mA/cm^2. The build-up pressure turns significantly smaller (~10 MPa) at the same current density, if the pore size is reduced. With a current density of 1 mA/cm^2, the hydrostatic pressure inside the pore can be exponentially increased to 20 MPa (R = 100 nm) and 15 MPa (R = 50 nm). The build-up pressure needs to be examined against the local fracture strength along grain boundary measured by micro-cantilever bending test to precisely predict the critical current density for dendrite initiation in practical conditions. Qualitatively, in order to improve the resistance to dendrite initiation of solid electrolyte, the size of pre-existing pores must be minimised; pores that are away from the interface whilst connected to surface must be avoided; and the grain boundary is ideally wide enough to allow sufficient extrusion and reduce the pressure build-up. The important role of the width of grain boundary in this model suggests why the oxide solid electrolyte with much higher fracture strength but narrower grain boundary could deliver a lower critical current density compared with the fragile sulphide solid electrolytes.

The proposed model for dendrite initiation is based on the assumption that lithium can be directly deposited into pre-existing pores along grain boundaries. However, the direct deposition of lithium into pores was barely experimentally investigated. To examine the direct deposition of lithium into pores during plating, the SPS Li_6PS_5Cl pellet was selected as the solid electrolyte, for its pores of smaller quantity but larger dimensions after densification. The SPS pellet after galvanostatic charge at 0.1 mA/cm^2 for 2 mAh/cm^2 was cross-sectioned with Plasma FIB-SEM to reveal the pores inside the pellet, **Fig. 5.5**. The combination of a low current density with a large capacity ensures sufficient filling of pores without any dendrite penetration.

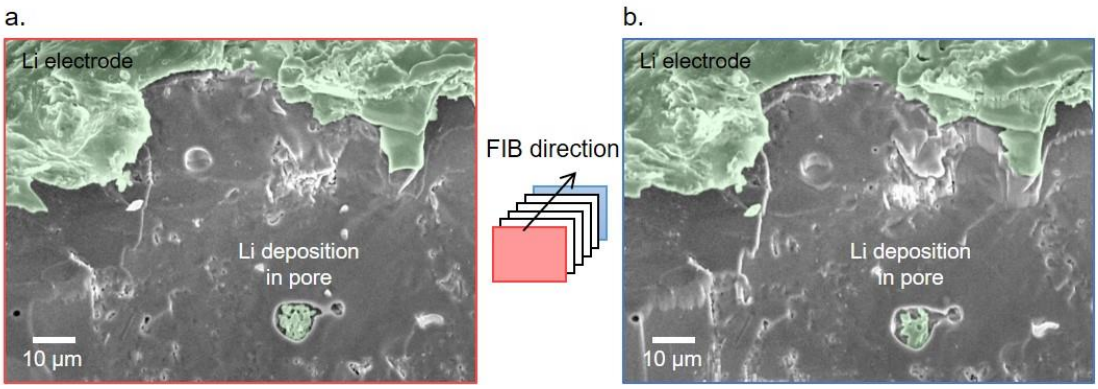

Fig. 5.5. Plasma FIB-SEM images from a series of cross-sections of the SPS Li_6PS_5Cl pellet after galvanostatic charge at 0.1 mA/cm^2 for a capacity of 2 mAh/cm^2. Green marks of the region of lithium in the SEM. A pore filled with lithium metal was observed in **a.** The rapid melting of the substance inside the pore after a few FIB slicing, similar to the lithium on the top, suggested its lithium nature.

After cross-sectioning, a large pore of almost 10 µm was observed to be filled with a substance, which presented similar morphology to the Li electrode on the top, **Fig. 5.5a**. While EDX does not work for freshly FIBed-out lithium in the vacuum chamber, the rapid melting of the substance during the PFIB sectioning, which was also observed for the Li electrode suggested the substance inside the pore is Li, **Fig. 5.5b**.

To elementally evidence the deposition of lithium inside the pores, DEMS measurement was performed on sintered Li_6PS_5Cl pellet charged under the same electrochemical conditions, with

the lithium electrode finely removed by polishing after charge. Lithium electrodes were also pressed onto a pristine pellet, which was rested under the same conditions and had the lithium electrodes finely removed using the same method. The samples were then transferred to DEMS without exposure to air for the detection of H_2, which originated from the residual deposited lithium inside the pores, **Fig. 5.6a**. Details of the DEMS measurement are shown in the Protocol section.

As shown in the plot of H_2 signals, no H_2 was detected in the pristine sample throughout the DEMS measurement of 30 mins, where the Li_6PS_5Cl pellet was completely dissolved at the end. For the sample after low current plating, no H_2 was detected at the start of DEMS measurement, suggesting a complete removal of Li electrodes on the surface. As the measurement proceeded, and the LiOH solution dissolved the outer part of the Li_6PS_5Cl pellet, clear H_2 signal was detected, suggesting the exposure of lithium inside the pores to the solution. While no other source of H_2 production was valid in the system, the DEMS results confirmed the existence of lithium metal inside the pores, even after charge at sufficiently low current density.

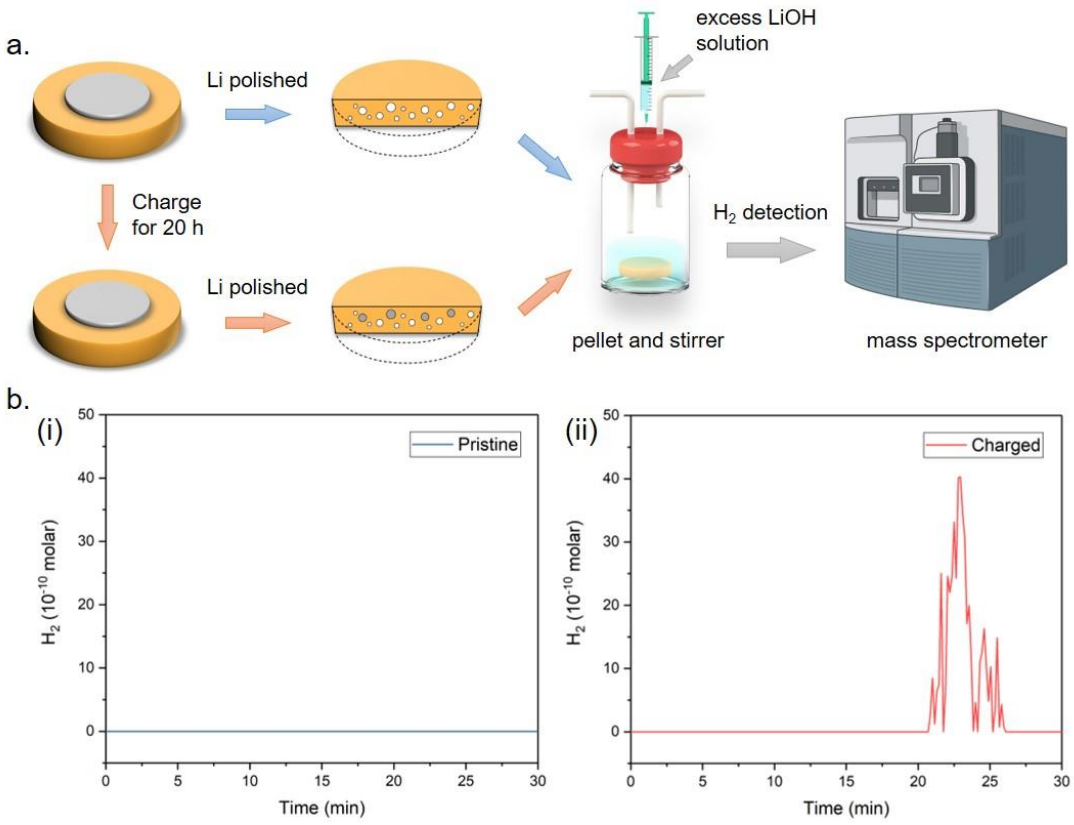

Fig. 5.6. Schematic illustrating the process of DEMS measurement, and the detected H_2 signals for the pristine and charged Li_6PS_5Cl pellets. **a.** a symmetric $Li/Li_6PS_5Cl/Li$ cell was charged/rested, and then polished to finely remove the lithium. The polished pellet was then transferred to an air-tight vial to react with excess of LiOH solution, where the generated gas was carried to the mass spectrometer and detected. **b.** H_2 signal detected since the injection of LiOH solution into the vial, for the pristine sample **(i)**, and the sample after charge **(ii)**.

While a model for dendrite initiation was proposed with its assumptions experimentally testified, one last question remained to be answered about dendrite initiation: why dendrites must emanate with spallations rather than directly form a transverse crack. The formation of spallations is attributed to the insufficient elastic energy stored by filling the pores in proximity to the Li/SE interface. As it is energetically harder to traverse the whole thickness of solid electrolyte, cracking returns to the interface, forming a spallation crack. Further lithium deposition fills the spallation crack, and the region underneath the spallation, where there is the highest current flux enhancement, will serve as the new Li/SE interface, initiating dendrites

again by filling the pores in close proximity, as observed in **Fig. 5.2c (iii)** & **(iv)**. The initiated cracks will then either propagate towards the other electrode, if there is sufficient elastic energy, or return to the interface and form a spallation once again. This nicely explains the observed emergence of new spallations at places where a spallation has formed.

5.3.3 The wedge-opening nature of dendrite propagation

While the dendrite initiation relies on the filling of pores to generate sufficient pressure in order to crack the solid electrolyte, the process of dendrite propagation is intrinsically different from initiation, as the dendritic cracks were observed to propagate without lithium filling the crack. While the *operando* observations suggested the wedge-opening nature of dendrite propagation, analytical modelling and simulation are needed to testify whether lithium can wedge-open the ceramic, given the low yield strength of lithium.

The dendrite initiation created a long crack (~200 μm) in the solid electrolyte, as observed in the *operando* XCT scans. The dendritic crack does not only propagate from the plated electrode towards the stripped electrode, but also along a plane that is orthogonal to the Li/SE interface. So instead of treating the dendrite as a lithium pillar inside a pipe, it is more appropriate to describe the dendrite as a planar crack partially occupied by a lithium film of certain thickness. The problem geometry of dendrite propagation is shown in **Fig. 5.7a**. A solid electrolyte with a straight crack as the initiated dendritic crack is considered. The plated electrode is placed on the top of the solid electrolyte, with a uniform stack pressure applied. The lithium dendrite, with the same width of the crack, propagates along the dry crack, but far behind the crack tip. As cross-sections orthogonal to the crack plane are all identical, the model can also be equivalently considered in 2D.

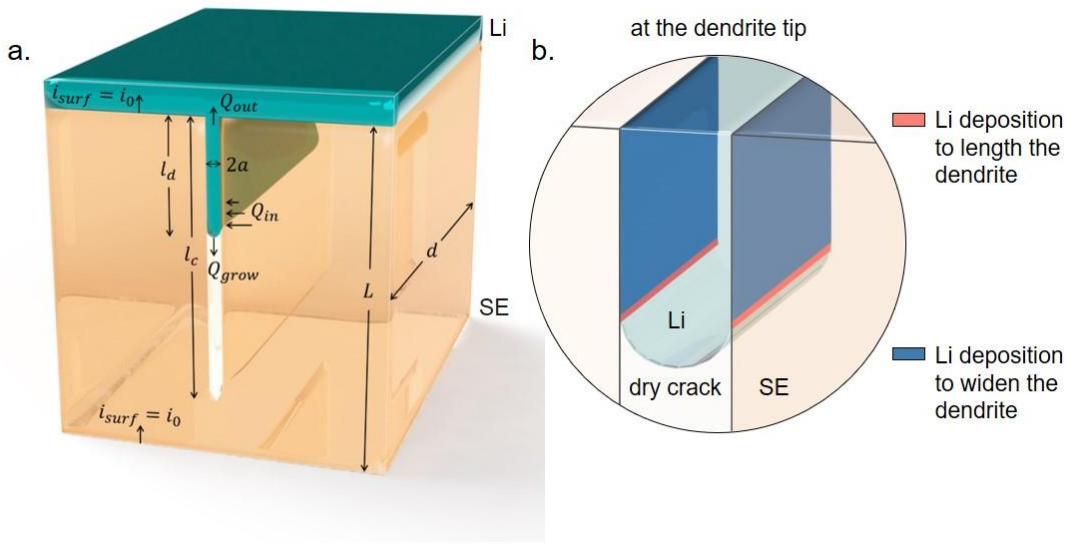

Fig. 5.7. a. Geometry of the dendrite propagation model. **b.** Schematic showing the magnified region near the dendrite tip, illustrating why lithium deposition inevitably leads to widening of the crack due to plating kinetics. The region where lithium deposition contributes to lengthening and widening of dendrite, are marked with red and blue, respectively.

As electrochemical charge starts, the deposited lithium drives the dendrite to lengthen and thicken, and further wedge-open the dendritic crack. The wedge-opening behaviour of the dendrite tip instead of a fast coating on the surface of dry cracks is rooted in the deposition kinetics at the dendrite tip. A magnified image of the region around dendrite tip is shown in **Fig. 5.7b**. Only the region that can be reached by both Li^+ from the solid electrolyte and e^- from the lithium metal allows lithium deposition to take place, i.e. the contact interface between the dendrite and the SE. While lithium deposition at the three-phase-joining region contributes directly to dendrite lengthening, as the deposited lithium can freely grow towards to empty space without any mechanical resistance (marked as the red region in **Fig. 5.7b**); over the majority of the surface area the lithium deposition primarily contributes to the thickening of the dendrite (marked as the blue region in **Fig. 5.7b**). Due to the current flux enhancement around the dendrite tip, the current density in the red region can be higher than that in the blue region. However, the difference in current density will be overwhelmed by the significant difference in their surface area. Without further propagation of the crack, the width of the crack is

essentially fixed due to the high stiffness of the electrolyte. Therefore, the deposited lithium in the blue region is forced to creep either towards the crack tip or to the root of dendrite, in order to accommodate the subsequent lithium deposition. As a result, the lithium dendrite is compressed; and a compressive stress, which is limited by the maximum yield strength of lithium is applied to surface of the crack, driving the crack to wedge-open.

The stress intensity factor (SIF) at the dry crack tip from the compressive stress on the crack under practice-relevant conditions is examined against the fracture toughness of the solid electrolyte by the following analytical modelling combined with finite element modelling, completed by Guanchen Li and Yang Chen. Dimensions of the sample, crack, and dendrite were adopted from the cell used for *operando* XCT scans, with a crack length l_c = 200 μm, crack width $2a$ = 2 μm, electrolyte thickness $L = 1$ mm, and dendrites length $l_d = 10$, 50, 100, 200 μm to present different status of dendrite propagation. The applied areal current density was set to 3 mA/cm^2, identical to the *operando* experiments. The crack tip was modelled as a semiellipse to avoid extreme stress concentration.

The behaviour of lithium:

The mechanical behaviour of lithium dendrite is a controversial topic of intense discussion. While lithium presents a considerably low yield strength of 0.7 MPa as a bulk[28], recent studies from Greer et al. demonstrated a two-order-higher yield strength of lithium in the compression of a micro-sized lithium pillar[29,30]. However, whether such size-dependent enhancement of a stand-alone lithium pillars can be applied to lithium dendrite, a thin film in contact with the rough surface of ceramic, remains unclear. The analytical modelling work by McMeeking et al. suggested that the size-dependent consideration by Greer et al might not hold for practical conditions, as any crack longer than 1 nm for oxide, and 1 pm for sulphide solid electrolytes will be wedged open at practical current density with the size-dependent enhancement[24].

Here, only the yield strength enhancement of lithium up to a few folds at considerable strain rates is taken into account, which originates from the plastic flow of lithium metal inside the

dendrite. As illustrated in **Fig. 5.6b**, the current distribution around the crack will induce non-uniform lithium deposition. Due to the lithium plating on the side of the dendrite, the pressure at the dendrite tip p_1 will be higher than that at the open crack p_0 and the Li/SE interface p_2. The pressure difference between p_0, p_1, and p_2 determines the creep flow of lithium at the tip and root of the dendrite. The governing equation of the lithium plastic flow is given by the momentum balance, **Eq. 5.7**:

$$-\vec{\nabla}p + \vec{\nabla}\cdot\left(\eta\dot{\vec{\varepsilon}}_p\right) = 0 \tag{5.7}$$

The pseudo-viscosity η in the equation is given by the plastic properties of lithium, **Eq. 5.8**:

$$\eta = K(\dot{\varepsilon})^{n-1} \tag{5.8}$$

where

$$\dot{\varepsilon} = \sqrt{2\dot{\vec{\varepsilon}}_p : \dot{\vec{\varepsilon}}_p} \tag{5.9}$$

and

$$\dot{\vec{\varepsilon}}_p = \frac{1}{2}\left(\vec{\nabla}\vec{v} + \vec{\nabla}\vec{v}^T\right) \tag{5.10}$$

The compressive stress distribution can then be solved by setting the pressure boundary conditions of p_1, p_2 and the velocity boundary conditions at the four edges of the lithium dendrite (two dendrite/SE interfaces, the front and root of lithium dendrites), given a certain current density distribution.

The role of current density:

The stack pressure and the applied current density are two external variables that affect the SIF at the crack tip. While stack pressure contributes towards the SIF, and more importantly restricts the extrusion of lithium from the dendrite root, and current density distribution defines the plastic flow of lithium, thus the distribution of compressive stress. Due to the remarkable current flux enhancement around the tip of dendrite, the current density distribution on the

surface of dendrite should not be simplified as a single value that equals to the areal current density at the interface; instead, the current density distribution should be precisely determined with modelling, given any given length of lithium dendrite or dry crack.

The electric potential associated with current density distribution can be solved with the Laplace's equation:

$$\nabla^2 \Phi = 0 \tag{5.11}$$

The Dirichlet boundary holds at the interface of lithium electrode and SE, where $\Phi = 0$ at the plating side, and $\Phi = 1$ at the stripping side. A Neumann boundary condition of $\partial\Phi = 0$ is applied to the edge of the dendritic crack. With these boundary conditions, the current density distribution can be plotted with different lengths of dendrites partially or fully filled the initiated crack (l_d = 10, 50, 100, 200 μm), **Fig. 5.8**. The current density has been normalised by the areal current density applied to the cell. The white strip on the bottom left corner represents the dendritic crack. As current density distribution is symmetric on both sides of the crack, only one side is shown in the **Fig. 5.8** for simplicity.

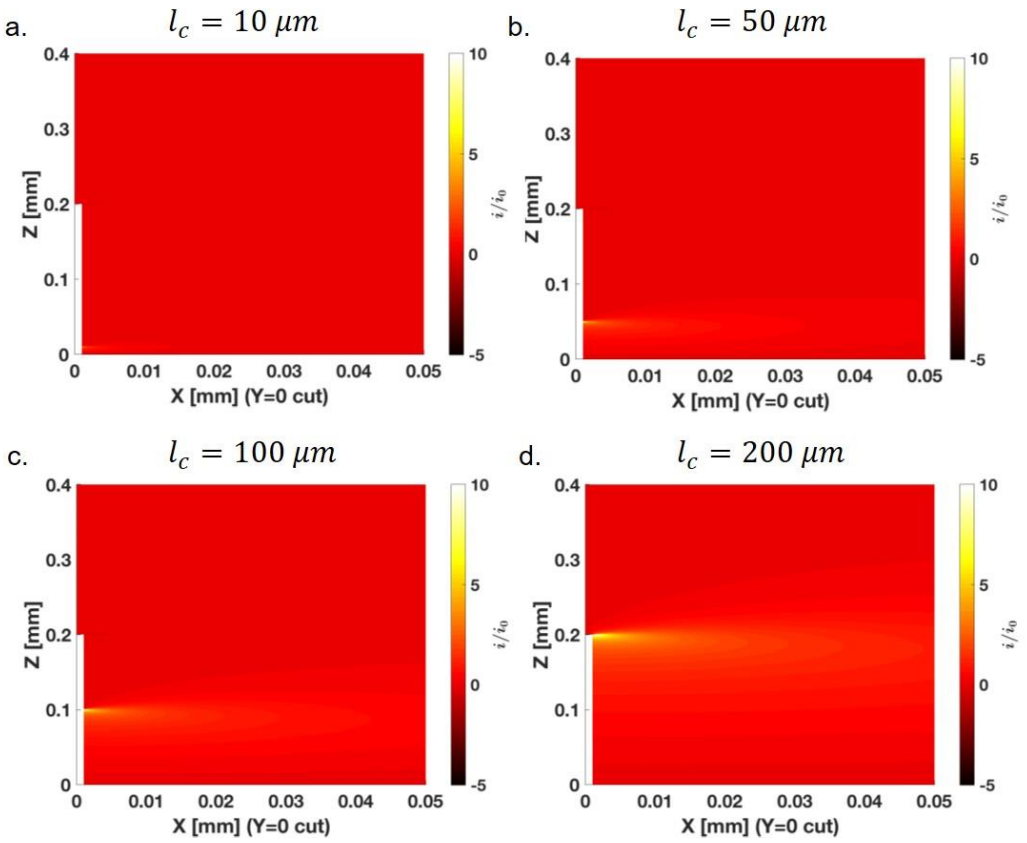

Fig. 5.8. Current density distribution around the dendritic crack with dendrites of different lengths filling the crack. The value of current density shown by the colour contour has been normalised to the areal current density at the interface. (Figure produced by Guanchen Li).

The obtained current density distribution could also be extracted, and expressed as a current density concentration factor (current density normalised to areal current density) along the length of dendrite from the root towards the crack tip, **Fig. 5.9**.

With the spatially resolved current density distribution, which provides the flow rate of lithium, the spatial distribution of compress stress from lithium can be obtained. At a quasi-steady state, where the length of crack and length of dendrite are known, the compressive stress from lithium deposition within the crack can be converted to an equivalent stress field applied to the solid electrolyte. The SIF can therefore be obtained, to be examined against the fracture toughness of the SE.

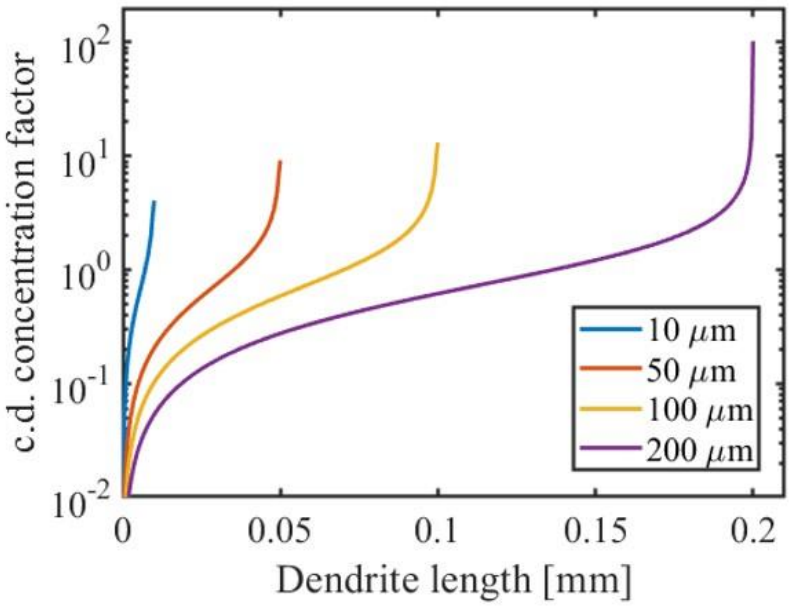

Fig. 5.9. Current density distribution along the surface of the dendrite from the root to the dendrite tip. Different colours represent dendrites of different lengths in a 200 μm long dendritic crack. (Figure produced by Guanchen Li).

The determination of SIF and CCD for dendrite propagation:

The stress field obtained using the FE model in Abaqus was used for the calculation of the stress intensity factor, K at the crack tip, using the J-integral method that is implemented in the software. The geometry of the solid electrolyte and crack were the same as aforementioned. 2D plane strain tetrahedral elements were used for the finite element mesh. The electrolyte was given a linear elastic material property, with Young's modulus of 22.1 GPa, and Poisson's ratio of 0.37 from nano-indentation. The simulated SIF was then examined against the fracture toughness of the SE, which was experimentally measured via nano-indentation. The roadmap of the modelling for dendrite propagation are shown in **Fig. 5.10a**, together with the schematic outlining the set-up of finite element modelling, **Fig. 5.10b**.

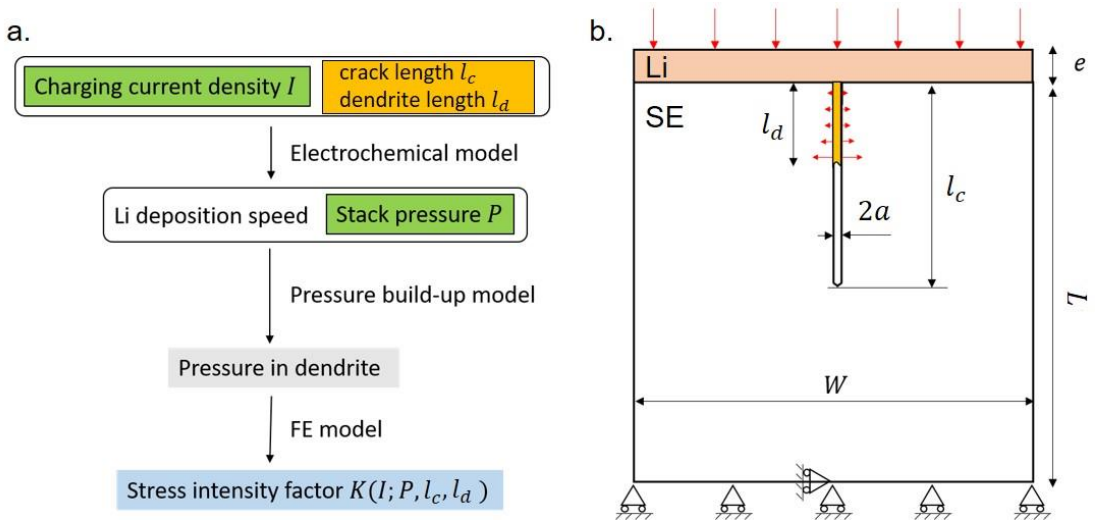

Fig. 5.10. a. Roadmap of the modelling for dendrite propagation. **b.** Geometry of the dendrite propagation model for finite element simulation. (Figure produced by Yang Chen).

By comparing the SIF with the fracture toughness of given solid electrolyte, a critical length of dendrite above which the dendritic crack is forced to propagate can be determined, given a certain current density; or a critical level of current density, above which the subsequent lithium deposition will drive a dendrite of a known length to wedge-open the dendritic crack.

It is noteworthy that while the distribution of current density and the SIF were both calculated in quasi-steady states, the actual process of dendrite growth is a continuous process with fast kinetics. A sufficiently large area under considerable compressive stress is required to achieve a critical SIF, the initiated crack wouldn't propagate as soon as the first lithium is deposited to fill the dry crack. Instead, sustainable lithium deposition can be expected to fill the crack after dendrite initiation, without wedging-open the crack further. Only when sufficient current flux enhancement is created with a dendrite of considerable length, does the plastic flow of lithium drive the dendritic crack to propagate further. Once the crack is propagated, the stress is released by the cracking of SE, sustainable lithium deposition takes place again, until the dendrite reaches a second critical length to propagate the crack again. This is consistent with a step-by-step propagation of the dendritic crack observed in our characterisations, along with a gradual lithium dendrite penetration into the crack, behind the crack tip.

5.3.4 Model predictions and pressureless lithium plating

Apart from explaining the process of the dendrite propagation, two important predictions are also made by the propagation model. Comparing the dendrite initiation with propagation, while considerable hydrostatic stress can be built up for initiation, as the deposited lithium is constrained inside the pore and is forced to be extruded out, the compressive stress of lithium during dendrite propagation is limited, as the dendrite can also creep towards the empty crack to release the stress. While the compressive stress terms for initiation and propagation both have the stack pressure applied to cell linearly added to the value, the stack pressure of a few MPa must play a much more significant role in dendrite propagation than dendrite initiation. That said, the effect of stack pressure on limiting the extrusion of lithium and aiding the compressive stress build-up is more pronounced during dendrite propagation than dendrite initiation. This suggests that the removal of a stack pressure could largely increase the critical current density for dendrite propagation, while its effect on the CCD for initiation is insignificant.

Secondly, while further current flux enhancement and increased SIF are expected as the dendrite inside the crack lengthens, an upper limit can be set to the SIF given a certain current density, which is the SIF when the initiated crack has been fully filled with the deposited lithium. If the SIF at the crack tip is still below the fracture toughness of SE when the initiated crack is filled by lithium, sustainable plating can be achieved, despite the initiated crack inside the solid electrolyte.

Motivated by the above two important predictions, cell cycling with no stack pressure but only ambient pressure applied was performed to testify whether sustainable cycling can be achieved with a remarkably increased current density. The cycling consists of a plating at the WE at a target current density, and a sufficiently slow stripping (0.05 mA/cm^2) for the same capacity (0.5 mAh/cm^2) to avoid any current hot spots from void formation at the interface. During cycling, the voltage was measured between the working electrode and a reference electrode on

the side of the working electrode, to reflect the propagation of dendrite by the drop in cell voltage. Cell cycling was conducted on identical cells with various plating current densities, until the short-circuit of the cell, or one hundred cycles was achieved without short-circuit. After several attempts, the critical current density below which the dendritic crack initiates but does no propagate even when filled with lithium metal was confirmed to be at 4.0 mA/cm^2 without stack pressure applied. This CCD for propagation is much higher than the reported CCD of argyrodite with stack pressure applied[31,32]. The differences in cycling behaviour and voltage evolution from cells cycled at below (4.0 mA/cm^2) and above (5.0 mA/cm^2) the CCD for propagation are shown in **Fig. 5.11**.

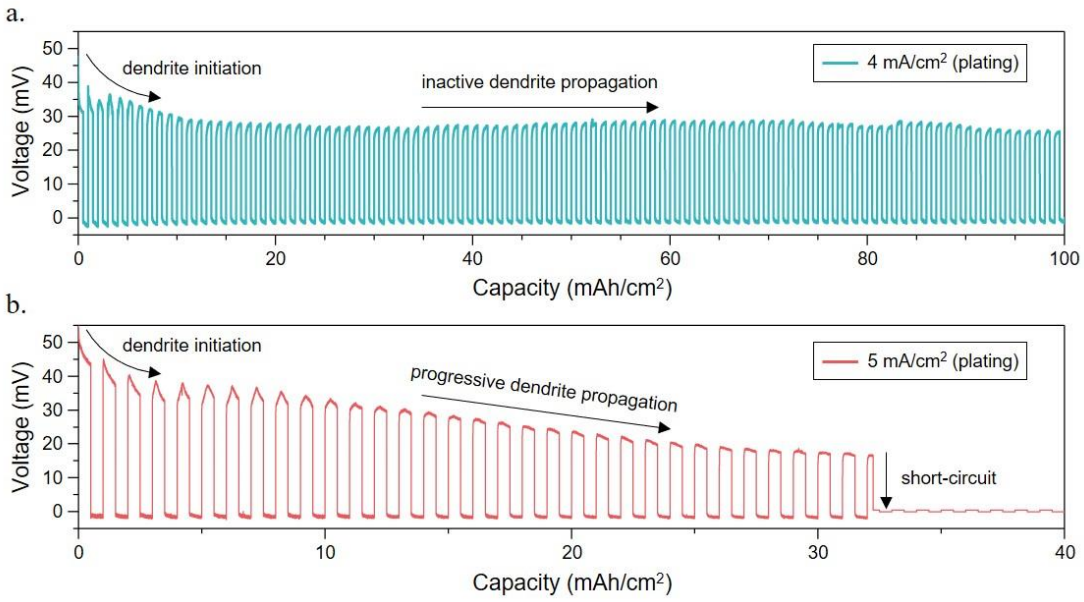

Fig. 5.11. Voltage versus capacity curve for pressureless cycling at a plating current density of **a.** 4.0 mA/cm^2 and **b.** 5.0 mA/cm^2, respectively. The cell voltage was measured between the working electrode and the reference electrode, with the drop in cell voltage demonstrating dendrite propagation into the solid electrolyte.

An apparent voltage drop was detected for both cells cycled at 4.0 mA/cm^2 and 5.0 mA/cm^2 in the first few cycles. The drop in cell voltage results from the dendrite initiation and the subsequent filling of dendritic crack with deposited lithium, which can both increase the effective contact area between the working electrode and the solid electrolyte. While the

gradual drop in cell voltage ceased for the cell cycled at 4.0 mA/cm^2 after a few cycles, suggesting the stop of dendrite propagation when the dendritic crack is filled; a continuous voltage drop was observed for the cell cycled at 5.0 mA/cm^2, corresponding to a progressive dendrite propagation across the solid electrolyte. With further propagation of the dendrite, the cell voltage continuously dropped until a short circuit at the 33rd cycle, as the dendrite reached the other electrode, forming an electronic conduction path. While cell failure was eventually achieved, it is noteworthy that it took a much larger capacity and number of cycles to reach a short circuit, compared with a cell cycled at the same current density with a stack pressure applied. This suggested the considerable extrusion of lithium from the dendrite towards the interface without any stack pressure applied, which effectively slowed down the rate of dendrite growth. In stark contrast, the cell cycled at 4.0 mA/cm^2 survived for 100 cycles without a short circuit.

The reliable cycling at a considerable current density of 4.0 mA/cm^2 achieved by simply removing the stack pressure, suggests the non-fatal nature of dendrite initiation in all-solid-state batteries. The dendrite initiation does not necessarily lead to a short-circuit, instead, the all-solid-state batteries can live with the initiated crack and maintain fully functional, as long as those cracks don't propagate further. This finding paves the way towards the practical application of all-solid-state batteries with great energy density as well as power density.

5.3.5 Performance of spark plasma sintered Li_6PS_5Cl pellet

As dendrite initiation and propagation both rely on the creation of cracks by the hydrostatic stress build-up as suggested by the models, to allow a faster flow of lithium (greater current density), the mechanical properties of the solid electrolyte need to improved. Therefore, advanced sintering technique, such as SPS, can be expected to optimise the performance of a solid electrolyte. Here, SPS is performed on Li_6PS_5Cl solid electrolyte inside an Ar-filled glovebox at various temperatures to compare the phase purity the structure of the resulting products. The method of SPS is detailed in the Protocol section (**Chapter 5.2.9**).

Li_6PS_5Cl powder was loaded into a graphite die and sintered via SPS at 250, 350, 400, 450, 550 ℃ with 50 MPa uniaxial pressure applied, respectively. The sintered pellets were carefully polished to remove any residual graphite on the surface, ground into powder, and analysed by PXRD to examine their phase purity, **Fig. 5.12**.

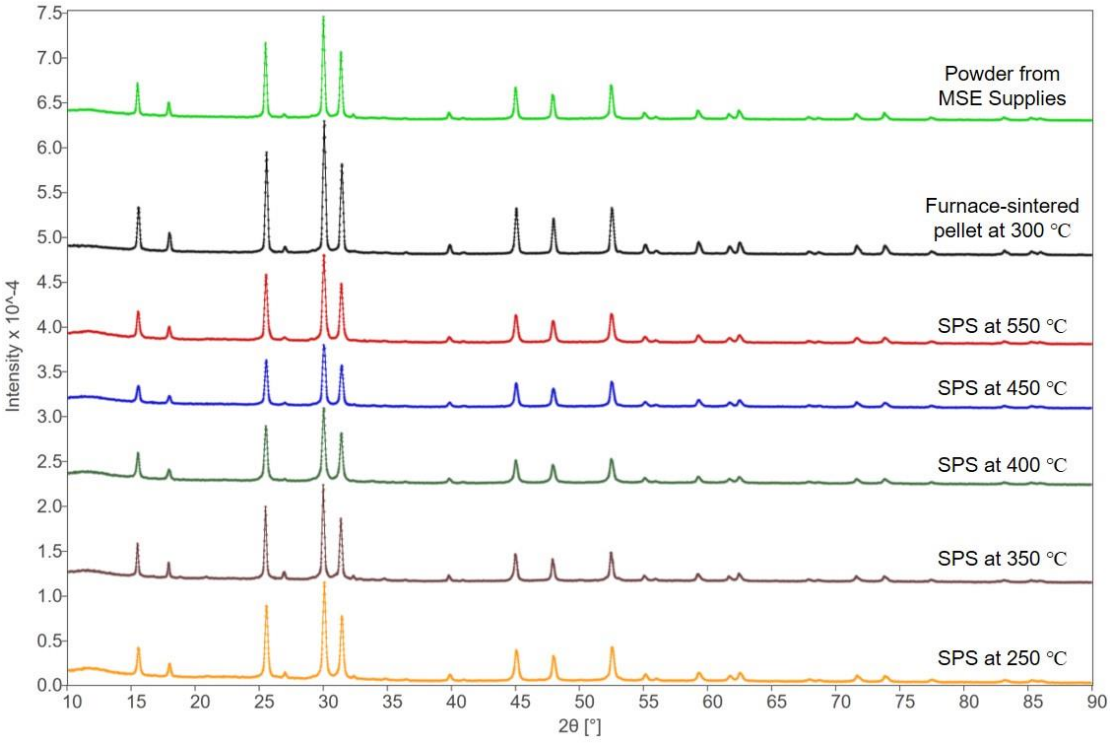

Fig. 5.12. PXRD patterns of pristine Li_6PS_5Cl powder as purchased, and powder from pellets sintered with a furnace inside the glovebox, and with SPS at 250, 350, 400, 450, 550 ℃, respectively. The identical diffraction patterns suggest no phase change or contamination arises due to SPS treatment.

As the pristine commercial powder from the furnace-sintered pellet and the powder from the SPS samples at various temperatures share identical PXRD patterns, it can be confirmed that no phase change or impurity arise due to SPS processing.

The SPS pellets were then cross-sectioned with an ultrasonic cutter to examine the extent of densification at different sintering temperatures, **Fig. 5.13**. A cross-sectional SEM from a furnace-sintered pellet, which was made by the standard routine of sample preparation (as detailed in **Chapter 4.2.4**) was added as a reference.

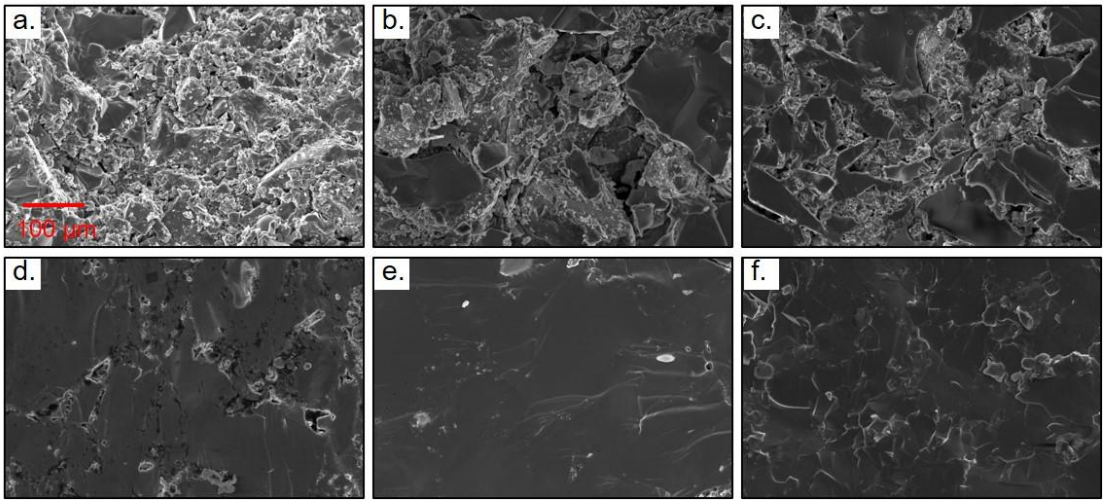

Fig. 5.13. Cross-sectional SEM images of argyrodite pellet from **a.** furnace-sintering, and SPS sintering at **b.** 250 ℃, **c.** 350 ℃, **d.** 400 ℃, **e.** 450 ℃, and **f.** 550 ℃. Apparent grain growth and pore elimination were observed as the sintering temperature increased.

Apparent grain growth and pore elimination were observed from the cross-sectional SEM images, suggesting a more effective densification by SPS as the sintering temperature increased. As porosity and broad grain boundaries contribute negatively to the ionic conductivity of solid electrolyte pellets, it is interesting to compare the conductivities of furnace-sintered pellets with SPS pellets. As samples sintered at 450 ℃ and 550 ℃ hardly maintained mechanical integrity after sintering, potentially due to rapid volume change, a pellet sintered at 400 ℃ by SPS was selected for conductivity measurement. The ionic and electronic conductivities, measured by the method specified in the Protocol are shown below in **Fig. 5.14**.

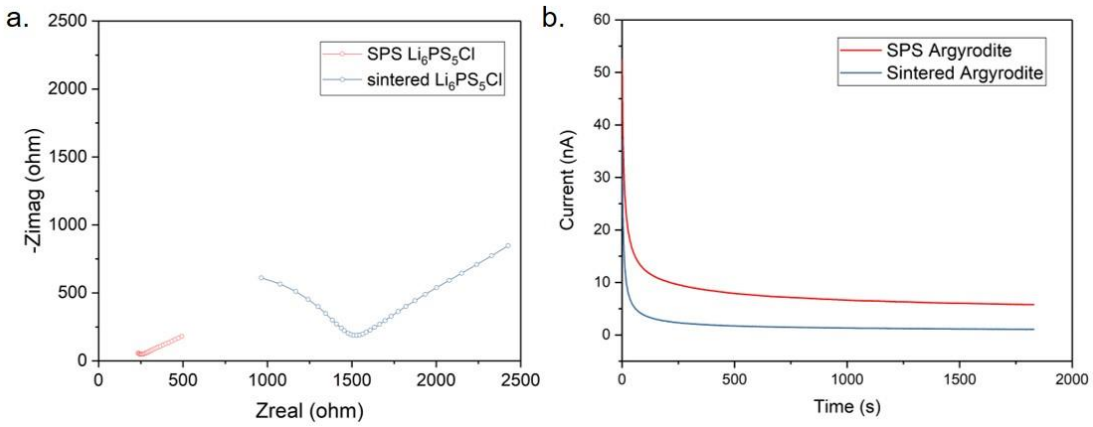

Fig. 5.14. Comparison of conductivities between SPS Li_6PS_5Cl pellet and furnace-sintered Li_6PS_5Cl pellet by **a.** EIS and **b.** potentiostatic charging. The electronic conductivity of pellet was determined with the potentiostatic charging, when a steady current was achieved with the given voltage bias.

As shown in the EIS curves, the Li_6PS_5Cl pellet sintered at 400 °C via SPS presents a much-improved total conductivity (7.35×10^{-3} S/cm) compared with the furnace-sintered Li_6PS_5Cl pellet (9.43×10^{-4} S/cm), **Fig. 5.13a**. To confirm the improved conductivity originates from structural densification rather than a remarkable improvement in electronic conductivity due to the potential graphite infiltration during SPS, the electronic conductivities of the above samples were measured and compared, **Fig. 5.13b**. The comparable electronic conductivities between the SPS pellet (1.17×10^{-7} S/cm) and the furnace-sintered pellet (1.55×10^{-8} S/cm) demonstrate no graphite infiltration into the sample. It is also noteworthy that the electronic conductivity of SPS pellet is enhanced from the furnace-sintered pellet for the same scale as for their ionic conductivities, suggesting that all the improvement in ionic conductivity can be attributed to a structural densification.

While the SPS pellets present a reduced porosity, and improved conductivity, it is important to examine its performance in cycling, regarding of resistance to dendrite formation. Rate tests were then performed on SPS and furnace-sintered pellets based on a two-electrode Li/Li_6PS_5Cl/Li symmetric cell set-up with a stack pressure of 7 MPa applied, **Fig. 5.15**.

Galvanostatic cycles were performed for a capacity of 1 mAh/cm^2 for charge/discharge and a current density increase of 0.25 mA/cm^2 after each cycle, until the short-circuit of the cell.

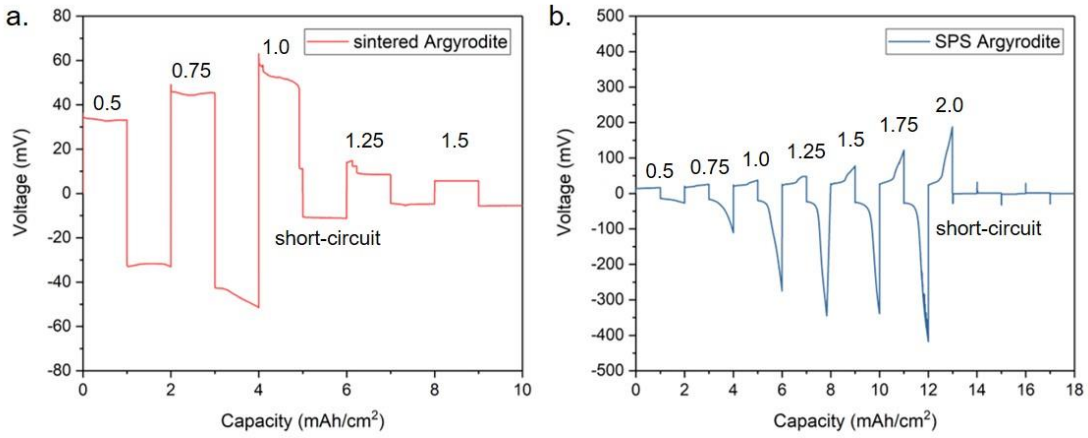

Fig. 5.15. Voltage versus capacity plot from rate tests on two-electrode symmetric cells with **a.** the furnace-sintered pellet and **b.** the SPS pellet. The numbers above the curve annotates the current density of the corresponding cycle. The short circuit during cycling was marked in the plot with text.

While a short circuit was detected at the cycle with a current density of 1.0 mA/cm^2 for the furnace-sintered sample, no short circuit was detected for the SPS pellet until the cycle at 2.0 mA/cm^2. With twice the CCD of a furnace-sintered sample, the SPS pellet certainly has a better resistance to dendrite formation, consistent with the model prediction. While SPS with the joint effects of heating and pressurisation can density the solid electrolyte to a satisfactory level (>98%) thus useful for proof-of-concept study, it is not applicable for large-scale applications due to its high-cost, low throughput, and strict requirement of vacuum. While SPS brings about multi-perspective changes to the solid electrolyte, including densification, open pore elimination, improvement in mechanical properties, and narrowing of grain boundaries, the effect of every single perspective must be investigated separately to figure out the dominant factor that contributes towards the improvement of cell performance. The result could suggest promising densification methods which are feasible in all-solid-state battery pipeline. Future work should also aim to test the mechanical properties of SPS samples, and compare that with

the furnace-sintered samples. More advanced method of cell testing is also needed, to separate the effect of solid electrolyte properties on dendrite initiation and propagation, respectively. In addition, other toughening method, such as fibre-reinforcement and transformation toughening might be employed to prevent the propagation of dry cracks. Such toughening methods with insignificant changes to other properties of solid electrolyte can help testify to what extent the dendrite propagation can be blocked merely from the mechanical perspective.

5.4 Conclusions

In this chapter, operando X-ray computed tomography with unprecedentedly high time resolution based on a synchrotron pink beam X-ray was employed to characterise the complete process of dendrite formation, from the very initiation until a complete short-circuit. The *operando* X-ray computed tomography reveals the different behaviour of dendrite initiation and dendrite propagation, suggesting the process of dendrite initiation associated with pore-filling, and the dendrite propagate, which is in essence a process of wedge-opening. Based on the observations and limitations of previous models, two models were proposed to explain the mechanisms of the dendrite initiation and propagation, respectively. The dendrite initiation model based on the hydrostatic stress build up during the lithium extrusion from a pore to the Li/SE interface nicely explains the rate-dependent characteristic of dendrite formation. Based on this model, sufficient stress build-up to initiate a crack at practice-relevant conditions can also be obtained, even when the extrusion of lithium is allowed. The effects of pore size, width of grain boundary, mechanical properties of the solid electrolyte on dendrite initiation were also discussed. The deposition of lithium into pores in proximity to the Li/SE interface was evidenced with PFIB-SEM and DEMS.

The dendrite propagation model explains how an initiated crack can be wedged-open in charge when the lithium dendrite is far behind the crack tip. The origin of a wedge-opening process was addressed with deposition kinetics. Electrochemical model was employed to calculate the

current density distribution around the surface of a dendrite, which was then used to model the plastic flow of lithium metal. The compressive stress resulting from the plastic flow of lithium was then calculated, and used to calculate the SIF at the crack tip via finite element modelling. Importantly, the dendrite propagation model predicts much more difficult crack propagation at given current densities when no stack pressure is applied. Pressureless cycling was then performed to testify the prediction. With the dendritic crack initiated but not further propagated, sustainable cycling at a current density up to 4.0 mA/cm^2 was achieved with the removal of stack pressure, suggesting the non-fatal nature of dendrite initiation.

Finally, SPS as an advanced sintering technique was employed to improve the performance of the solid electrolyte by eliminating open pores and enhancing the mechanical properties. Verified by PXRD and SEM, considerable densification of Li_6PS_5Cl was achieved, without any phase change or involvement of impurity. Based on the effective densification of pellets, greatly enhanced ionic conductivity and resistance to dendrite formation were also achieved. However, due to the barriers of using SPS as a scalable technique, alternative densification methods that could provide comparable densification with low cost, such as hot-pressing or warm isostatic press should be investigated.

To further complement the model, extensive efforts are now needed with comprehensive mechanical tests on solid electrolyte and lithium, from nanoscale to a cell level. While the dendrite model explains the fundamental mechanisms of dendrite initiation and propagation, and guides effective strategies to block the dendrite, systematic research is required to investigate the separate effects of each factor on cell failure, by employing strategies that may only change one aspect of electrolyte property at a time. Such results could guide the further development of solid electrolytes, improving the cycling performance of all-solid-state batteries with the most cost-effective approaches.

5.5 References

1. Wu, B. *et al.* The role of the solid electrolyte interphase layer in preventing Li dendrite growth in solid-state batteries. *Energy Environ. Sci.* **11**, 1803–1810 (2018).

2. Marbella, L. E. *et al.* ^{7}Li NMR Chemical Shift Imaging to Detect Microstructural Growth of Lithium in All-Solid-State Batteries. *Chem. Mater.* **31**, 2762–2769 (2019).

3. Aguesse, F. *et al.* Investigating the dendritic growth during full cell cycling of garnet electrolyte in direct contact with Li metal. *ACS Appl. Mater. Interfaces* **9**, 3808–3816 (2017).

4. Cheng, E. J., Sharafi, A. & Sakamoto, J. Intergranular Li metal propagation through polycrystalline $Li_{6.25}Al_{0.25}La_3Zr_2O_{12}$ ceramic electrolyte. *Electrochim. Acta* **223**, 85–91 (2017).

5. Manalastas, W. *et al.* Mechanical failure of garnet electrolytes during Li electrodeposition observed by in-operando microscopy. *J. Power Sources* **412**, 287–293 (2019).

6. Kazyak, E. *et al.* Li Penetration in Ceramic Solid Electrolytes: Operando Microscopy Analysis of Morphology, Propagation, and Reversibility. *Matter* **2**, 1–24 (2020).

7. Porz, L. *et al.* Mechanism of Lithium Metal Penetration through Inorganic Solid Electrolytes. *Adv. Energy Mater.* **7**, 1–12 (2017).

8. Krauskopf, T. *et al.* The Fast Charge Transfer Kinetics of the Lithium Metal Anode on the Garnet-Type Solid Electrolyte $Li_{6.25}Al_{0.25}La_3Zr_2O_{12}$. *Adv. Energy Mater.* **2000945**, (2020).

9. Shen, F., Dixit, M. B., Xiao, X. & Hatzell, K. B. Effect of Pore Connectivity on Li Dendrite Propagation within LLZO Electrolytes Observed with Synchrotron X-ray Tomography. *ACS Energy Lett.* **3**, 1056–1061 (2018).

10. Dixit, M. B. *et al.* In Situ Investigation of Chemomechanical Effects in Thiophosphate Solid Electrolytes. *Matter* **3**, 2138–2159 (2020).

11. Seitzman, N. *et al.* Operando X-ray Tomography Imaging of Solid-State Electrolyte Response to Li Evolution under Realistic Operating Conditions. *ACS Appl. Energy Mater.* **12**, 59 (2021).

12. Otoyama, M. *et al.* Visualization and Control of Chemically Induced Crack Formation in All-Solid-State Lithium-Metal Batteries with Sulfide Electrolyte. *ACS Appl. Mater. Interfaces* (2021). doi:10.1021/acsami.0c18314

13. Wu, X. *et al.* Operando Visualization of Morphological Dynamics in All-Solid-State Batteries. *Adv. Energy Mater.* **9**, 1–10 (2019).

14. Seitzman, N. *et al.* Toward all-solid-state lithium batteries: Three-dimensional visualization of lithium migration in β-Li_3PS_4 ceramic electrolyte. *J. Electrochem. Soc.* **165**, A3732–A3737 (2018).

15. Doux, J. *et al.* Stack Pressure Considerations for Room Temperature All-Solid-State Lithium Metal Batteries. *Adv. Energy Mater.* 1903253 (2019). doi:10.1002/aenm.201903253

16. Ning, Z. *et al.* Visualizing plating-induced cracking in lithium-anode solid-electrolyte cells. *Nat. Mater.* 1–9 (2021). doi:10.1038/s41563-021-00967-8

17. Hao, F., Wang, W. & Mukherjee, P. P. Electrochemical-Reaction-Driven Interfacial Stress in a Solid-Solid Layered Architecture ELECTROCHEMICAL-REACTION-DRIVEN... HAO, WANG, and MUKHERJEE. *Phys. Rev. Appl.* **11**, 34038 (2019).

18. Raj, R. & Wolfenstine, J. Current limit diagrams for dendrite formation in solid-state electrolytes for Li-ion batteries. *J. Power Sources* **343**, 119–126 (2017).

19. Mo, F. *et al.* Inside or Outside: Origin of Lithium Dendrite Formation of All Solid-State Electrolytes. *Adv. Energy Mater.* **9**, 1–10 (2019).

20. Ma, J., Chen, B., Wang, L. & Cui, G. Progress and prospect on failure mechanisms of solid-state lithium batteries. *J. Power Sources* **392**, 94–115 (2018).

21. Barroso-Luque, L., Tu, Q. & Ceder, G. An Analysis of Solid-State Electrodeposition-Induced Metal Plastic Flow and Predictions of Stress States in Solid Ionic Conductor Defects. *J. Electrochem. Soc.* **167**, 020534 (2020).

22. Athanasiou, C. E., Jin, M. Y., Ramirez, C., Padture, N. P. & Sheldon, B. W. High-Toughness Inorganic Solid Electrolytes via the Use of Reduced Graphene Oxide. *Matter* **3**, 212–229 (2020).

23. Feldman, L. A. & De Jonghe, L. C. Initiation of mode I degradation in sodium-beta alumina electrolytes. *J. Mater. Sci.* **17**, 517–524 (1982).

24. Klinsmann, M., Hildebrand, F. E., Ganser, M. & McMeeking, R. M. Dendritic cracking in solid electrolytes driven by lithium insertion. *J. Power Sources* **442**, 227226 (2019).

25. Gong, C. *et al.* Revealing the Role of Fluoride-Rich Battery Electrode Interphases by Operando Transmission Electron Microscopy. *Adv. Energy Mater.* **11**, 2003118 (2021).

26. Peng, Z., Freunberger, S. A., Chen, Y. & Bruce, P. G. A reversible and higher-rate Li-O2 battery. *Science (80-.).* **337**, 563–566 (2012).

27. Bucci, G. & Christensen, J. Modeling of lithium electrodeposition at the lithium/ceramic electrolyte interface: The role of interfacial resistance and surface defects. *J. Power Sources* **441**, (2019).

28. Masias, A., Felten, N., Garcia-Mendez, R., Wolfenstine, J. & Sakamoto, J. Elastic, plastic, and creep mechanical properties of lithium metal. *J. Mater. Sci.* **54**, 2585–2600 (2019).

29. Citrin, M. A. *et al.* From ion to atom to dendrite: Formation and nanomechanical behavior of electrodeposited lithium. *MRS Bull.* 1–14 (2020). doi:10.1557/mrs.2020.148

30. Xu, C., Ahmad, Z., Aryanfar, A., Viswanathan, V. & Greer, J. R. Enhanced strength and temperature dependence of mechanical properties of Li at small scales and its implications for Li metal anodes. *Proc. Natl. Acad. Sci.* **114**, 57–61 (2017).

31. Hänsel, C. & Kundu, D. The Stack Pressure Dilemma in Sulfide Electrolyte Based Li Metal Solid-State Batteries: A Case Study with Li_6PS_5Cl Solid Electrolyte. *Adv. Mater. Interfaces* 2100206 (2021). doi:10.1002/admi.202100206

32. Liu, G. *et al.* Densified Li_6PS_5Cl Nanorods with High Ionic Conductivity and Improved Critical Current Density for All-Solid-State Lithium Batteries. *Nano Lett.* **20**, 6660–6665 (2020).

Chapter 6. Perspectives and Future Work

Previous studies demonstrated that Li dendrite formation can occur in all-solid-state batteries, leading to short-circuit and cell failure, despite the rigid nature of solid electrolytes. To enable the large-scale application of all-solid-state batteries, the failure mechanisms of all-solid-state batteries must be well understood, to guide the effective strategies that can eliminate Li dendrite formation. This thesis demonstrated the degradation behaviours of void formation and dendrite formation on Li stripping/plating, respectively, at the Li/SE interface. While the dendrite formation on plating directly leads to cell failure, the void formation on stripping leads to interfacial current loss, local current flux enhancement, and eventually dendrite formation and cell failure on the subsequent plating. In order to maximise the current density that an all-solid-state battery can be charged and discharged at, future efforts are needed to prevent void and dendrite formation, based on mechanisms revealed in this thesis.

The results presented in **Chapter 3** reveal that the void accumulation only takes place when Li is stripped from the interface at above the CCS, and that the CCS can be increased with the external stack pressure applied to the cell. It is also shown in **Chapter 3**. that a combination of moderate stack pressure and increased cycling temperature can effectively increase the CCS. However, maintaining a stack pressure of a few MPa is likely to be expensive and technically challenging in practice-relevant conditions. In order to achieve reliable cycling at current densities comparable with commercial liquid state batteries (5.0 mA/cm^2), further measures must be taken. One promising approach is to improve the Li diffusion at the interface with the application of an alloy interlayer. The alloy interlayer not only brings about a fast Li diffusion to the interface but also serves as a buffer layer to maintain the interfacial contact. Recent studies suggest that intercalation materials for Li, such as graphite, can also serve as the anode interlayer to avoid void formation. Further investigations need to be conducted to mechanistically understand the role of the interlayer and optimise the cell performance. In

addition, the interfacial protrusion shown in **Chapter 3** addresses the importance of understanding the interfacial reactivity. The observation of interfacial protrusion on Li_3N electrolyte, which is believed to be stable against Li, and the associated void accumulation, highlights the importance of an advanced understanding of interfacial stability, especially during electrochemical operation. Future work will focus on the characterisation of the decomposition product, as well as the theoretical explanation of why the interfacial protrusion takes place.

The results presented in **Chapter 4** reveal that the dendrite formation in all-solid-state batteries begins with solid electrolyte spallation and that the dendritic crack propagation is far ahead of the Li deposition that fills the dry crack and leads to cell short-circuit. The fact that dendrites in all-solid-state batteries propagate as a dry crack, and is later filled by lithium deposition, suggests that dendrite formation in all-solid-state batteries is likely to be prevented with solid electrolyte toughening that blocks the dry crack propagation. Work is now underway to explore the effectiveness of fibre reinforcement and transformation toughening on blocking the dendrite formation in all-solid-state batteries. While the mechanistic investigation on dendrite propagation has guided strategies to block the dendrite, the origin of spallation and its fundamental correlation with a transverse crack remain unclear. As the precursor of dendrite formation and cell failure, future efforts should focus on the mechanistic investigation of spallation and effective prevention.

The work in **Chapter 5** demonstrates the whole process of dendrite initiation and propagation in all-solid-state batteries. Models have been proposed to explain the dendrite initiation and dendrite propagation, respectively, based on the experimental observations. Future work in the short term will focus on the proper determination of local fracture strength, fracture toughness of solid electrolyte, and the mechanical properties of lithium metal in a small scale. As highly sensitive materials to the atmosphere, reliable mechanical properties of lithium and solid electrolyte are rare in literature. Proper mechanical tests are underway with specially designed experimental equipment. As the dendrite initiation has been attributed to the hydrostatic stress

build-up due to the Li deposition into a pore connected to the interface, pore filling and solid electrolyte densification need to be investigated as promising approaches to prevent dendrite formation. While SPS has been employed in this work to densify the solid electrolyte, with success, systematic investigation is still needed to densify the solid electrolyte to the greatest extent. In the same spirit, filling the pores with a second phase, such as polymer, could serve as an effective strategy to prevent dendrite initiation, and thus shall be investigated. Regarding the dendrite propagation, in addition to the approaches of ceramic toughening, the effect of pressure on dendrite propagation needs to be addressed. With the removal of the stack pressure, the CCD for propagation has been effectively improved in this work, suggesting cell charge at a rate comparable with liquid state batteries is achievable in all-solid-state batteries by simply removing the stack pressure. Although stack pressure seems critical during stripping to eliminate void formation, could a pressureless stripping be achieved with interfacial modification, a practical all-solid-state battery for large-scale application could be within reach.